3-24-2016

Tunable Terahertz Metamaterials with Germanium Telluride Components

Christopher H. Kodama

TUNABLE TERAHERTZ METAMATERIALS WITH GERMANIUM TELLURIDE COMPONENTS

THESIS

Christopher H. Kodama, Second Lieutenant, USAF

AFIT-ENG-MS-16-M-025

DEPARTMENT OF THE AIR FORCE
AIR UNIVERSITY

AIR FORCE INSTITUTE OF TECHNOLOGY

Wright-Patterson Air Force Base, Ohio

AFIT-ENG-MS-16-M-025

TUNABLE TERAHERTZ METAMATERIALS WITH GERMANIUM TELLURIDE COMPONENTS

THESIS

Presented to the Faculty

Department of Electrical and Computer Engineering

Graduate School of Engineering and Management

Air Force Institute of Technology

Air University

Air Education and Training Command

In Partial Fulfillment of the Requirements for the

Degree of Master of Science in Electrical Engineering

Christopher H. Kodama, BS

Second Lieutenant, USAF

March 2016

AFIT-ENG-MS-16-M-025

TUNABLE TERAHERTZ METAMATERIALS WITH GERMANIUM TELLURIDE COMPONENTS

Christopher H. Kodama, BS

Second Lieutenant, USAF

Committee Membership:

Ronald A. Coutu, Jr., Ph. D.
Chairman

Michael Havrilla, Ph. D.
Member

Michael A. Marciniak, Ph. D.
Member

AFIT-ENG-MS-16-M-025

Abstract

Terahertz (THz) technology is an emerging field with many exciting applications. THz waves can be used to locate explosives and illicit drugs in security applications, or DNA and other molecule resonances in medical applications. THz frequencies represent the next level of modern, high-speed computing, but they also can be used for covert battlefield communications links. Metamaterials are an integral part of THz technology because they can be used to create exotic material properties—permittivities and permeabilities—in a part of the frequency spectrum that is otherwise rather empty and passive. This work aims to acquire a fuller understanding of THz metamaterials in terms of background and theory, and then use this understanding to create a few novel, actively tunable structures using the phase-change material germanium telluride.

Acknowledgements

I would like to thank several people for helping me with my thesis. I could not have done it all without ample mentorship from my advisor, Dr. Coutu, especially during the fabrication and troubleshooting of my devices. The cleanroom lab technicians Rich Johnston and Adam Fritzche were invaluable in my project as well. Rich trained me on several pieces of equipment in the cleanroom and performed several metal deposition runs on my request; Adam helped set up much of the equipment that I used in the test lab.

I am grateful to Maj Jim Sattler, Maj Tod Laurvick, and Capt Rob Lake for always being available for questions and discussion, as well as assisting me with various processes in the cleanroom such as mask generation and metal deposition. I would especially like to thank Capt Lake for revising the final drafts of my thesis. The assistance I received from Brian Crabtree for custom parts, Jason Hickey for metal evaporation, Doug McFarland for wafer dicing, and Eric Kreit for inkjet printing is greatly appreciated. My thanks also goes to Capt Alex Gwin, for helping me during the initial phases of my project and being willing to answer a few of my questions even after being transferred out-of-state. I would also like to thank Capt Jimmy Lohrman for being a great and cheerful fellow classmate and colleague. With a class of only two Master's students total in the microelectronics program, my time here would have been a lot more solitary without him.

Finally, I would like to thank my family for encouraging me to apply for AFIT, and Elena Chong Loo for her patient support and encouragement during the most difficult times of my thesis work.

Table of Contents

List of Figures

List of Tables

TUNABLE TERAHERTZ METAMATERIALS WITH GERMANIUM TELLURIDE COMPONENTS

1. Introduction

Many physical properties of a material, such as refractive index or Poisson's ratio, are actually the result of taking the averaged response of billions of atoms after being exposed to some force [1]. This force is typically caused by electromagnetic [1] or acoustic waves [2]. In the field of metamaterials, "meta-atoms" are designed to create an effective material response similar to the one that atoms would provide. For electromagnetic metamaterials, these meta-atoms need to be at least an order of magnitude smaller than the wavelength of the desired operating frequencies [1].

The appeal of electromagnetic metamaterials is the ability to artificially create custom material characteristics (refractive index, dielectric constant, permeability constant) without having to depend on the fixed characteristics of existing materials. These metamaterials can also be designed to have exotic properties not seen in any natural material. V. G. Veselago was the first person to consider the physical properties that would result from negative values of permeability and permittivity, and in 1968, he wrote a paper describing these effects. Materials with simultaneously negative permittivity and permeability are known as left-handed media [1].

Electromagnetic waves in left-handed media travel with a negative phase velocity, and exhibit negative refraction on a boundary between an ordinary and a left-handed medium. Further examination of the phenomenon of negative refraction reveals that left-handed concave and convex lenses have reversed behavior, and a flat slab of left-handed material can even be utilized as a lens [3]. Other exotic effects include inverse versions of

the Doppler effect, Cerenkov radiation (i.e. radiative shock waves induced by high-speed particles traveling through a dielectric medium), and Goos-Hänchen shift (i.e. a finite lateral shift between an incident beam of finite extent and its reflected counterpart) [1].

Although Veselago had established some theoretical groundwork for understanding negative-index materials, experimental demonstration of such materials would not occur for another thirty years [3], [4].

The first serious examination into the fabrication of materials with specialized effective permeabilities and permittivities was performed by J. B. Pendry in the late 1990s. In 1998, he theoretically and experimentally demonstrated that a thin wire mesh would be able to excite low frequency plasmons, meaning that the mesh could have customized, and even negative, effective (homogeneous) permittivity values at lower frequencies [4]. A year later, he proposed a dual split-ring resonator (SRR) structure which could similarly produce a desired effective permeability (including negative values) in the GHz range [5]. The structures he proposed, especially the split-ring resonator structure, are now ubiquitous in metamaterial devices at all frequencies.

The unique properties of metamaterials make them prime candidates for research in the RF and photonics fields, where metamaterials can be used for applications such as lensing, beam steering, and phase shifting. Metamaterials have also greatly advanced the field of cloaking by freeing up the restriction of only being able to use naturally occurring materials and their material properties. Several different cloaking techniques have already been demonstrated using metamaterials [6]–[9].

Another field that can greatly benefit from the use of metamaterials is the rather new field of terahertz (THz) devices and technology. THz technologies have a myriad of military and scientific applications, ranging from covert battlefield communications, to explosives screening and biomedical imaging, to space astronomy [10]. THz-range metamaterials have micron-sized (10^{-6}) dimensions, which are easily fabricated with micromachining techniques commonly used for microelectromechanical systems (MEMS) and integrated circuits.

The purpose of this work is to design, simulate, and fabricate novel meta-atom structures in the THz frequency range. In particular, germanium telluride (GeTe) will be analyzed for its applicability to create actively tunable THz metamaterials (MMs).

2. Literature Review

2.1. The Terahertz Spectrum: Concepts and Applications

The terahertz region is defined as the range of frequencies from 300 GHz to 10 THz [10], [11]. This corresponds to free-space wavelengths from 1 mm to 30 μm. The THz region defined on various scales is shown in Fig. 1. This range of frequencies is typically referred to as the "THz Gap" because of the historical inability of most electrical and optical methods to produce waves in this frequency range [10], [11].

2.1.1. THz Generation

From the perspective of electrical devices, the amplifiers and diodes that are required to create THz radiation would need to have incredibly fast switching speeds which are beyond the capabilities of most modern, high-speed electronic devices. However, research on the fabrication of THz-range electrical components is ongoing and making progress [12]–[14]. For example, methods such as diode-based harmonic

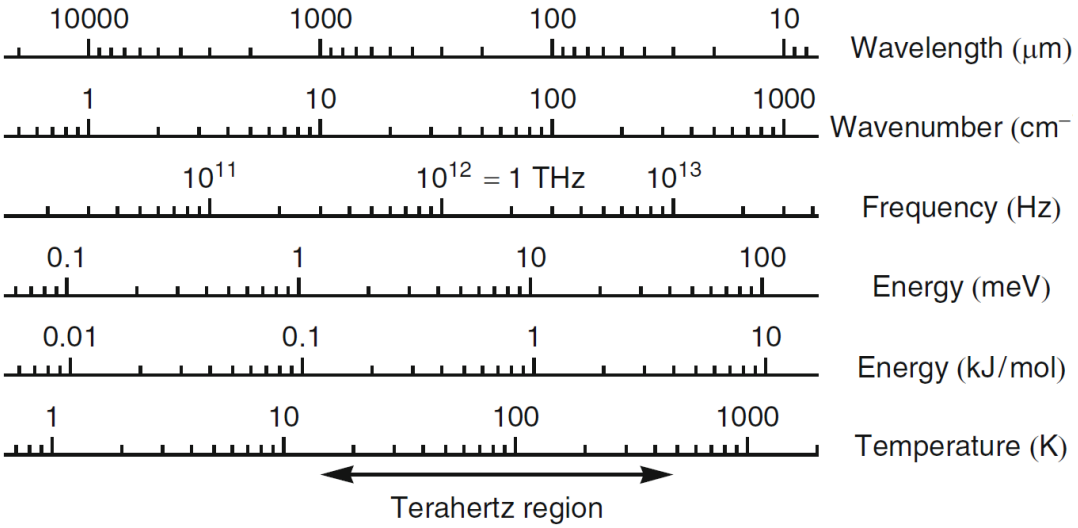

Fig. 1. The terahertz region, shown with respect to several different scales [10]**.**

generators and backward wave oscillators have been developed to produce radiation in the low THz range [10].

From the optical device viewpoint, THz waves are difficult to generate because THz photon energies are much smaller than the bandgaps of ordinary semiconductors (e.g. 1 THz photon has an energy of 4.14 meV). Therefore, in order to generate THz waves via electron band transitions, structures such as superlattices and others are required to artificially create the necessary band structure to support THz radiation [15].

Most typical methods currently utilized to generate THz waves do not generally fall directly in the electrical (antenna-like) or optical (photons from electron band transitions) categories. Most of these methods require significant infrastructure and are best suited for laboratory applications. For example, the first sources of THz radiation were from radiative emissions of thermally heated solids and plasmas at around 1000 to 5000 K [10]. Another technology, which can be used to make radiation of almost any frequency, is a free electron laser (FEL). An FEL produces radiation by sending an electron beam through a large array of north and south magnets known as a “wiggler” [15]. The magnetic field forces the electrons to oscillate, which causes them to radiate at the oscillation frequency. THz waves can also be created with certain molecular lasers. Laser excitation of methanol (CH_3OH) creates transitions between rotational energy states of the methanol molecules, which in turn emit THz radiation [15]. Rectification of optical signals via nonlinear crystals can also produce THz radiation, analogous to the operation of diodes rectifying an AC signal [15].

All of the methods described above essentially create single- or harmonic-frequency THz radiation. If a more broadband signal is desired, like for spectroscopy applications, a photoconductive antenna can be used instead. In a photoconductive antenna, electrons in a high-mobility semiconductor such as gallium arsenide (GaAs) are photo-excited with a femtosecond laser pulse, and then accelerated (and causing radiation) due to the presence of a strong DC bias voltage. The physics of this process will be examined in detail in a later section.

2.1.2. THz Applications: Communications

Despite difficulties in producing THz radiation, there is much motivation behind present research in the THz regime. For instance, THz waves have a niche application in communications [16]. THz wave communication is desired in order to make faster communications links, since it would be three orders of magnitude faster than current wireless signaling frequencies. Due to the directivity of THz radiation, any THz communication link would have to be line-of-sight [10]. The strong attenuation of certain THz frequencies through water vapor also places some limitations on bandwidth, as shown in Fig. 2. With these properties in mind, the main applications for THz communications are short range / indoor and satellite communications links, where the main disadvantages to THz waves are mitigated [16].

One additional application for THz communication is for secure military communication links. The Federici text summarizes the main characteristics and advantages of THz communications in this context, as described below.

> Some of the characteristics of THz systems which enable them to operate as secure communications links are (a) highly directional beams compared to microwave communications at the same transmitter aperture; (b) less scattering of radiation compared to IR wireless; (c) limited propagation distance due to atmospheric attenuation; (d) large channel bandwidth for spread spectrum techniques which enable anti-jamming and low probability of detection systems; and (e) hidden THz signals in the background noise [16].

These characteristics put it at an advantage over both IR and microwave communications links in some aspects.

2.1.3. THz Applications: Spectroscopy

One of the most promising applications for THz technology is spectroscopy [11]. Since the rotational and vibrational resonant frequencies of many liquid and gaseous

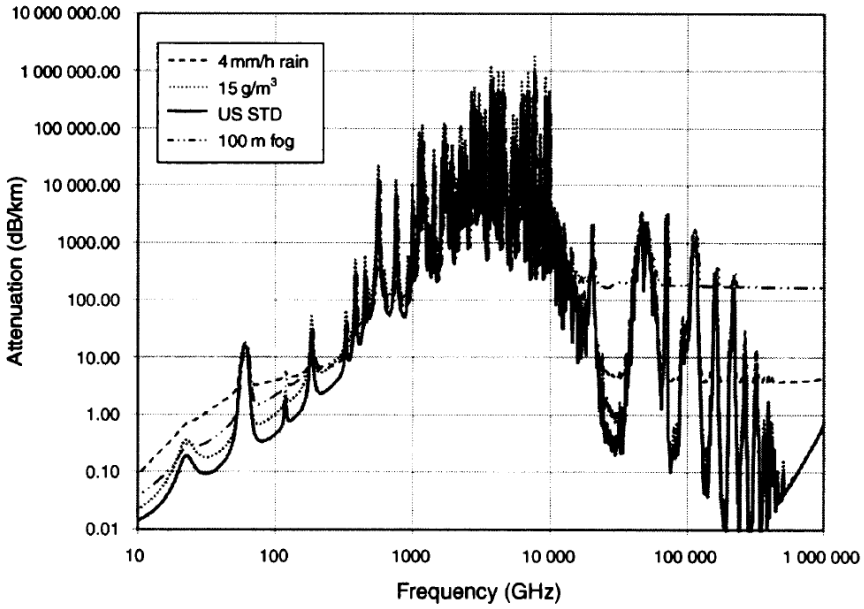

Fig. 2. Atmospheric attenuation from the gigahertz to the infrared range [16]**.**

molecules are in the THz range [11], materials can be uniquely characterized by their THz “signature” using THz spectroscopy [17]–[19]. At frequencies below 3 THz, THz time-domain spectroscopy is preferable over far-IR Fourier transform spectroscopy due to an improved signal-to-noise ratio [20]. In addition, spectroscopy can help determine the fit parameters of electrical device models, such as the Drude model for metals, as well as, advanced superconductor models and dielectric constants of thin films [21]. THz spectroscopy is also applicable in the medical field, because the vibrational modes of many biological molecules, such as DNA and protein, are in the THz region and are detectable via spectroscopy.

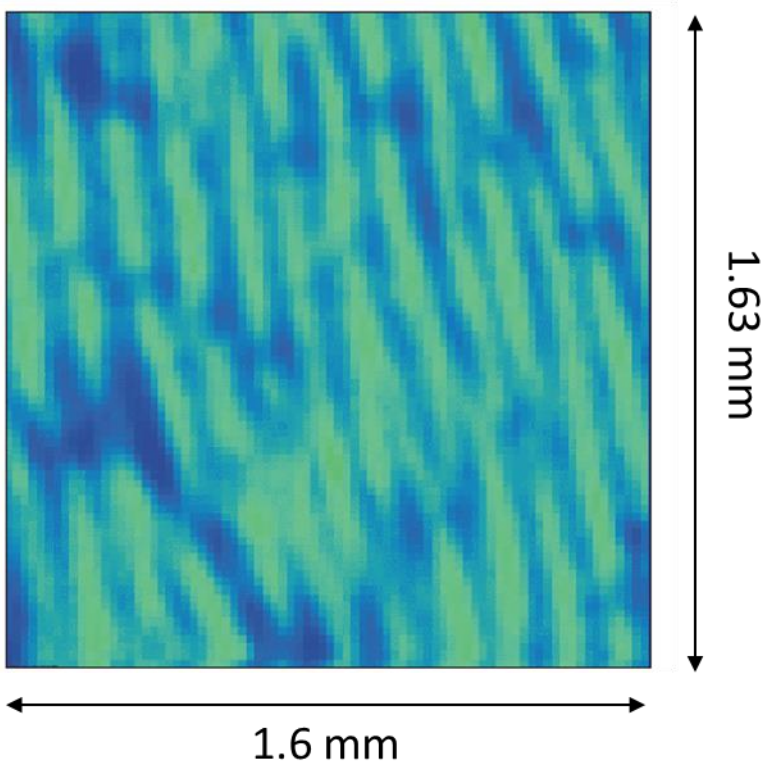

Fig. 3. Falsely colored image of an onion cell membrane, where the tissue membrane structure is clearly visible [21]**.**

Table 1. Absorbance peak points of some dangerous and illegal materials [22].

Material	Feature band centre position frequency (THz)	Reference
Explosive		
Semtex-H	0.72, 1.29, 1.73, 1.88, 2.15, 2.45, 2.57	[12]
PE4	0.72, 1.29, 1.73, 1.94, 2.21, 2.48, 2.69	[12]
RDX/ C4	0.72, 1.26, 1.73	[12, 14, 27]
PETN[a]	1.73, 2.51	[12]
PETN[b]	2.01	[16]
HMX[a]	1.58, 1.91, 2.21, 2.57	[12]
HMX[b]	1.84	[16]
TNT[a]	1.44, 1.91	[12]
TNT[b]	1.7	[16]
TNT	5.6, 8.2, 9.1, 9.9	[20, 27]
NH_4NO_3	4, 7	[16, 22]
Drugs		
Methamphetamine	1.2, 1.7–1.8	[23]
MDMA	1.4, 1.8	[23]
Lactose α-monohydrate	0.54, 1.20, 1.38, 1.82, 2.54, 2.87, 3.29	[12]
Icing sugar	1.44, 1.61, 1.82, 2.24, 2.57, 2.84, 3.44	[12]
Co-codamol	1.85, 2.09, 2.93	[12]
Aspirin, soluble	1.38, 3.26	[12]
Aspirin, caplets	1.4, 2.24	[12, 23]
Acetaminophen	6.5	[19]
Terfenadine	3.2	[19]
Naproxen sodium	5.2, 6.5	[19]

[a] Samples are prepared as pellets using spectrographic-grade polyethylene.
[b] Samples are ordered as compressed pellets from Accurate Energetics LLC. All materials are in sensitized form (water-free).

As an extension to spectroscopy, spectral THz scans can be taken over a two-dimensional space and pieced together to form images, like the one shown in Fig. 3. In this fashion, THz imaging can be used for many applications, such as studying cellular structure in biological applications, or for quality control of large sheets of dry, dielectric materials [21]. Near-field techniques applied to THz waves can help increase the resolution of THz imaging as well.

THz spectroscopy also has applications in security screening. THz waves can pass through most nonmetal materials, such as packaging, cardboard, clothing, and shoes, without much attenuation [22]. Many explosives, as well as chemical and biological

agents, have characteristic THz signatures, which can be identified with spectroscopy and are distinguishable from normal materials, such as clothing and skin [22]. Table 1 shows a list of some materials and their THz resonances. Dangerous but nonmetal items, like ceramic knives, can also be distinguished with THz screening [23]. The scan resolution of THz screening is also better than existing, millimeter-wave systems due to the smaller THz wavelengths. Studies have shown that typical THz scanning systems would pose a minimal health risk to both the operators and the people being scanned [22]. THz energy quickly dissipates as heat in the first 100 microns of skin tissue, due to the high water content in skin [22].

2.1.4. Theory of THz Time-Domain Spectroscopy

The main method of performing spectroscopy in the THz frequency range is through THz Time-Domain Spectroscopy (THz-TDS). In THz-TDS, broadband THz pulses are Fourier-transformed in order to obtain spectral data. Unlike some other methods of spectroscopy, THz-TDS has the advantage of capturing phase information about detected THz signals [11]. One main method of producing a broadband THz signal is with photoconductive generation on a high-speed semiconductor.

2.1.4.1. Photoconductive THz Generation

Electromagnetic waves can be generated by accelerating electrical charges. Strongly accelerated electric currents produce radiating waves with a broad bandwidth. These are the fundamental principles behind the physics of the photoconductive THz antenna. Fig. 4 describes the THz generation process in six steps.

The image in Fig. 4(a) is a top level view of the generating structure on the substrate. The black lines represent metal wires (i.e. a coplanar waveguide) connected to

a DC voltage. The substrate is a high-mobility semiconductor, such as GaAs, and the arrows represent the electric field produced by the DC voltage. In Fig. 4(b), a laser is pulsed in the femtosecond range onto the substrate. If the photon energy of the laser pulse is larger than the bandgap energy of the semiconductor, free carriers will be

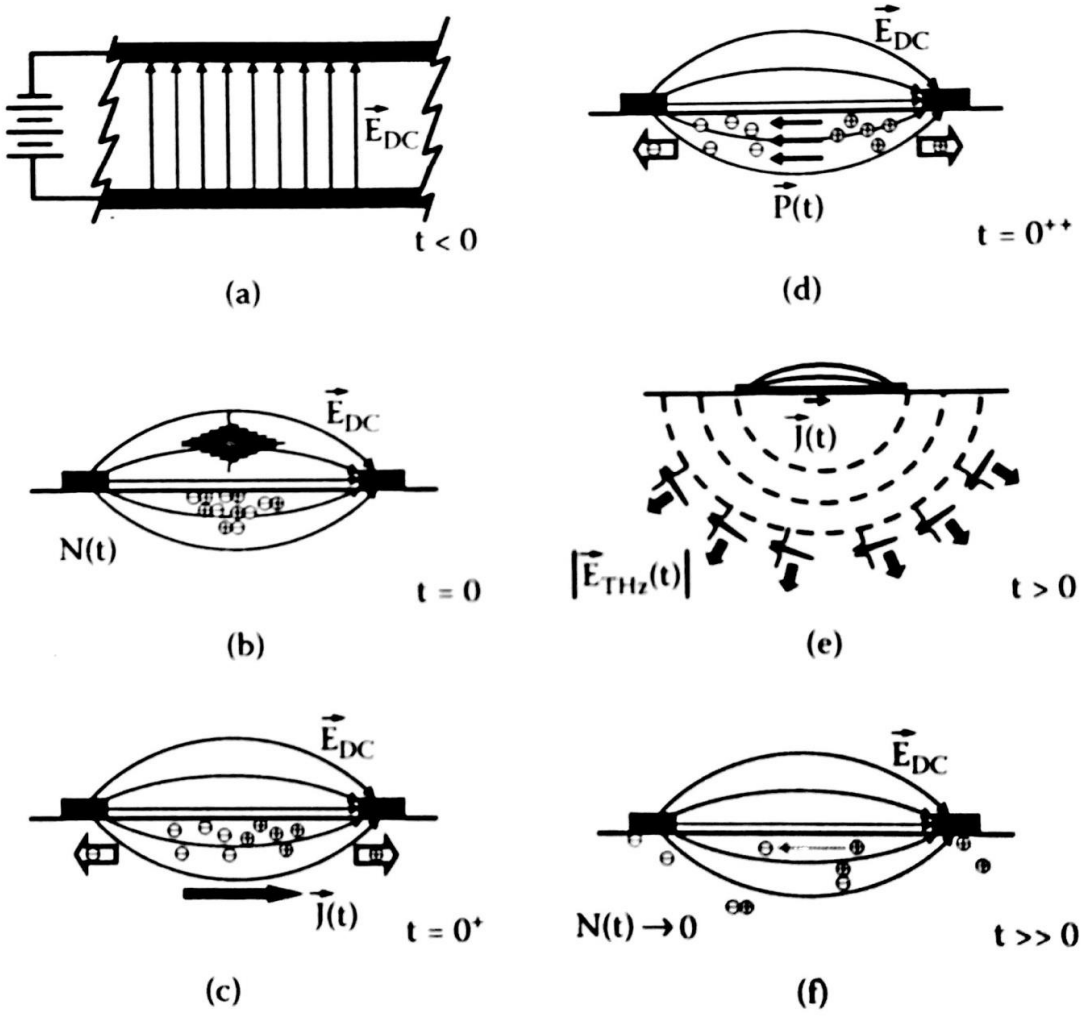

Fig. 4. Photoconductive terahertz generation. The high voltage bias in (a) allows the photoexcited electrons produced in (b) to accelerate rapidly, producing a strong current (c) and polarization field (d). This results in broadband terahertz radiation (e) until the electron distribution reaches equilibrium (f) [11]**.**

spontaneously created in the semiconductor. These free carriers will be strongly accelerated immediately upon creation, due to the presence of the DC electric field. These steps are shown in Fig. 4(c) and 4(d). The accelerated charges then generate electromagnetic radiation, as shown in Fig. 4€, and then eventually recombine back into a steady state condition, as in Fig. 4(f).

The photoconductive process can be understood on a more analytical level by examining how the electric field evolves over time. The electric field is caused by the moving charge carriers in the GaAs substrate, which in turn are generated by the incoming laser pulse. The carrier density evolves over time as

$$N(t) = \int_0^t G(\tau)d\tau - N_0 e^{-\frac{t}{\tau_c}}, \quad (1)$$

where $G(\tau)$ is the generation rate, τ_c is the carrier lifetime, and N_0 is the total number of carriers generated [11]. The integral term in the carrier density equation describes N(t) at time scales of the laser pulse, while the second term describes the evolution of the carrier density at longer times [11]. From the carrier density equation, the current density as a function of time can be described by

$$J(t) = N(t) \cdot e \cdot v(t), \quad (2)$$

where e is the carrier charge and v(t) is the carrier velocity [11]. In order to determine the time-dependent velocity of the carriers, the forces acting upon the charges must be considered. The carriers are simultaneously accelerated by the static electric field in the substrate and decelerated via lattice scattering. This can be modeled by the differential equation

$$\frac{dv(t)}{dt} = -\frac{v(t)}{\tau_s} + \frac{e}{m^*}E(t), \\ = -\frac{v(t)}{\tau_s} + \frac{e}{m^*}\left(E_{DC} + P(t)\right), \tag{3}$$

where τ_s is the characteristic scattering time, m^* is the carrier effective mass, E_{DC} is the static electric field, and $P(t)$ is the polarization field. The electric field in the substrate consists of two components: the DC electric field E_{DC} artificially introduced via the coplanar waveguide, and the oppositely oriented polarization field $P(t)$ caused by the separation of charges in the material. The two components are shown in Fig. 4(d). The polarization field changes over time according to

$$\frac{dP(t)}{dt} = -\frac{P(t)}{\tau_R} + N(t) \cdot e \cdot v(t), \tag{4}$$

where τ_R is the carrier relaxation time. The equations for velocity and polarization field form a system of differential equations which is sufficient enough to solve for $P(t)$ and $v(t)$. Then, using $J(t)$ and $P(t)$, Maxwell's equations for a current source,

$$\nabla \times \vec{E}_{RAD}(t) = -\mu \frac{\partial \vec{H}_{RAD}(t)}{\partial t}, \\ \nabla \times \vec{H}_{RAD}(t) = \vec{J}(t) + \varepsilon_0 \frac{\partial \vec{E}_{RAD}(t)}{\partial t} + \frac{\partial \vec{P}(t)}{\partial t}, \tag{5}$$

can be used to determine the radiated fields. These equations model a Hertzian dipole in a dielectric half-space, which has numerical and analytical solutions [11]. One key property of a Hertzian dipole in a dielectric half-space is that significantly more radiation is

emitted through the dielectric side rather than through the air side, by a factor of n^3, where n is the index of refraction of the dielectric. This significantly enhances the directivity of the antenna and aids in the collection and collimation of the radiated THz fields [11]. Modifications to the substrate geometry can help further shape the THz radiated beam.

2.1.4.2. Photoconductive Detection

Photoconductive detection is similar in theory to photoconductive radiation. An illustration of the THz detection/sampling scheme is shown in Fig. 5. In this method, a laser pulse is aimed at a gap between two metal lines on a high-speed semiconductor, as shown in Fig. 5(d). When the laser is fired, the excitation temporarily creates a conductive bridge between the two metal strips, due to the photo-excitation of carriers in the semiconductor gap. If, at the exact time the laser is fired, there happens to be a THz wave passing through the gap (shown in Fig. 5(b) and 5(c)), then the THz electric field will affect the carriers and induce a small current in the setup.

The induced small current can then be detected after being passed through a high-sensitivity current amplifier. One iteration of this method can reveal one ‘time slice’ of the THz wave by looking at how much current was induced at each time interval, as shown in Fig. 5€. By sending the exact same THz pulse numerous times and varying the relative delay of the laser pulse, one can piece together the full shape of a THz wave.

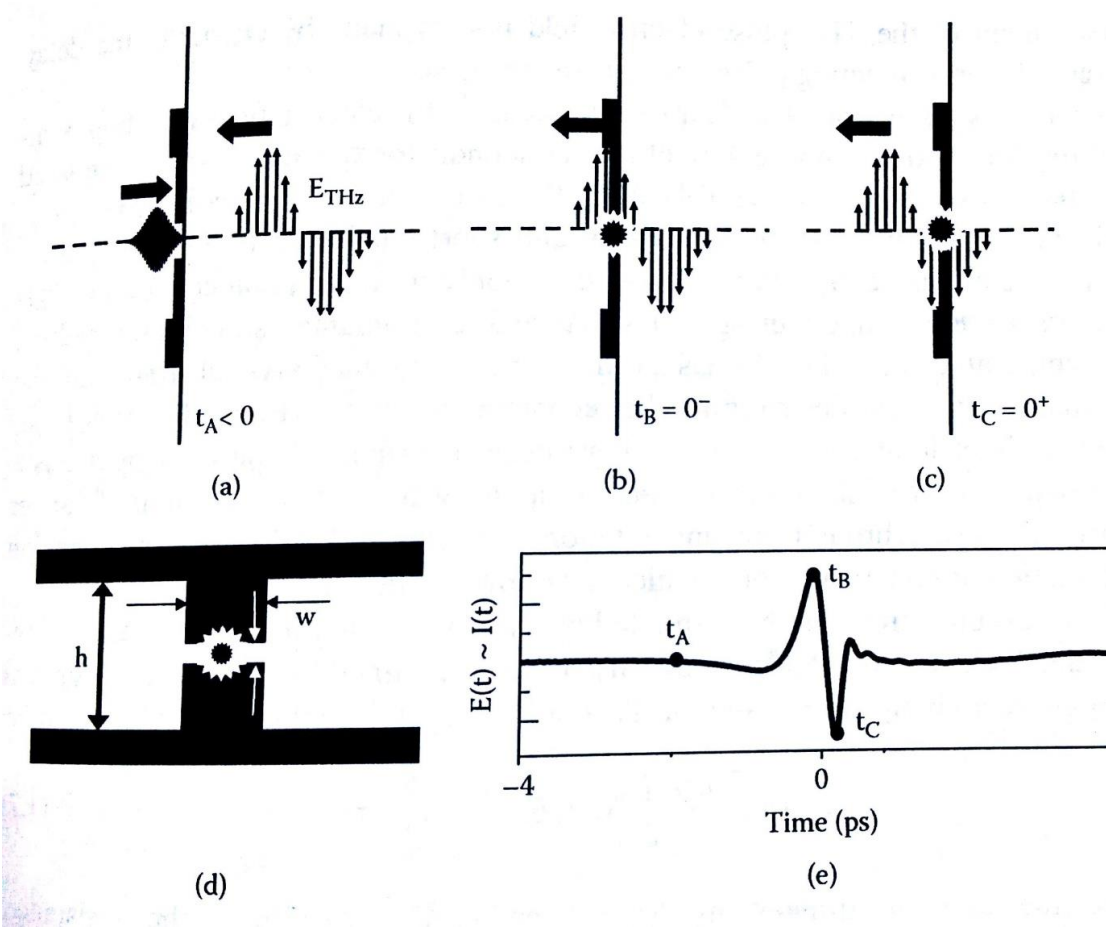

Fig. 5. Detecting terahertz radiation. A terahertz pulse is sent many times, incident to a gap between metal lines on a semiconducting substrate. At each iteration, a laser pulse with varying time delay is sent to the same gap, temporarily creating a conductive bridge and allowing the terahertz pulse to be sampled at that moment in time [11]**.**

2.1.5. Analysis of THz-TDS data

After collecting the full waveform of a THz pulse, the data needs to be Fourier-transformed in order to analyze its spectral components [11]. Fig. 6(a) shows the waveform of a THz pulse propagating through nitrogen, and the solid line in Fig. 6(b) shows the spectrum of that pulse. The dips in the transmission at 5.2 and 8.0 THz are

absorptions caused in the detector and the emitter [24]. This is important to note, as these dips will appear in every measurement taken with this particular test setup. The dashed line of Fig. 6(b) represents the spectrum of a pulse that propagated through a polytetrafluroethylene (PTFE) sample. This spectrum contains two additional dips at 15.1 and 19.2 THz. Since these dips were not present in the previous pulse, it is evident that these two notches represent resonances caused by the PTFE sample; in this specific case, these two dips were caused by the scissoring and wagging vibrations of carbon fluoride (CF_2) molecules [24].

In order to isolate the resonances of a sample measurement from the resonances of the measurement system, the spectrum of the sample can be divided by the response of an "empty" pulse containing no sample—this pulse is typically referred to as the "reference" pulse [15], [25], [26], and the resulting quotient is typically referred to as the transmission spectrum [24]. This quotient is defined as

$$\mathrm{T} = \frac{\mathrm{E}_{\mathrm{sample,received}}}{\mathrm{E}_{\mathrm{reference,received}}}, \tag{6}$$

where $\mathrm{E}_{\mathrm{sample,received}}$ is the measured spectrum of the sample pulse and $\mathrm{E}_{\mathrm{reference,received}}$ is the measured spectrum of the reference pulse. The absorbance function is also commonly used when examining resonant points of material responses:

$$\mathrm{A} = -20\log_{10}|T|. \tag{7}$$

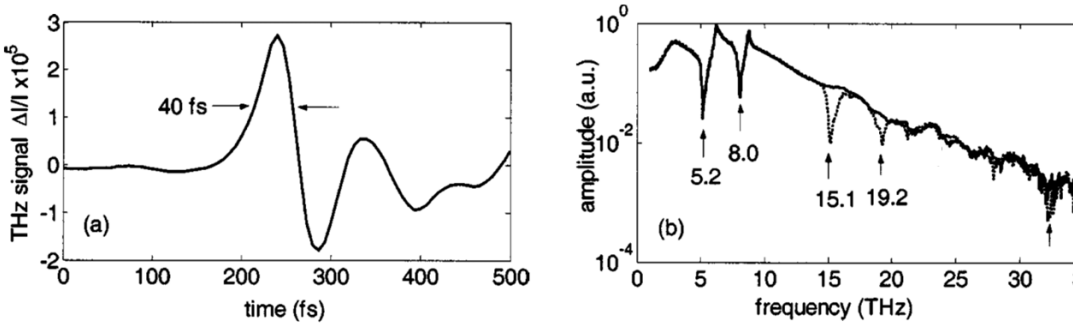

Fig. 6. (a) The temporal electric field amplitude of a terahertz pulse propagating through nitrogen. (b) The amplitude spectrum of two terahertz pulses. The solid line is the spectrum of the pulse shown in (a). The dashed line is the spectrum of a pulse that propagated through a polytetrafluroethylene sample [27]**.**

When looking at the absorbance of a material, resonant points are represented by peaks, as shown in Fig. 7. THz-TDS can provide an easy method of identifying a material if its resonant peaks are known.

2.1.5.1. Substrate Characterization

In addition to characterizing materials by their THz resonances, THz-TDS can be used to accurately calculate the complex index of refraction of materials [27]. The complex index of refraction $\tilde{n}$, defined as

$$\tilde{n} = n - ik, \tag{8}$$

gives two pieces of information that can help identify and characterize materials [25]. The real component of $\tilde{n}$, typically called n, is the same as the standard index of refraction, and represents the relative speed of light the material compared to light traveling in vacuum. The imaginary component, referred to as k, accounts for the amount of energy dissipation which occurs when light travels through the material.

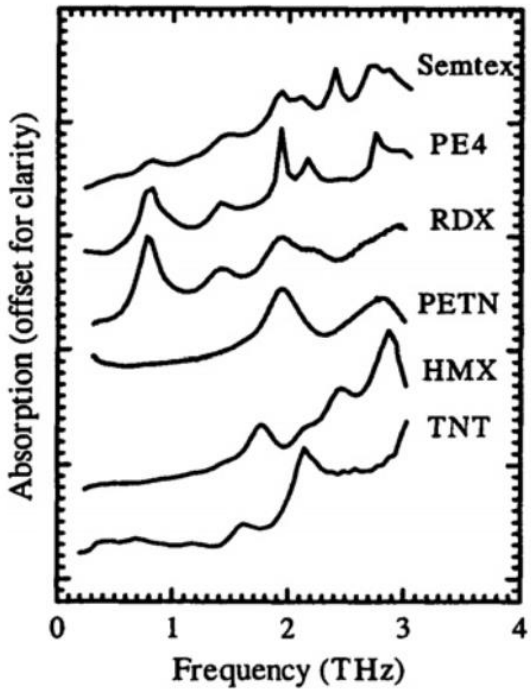

Fig. 7. Absorbance spectra of various drugs and explosives. The resonant peaks of each material are clearly distinguishable [22]**.**

For metamaterial (MM) applications, materials with a real component of $\tilde{n}$ close to unity are typically desired because they cause less frequency "red-shifting" to occur in the resonant frequency of MMs fabricated on the material (compared to the resonant frequency of an array of MMs suspended in free space). In addition, the amount of loss in a metamaterial usually needs to be minimized, so k is desired to be as small as possible.

Accurate values for $\tilde{n}$ cannot be determined directly from THz-TDS measurements in the lab, but rough estimates can be produced. If a rough approximation is all that is needed, the complex index of refraction can be calculated by only using time and amplitude data from the figure as well as some arithmetic. If one makes the approximation of linear phase dispersion, the index of refraction is calculated using

$$n = c\frac{\Delta t}{L} + 1, \tag{9}$$

where n is the index of refraction, c is the speed of light, Δt is the time delay between the reference and sample pulse maxima, and L is the thickness of the sample [15]. In addition, the imaginary component k can be approximated by using the above-calculated refractive index and the spectral data of the pulses as

$$k = -\frac{c}{\omega L}\ln\left(\frac{\tilde{E}_s}{\tilde{E}_r \cdot T_L}\right), \tag{10}$$

where k is the attenuation coefficient, ω is the angular frequency (i.e. $2\pi f$), E_r is the Fourier-transformed reference E field, E_s is the Fourier-transformed sample E field, and

$$T_L = \frac{4n_{sample}}{\left(n_{sample} + 1\right)^2}. \tag{11}$$

These simple equations can be used if the material is linear, i.e. the dispersion and attenuation of light through the material is linear. For a more general result which can produce dispersive, frequency-dependent complex indices of refraction, an iterative approximation process must be used.

In order to understand the derivation behind the iterative process, the transmission path of the THz pulse during a THz-TDS measurements must be examined and mathematically modeled. Fig. 8 shows the optical paths of THz beams during a reference measurement and a sample measurement.

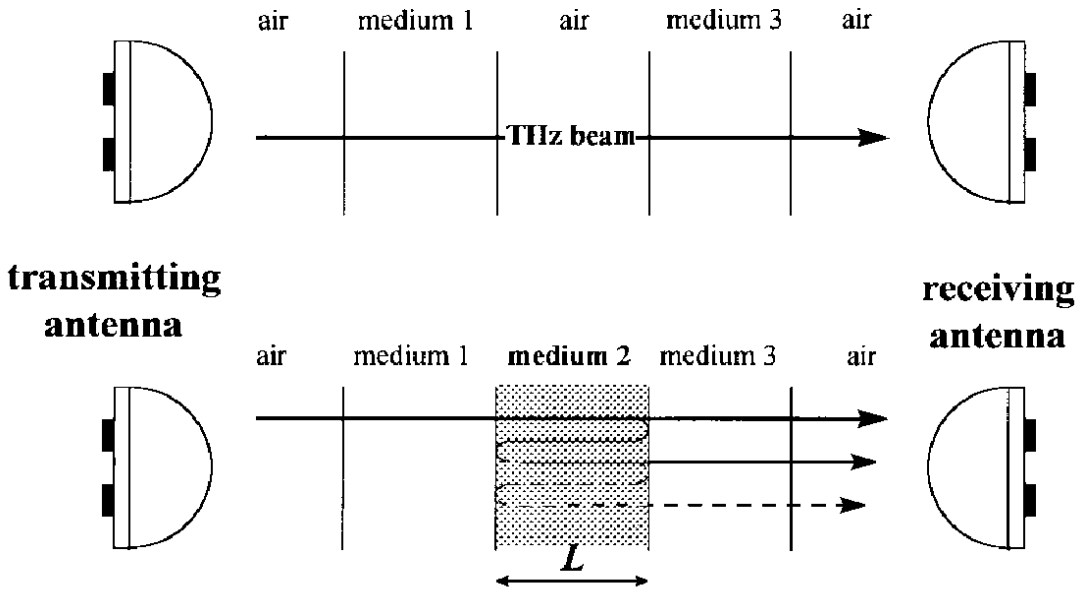

Fig. 8. Path of the terahertz beam, with and without the sample. With modifications [25]**.**

The transmission spectrum, which the THz-TDS system can measure, is defined as the ratio between the sample and reference electric fields at the receiving antenna side [25]:

$$T = \frac{E_{sample,received}}{E_{reference,received}} = \frac{E_{sample,received}/E_{transmitted}}{E_{reference,received}/E_{transmitted}} = \frac{S_{sample}}{S_{reference}}, \quad (12)$$

where $E_{sample,received}$ is the received sample spectrum, $E_{reference,received}$ is the received reference spectrum, $E_{transmitted}$ is the transmitted pulse spectrum, S_{sample} is the transmission coefficient of the sample measurement, and $S_{reference}$ is the transmission coefficient of the reference measurement.

$E_{sample,received}$ and $E_{reference,received}$ are directly measured from THz-TDS, and can be used to calculate the transmission spectrum, T, from measured data. S_{sample} and $S_{reference}$ cannot be determined from the measured data, since they require $E_{transmitted}$, which is not measured using THz-TDS. As Equation (12) shows, however, the ratio of $E_{sample,received}$ to $E_{reference,received}$ is equivalent to the ratio of S_{sample} to $S_{reference}$.

S_{sample} and $S_{reference}$ are important to the extraction process because these quantities can be put in terms of the complex index of refraction of the material under test. S_{sample} and $S_{reference}$ can be modeled by determining the electromagnetic reflection, transmission, and propagation coefficients between the various interfaces. These coefficients, when looking at an interface between a material 'a' with $\tilde{n}_a$ and a material 'b' with $\tilde{n}_b$, are defined by the following equations [26]:

$$T_{ab} = \frac{2\tilde{n}_a}{\tilde{n}_a + \tilde{n}_b}, \tag{13}$$

$$R_{ab} = \frac{\tilde{n}_a - \tilde{n}_b}{\tilde{n}_a + \tilde{n}_b}, \tag{14}$$

$$P_a(z) = \exp\left[-\mathrm{j}\frac{\tilde{\mathrm{n}}_\mathrm{a}\omega\mathrm{d}}{\mathrm{c}}\right]. \tag{15}$$

The last equation, $P_a(z)$, describes the phase shift and attenuation that occurs when light passes a distance z through material 'a.' With these definitions, the S_{sample} and $S_{reference}$ can be explicitly defined with the following equations [25]:

$$\mathrm{S_{reference}} = \mathrm{P_{air}(L)}, \tag{16}$$

$$\mathrm{S_{sample}} = \mathrm{T_{air,sample}} \cdot \mathrm{P_{sample}(L)} \cdot \mathrm{T_{sample,air}} \cdot \mathrm{FP(L)}, \tag{17}$$

$$\mathrm{FP(L)} = \sum_{\mathrm{k=0}}^{\infty} \left\{\mathrm{R_{sample,air}} \cdot \mathrm{P_{sample}(L)} \cdot \mathrm{R_{sample,air}} \cdot \mathrm{P_{sample}(L)}\right\}^{\mathrm{k}}. \tag{18}$$

The FP (Fabry-Perot) term accounts for the infinite amount of delayed internal reflections which inevitably occur during electromagnetic wave transmission through a dielectric. If the acquired data can be properly windowed in order to remove FP reflections, the FP term in the model can be ignored (i.e. FP = 1).

S_{sample} and $S_{reference}$ can be used to determine the transmission coefficient, which is what is measured with using THz-TDS, in terms of the complex $\tilde{n}$ of the sample. If the reference is an open air measurement, then the following equation can be utilized to find the sample index of refraction [25]:

$$\begin{aligned} \mathrm{T} &= \frac{\mathrm{S_{sample}}}{\mathrm{S_{air}}} \\ &= \frac{4\tilde{\mathrm{n}}_{\mathrm{sample}}\tilde{\mathrm{n}}_{\mathrm{air}}}{\left(\tilde{\mathrm{n}}_{\mathrm{sample}} + \tilde{\mathrm{n}}_{\mathrm{air}}\right)^2} \cdot \exp\left[-\mathrm{j}\left(\tilde{\mathrm{n}}_{\mathrm{sample}} - \tilde{\mathrm{n}}_{\mathrm{air}}\right)\frac{\omega \mathrm{L}}{\mathrm{c}}\right] \cdot \mathrm{FP(L)}, \end{aligned} \tag{19}$$

where $\mathrm{S_{sample}}$ is the transmission coefficient of the sample, $\mathrm{S_{air}}$ is the transmission coefficient of the air reference, $\tilde{\mathrm{n}}_{\mathrm{sample}}$ is the complex index of refraction of the sample, $\tilde{\mathrm{n}}_{\mathrm{air}}$ is the complex index of refraction of the air used in the reference measurement, j is the imaginary constant, ω is angular frequency, L is the length of the sample, c is the speed of light, and FP(L) is the Fabry-Perot term, as a function of sample length.

Due to the complexity of the above transmission equation, $\tilde{\mathrm{n}}_{\mathrm{sample}}$ cannot be precisely found by substituting in the measured transmission and using algebra, unless some simplifying assumptions are made. Instead, an iteration scheme must be used to approximate $\tilde{\mathrm{n}}_{\mathrm{sample}}$. The first method described here was developed by Duvillaret *et al.*

in 1996. They used a modified Newton-Rhapson root-finding method to solve for the complex index of refraction. Instead of taking the direct difference of the measured and approximate transmission values, they utilized a cost function which took the difference between the logarithms and the phases of the measured and approximate transmission coefficients; this modification helps find solutions that are smooth and continuous. Their cost function δ is defined as

$$\begin{aligned} \delta &= \delta\rho^2 + \delta\phi^2, \\ \delta\rho &= \ln[|T|] - \ln[|\mathrm{T}_{\mathrm{measured}}|], \\ \delta\phi &= \arg[T] - \arg[\mathrm{T}_{\mathrm{measured}}], \end{aligned} \tag{20}$$

where δ is the cost function, $\mathrm{T}_{\mathrm{measured}}$ is the measured transmission spectrum, and T is the modeled transmission spectrum [25].

With their cost function δ, they defined their iterative steps using the matrix equation

$$\begin{bmatrix} n_{p+1} \\ k_{p+1} \end{bmatrix} = \begin{bmatrix} n_p \\ k_p \end{bmatrix} - A^{-1} \cdot \vec{\nabla}\left\{\delta\left(\begin{bmatrix} n_p \\ k_p \end{bmatrix}\right)\right\}, \tag{21}$$

where A is the hessian matrix (matrix of second partial derivatives) of δ, and $\vec{\nabla}\delta$ is the gradient of δ [25]. For their initial estimates, they used

$$\begin{aligned} n_0 &= n_1 + \frac{arg[\mathrm{T}_{\mathrm{measured}}]}{\omega L/c}, \\ k_0 &= -\frac{c}{\omega L}\ln X\,, \end{aligned} \tag{22}$$

where ω is the angular frequency, L is the length of the sample, n_1 is the index of air, c is the speed of light, $T_{measured}$ is the measured transmission coefficient, and X is the solution to the cubic equation,

$$\begin{aligned} &AX^3 + X = D, \\ &A = \frac{(n_2 - n_1)(n_2 - n_3)}{(n_2 + n_1)(n_2 + n_3)} \cdot \cos\left(2n_2 \frac{\omega L}{c}\right), \\ &D = \frac{(n_2 + n_1)(n_2 + n_3)}{2n_2(n_1 + n_3)} \cdot \exp\left(-k_{air} \frac{\omega L}{c}\right) \cdot |T_{measured}|, \end{aligned} \tag{23}$$

where n_2 is the sample index, n_3 is the index of the material behind the sample, and k_{air} is the attenuation constant of air [25].

This method is difficult to implement, since it requires gradients, Hessian matrices, and roots to a cubic polynomial. The advantage of this method, though, is that it generates very accurate results regardless of substrate thickness.

A much simpler method, known as fixed-point iteration, was developed by Withayachumnankul *et al.* in 2005. His iteration steps and starting values were defined as

$$\begin{aligned} n_{p+1} &= n_{\text{air}} - \frac{c}{\omega L}\left\{\arg[T_{\text{measured}}] - \arg\left[\frac{4\left(n_p - j \cdot k_p\right) \cdot \tilde{n}_{\text{air}}}{\left(\left(n_p - j \cdot k_p\right) + \tilde{n}_{\text{air}}\right)^2}\right]\right\}, \\ k_{p+1} &= -\frac{c}{\omega L}\left\{\ln|T_{\text{measured}}| - \ln\left|\frac{4\left(n_p - j \cdot k_p\right) \cdot \tilde{n}_{\text{air}}}{\left(\left(n_p - j \cdot k_p\right) + \tilde{n}_{\text{air}}\right)^2}\right|\right\}, \\ n_0 &= n_{\text{air}} - \frac{c}{\omega L}\arg[T_{\text{measured}}], \\ k_0 &= -\frac{c}{\omega L}\ln|T_{\text{measured}}|, \end{aligned} \tag{24}$$

where n_{p+1} is the next iteration of index approximation, n_{air} is the index of refraction of air, c is the speed of light, ω is the angular frequency, L is the sample length, $T_{measured}$ is

the measured transmission coefficient, n_p is the current iteration of index approximation, k_{p+1} is the next iteration of attenuation constant approximation, k_p is the current iteration of the attenuation constant approximation, $\tilde{n}_{air}$ is the complex index of refraction of air, n_0 is the initial guess for index, and k_0 is the initial guess for attenuation constant [26].

This method is very simple to implement, requiring only complex function evaluations and algebra. However, this method does not converge for all possible scenarios. Fig. 9 shows the region of convergence for this method.

2.1.6. Summary

The THz spectrum has a lot of potential for novel applications, ranging from communications to bomb screening. Unfortunately, due to the fact that most materials are

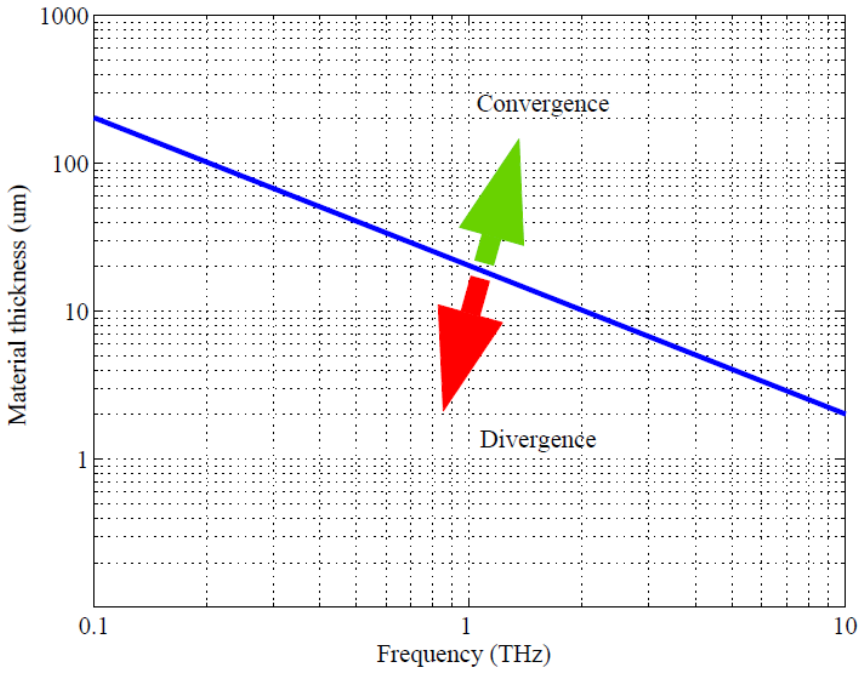

Fig. 9. Convergence line for the fixed-point iteration method for terahertz material extraction [26]**.**

transparent in the THz frequency range, controlling THz waves via modulation and other techniques is much more difficult when compared to electronic or optical devices and systems. This is where metamaterials can potentially play a large role. Since metamaterials can, in theory, be specifically designed to have certain material properties, they can interact with THz waves in ways that normal materials cannot [28], [29].

2.2. Split-Ring Resonator Characterization

The split-ring resonator (SRR), first proposed by Pendry in 1999, is the fundamental unit cell used in a multitude of metamaterial designs [5], [28]–[45]. As the name suggests, SRRs are sub-wavelength devices shaped like a split ring, meant to resonate when coupled with a certain frequency of electromagnetic light. The first SRRs proposed by Pendry consisted of two circular, concentric rings, as shown in Fig. 10(a). For the sake of simplicity and ease of fabrication, SRRs fabricated in the THz range typically have the shape shown in Fig. 10(b).

Although in theory, pieces of metal in any geometrical shape can be utilized as a resonator (albeit at frequencies determined by the geometry), the SRR has two characteristics that make it desirable for use in metamaterials. Firstly, the SRR couples well with the magnetic portion of electromagnetic waves due to its loop-like structure.

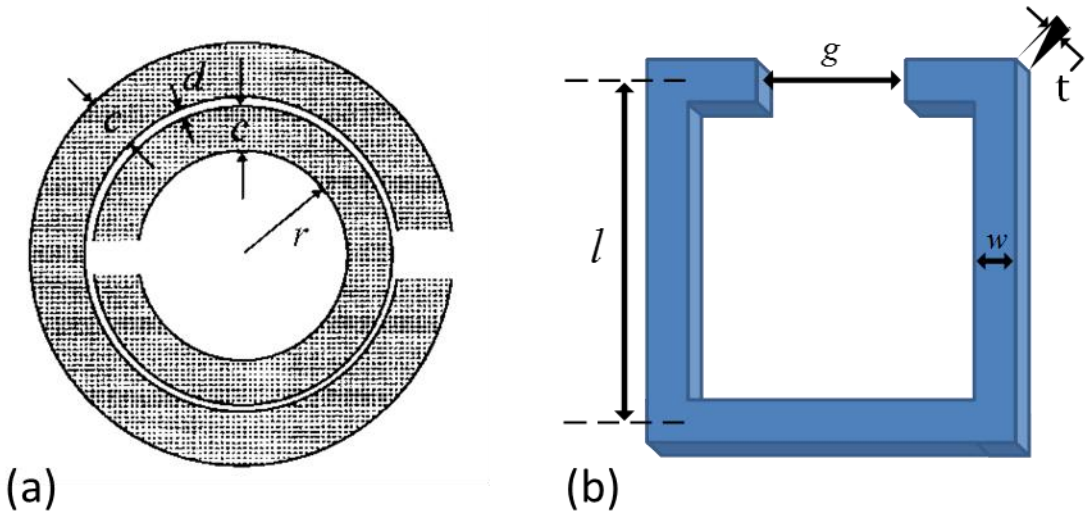

Fig. 10. (a) Original SRR proposed by Pendry [3]; (b) One typical SRR used in current terahertz research [29]**.**

This potentially allows SRR-containing metamaterials to have a frequency band with negative permeability.

Second, the SRR can be easily conceptualized as a simple LC resonator circuit, which allows one to quickly predict its lowest order resonant frequency. As a base-level approximation, the entire loop (ignoring the gap) can be considered as a one-turn inductor, and the gap can be modeled as a parallel-plate capacitor. These quasi-static assumptions require that the dimensions of the SRR be much smaller than the wavelength of electromagnetic fields assumed to be passing through them, which conveniently is the same requirement needed to produce effective material properties from metamaterials. The wavelength of electromagnetic waves in free space at 1THz is 300 microns, so metamaterials designed to operate in this range should have dimensions of around 30

microns or less. The basic equations for the inductance and capacitance and the estimated resonant frequency equation are

$$L \approx \mu_0 \frac{l^2}{t}, \tag{25}$$

$$C \approx \varepsilon_r \varepsilon_0 \frac{t\,w}{g}, \tag{26}$$

$$f_{ideal} \approx \frac{1}{2\pi}\sqrt{\frac{1}{LC}} = \frac{1}{2\pi}\frac{c}{\sqrt{\epsilon_r}}\sqrt{\frac{g}{wl^2}}, \tag{27}$$

where t is the thickness of the SRRs, μ_0 is the vacuum permeability constant, l is the SRR side length, ε_r is the relative dielectric constant, ε_0 is the vacuum permittivity constant, w is the line width of the SRR, g is the gap width of the SRR, and c is the speed of light in vacuum [44], [46], [47]. This model can only predict the resonant frequency within an order of magnitude. If more accuracy is desired, more precise equations need to be utilized for the inductance and capacitance terms. These would account for non-idealities such as the finite width of the wire in inductance calculations and the fringing electric fields in capacitance calculations.

2.2.1. Inductance Modeling

The inductances of various loop shapes were studied extensively by many parties in the 19th and early 20th centuries, including Maxwell, Kirchoff, Coursey, Lyle, and Nagaoka [46], [47]. Many of the formulas and approximations developed during this time were collected, organized, and published by Grover and Rosa, in a series of journal publications geared toward engineers [47]–[50]. There are several inductance formulas

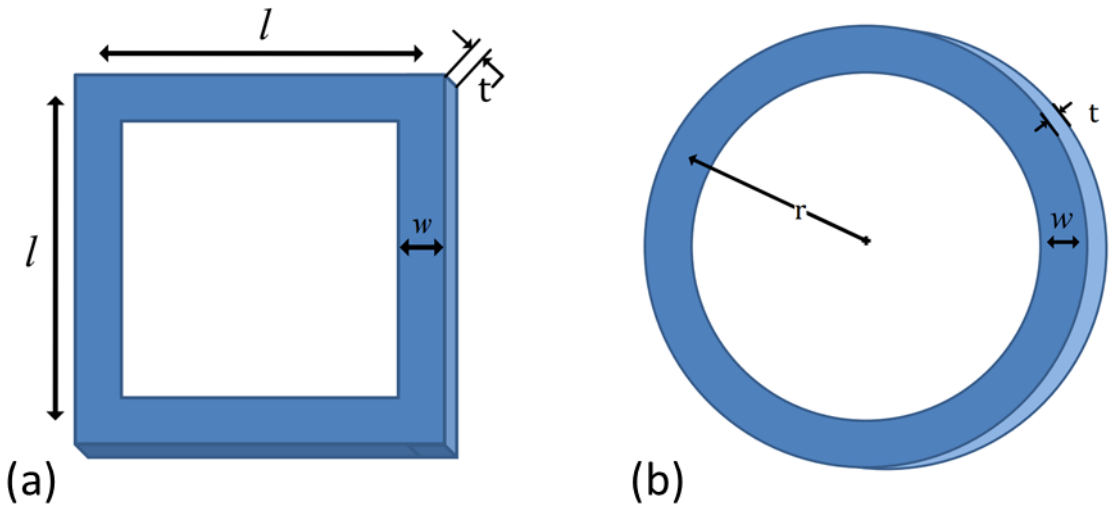

Fig. 11. Loop models used for calculating inductance: a) square loop b) circular loop.

that are applicable for split-ring resonator loops, depending on the amount of accuracy or simplicity desired.

The inductance of a typical THz-range SRR is modeled as a square loop with a modest wire width and a relatively small thickness, as shown in Fig. 11(a). Photolithographic diffraction limitations prevent the wire width from being too small, and the wire thickness is usually limited by the metal deposition process. The gap in the SRR is assumed to be negligible for the inductance calculation.

One way of approximating the loop inductance in Fig. 11(a) is by breaking down the loop into smaller sections, each with a partial inductance [51]. The loop can be simplified to two pairs of identical parallel lines: a horizontal set A and a vertical set B. The total inductance of set A can be calculated by adding together the self-inductances of

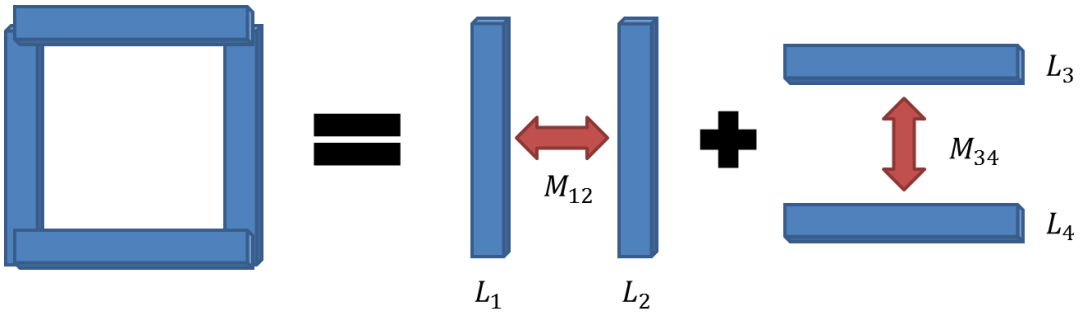

Fig. 12. Splitting of a loop inductance into partial self and mutual inductances. The red terms are subtracted from the sum of the blue terms.

the two parallel lines and subtracting twice the mutual inductance of the parallel lines from that sum; the same can be done for set B, as shown in Fig. 12. With

$$L_A = L_1 + L_2 - 2\,M_{12}, \tag{28}$$

$$L_B = L_3 + L_4 - 2\,M_{34}, \tag{29}$$

the total inductance is then $L_A + L_B$ minus the mutual inductance between the two sets. However, since the lines in sets A and B are perpendicular to each other, there is no mutual inductance between the two sets:

$$L_T = L_A + L_B - 2\,M_{AB} = L_A + L_B. \tag{30}$$

This simplifies the problem into finding the self-inductances of rectangular bars and the mutual inductances between parallel bars. One final consideration involves the precise dimensions of the straight inductors in the model, as shown in Fig. 13. Utilizing four equal pieces like in Fig. 13(a) would simplify equations, since that would result in $L_1 = L_2 = L_3 = L_4$ and $M_{12} = M_{34}$, but does not fully account for the corners of the square loop [51]. Fig. 13(b) more accurately models the loop, but requires the calculation

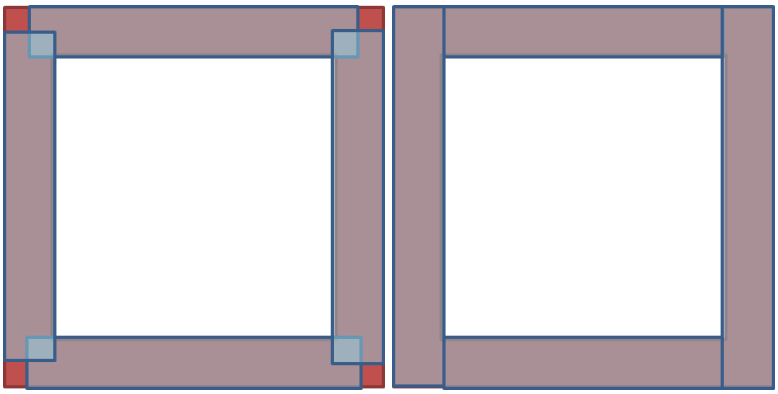

Fig. 13. Methods of modeling a square inductor loop, using (a) identical inductor segments for simplicity, or (b) different segments for accuracy.

of two different inductor segments. The basic equation for the self (or mutual) inductance of any geometric bar is dependent on two parameters, its length l and another parameter:

$$L = 2\frac{\mu}{4\pi}\left[l\ln\left(\frac{l+\sqrt{l^2+R^2}}{R}\right)-\sqrt{l^2+R^2}+R\right], \quad (31)$$

$$M = 2\frac{\mu}{4\pi}\left[l\ln\left(\frac{l+\sqrt{l^2+D^2}}{D}\right)-\sqrt{l^2+D^2}+D\right], \quad (32)$$

where R and D represent geometric mean distances: R is the geometrical mean width of the cross section of the bar; D is the geometric mean distance between two bars, each with a specific cross-section. Geometric mean distance formulas can be calculated using the method described in [47]. For rectangular bars, the R and D values are shown in equations (33) and (34). For parallel rectangular bars, the geometric mean distance D is approximately equal to the center-to-center distance between the two bars [47]. The resulting equations are

$$\mathrm{R_{Bar}} = \sqrt{t^2 + w^2}\exp\left[-\frac{1}{6}\frac{t^2}{w^2}\ln\left(\sqrt{1 + \frac{w^2}{t^2}}\right)\right.$$
$$-\frac{1}{6}\frac{w^2}{t^2}\ln\left(\sqrt{1 + \frac{t^2}{w^2}}\right) + \frac{2}{3}\frac{t}{w}\tan^{-1}\frac{w}{t} \quad (33)$$
$$\left.+\frac{2}{3}\frac{w}{t}\tan^{-1}\left(\frac{t}{w}\right) - \frac{25}{12}\right] \approx 0.2235(w + t),$$

$$\mathrm{D_{Bar}} = d, \quad (34)$$

where the variables in the equations correspond to the dimensions in Fig. 14.

Since the SRRs have small thicknesses, the bars can alternatively be modeled as coplanar, infinitesimally thin tapes. In this approximation, the values of R and D are

$$R_{Tape} = w\, e^{3/2}, \quad (35)$$

$$D_{Tape} = d^{-\left(\frac{d^2}{w^2}\right)}(-w + d)^{\frac{(w-d)^2}{2\,w^2}}(w + d)^{\frac{(w+d)^2}{2w^2}}e^{3/2}, \quad (36)$$

where the variables in the equations correspond to the dimensions in Fig. 14.

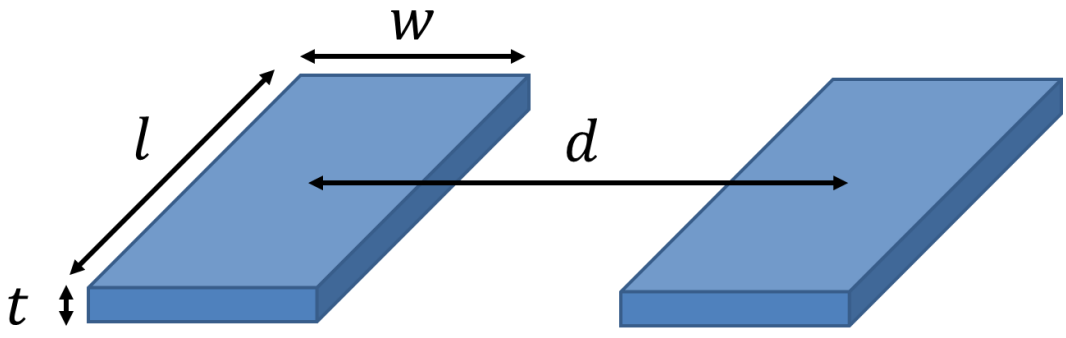

Fig. 14. Labeled dimensions of an inductive bar pair.

Another useful model is the inductance between two parallel, thin plates. In this model, w in Fig. 14 would vanish to zero, while t remains finite. The resulting equations are

$$R_{Plate} = t\, e^{3/2}, \tag{37}$$

$$D_{Plate} = \exp\left[\frac{1}{2t}\left(4d\tan^{-1}\frac{t}{d} + t(-3+\ln[d^2+t^2]) - \frac{d^2\ln\left[1+\frac{t^2}{d^2}\right]}{t}\right)\right], \tag{38}$$

where the variables in the equations correspond to the dimensions in Fig. 14.

Although it seems to detract from the model, neglecting the wire thickness can be a valid assumption for SRRs due to high frequency effects, as shown in Fig. 15. At DC, current is uniformly distributed throughout the metal it is flowing through. At frequencies above DC, the alternating current becomes constrained (i.e. due to eddy currents) in the outer "skin" of the metal, with the skin having an effective thickness known as the "skin depth" [47]. The skin depth is a function of frequency and the losses in the metal. At high enough frequencies, the skin depth becomes infinitesimally small and the current can be thought of as flowing along the surface of the conductor. For the square loop, the current would flow along the inner edge of the loop, since this would be the shortest path, and thus the least resistive path.

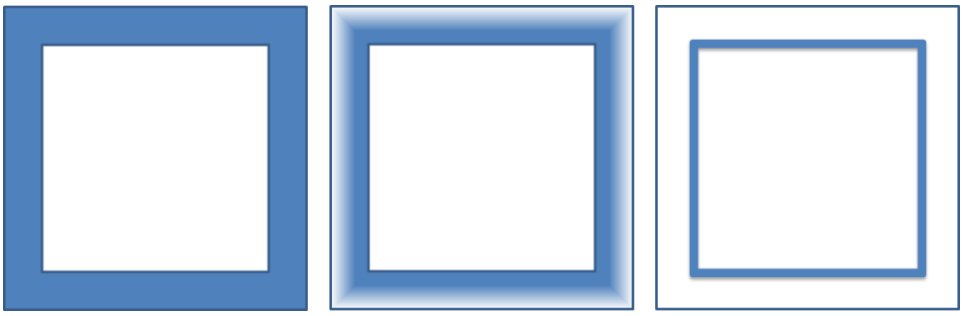

Fig. 15. Changes in current distribution in an inductive loop, ranging from DC on the left to high frequencies on the right

Although SRR in consideration is square, there are also several closed-form expressions for the inductance of a circular loop that provide good approximations [47]. A circular loop with an equivalent enclosing area as the square, such that $l^2 = \pi\, r^2$, is expected to have an inductance which is slightly smaller than that of the square loop [48]. Maxwell's approximate formula below applies to circular loops with a rectangular cross-section. This model is used in several other papers, including [44] and [43], although with many of the higher order terms neglected:

$$L_{Maxw} = \mu\, r \left(\log\left(8\frac{r}{R_{Bar}}\right)\left(1 + \frac{3R_{Bar}^2}{16r^2}\right) - \left(2 + \frac{R_{Bar}^2}{16r^2}\right)\right) \qquad (39)$$

where R_{bar} is the geometric mean distance of a metal bar and r is the radius of the circular loop [47].

A formula by Weinstein corrected some slight errors in Maxwell's derivation, resulting in a much more complicated equation,

$$
\begin{aligned}
&\mathrm{L_{Wein}} = \mu\, r\, (\lambda + \gamma),\\
&\lambda = \ln\frac{8r}{w} + \frac{1}{12} - \frac{\pi x}{3} - \frac{1}{2}\ln(1+x^2) + \frac{1}{12x^2}\ln(1+x^2\,)\\
&\qquad\qquad + \frac{1}{12}x^2\ln\left(1+\frac{1}{x^2}\right) + \frac{2}{3}\left(x-\frac{1}{x}\right)\tan^{-1}x\,,\\
&\gamma = \frac{\mathrm{w}^2}{96r^2}\left[\left(\ln\frac{8r}{w} - \frac{1}{2}\ln(1+x^2)\right)(1+3x^2) + 3.45x^2 + \frac{221}{60}\right.\\
&\qquad\qquad - 1.6\pi x^3 + 3.2x^3\tan^{-1}x - \frac{1}{10}\frac{1}{x^2}\ln(1+x^2)\\
&\qquad\qquad \left. + \frac{1}{2}x^4\ln\left(1+\frac{1}{x^2}\right)\right],
\end{aligned}
\tag{40}
$$

where $\mathrm{x} = \mathrm{t}/\mathrm{w}$, t is the thickness of the loop, and w is the width of the loop wire [47].

Rayleigh and Niven derived the following formula for the inductance of a short, thin circular loop, neglecting the loop width:

$$
\mathrm{L_{RN}} = \mu\, r\left[\ln\frac{8r}{t} - \frac{1}{2} + \frac{t^2}{32r^2}\left(\ln\frac{8r}{t} + \frac{1}{4}\right)\right], \tag{41}
$$

where r is the radius of the loop and t is the thickness of the loop [47].

Similar to the thin, parallel-plate model, this approximation is useful for modeling high-frequency behavior, and has the added benefit of being incredibly simple compared to the other models; in fact, the squared term can typically be neglected without much error.

In the near-infrared and optical frequency range, another inductive term comes into play: kinetic inductance [35], [43]. Kinetic inductance accounts for the inertia of

conduction electrons, which becomes significant when the operating wavelength is on the order of the SRR dimensions. For a split circular ring, the kinetic inductance is

$$L_{Kin} = \frac{(2\pi r - g)}{wt\omega_p^2 \varepsilon_0}, \quad (42)$$

where ω_p is the plasma frequency of the metal, and ε_0 is the free space permittivity constant [44]. For a square loop, the $2\pi r$ in the expression can be replaced with the perimeter of the square.

2.2.2. Capacitance Modeling

Many approximations exist for calculating the fringing capacitance between parallel plates. However, many of these models assume that the plates are moderately square-shaped and have a small gap width. On the other hand, SRRs, especially THz-range SRRs, typically have a relatively large gap due to fabrication limitations, and the capacitance plates are very narrow and wide due to the thin layer of gold used in depositions; the gap capacitance in an SRR deviates strongly from the ideal parallel plate model.

With the goal of finding the capacitance of an arbitrary microstrip patch, Edward Kuester wrote a report in which he collected various capacitance approximations and developed his own solutions. Another valuable source is a book published by Iossel, which describes multiple methods of theoretically determining capacitance and lists many of the resulting formulas as well.

There has been a long history of research on determining the capacitance of circular plates [52]. Disks were preferred in analysis due to their rotational symmetry,

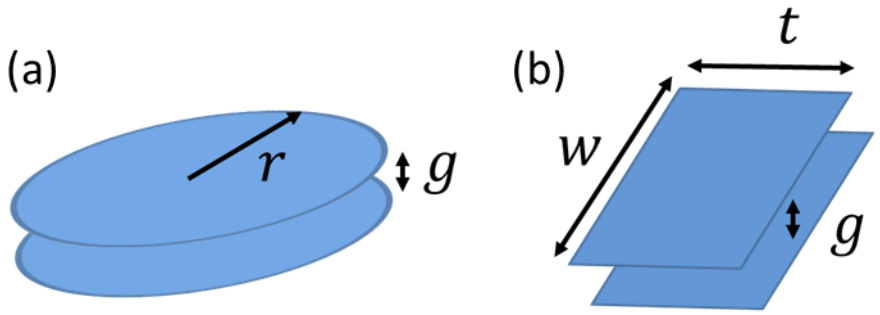

Fig. 16. Dimensions used for capacitance calculations of (a) two circular and (b) two rectangular plates

which leads to simple mathematical descriptions of plates in cylindrical coordinates. Approximations for the parallel-plate capacitance between disks have been calculated by Clausius, Kirchoff, Cooke, Serini, Shaw, and many others [46], [52]–[66]. Unfortunately, as mentioned earlier, all of these assumed a reasonably small gap size, and are not applicable for SRRs. There are a few researchers, notably Boulgakov and Iossel, who studied the opposite extreme, when the gap size between circular plates approached infinity [52]. Boulgakov's formula is

$$C_{Boul} = \frac{2\pi\,\varepsilon\,r}{\tan^{-1}\left(\frac{g}{r}\right)}, \tag{43}$$

where r is the plate radius, g is the gap length between plates, and ε is the permittivity of the material between the plates [52].

Taking the limit when $g \gg r$ and with some slight rearrangement, Boulgakov's formula can be expressed in terms of the self-capacitance of a circular disk as

$$C_{eff} = \frac{\frac{C_0}{2}}{1 - \frac{C_0}{4\pi\varepsilon\, g}}, \tag{44}$$

$$C_0 = 8\,\varepsilon\, r \text{ (for circular plates)}, \tag{45}$$

where r is the plate radius, g is the gap length between plates, and ε is the permittivity of the material between the plates [52].

This form for the capacitance is useful because it suggests that the capacitance between parallel plates of any geometry can be calculated (within the large-gap limit) by replacing C_0 in the formula with the self-capacitance of any desired plate geometry. The self-capacitance of a rectangular plate, which is of interest for the SRR scenario, can be found in two ways. In his text, Iossel provides two approximation formulas for the self-capacitance of a rectangle:

$$C_{Rect1} = \frac{2\pi\varepsilon\, w}{m \ln\left[\frac{1+\sqrt{1+m^2}}{m}\right] + \ln\left[m+\sqrt{1+m^2}\right] + \frac{1}{3m} + N}, \tag{46}$$

$$N = \frac{m^2}{3} - (1+m^2)\frac{\sqrt{1+m^2}}{3m},$$

$$C_{Rect2} = \frac{2\pi\epsilon\, w}{\ln[4\,m]}, \tag{47}$$

where w is the plate width, t is the plate length, ε is the permittivity of the material surrounding the plate, and $m = \frac{w}{t}$ [58]. The first equation was determined by Dwight in the 1930s [59], and is a rough approximation to within 8% [67]. The second approximation is valid for values of $\frac{w}{t} > 100$ [68].

The self-capacitance of a rectangular plate can also be found by first calculating the effective radius of the plate and substituting it in for C_0, or directly into Boulgakov's formula for circular plates:

$$C_0 = 8\,\varepsilon\,r_{eff} \text{ (for arbitrary shapes)}, \tag{48}$$

$$C_{Boul} = \frac{2\pi\,\varepsilon\,r_{eff}}{\tan^{-1}\left(\frac{g}{r_{eff}}\right)} \text{ (for abritrary shapes, } g \gg r), \tag{49}$$

where r_{eff} is the effective circular radius, g is the gap length between plates, and ε is the permittivity of the material between the plates.

For the case of the rectangular plate, Kuester cites an approximation from De Meulenaere and Van Bladel for the effective radius when the plate is wide and thin (w ≫ t) as

$$r_{eff} \approx \frac{w\sqrt{\pi}}{2\ln\frac{4w}{t}}, \tag{50}$$

where w is the width of the rectangular plate and t is the length of the plate [69].

Kuester also derived a semi-empirical capacitance formula for small microstrips in terms of effective radius, which can be adapted to the present parallel-plate capacitance situation with some symmetry observations, namely by setting the microstrip-ground plane height to half the SRR gap length, and halving the subsequent capacitance [52], [58]:

$$\mathrm{C} = \frac{\pi(\varepsilon + \varepsilon_0) r_{eff}}{\tan^{-1}\left[f\left(\frac{\varepsilon}{\varepsilon_0}\right)\frac{(g/2)}{r_{eff}}\right]},$$
$$f(x) = \frac{x-1}{x \ln\frac{2x}{x+1}}, \tag{51}$$

where r_{eff} is the effective circular radius of the plates, g is the gap length between plates, ε is the permittivity of the material between the plates, and ε_0 is the vacuum permittivity constant.

I have also devised an empirical formulation of the square capacitor case, based on the 3D superposition of an exact 2D capacitance solution by Palmer, in an earlier work [70]. Although more accurate than the ideal parallel-plate model, it does not take into account the effects of the corners, and is in general less accurate than Boulgakov's formula. The approximation is

$$C = \beta\varepsilon_0 \frac{w\,t}{g} + \varepsilon_0 \Delta \cdot (w + t) - \varepsilon_0 \left[\mathrm{t}\,\Gamma\left(\frac{w}{g}\right) + w\,\Gamma\left(\frac{t}{g}\right)\right],$$
$$\Gamma(R) = \frac{(1.290)\ln(R)^2 - (5.801)\ln(R) + 6.416}{\ln(R)^2 - (5.782)\ln(R) + 26.971}, \tag{52}$$
$$\beta = 1.0367;\ \Delta = 1.3233,$$

where g is the gap length between plates, w is the width of a plate, t is the length of a plate, and ε_0 is the vacuum permittivity constant [70].

Another capacitive term which needs to be considered for SRRs is the surface capacitance of the ring itself. This term becomes especially important if the gap capacitance is small, which is usually the case when the gap dimension is relatively large.

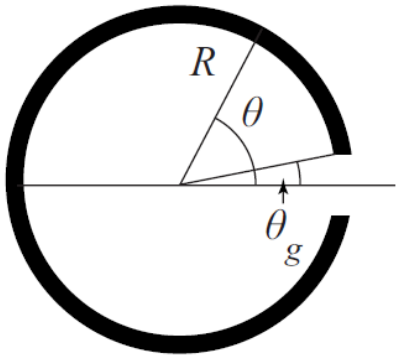

Fig. 17. Top view of SRR used in Sydoruk's derivation, showing relevant parameters. θ_g is approximated as $\frac{g/2}{R}$ [44].

Sydoruk utilized an electric field formulation derived by Allan and Segre for a gapped cylinder in order to find the surface capacitance of an SRR [44]:

$$\begin{aligned} C_{surf} &= \varepsilon_0(t+w)\int_{\theta_g}^{\pi}\frac{\cot\frac{\theta}{2}}{\pi-\theta}d\theta \approx \frac{\varepsilon_0(h+w)}{\pi}\int_{\theta_g}^{\pi}\cot\frac{\theta}{2}d\theta \\ &\approx \frac{2\,\varepsilon_0(h+w)}{\pi}\ln\frac{4R}{g}, \end{aligned} \tag{53}$$

where ε_0 is the vacuum permeability constant, t is the ring thickness, w is the ring width, R is the ring radius as shown in Fig. 17, and g is the length of the gap [44].

As seen in the formula, the surface capacitance integrates over the circumference of the ring. In order to make this formula applicable for square SRRs, a ring with the same perimeter of the square SRR should be used, such that $2\pi R = 2l$. Thus, for a square SRR, the surface capacitance can be roughly approximated as:

$$C_{surf} \approx \frac{2\,\varepsilon_0(h+w)}{\pi} \ln \frac{4l}{g\pi}, \tag{54}$$

where ε_0 is the vacuum permeability constant, t is the loop thickness, w is the loop width, l is the loop length, and g is the length of the gap.

2.2.3. Substrate Effects

All of the inductance and capacitance formulas thus far have assumed that the SRR was suspended in free space. In reality, the SRRs would be placed on top of a dielectric substrate. The substrate will not affect the inductance unless the substrate is magnetic. The capacitance, though, will be increased due to the relative permittivity of the substrate. This will result in a decrease in the resonant frequency of the SRR. Due to the complexity of solving such a problem, the substrate effect is usually accounted for by substituting an empirically determined effective permittivity into the capacitance part of the SRR model.

$$\varepsilon_{eff} = \varepsilon_{r.eff} \cdot \varepsilon_0 = \big(\alpha\,\varepsilon_r + (1-\alpha)\big) \cdot \varepsilon_0, \tag{55}$$

where ε_r is the relative permittivity constant of the substrate, ε_0 is the vacuum permittivity constant, and α is the fill factor coefficient [40]. α can be empirically determined through simulations and is expected to mostly be a function of SRR thickness [40]. It is typically close to 1/2.

2.2.4. Plasmonic Resonances

The lowest order resonance of a SRR can be aptly described by a quasistatic model incorporating capacitors and resistors. The higher order resonances, however, cannot be modeled in such a manner. The original SRR in Fig. 10(a) can be viewed as a

transmission line due to the presence of two distinct conductors, and was modeled as such in [34]. The single SRR in Fig. 10(b) has only one conductor and thus cannot support any transmission line modes. Single SRRs can, however, produce plasmon resonances, which are evanescent modes confined to surfaces. These plasmonic resonances occur at frequencies that have half- wavelengths which are multiples m of the perimeter of the SRR [1]:

$$\mathrm{f_{dip}} = \frac{c}{\sqrt{\varepsilon_{r.eff}}} \frac{1}{(4\,l - g)} \cdot \frac{m}{2}, \tag{56}$$

where c is the speed of light, $\varepsilon_{\mathrm{r.eff}}$ is the effective permittivity constant, l is the side length of the square SRR, g is the gap length of the SRR, and m is a positive integer greater than or equal to 1. In addition, as mentioned by [37], the LC resonance can also be interpreted as the lowest order plasmon resonance, with $\mathrm{m} = 1$ in the above equation.

2.2.5. Effective Homogeneous Properties of SRRs

The permittivity and permeability constants of materials are the macroscopic result of electric and magnetic dipoles on the molecular and atomic scale. Likewise, the effective homogeneous material properties of a metamaterial depend on the types of electric and magnetic dipoles contained within a unit cell, and how those dipoles can be excited. In [71], it is shown through a quasi-static analysis that the original SRR structure proposed by Pendry in Fig. 10(a) has cross-polarization effects, which means that it has electric and magnetic dipoles which can both be excited by electric and magnetic fields. This leads to bianisotropy, meaning that the magnetic flux density $\vec{\mathrm{B}}$ and electric displacement field $\vec{\mathrm{D}}$ are dependent on both the electric field $\vec{\mathrm{E}}$ and the magnetic field $\vec{\mathrm{B}}$. Using a similar approach to that used in [71], it can similarly be shown that the single

SRR structure in Fig. 10(b) will also display cross-polarization, leading to bianisotropy in the electromagnetic response of metamaterials with that unit cell. In general, cross-polarization can be mitigated by introducing inversion symmetry into the unit cell and eliminating one of the dipoles [1]. In the case of the SRR in Fig. 10(b), adding another gap to the opposite side of the ring will create an additional electric dipole, and the oppositely-facing dipoles formed by the two gaps will cancel each other out.

Symmetry arguments can also be utilized in order to characterize the structure of the effective homogeneous properties of materials [72]. One important concept in crystallography is Neumann's Principle, which states that "the symmetry of any physical property of a crystal must include the symmetry elements of the point group of the crystal" [73]. In other words, the symmetrical properties of a crystal unit cell (and in extension, a metamaterial unit cell such as an SRR) are manifested in symmetrical properties of the overall bulk structure. Curie's principle is also important for determining the symmetry of artificial media. Curie's principle states that the overall symmetry of an artificial medium is the intersection of the symmetry groups of the shape of inserted periodic structures, the periodic arrangement of these structures, the host material, and the symmetry of the external perturbation [74]. Fig. 18 displays the symmetry planes and axes for a SRR and a square loop resonator unit cell.

If the unit cells shown in Fig. 18 are assumed to be arranged in a tetragonal fashion inside an isotropic host medium, application of Curie's law results in the overall symmetry of the metamaterial being the same as the symmetry of the unit cell, since the elements of the unit cell symmetry group are all contained in the symmetry groups of the periodic arrangement and the host material.

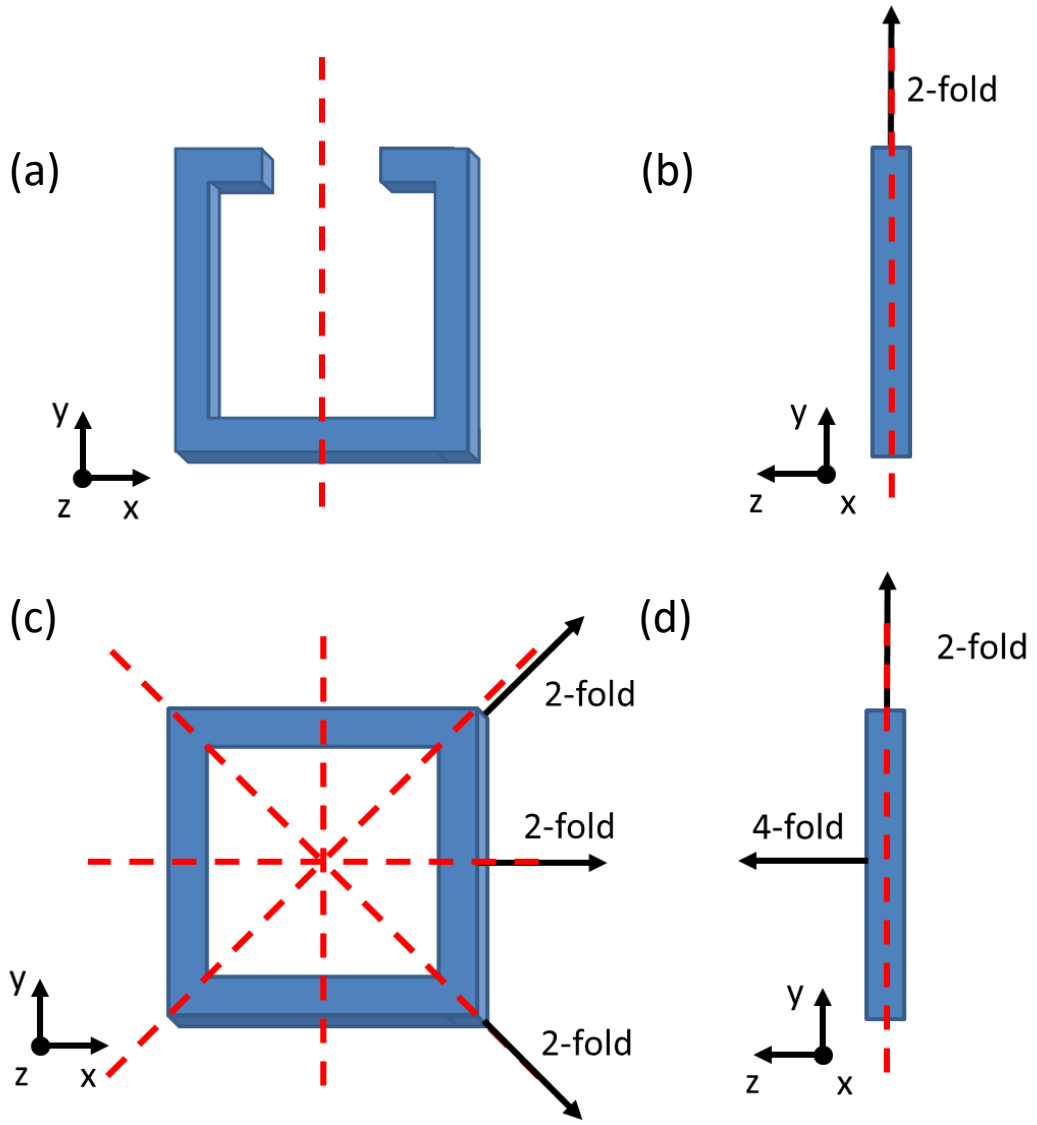

Fig. 18. Symmetry planes of reflection (shown in red) and axes of rotation (shown with black arrows) for two unit cells. The images in (a) and (b) show the symmetry of a split-ring resonator. (c) and (d) show the symmetry of a square ring resonator.

The expected structure of the permeability and permittivity tensors can be determined by solving the equations

$$[\mathrm{A}]\,\overleftrightarrow{\varepsilon} = \overleftrightarrow{\varepsilon}\,[A], \tag{57}$$

$$[\mathrm{A}]\,\overleftrightarrow{\mu} = \overleftrightarrow{\mu}\,[A], \tag{58}$$

where A is a matrix representing a geometrical transform to which the metamaterial is symmetric, $\overleftrightarrow{\varepsilon}$ is the permittivity tensor, and $\overleftrightarrow{\mu}$ is the permeability tensor [75]. Solving a system of equations using (57) and (58) with different A matrices will yield a final expected form for the material tensors. In addition to the permeability and permittivity tensors, the forms of the cross-coupling tensors $\overleftrightarrow{\xi}$ and $\overleftrightarrow{\zeta}$ can also be found using a slightly more complicated relation. As examples for A, the matrix representation of a 180 degree rotation about the z axis is represented by

$$\mathrm{R_z} = \begin{bmatrix} -1 & 0 & 0 \\ 0 & -1 & 0 \\ 0 & 0 & 1 \end{bmatrix}, \tag{59}$$

and likewise for a reflection across the $(\mathrm{x} = 0)$ plane,

$$\mathrm{R_z} = \begin{bmatrix} -1 & 0 & 0 \\ 0 & 1 & 0 \\ 0 & 0 & 1 \end{bmatrix}. \tag{60}$$

Solving (57) and (58) using the symmetries shown in Fig. 18(a) and 18(b), the structure of $\overleftrightarrow{\varepsilon}$ for a metamaterial with a SRR unit cell in a tetragonal lattice surrounded by an isotropic material is

$$\overleftrightarrow{\varepsilon} = \begin{bmatrix} \varepsilon_{11} & 0 & 0 \\ 0 & \varepsilon_{22} & 0 \\ 0 & 0 & \varepsilon_{33} \end{bmatrix}, \tag{61}$$

indicating that such a metamaterial will be biaxial ($\overleftrightarrow{\mu}$ will also have the same biaxial form). A metamaterial made with the square ring resonator shown in Fig. 18(c) and

18(d), in a tetragonal lattice and in an isotropic host medium, will have the permittivity tensor structure

$$\overleftrightarrow{\varepsilon} = \begin{bmatrix} \varepsilon_{11} & 0 & 0 \\ 0 & \varepsilon_{11} & 0 \\ 0 & 0 & \varepsilon_{33} \end{bmatrix}, \tag{62}$$

so this metamaterial will be uniaxial ($\overleftrightarrow{\mu}$ would also have the same uniaxial form).

2.2.6. Summary

This section covered some of the fundamental concepts necessary for characterizing split-ring resonators in the THz frequency range. Next, the current progress in THz metamaterial devices will be reviewed in detail.

2.3. Terahertz Metamaterials

A thorough review of the progress of THz metamaterials can be found in [29]. Metamaterials with magnetic resonances in the THz range were first demonstrated by Yen, Padilla, and Fang in 2004 [31]. They utilized ellipsometry to measure a planar array of double split ring resonators as shown in Fig. 19 below. By using an oblique angle for the incident wave, they were able to strongly couple into the magnetic modes of the SRRs.

SRRs are not the only method of generating a resonant THz response; simpler structures like rectangular hole arrays support surface wave polariton (SPP) resonant modes that can also strongly enhance incident THz radiation [76].

2.3.1. Actively Tunable THz Metamaterials

In order for metamaterials to be useful in dynamical applications such as modulation, an active component needs to be added into the metamaterial so that its

resonance can be controlled [77]. [28], [78]–[80] are a few excellent references on the progress of active THz metamaterials.

The first demonstration of an active metamaterial was from Padilla *et al.* in 2006 [36]. Using single SRRs on a GaAs substrate, they were able to shunt the SRR response by using an optical pump. Without any optical excitation, the SRR sample exhibits a strong resonance at a single frequency. When the optical pump is activated, it photo-excites carriers across the entire surface of the GaAs wafer, which effectively makes the entire substrate surface act as a metal. This in turn nullifies the effects of the SRR array. Nonlinear response can also be achieved if SRRs are fabricated on doped GaAs layers [81]. In this case, incident THz radiation of low levels will cause metal-like response due to the metallic nature of the doped GaAs layer. However, with increasing THz field strengths, intervalley scattering will become more frequent, causing decreased carrier mobility and therefore conductivity. With decreased conductivity in the GaAs layer, the SRR resonance becomes more prominent, and a notch appears in the transmission. At

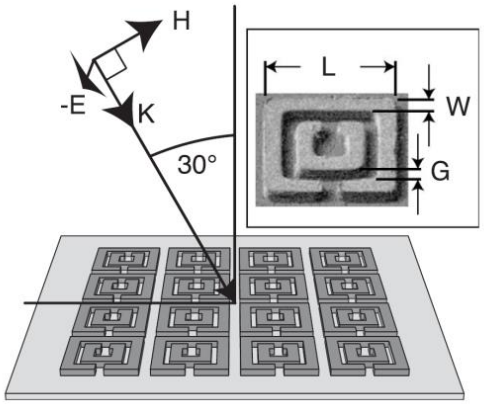

Fig. 19. First demonstration of terahertz split-ring resonator resonances via ellipsometry [31]**.**

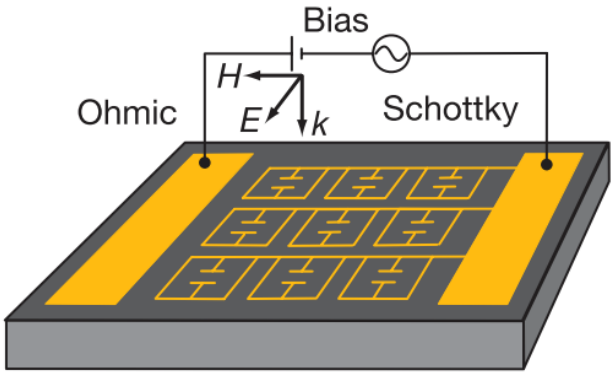

Fig. 20. Modulation of split-ring resonator resonances via voltage biasing of Schottky connections [79]**.**

even higher incident radiation strengths, impact ionization in the gaps of the SRRs causes the conductivity to increase again, suppressing SRR response.

Later that year, Chen and Padilla further demonstrated modulation via voltage biased SRRs on an n-GaAs layer, with the SRR-nGaAs junction acting as a Schottky contact [78], [79]. Their design is shown in Fig. 20. Without a bias voltage, the presence of the doped layer effectively removes any sort of resonant response. When a high enough voltage is applied between the SRRs and the n-GaAs layers, a depletion region will form underneath the SRRs. This depletion region electrically isolates the SRRs from the n-GaAs layer, and produces a resonance when excited by an incident THz wave.

In 2007, Chen *et al.* demonstrated frequency shifting modulation through the use of SRRs enhanced with silicon in the capacitor gaps, as shown in Fig. 21 [39]. When the SRRs are exposed to laser pulses, photoexcited carriers in the silicon extend the effective size of the internal SRR capacitor, and modulate the resonant frequency of the structure.

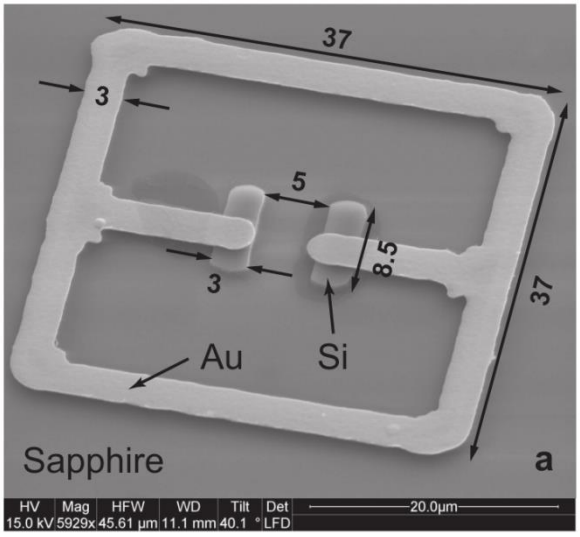

Fig. 21. Split-ring resonator with silicon capacitor plates to allow modulation through photoexcitation [39]**.**

Photoconductors and Schottky diodes are not the only elements that have been introduced into THz metamaterials. Shrekenhamer and Rout created a novel THz metamaterial design that incorporated high electron mobility transistors (HEMTs) in the gaps of SRRs in order to achieve tunability [82]. Their SRR design is shown in Fig. 22. At a zero volt gate bias, a 2D electron gas channel was naturally formed between the two sides of the split ring resonator, which serve as the source and drain of the pHEMT. This shorts the splits of the SRR and removes a resonance from the structure's response. When a negative bias is applied to the gate, the channel is eliminated, and the SRR resonates properly at the desired frequency.

2.3.1.1. MEMS Metamaterials

The four previously mentioned active metamaterial structures utilized electrical properties, namely semiconductors and semiconductor junctions, to achieve tunability in the THz frequency range. In addition, mechanically tunable SRRs have been made using

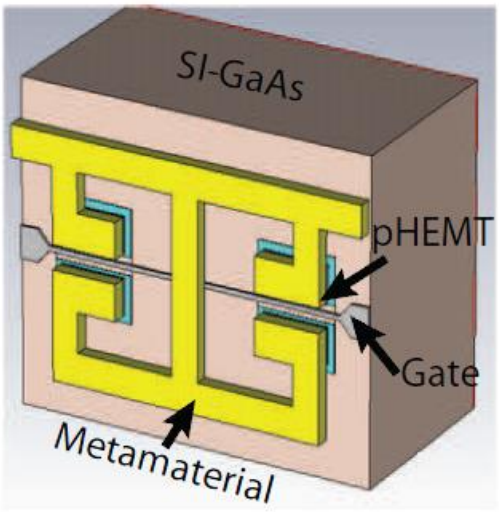

Fig. 22. Split-ring resonator with incorporated high electron mobility transistors (HEMTs) for a modulation effect [82]**.**

MEMS processes. Coutu *et al* have utilized MEMs cantilever beams arrays to create electrostatically tunable meta-atoms in the RF frequency range [83]. There have also been many designs of THz-range meta-atoms using MEMS. In one design, the resonance of SRRs are altered via bi-material cantilevers [42]. This design is shown in Fig. 23(a). In the initial rest state, the cantilevers are bend downwards due to residual stresses during the fabrication process. This shorts the SRR gaps and eliminates the LC resonance. When the device is heated, the difference in thermal expansion coefficients of the top and bottom materials in the cantilever causes the beam to straighten out, thus removing the electrical contact and restoring the LC resonance. The research in [84] took a slightly different MEMS approach by treating the capacitor arms themselves as bimaterial cantilevers, which are designed to have an initial deflection and can be lowered with an external voltage. An image of this concept is shown in Fig. 23(b).

In another MEMs design, bi-material cantilevers are used to actively change the in-plane orientation of SRRs, as shown in Fig. 23(c) [85]. By increasing the angle of incidence of the incoming electromagnetic wave with respect to the metamaterial unit cell, the magnetic coupling between the SRRs and the incident wave can be enhanced. This in turn increases the resonant response of the SRR and can cause more pronounced shifts in the effective permeability of the metamaterial.

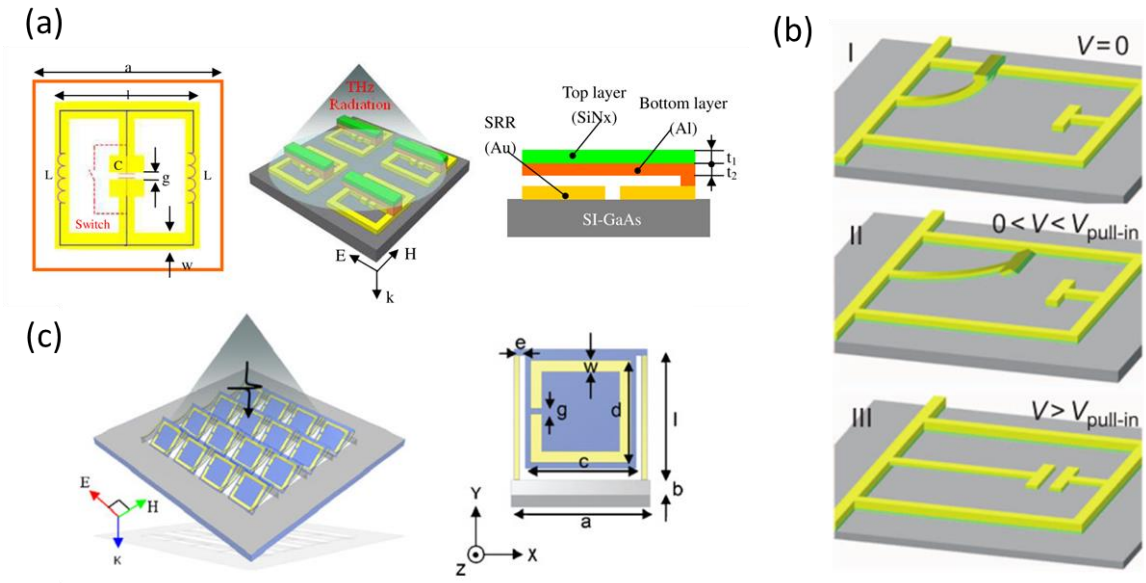

Fig. 23. Various microelectromechanical systems (MEMS) incorporated, tunable split-ring resonator (SRR) elements operating in the terahertz (THz) frequency range. In (a), modulation of a THz SRR is shown using bi-material cantilevers [42]**. The design in (b) uses bi-material cantilevers for the inner capacitive gap arms of THz SRRs, achieving modulation when these arms are deflected** [84]**. The third design in (c) shows structurally tunable THz SRRs using bi-material cantilevers to bend the entire array in different directions** [158]

2.3.1.2. Metal-Insulator Transition and Phase Change Metamaterials

Another avenue for achieving controllable metamaterials is through the use of special classes of materials such as phase change materials (PCMs) and metal-insulator transition (MIT) materials. PCMs and MIT materials are classes of materials that have vastly different electrical and/or optical properties based on their crystallographic alignment [86], [87]. Furthermore, transitions between crystalline and amorphous states can be achieved rapidly, typically through thermal, optical, or electrical excitations. This property of PCMs and MIT materials make them very desirable for switching and memory applications [88].

Bouyge *et al*. demonstrated a reconfigurable bandpass filter utilizing vanadium dioxide switches on SRRs in the microwave range, shown in Fig. 24 [89]. Vanadium dioxide is a commonly used MIT material with a transition temperature of 340K [87]. Using vanadium dioxide as a reconfigurable switch, they were able to electrically connect or disconnect patches of metal to the SRR, thus altering the resonance of the structure.

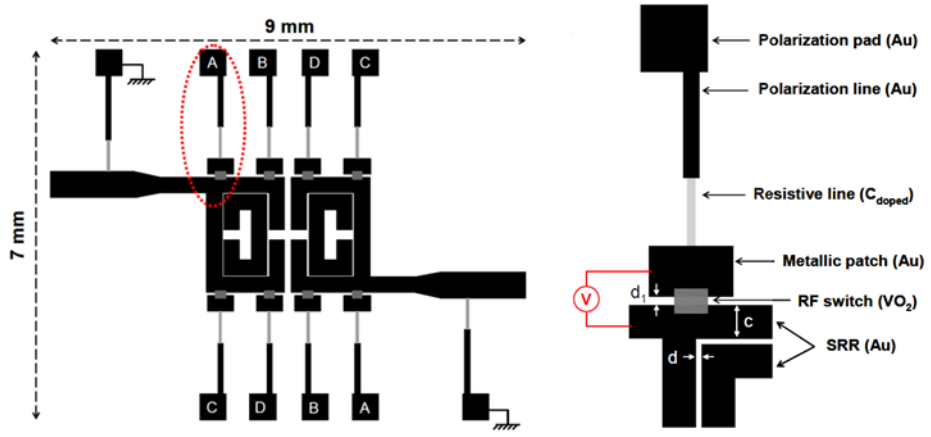

Fig. 24. Split-ring resonator unit cell with vanadium dioxide interconnects for tunability [89]**.**

Active metamaterial structures operating in the near-infrared range have also been created using vanadium dioxide (VO_2), and are shown in Fig. 25 [90]. The planar hybrid structure shown can switch between electrically appearing as a normal metamaterial surface when the VO_2 is insulating, or a full metal plane when the VO_2 has transitioned to

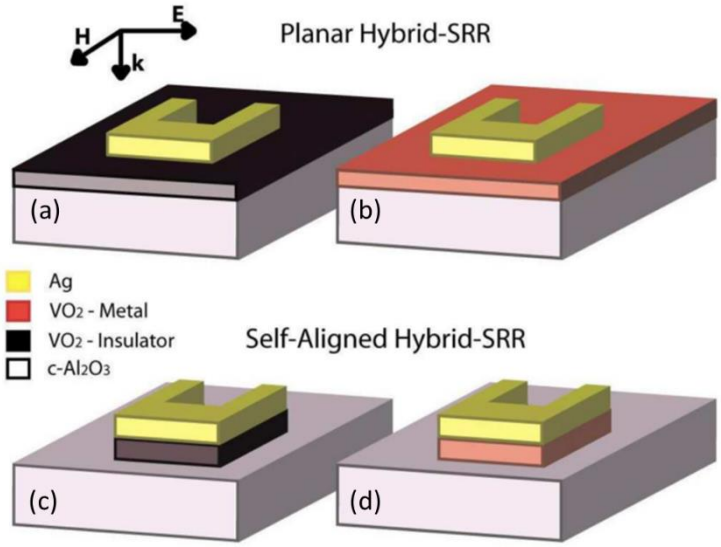

Fig. 25. Near-infrared metamaterials with vanadium dioxide (VO_2). In (a) and (b), gold split ring resonators (SRRs) are fabricated on a layer of VO_2. In (a), before transitioning the VO_2 layer, the VO_2 acts like a dielectric and the SRR response is dominates the behavior of the device. In (b), while the VO_2 layer is transitioned, the VO_2 layer is metallic and the overall response of the material is that of a flat metal plane. In (c) and (d), the SRRs have two materials in their thickness, a metal layer and a VO_2 layer. Before transitioning, as shown in (c), the VO_2 is a dielectric, which only affects the response of the SRR with a small red-shift. In (d), during the VO_2 transition to a metallic phase, the effective metal thickness of the SRR doubles, which slightly increases the resonant frequency of the device [90]**.**

the conductive state. The VO_2 in the self-aligned hybrid SRR causes a slight, phase-dependent shift in the resonant frequency of the SRR before and after transition.

The hysteretic nature of the VO_2 transition naturally makes it intriguing for possible memory applications [87]. In [91], "memory metamaterials" utilizing VO_2 are investigated. Although it may seem counterintuitive to expect permanent memory effects from a volatile material such as VO_2, the hysteretic nature of the transition creates slight changes in the conductivity and dielectric constant of the material, before and after transitioning, as shown in Fig. 26 [91]. By using voltage pulses, the resonant frequency can be shifted, and remain shifted due to the hysteresis of the vanadium oxide conductivity and permittivity.

Although they have not been as thoroughly investigated as much as MIT materials such as VO_2, PCMs have also been applied in some rudimentary metamaterial and

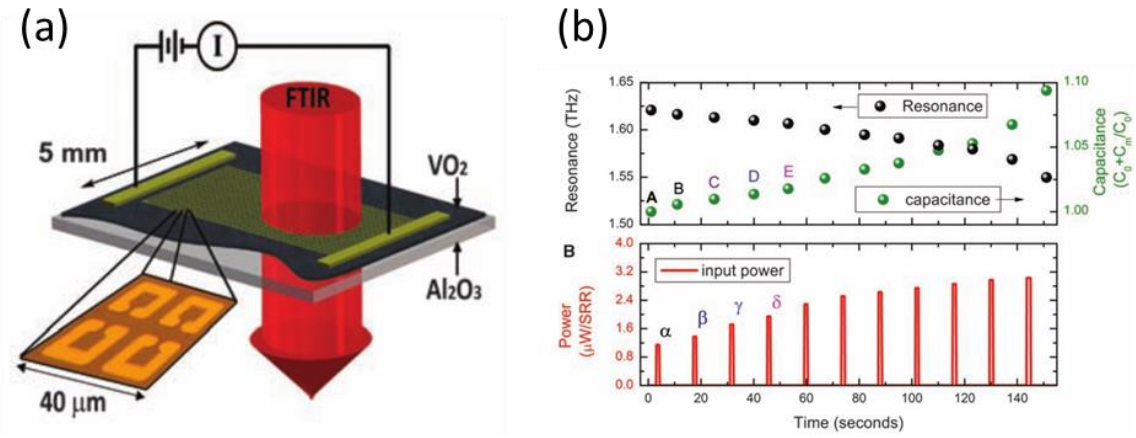

Fig. 26. Electrically controlled terahertz split-ring resonators incorporating vanadium dioxide. An overview of the structure and measurement setup is shown in (a). The graphs in (b) show a gradual shifting of resonance frequency with respect to pulse shape [91]**.**

plasmonics designs. A dynamic metamaterial switch utilizing germanium antimony telluride (GST) is shown in Fig. 27 [92]. This switch is controlled by a short laser pulse, which can transition the GST between the conductive and insulating states. In addition to GST, the chalcogenide gallium lanthanum sulphide (GLS) has also been shown to have potential for an active, plasmonics-based switch [93], as well as, a tunable layer for metamaterials in the infrared range [94].

2.3.2. Summary

Several novel structures have been proposed in the literature to create actively tunable THz metamaterials, using concepts ranging from basic semiconductor physics to MEMS. Out of all these avenues, PCMs have not been as heavily utilized, and thus represent a relatively open area of research. This thesis focuses on metamaterials that have PCM—specifically Germanium Telluride—components to them. As such, the underlying theory behind PCMs will be investigated in detail.

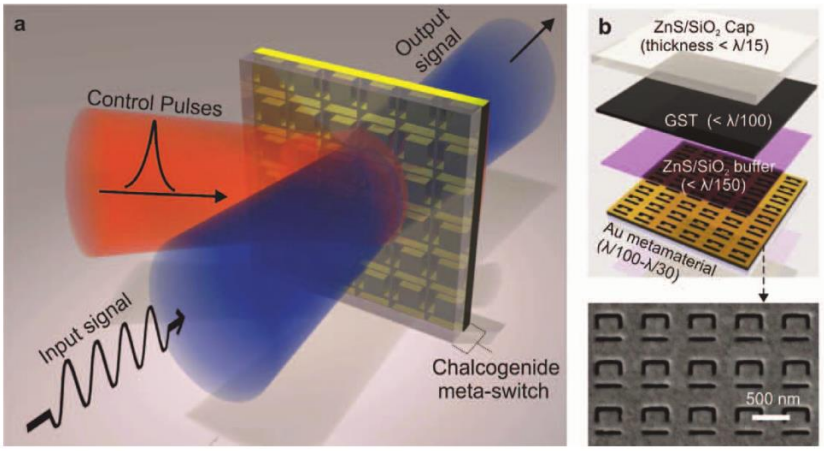

Fig. 27. Dynamic metamaterial absorber with incorporated phase change material layer [92]**.**

2.4. Phase Change Materials

Phase-change materials are a class of materials which undergo a drastic, nonvolatile change in optical or electrical properties upon optical, thermal, or electrical stimulation. Alan Waterman of Yale University was the first to discover the peculiar properties of a PCM during his investigation of molybdenum disulfide in the early 1900s. He observed a region of negative resistance in the material, and, after reaching a certain threshold voltage, he found that the resistivity of the material was permanently changed. Lacking modern, high-speed electronics and tools crystallography characterization, he considered the change to be permanent and was unaware of how or why the change occurred [86].

Unbeknownst to Waterman, the resistivity of the material could, in fact, be reverted back to the amorphous state, by using a very fast thermal, optical, or electrical pulse. The first person to consistently demonstrate reversible switching was Stanford Ovshinsky in the 1960s and 70s, using devices composed of a specific ratio of tellurium, arsenic, silicon, and germanium [95], [96]. Since then, PCMs have been extensively researched for optical and solid-state digital memory applications, and have led the ubiquity of devices such as CDs and DVDs.

The general temperature profiles required to switch between the two crystalline phases in a PCM are shown in Fig. 28 [97]. A PCM will naturally crystallize after being heated past its crystallization temperature, so a long pulse can be used for this purpose. On the other hand, a short, strong pulse is needed for amorphization. Such a pulse would "melt-quench" the material, transitioning it briefly from its crystalline state to a liquid state, and from there into an amorphous state. A large heat sink is required to adequately

"quench" the heat produced during the amorphization process. In optical and electrical memory devices, adequate heat-quenching scenarios are created by using very thin layers of PCMs and having some sort of metal surface nearby to serve as a heat sink [97].

There are two methods by which amorphous PCMs experience crystallization upon heating. The first method is nucleation and the second is growth [97]. In nucleation-type crystallization, small, crystallized nuclei of PCMs appear upon heating past the crystallization temperature. As the heating continues, these nuclei grow larger, combining with other nuclei along the way, until the entire solid is in a crystalline state. Nucleation is very fast and typically can occur within tens of nanoseconds [97]. Nucleation-type crystallization always occurs if the entire bulk of the PCM was initially in the amorphous state. If the majority of the bulk is crystalline with small regions of amorphous material (which is the case for most PCM memory applications), then those amorphous regions can experience growth-type crystallization as well. In this situation, not only will small

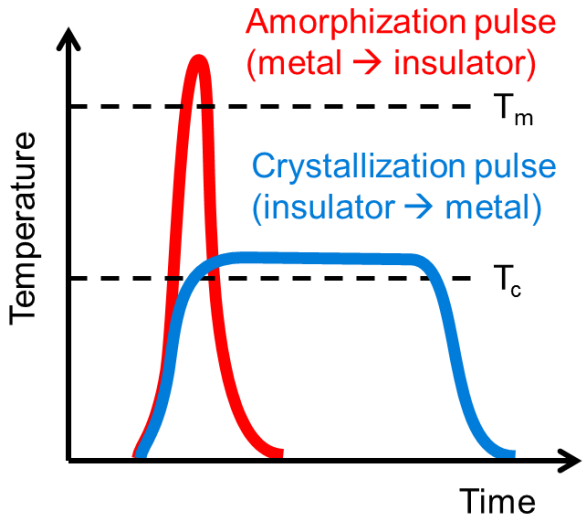

Fig. 28. Generalized temp vs time curves for the crystallization and amorphization of phase change materials.

nuclei begin to form in the amorphous area, but the surrounding crystalline material will also promote crystallization at the boundaries of the amorphous region, causing the volume of the amorphous area to shrink over time [97].

Many of the PCMs used in commercial applications are chalcogenides, which are compounds containing an element from the set of chalcogens (sulfur, selenium, tellurium) on the periodic table. Many chalcogenides have phase-change properties due to their poor ability to form glasses, which allows them to switch crystalline phases very quickly [98]. Some examples of chalcogenide PCMs include stoichiometric variations of GeSbTe, InSbTe, AgSbTe, and GeTe [87].

2.4.1. Germanium Telluride

Germanium Telluride (GeTe) is a binary chalcogenide with a rhombodehral structure, which can be visualized as a distorted rocksalt crystal structure [99]. The crystal structure of GeTe is shown in Fig. 29.

GeTe undergoes a nonvolatile insulator-to-metal transition when heated to approximately 200 ºC. Like all other PCMs, the transition is irreversible in the sense that simply cooling the metallic GeTe will not cause the material to revert back into an amorphous insulator. GeTe has been shown to amorphize with laser pulses and joule heating pulses [87]. Different stoichiometries and thicknesses of GeTe have significantly different crystallization times and slightly varying temperatures; for example, $Ge_{15}Te_{85}$ crystallizes in 100µs at 160 ºC, while $Ge_{50}Te_{50}$ crystallizes in 50 ns at 180 ºC [100], [101].

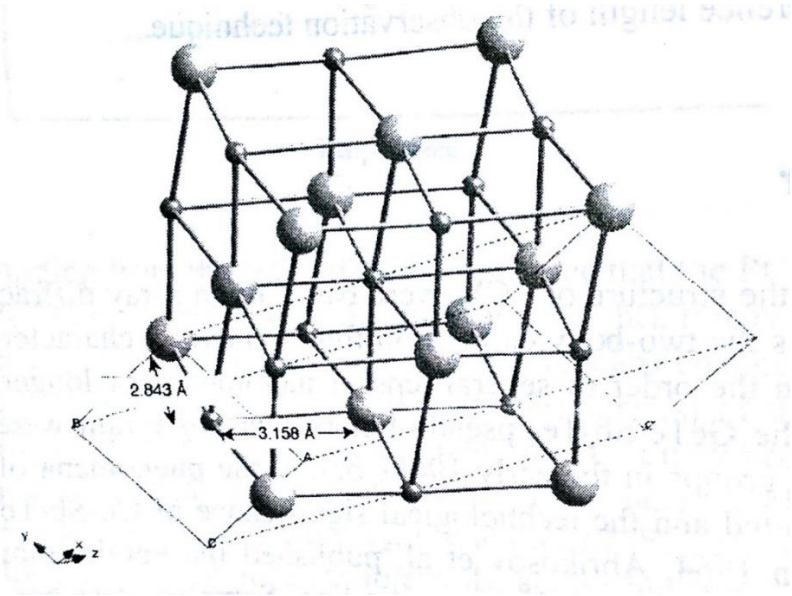

Fig. 29. GeTe has a distorted NaCl crystal structure [99]**.**

From transport studies, crystalline GeTe is known to have degenerate p-type conduction, although from theoretical studies, the rhombohedral phase is predicted to be semiconducting with a band gap between 0.4 and 0.7 eV [102]. Through computer models and simulations, this discrepancy was shown to be caused by germanium vacancies in the lattice. Overall, 10 percent of the germanium sub-lattice is estimated to be vacancies. [103]

One striking feature of GeTe that distinguishes it from other PCMs is the significant difference in resistivity between its crystalline and amorphous states: six orders of magnitude. The phase-change properties of GeTe have been shown to extend all the way into the THz range [88], [104]. GeTe's large on/off resistance ratio, fast crystallization / amorphization times, and its excellent high frequency characteristics make it a popular research topic for various high-speed switching applications [105]–

[108], as well as many nonlinear electronics applications, including the active adjustment of metamaterial devices [88].

2.4.2. Summary

Although GeTe has been well studied and characterized, there have been relatively few applications of GeTe in actual devices, due to the fact that the material has been overshadowed by alloys of its relative, germanium antimony tellurium (GST), which was found to have more consistent crystallization times [99]. For research purposes, however, GeTe offers the advantage of simplicity, as it can easily be deposited via sputtering. There is much potential for PCMs to play a larger role in the field of actively tuned metamaterials. This thesis investigates the use of GeTe in metamaterials of the THz frequency range, but the concept of PCM-incorporated metamaterials applies equally for lower and higher frequency bands as well.

2.5. Heat Transfer: Theory and GeTe Switching Examples

In order to be able to transition GeTe between its crystalline and amorphous states, thermal energy must be transferred into the material using one of the generalized pulse shapes shown in Fig. 28 [97]. The crystallization pulse must raise the temperature of the GeTe layer past its crystallization temperature at approximately 470 K; the amorphization pulse must briefly raise the temperature of the GeTe layer slightly past its melting point at 996 K [99], and there additionally must be enough of a heat sink around the GeTe layer to quickly quench the heat after the pulse occurs.

There are two methods of thermal energy transfer that have been proven to successfully transition GeTe films: Joule heating [105]–[108] and laser heating [109], [110].

2.5.1. Joule Heating Theory

The concept of Joule heating can be applied to GeTe switching in two different ways: A current can be sent directly through a GeTe layer to heat it (i.e. direct heating), or sent through an auxiliary heating resistor nearby a GeTe layer (i.e. indirect heating). In either case, the initial source of heat can be modeled as a resistive bar with a voltage across it. The heat generated per unit length per unit time from current flowing through such a resistive bar is

$$\mathrm{Q_{heat}} = \frac{\mathrm{AV^2}}{\rho\, l^2}, \tag{63}$$

where A is the cross-sectional area of the bar, V is the voltage across the bar, ρ is the resistivity of the bar, and l is the length of the bar [111]. The temperature T along the bar is described by the differential equation

$$\mathrm{k_s}\frac{\mathrm{d^2}T}{\mathrm{dx^2}} - \frac{k_a S}{A\, l}(T - T_s) + \frac{Q_t}{A} = 0, \tag{64}$$

where $\mathrm{k_s}$ is the thermal conductivity of the bar, $\mathrm{k_a}$ is the thermal conductivity of the surrounding space, S is the shape factor of the bar, A is the cross-sectional area of the bar, l is the length of the bar in the x-direction, $\mathrm{T_s}$ is the temperature of the surrounding space, and $\mathrm{Q_t}$ is the generated heat per unit length per unit time [111]. The first term in the equation describes thermal transport across the length of the bar. The second term describes the heat conducting out of the sides of the bar, into the surrounding space.

If the temperatures on both ends of the bar are assumed to be equal to the temperature of the surrounding space, (93) has the solution

$$\mathrm{T} = \mathrm{T}_0 + \frac{p}{\mathrm{m}^2}\left[1 - \cosh(m\,x) - (1 - \cosh(m\,l))\frac{\sinh(m\,x)}{\sinh(m\,l)}\right], \tag{65}$$

$$\mathrm{m} = \sqrt{\frac{\mathrm{k_a} S}{A\,l}}, \tag{66}$$

$$\mathrm{p} = \frac{\mathrm{Q_t}}{k_s A}, \tag{67}$$

where T_0 is the initial temperature of the bar, and all other variables are the same as in (64). Many of the parameters that the solution depends on, such as the resistivity of the heater and the thermal conductivity of the other elements, can easily be found in the literature. The most difficult term to determine is the shape factor, S, because it depends on the geometry of elements surrounding the bar [111]. This simplified model neglects several parameters, such as heat flow out of the ends of the bars, and only considers the temperature of the bar in the steady state.

If the method being considered is direct heating, the thermal parameters of GeTe can used for the bar, and the geometries and voltages be adjusted to find the correct values of temperature for GeTe crystallization and amorphization. If indirect heating is being considered, the bar is thought to be some other resistive material, and additional calculations have to be made to determine the temperature gradient between the heater and the GeTe layer. Due to the sharply increasing complexity of temperature characterization as simplifications are removed, computer simulations of the heat equation have been commonly used to characterize the temperature profile of GeTe heating devices [105]–[107]

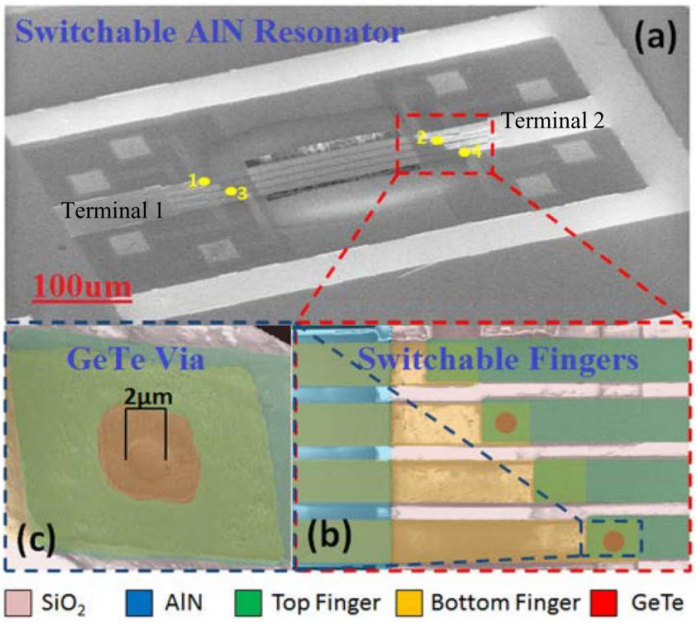

Fig. 30. An aluminum nitride resonator using microelectromechanical systems fabrication technology and a germanium telluride switching element [108]**.**

2.5.2. Joule Heating Examples

Nukala *et al.* have demonstrated reversible switching through electrical heating of GeTe nano-wires [112]. In addition, Hummel *et al*. used GeTe to add switchable control to aluminum nitride (AlN) MEMS resonators [108]. Optical images of their design are shown in Fig. 30. They utilized a direct heating approach, sending current pulses through a GeTe film in order crystallize and amorphize it through direct joule heating. A 1V / 300µs pulse was used for crystallization and a 2.5V / 4µs pulse was used for amorphization. Their vertical, direct-heating method is similar to the types of designs used for memory applications of phase-change materials [113], [114].

El-Hinnawy *et al*. have been investigating the use of GeTe in RF switching by utilizing an auxiliary joule heating element [105]–[107]. An image of their design is

shown in Fig. 31. The RF signal passes through the GeTe layer and its metal contacts, and a NiCr alloy is used as an indirect heater. The GeTe and the NiCr layer are separated by a thin layer of silicon nitride for electrical isolation. The heat produced by current pulses passing through the NiCr heater affects the GeTe layer adjacent to it, allowing it to crystallize and amorphize depending on the strength and duration of the pulses. Fig. 32

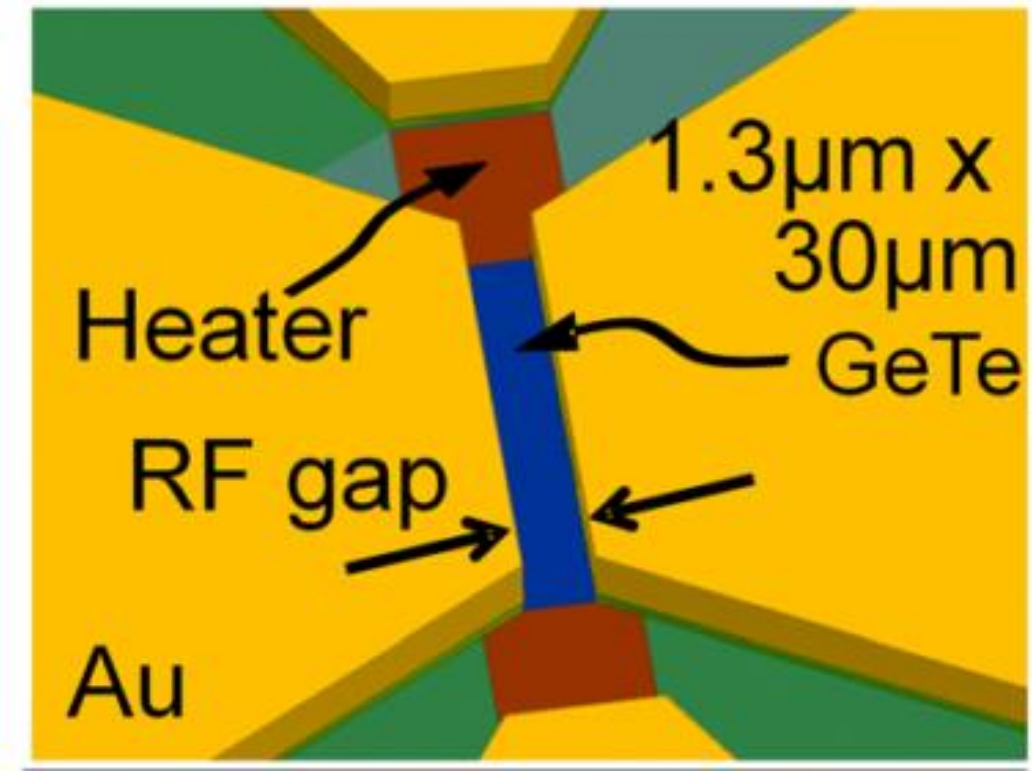

Fig. 31. A germanium telluride indirect heating design for high-speed switching. A film of germanium telluride (GeTe) fills a gap between to large gold (Au) pads creating a path for radio frequency (RF) waves. The conductivity of the GeTe film determines whether the path is open or closed. The underlying heating element can switch the GeTe film from an insulating or conducting state using short voltage pulses on the order of nano- and microseconds [106]**.**

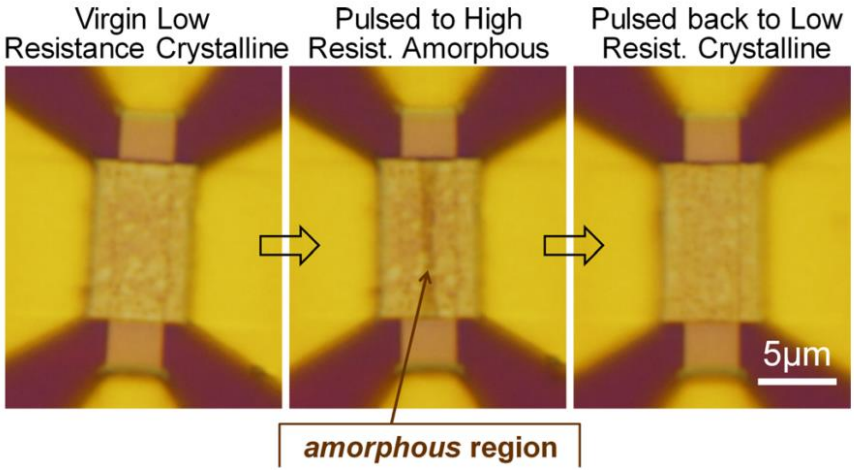

Fig. 32. Images of indirect switching using indirect crystallization and amorphization of germanium telluride, showing visible amorphous region after thermal pulse [106]**.**

shows visible signs of the phase transition in the material. This design required a 17V / 1.5μs pulse for crystallization and a 30V / 100ns pulse for amorphization.

2.5.3. Laser Pulsing Theory

In laser pulsing of a GeTe film, the energy of the laser is transferred into heat in the GeTe film, providing enough heat for either crystallization or amorphization. The energy of a laser incident in and on an absorbing surface, as a function of the depth z into the surface, can be modeled as

$$S(z) = \alpha I_0 (1 - R) \exp(-\alpha z), \tag{68}$$

where α is the optical absorption coefficient, R is the reflectivity of the surface, and I_0 is the intensity of the laser beam [115]. If the laser pulses are assumed to be on the nanosecond time scale, it can safely be assumed that all of the optical energy absorbed

from the laser turns into heat [115]. The one-dimensional heat equation describing this scenario is

$$\rho c_p \frac{\mathrm{dT}}{\mathrm{dt}} = \frac{\mathrm{d}}{\mathrm{dz}}\left(k_s \frac{dT}{dz}\right) + S(z), \tag{69}$$

where ρ is the density of the absorbing material, $\mathrm{c_p}$ is the specific heat of the material at constant pressure, $\mathrm{k_s}$ is the thermal conductivity of the material, and S(z) is as defined in (68) [115]. This equation can be solved in many different manners, depending on which additional approximations are subsequently used. Two metrics can be compared against each other to help determine which solution to use. The first is the thermal penetration depth

$$\mathrm{d_{therm}} = \sqrt{\mathrm{D\tau}}, \tag{70}$$

where $\mathrm{D} = \mathrm{k_s}/\rho c_p$ is the thermal diffusivity coefficient and τ is the pulse width of the laser [115], and the second is the optical penetration depth

$$\mathrm{d_{optical}} = \frac{1}{\alpha}, \tag{71}$$

where α is the absorption coefficient of the material at the wavelength of the laser [115]. If $\mathrm{d_{optical}} \ll \mathrm{d_{therm}}$, then the energy of the laser is being transferred to a thin layer on the surface of the absorbing material, and the laser absorption can be viewed as only occurring on the surface of the material rather than happening throughout the bulk of the material with exponential decay [116]. With this simplification, the transient temperature distribution of the substrate is the temporally piecewise function

$$\begin{aligned}
\mathrm{T}(\mathrm{z},\mathrm{t}<\tau) &= \frac{2\alpha \mathrm{I}_0(1-R)}{\mathrm{k_s}}\sqrt{Dt}\cdot \mathrm{ierfc}\left[\frac{\mathrm{z}}{2\sqrt{\mathrm{Dt}}}\right], \\
\mathrm{T}(\mathrm{z},\mathrm{t}>\tau) &= \frac{2\alpha \mathrm{I}_0(1-R)}{\mathrm{k_s}}\left\{\sqrt{Dt}\cdot \mathrm{ierfc}\left[\frac{\mathrm{z}}{2\sqrt{\mathrm{Dt}}}\right] - \sqrt{D(t-\tau)}\right. \\
&\quad \left.\cdot \mathrm{ierfc}\left[\frac{\mathrm{z}}{2\sqrt{\mathrm{D(t-\tau)}}}\right]\right\},
\end{aligned} \tag{72}$$

where α is the absorption coefficient of the material at the laser wavelength, $\mathrm{I_0}$ is the intensity of the laser, R is the reflectance of the surface, $\mathrm{k_s}$ is the thermal conductivity of the material, D is the thermal diffusivity coefficient of the material, τ is the length of the laser pulse, and ierfc[x] is the integrated complementary error function [115], [116] defined as

$$\mathrm{ierfc}[\mathrm{z}] = \int_{\mathrm{z}}^{\infty} \mathrm{erfc}(\xi)d\xi, \tag{73}$$

and with erfc[x] defined as

$$\mathrm{erfc}[x] = 1 - \frac{2}{\sqrt{\pi}}\int_0^x \exp[-t^2]\,dt. \tag{74}$$

If the surface absorption approximation does not hold, the solution to the heat equation has a slightly more complicated form [115], [117]:

$$\begin{aligned}
\mathrm{T}(\mathrm{z},\mathrm{t}) = \frac{\alpha \mathrm{I}_0(1-R)}{k_s}&\left\{2\sqrt{Dt}\cdot \mathrm{ierfc}\left[\frac{\mathrm{z}}{2\sqrt{\mathrm{Dt}}}\right] - \frac{1}{\alpha}\exp[-\alpha z]\right. \\
&+ \frac{1}{2\alpha}\exp[\alpha^2 Dt] \\
&\cdot \left(\exp[-\alpha z]\cdot \mathrm{erfc}\left[\alpha\sqrt{\mathrm{Dt}} - \frac{z}{\sqrt{Dt}}\right] + \exp[\alpha z]\right. \\
&\left.\left.\cdot \mathrm{erfc}\left[\alpha\sqrt{\mathrm{Dt}} + \frac{\mathrm{z}}{\sqrt{\mathrm{Dt}}}\right]\right)\right\},
\end{aligned} \tag{75}$$

where α is the absorption coefficient of the material at the laser wavelength, I_0 is the intensity of the laser, R is the reflectance of the surface, k_s is the thermal conductivity of the material, D is the thermal diffusivity coefficient of the material, τ is the length of the laser pulse, ierfc[x] is as defined in (73), and erfc[x] is as defined in (74).

The temperature evolution of a thin film on a substrate can also be calculated, if the surface absorption simplification is also assumed. In this case, the heat equations for the film and substrate become

$$\begin{aligned} \frac{\partial \mathrm{T_f}(z_f,t)}{\partial \mathrm{t}} &= \mathrm{D_f}\frac{\partial^2 T_f(z_f,t)}{\partial {z_f}^2}, \qquad 0 \le z_f \le Z \\ \frac{\partial \mathrm{T_s}(z_s,t)}{\partial \mathrm{t}} &= \mathrm{D_s}\frac{\partial^2 T_s(z_s,t)}{\partial {z_s}^2}, \qquad 0 \le z_s \le \infty \end{aligned} \tag{76}$$

where T_f is the film temperature, D_f is the thermal diffusivity coefficient of the film, z_f is the depth into the film, Z is the total thickness of the film, T_s is the substrate temperature, D_s is the thermal diffusivity coefficient of the substrate, and z_s is the depth into the substrate [115], [118]. The following continuity and boundary conditions must also be met:

$$\mathrm{T_f}(Z,t) = T_s(0,t), \tag{77}$$

$$\mathrm{k_f}\frac{\partial \mathrm{T_f}(z_f,t)}{\partial \mathrm{z_f}} = \mathrm{k_s}\frac{\partial \mathrm{T_s}(z_s,t)}{\partial \mathrm{z_s}}, \tag{78}$$

$$-\mathrm{k_f}\frac{\partial \mathrm{T_f}(0,t)}{\partial \mathrm{z_f}} = I_0 A_f, \tag{79}$$

$$\mathrm{T_s}(\infty,\mathrm{t}) = 0, \tag{80}$$

where in addition to the variables stated in (76), k_f is the thermal conductivity of the film, k_s is the thermal conductivity of the substrate, I_0 is the intensity of the laser, and A_f is the surface absorptance of the thin film [115], [118].

This system of partial differential equations can be converted into a more straightforward, solvable problem by using Laplace and inverse Laplace transforms. The closed-form solutions to the temperatures of the film and substrate are infinite series of the form

$$T_f(z_f,t) = \sum_{n=0}^{\infty} \frac{I_0 A_f}{k_f} B^{n+1} \left[\frac{L_f}{\sqrt{\pi}} \exp\left(-\frac{a_n^2}{L_f^2}\right) - a_n \operatorname{erfc}\left(\frac{a_n}{L_f}\right)\right] + \sum_{n=0}^{\infty} \frac{I_0 A_f}{k_f} B^{n} \left[\frac{L_f}{\sqrt{\pi}} \exp\left(-\frac{b_n^2}{L_f^2}\right) - b_n \operatorname{erfc}\left(\frac{b_n}{L_f}\right)\right], \tag{81}$$

$$T_s(z_s,t) = \sum_{n=0}^{\infty} \frac{2 I_0 A_f}{k_f} \frac{B^n}{1+\varepsilon} \left[\frac{L_f}{\sqrt{\pi}} \exp\left(-\frac{g_n^2}{L_f}\right) - g_n \operatorname{erfc}\left(\frac{g_n}{L_f}\right)\right], \tag{82}$$

where in addition to the variables mentioned in earlier statements,

$$a_n = 2Z(1-n) - z_f, \tag{83}$$

$$b_n = 2nZ + z_f, \tag{84}$$

$$g_n = (1+2n)Z + z_s \sqrt{\frac{D_f}{D_s}}, \tag{85}$$

$$L_f^2 = 4 D_f t, \tag{86}$$

$$B = \frac{1-\varepsilon}{1+\varepsilon}, \tag{87}$$

$$\varepsilon = \frac{k_s}{k_f} \sqrt{\frac{D_f}{D_s}}, \tag{88}$$

In most cases, the summation can be truncated at $n = 10$ for a good approximation [115]. This model most accurately describes the laser heating of a GeTe thin film, so long as the laser pulse parameters and the material properties of GeTe (i.e. thermal and optical penetration depth) meet the requirements for the surface absorption simplification. As was the case with Joule heating, numerical simulations become a much simpler approach if additional simplifications need to be removed from the laser heating model [115].

2.5.4. Laser Pulsing Examples

A few specific wavelengths, pulse durations, and pulse strengths that result in crystallization/amorphization of GeTe of certain thicknesses have been experimentally determined. In [109], 20-nm GeTe was reliably transitioned using 8-ns, 800-nm wavelength pulses of varying fluence. 74 mJ/cm^2 was required for initial amorphization (63 mJ/cm^2 for repeated amorphization) and 28 mJ/cm^2 was required for crystallization. In [110], 20-ns, 248-nm laser pulses were used with varying fluences to crystallize and amorphize a 60-nm GeTe film. For crystallization, at least five consecutive 20-ns pulses at a 130-mJ/cm^2 fluence were needed to crystallize the initially amorphous film. Using 20 consecutive 20-ns pulses, crystallization could be achieved with 20-mJ/cm^2 fluences or greater. These films were further found to amorphize with a single 20-ns laser pulse with 182-mJ/cm^2 fluences or greater.

2.5.5. Summary

This section has described the basic theory of heat transfer via Joule heating and optical absorption. It is important to understand the theory in order to understand how to

transition GeTe films using the correct voltage or laser parameters. This section has also reviewed some research where thin films have been successfully transitioned.

2.6. Fabrication Processes

There are three main microfabrication techniques that are used in order to create structures and devices in the fields of microelectronics and micro-electromechanical systems (MEMS). These techniques are bulk micromachining, surface micromachining, and microforming. These techniques are often used in conjunction with each other to create complete, robust devices. Some additive manufacturing techniques will also be briefly discussed.

2.6.1. Bulk Micromachining

In bulk micromachining, a device is fabricated into the bulk of a substrate wafer via wet and/or dry etching. A simple wet etch is typically isotropic, and may not be adequate for a given bulk micromachining design. For a wet etch, something as simple as agitation-less processing can partially change the isotropy of the etch [119]. For crystalline materials, etchants have different etch rates for different crystallographic planes of the crystalline material. For example, silicon has a high <100> etch rate and a slow <111> etch rate, resulting in pyramid- or trapezoidal prism-shaped etch cavities on (100) silicon wafers [119]. Deep reactive ion etching (DRIE) is another special technique that can be used to high aspect ratio structures through sequential reactive ion etching (RIE) of a sidewall-protected cavity [120].

2.6.2. Surface Micromachining

Surface micromachining involves the sequential deposition of material layers on a substrate. For this work, surface micromachining techniques were primarily used, due to the planar nature of the THz SRRs.

Materials can be deposited through a variety of physical- and chemical-based methods. Evaporation deposition creates non-conformal deposition profiles that are useful for easy liftoff, but is limited in range of materials due to its vapor pressure requirements [119]. On the other hand, sputter deposition can be used with a wide variety of materials because of its kinetic nature. However, a bilayer liftoff or etching process must be used to pattern sputtered depositions due to the conformal nature of the deposited film. In addition to these two processes, the many variants of chemical vapor deposition (CVD) can also be used for the thin film deposition of high quality films [121]. In CVD processes, thin films are deposited as a byproduct of gases and/or plasmas. The main drawback for CVD is a restricted range of allowable temperature and a limited amount of materials that can be viably produced with chemical reactions [121].

2.6.3. Microforming

In microforming processes, also known as high aspect ratio micromachining (HARM), a patterned photoresist layer is used as a mold for a subsequent layer of electroplated metal. If thick photoresists are used, very high aspect ratio structures can be created in this way. LIGA is an example of one such microforming process. LIGA is an acronym for the three German words Lithographie, Galvanoformung, and Abformung, which respectively stand for lithography, electroplating, and polymer replication [119], [122], [123]. In the LIGA process, low atomic mass polymers such as PMMA are used in

conjunction with x-ray lithography to create very high aspect ratio patterns, on the order of hundreds of microns. Although PMMA is rather soft, it can be used as a mold for other materials, which can be deposited via electroplating and other means. Other thick photoresists such as SU-8, or multiple layers of SF-11, can also be used as a much cheaper (but lower quality) alternative to create high aspect ratio structures [119].

2.6.4. Additive Manufacturing

Additive manufacturing is a method of creating a three-dimensional model through successively deposited layers of material [124], [125]. The demand for scientists, doctors, and students to rapidly create prototypes using additive manufacturing methods has led to a recent rise in its popularity [125]. There are several types of additive manufacturing processes. One of the first to be developed was stereolithography, in which a UV laser cures and hardens successive layers of a liquefied polymer [124]. In fused deposition modeling, a thin filament of thermoplastic is melted in a print head and extruded in sub-millimeter thicknesses [124]. Although initially limited to plastics, deposition of wax, metals, and ceramics have since been demonstrated using this process [125]. Inkjet printing utilizes inks dissolved or dispersed in solvents, which are then ejected from a nozzle and impacted on a substrate, where the solvent evaporates and the ink remains [125]. Although the technology is most commonly known for two-dimensional printing, three-dimensional printing is possible through the use of pre-patterned layers [125]. Selective laser sintering utilizes a laser beam to selectively sinter or fuse particles of a layer, sequentially building up a 3D part [124]. A variety of metals and plastics can be deposited with this method [126]. Additive manufacturing of metals is especially of interest for military applications, since it would allow for speedy repair of

active machinery [126]. Currently one of the major obstacles of utilizing additive manufacturing of metals is figuring out how to prove consistent reliability of additively manufactured parts [126].

2.7. Summary

This chapter has described the main theoretical concepts that were necessary for conducting the research described in this work. The THz spectrum and the physics of the THz spectroscopy measurement process—generation and detection— have been explained in detail, and a physical model used to extract material parameters from the measurement process has been described. A thorough LC-resonance characterization of THz split-ring resonators has also been performed, with a brief discussion on the prediction of higher-order resonances as well. The field of THz MMs is currently very active, and several published SRR designs have been reviewed. The general concepts of phase change materials, especially germanium telluride, have been described, with an additional focus on heat transport phenomena which can be used to transition GeTe films. Finally, a high-level summary of the various methods of MEMS fabrication has been presented. The following section will describe in detail the methodology of the many experiments performed in this work.

3. Methodology

3.1. Terahertz Spectroscopy Measurements

The TPS Spectra 3000 from Teraview was used to characterize metamaterials and substrates over the THz frequency range. This system utilizes the photoconductive THz generation and detection techniques described in the theory section. An ultrashort Ti-Sapphire laser was used for gating of the semiconductor emitter and receiver [127]. The effective range of measurements from the machine is from 0.06 to 3 THz.

An image of the main components of this device is shown in Fig. 33. During a measurement, a sample is first fixed to a sample holder and placed inside the measurement area of the THz spectrometer, in the path of the THz beam, as in Fig. 33(b). A lid is placed over the measurement area, and the chamber is left alone for five minutes while it is filled with nitrogen. This removes any moisture from the chamber, which is important due to interferences which can be caused by dipole resonances of water. After purging the moisture in the chamber, a measurement can be started using the integrated computer. For the data in this thesis, each measurement consisted of 5,000 sequential scans, taken at a rate of 30 scans per second. The large amount of averaging helps improve the signal-to-noise ratio of the data collected. After the measurement finishes, the lid can be removed and the sample replaced. As mentioned in the theory section, two measurements must be made for each device in order to get meaningful transmission data: a reference measurement and a sample measurement. Although the software in the system calculates the Fourier transform of the data, the raw time domain data was separately analyzed and Fourier-transformed using a MATLAB® script to allow for more control.

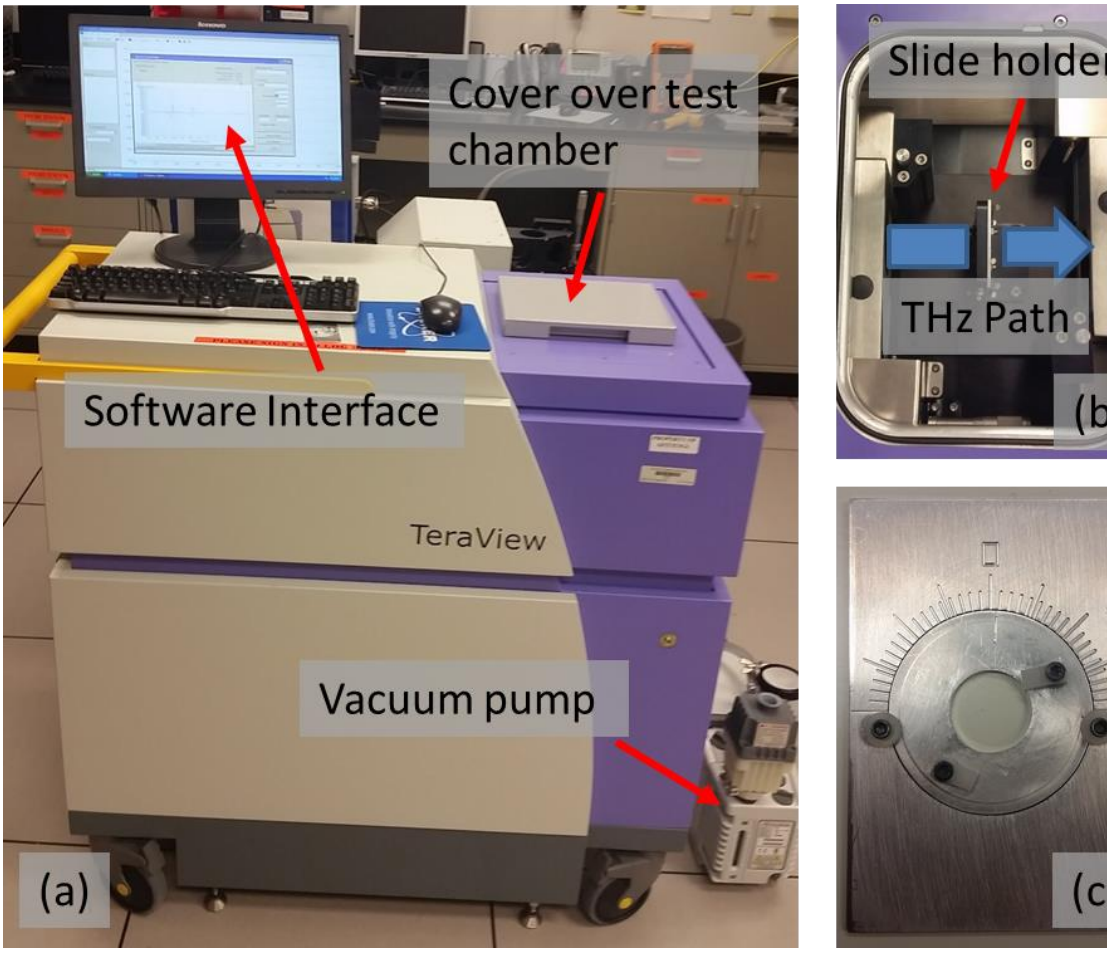

Fig. 33. (a) Overview of TeraView TPS 3000 machine. Samples are placed in the test chamber on the righthand side of the machine. The vacuum pump shown is used with the thermal heating module. (b) An interior view of the measurement chamber. Sample slides are placed in the middle of the terahertz beam path. (c) A customized rotational sample holder designed with help from the school model shop.

3.1.1. In-Situ Thermal Heating

The thermal module for the TPS Spectra 3000 can enable in-situ heating measurements of sample pieces. Images of the thermal module are shown in Fig. 34. During an in-situ thermal measurement, the sample is placed in a special sample holder,

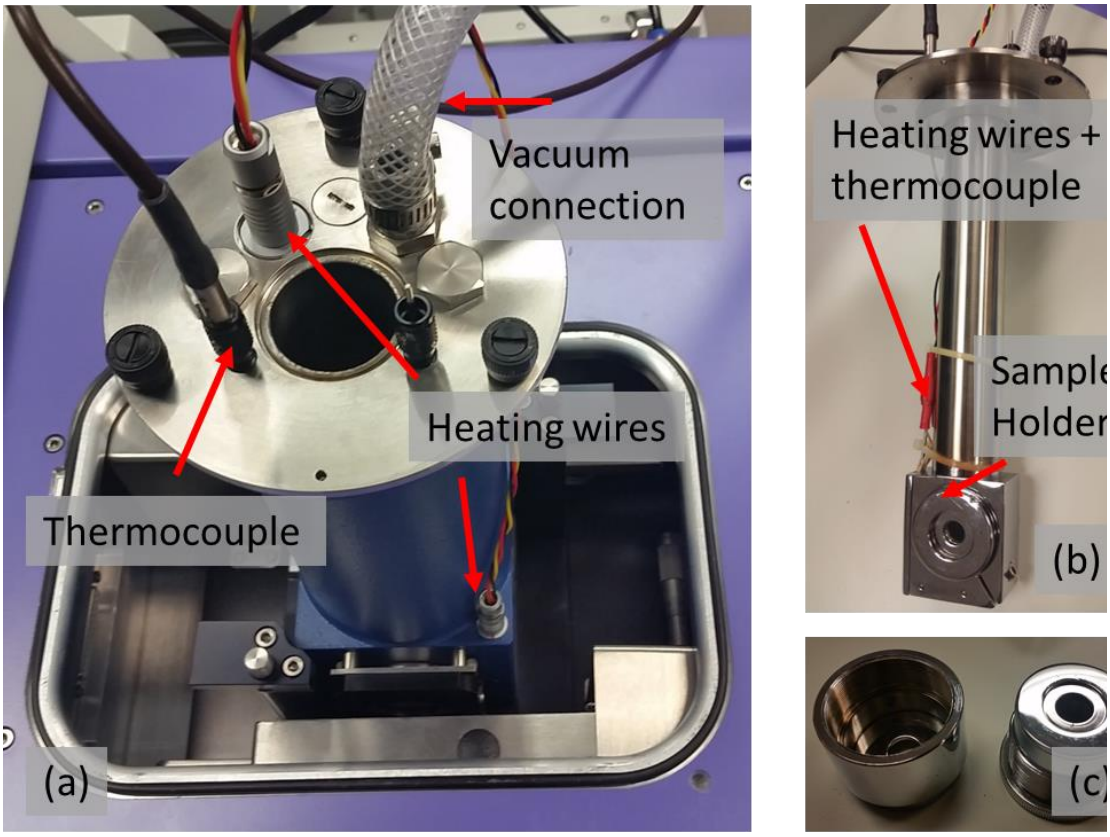

Fig. 34. (a) Overview of the thermal module for terahertz testing. Thermocouple and heating wires control and monitor the temperature inside the module. A vacuum connection provides thermal insulation. (b) Interior section of the thermal cell, showing position of the wires and sample with respect to the length of the module. (c) Cylindrical, screw-in sample holder for the temperature module. Samples are wedged between two round metal plates.

which is in turn placed in a sealed, cylindrical heating cell. The air in the cell is evacuated using a vacuum pump for thermal insulation. An external controller moderates the thermal cell temperature using two heating elements and a thermal couple inside the cell. The controller is programmed to rise to a given set temperature at a rate of 10 ºC per minute. During the measurement process, the samples were left in the heating chamber

for at least five additional minutes after the temperature controller outputted the desired temperature in order to ensure that the temperature was constant across the entire temperature cell.

3.2. Lithographic Patterning Processes

In any microfabrication process, lithography is a crucial step which allows one to pattern specific shapes on the surface of a wafer. The following sections describe the specific steps of two patterning processes that are compatible with lift-off processes. Process follower tables for these patterning steps are also included in the Appendix.

3.2.1. S1818 Patterning

S1818 is a positive photoresist with micron-range thicknesses that is compatible with lift-off processes. The patterning process for 1818 photoresist is as follows:

The substrate is cleaned with an acetone / methanol / DI water rinse on the spinner. Each liquid is applied for 30 seconds each, with overlap between liquid applications in order to allow for continuous liquid flow on the surface of the substrate. After the final 30-second DI water rinse, the substrate is air-dried with the nitrogen gun. The substrate is then coated with 1818 photoresist via a spinner at 4,000 RPM for 30 seconds, followed by a 2-minute bake at 110 ºC.

After photoresist application, the sample is exposed for 8 seconds in the MJB3 mask aligner and is subsequently developed for 30 seconds in a DI water and 351 developer mixture at a ratio of 5 to 1. Finally, the sample is cleaned for 30 seconds in DI water and air-dried with the nitrogen gun. After that, the sample is fully patterned and ready for inspection.

3.2.2. Bilayer (SF-11 and S1805) Patterning

The bilayer process utilizes both the photoresists SF-11 and S1805, and is the most ideal method for lift-off processes. The following paragraph describes the bilayer patterning process.

The substrate is first cleaned with the same acetone / methanol / DI water rinse procedure (30 seconds each) used in 1818 patterning. After that, the substrate is placed on a 200 °C hotplate for 2 minutes. The substrate is then briefly air-cooled using nitrogen, and then placed on a spinner and coated with SF-11 photoresist at 4,000 RPM for 30 seconds. If the sample is a full wafer, some precaution must be taken to intercept the wisps of SF-11 strands that form when the excess photoresist is spun off the wafer. After the spinning process, the sample is placed on the 200 °C hotplate again for 2 minutes. Next, after briefly cooling the wafer again with nitrogen, the wafer is coated with a layer of 1805 photoresist, using the spinner at 4,000 RPM for 30 seconds. This step is followed by another bake, this time at 110 °C for 75 seconds.

The substrate is then patterned with a mask aligner and subsequently developed in a spinner for 30 seconds using a 5:1 DI water and 351 developer mixture. This patterns the 1805, but not the SF-11 underneath. After successful inspection of the pattern under the microscope, the sample is placed under the deep-UV flood exposure lamp for 200 seconds, and then developed in a bath of 101 developer for 1 minute. The combination of the deep-UV exposure and the 101 developer patterns the SF-11 with a slightly larger undercut compared with the 1805 pattern, which creates the desired protective lip of 1805 over the SF-11.

3.3. Probe Station Measurements

A Micromanipulator probe station was used extensively in order to test the fabricated GeTe indirect heating test devices. A probe station is a method of electrically interfacing between external equipment (i.e. signal generators, multimeters) and devices fabricated on a wafer. An image of a probe station is shown in Fig. 35.

The probe station has four probes, which are adjustable in three different axes. At the end of each of the probes is a metallic probe tip. These probe tips can be manipulated to land on contact pads in a wafer design. Before each measurement, the probe tips were placed on a well-defined conductive surface to verify that there is a low contact resistance between the probe tips – 2 to 3 ohms. The Micromanipulator station also has a camera

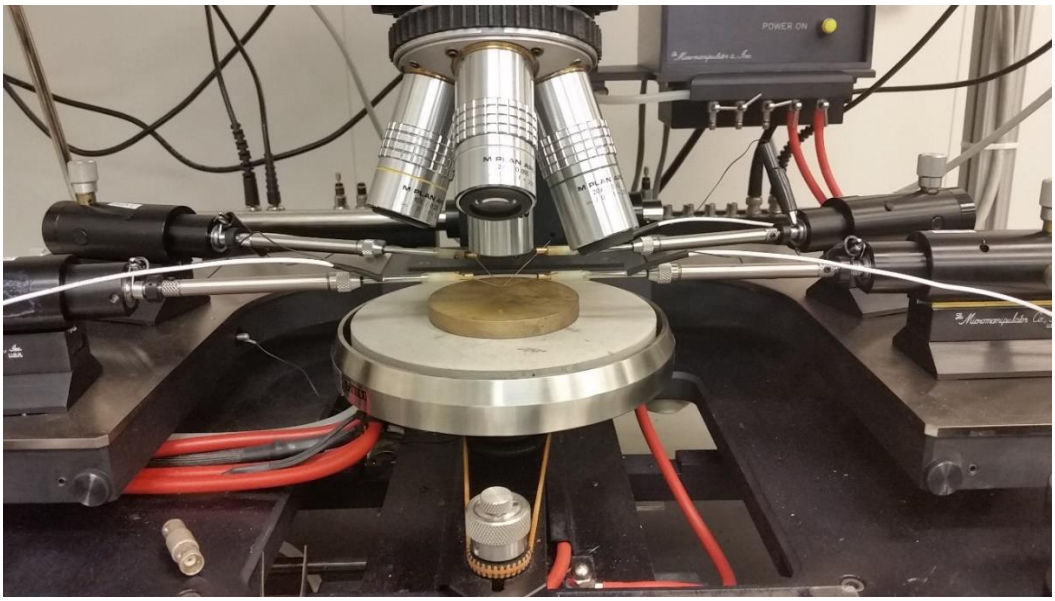

Fig. 35. Probe station test setup. Stage can freely be moved laterally, and also vertically in defined steps. Individual probes can be manipulated in three dimensions. The stage can also be thermally heated up to approximately 400 Celsius.

attached to the microscope which can be used to take videos and photos of designs under test.

3.4. Substrate Characterization

THz-TDS was used to characterize the transmission properties of quartz, silicon, and sapphire wafers. Each wafer was measured in the THz machine using the procedure described in the previous section. An open-air measurement was used as the initial reference for each material. In addition, the actual thicknesses of each of the wafer pieces were measured with a digital caliper. The thicknesses, along with the transmission data from the TPS Spectra 3000, were input into the fixed-point algorithm mentioned in the theory section in order to produce highly accurate approximations for the complex index of refraction for each of the materials. The nominal material specifications of each of the wafers are shown in Table 2.

Table 2. Nominal properties of substrates used in terahertz characterization study.

	Quartz	**Silicon**	**Sapphire**
Doping	Intrinsic	Intrinsic	Intrinsic
Thickness	12 mm	1 mm	560 μm
Orientation	X-cut	(100)	C-plane

3.5. SRR Computer Simulations

Full-wave electromagnetic simulations in CST Studio Suite were utilized to predict and validate the resonant behavior of various metamaterial structures designated for fabrication. In addition, the simulations helped validate some of the analytical equations that are used to predict the LC resonant frequencies of SRRs.

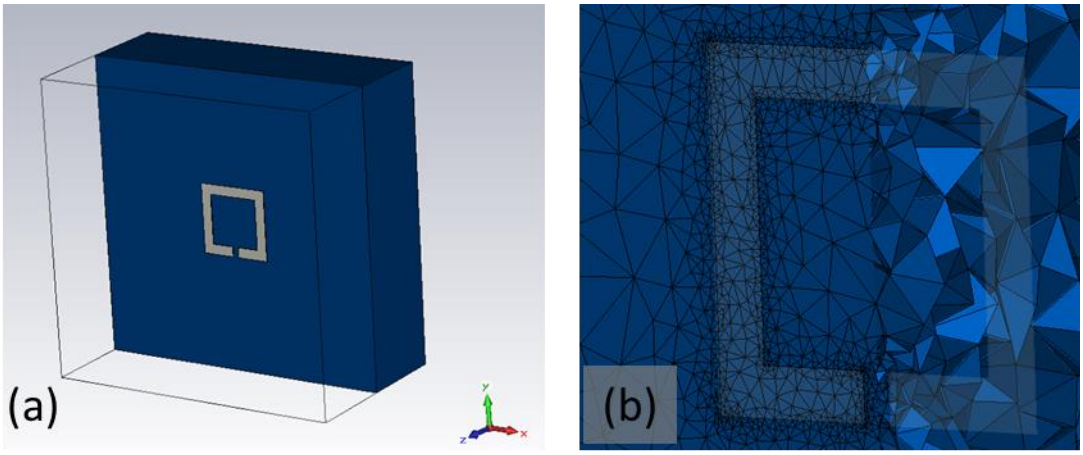

Fig. 36. SRR model. An overview of the model is shown in (a). A slice showing the tetrahedral meshing of the model is shown in (b).

Fig. 36 shows an example of one such model. All of the simulation models assumed lossless dielectrics and perfect electrical conductors (PECs) for metals. The metamaterial being simulated was an infinitely long 2-D array of split-ring resonator elements. Due to the x- and y-periodic nature of the model, periodic boundary conditions and excitations are used in the model. These conditions make use of Floquet's theorem to determine the frequency-domain response of an infinitely wide periodic array of elements, using only the simulation domain of a single unit cell.

Although in reality the substrate has a finite thickness, modeling the entire thickness of the substrate was not feasible in simulation, due to its significantly larger dimensions when compared to the SRR elements. Instead, the z-min waveguide port in the model was placed flush against the substrate, creating an infinite half-plane scenario. Since the waveguide ports are programmed to automatically match its propagation constant with the material to which it is adjacent, this has the added benefit of removing Fabry-Perot type resonances from the simulation.

The CST frequency domain solver with adaptive tetrahedral mesh was used for all of the SRR simulations. The frequency domain solver generates a system of equations at a given frequency based on a physical model, and then solves that system of equations [128]. This results in a solution (typically S-parameters) for the given frequency; this process can be repeated multiple times at different frequencies in order to get a fuller spectral understanding of the model.

A mesh breaks down a model into smaller, discrete blocks. As its name states, the tetrahedral mesh discretizes a model into tetrahedron-shaped blocks. Varying the size of these blocks represents a tradeoff between accuracy and computation time. The frequency domain solver can help easily balance between accuracy and computation time with its adaptive meshing procedure. In this procedure, the model is solved over a few frequencies, resulting in field solution data for those frequencies. Next, the mesh in the model is slightly decreased, and the results over the given frequencies are re-calculated, and field data re-generated. The field data from the two runs are compared and used to calculate an estimated amount of error in the solution [129]. If the estimated error is above a defined threshold, the mesh is further adapted at points in the model where the estimated error is high, and the model is re-run. This process repeats until the estimated error is below the desired threshold, or a maximum number of iterations is reached.

In this thesis, the adaptive mesh parameters were set with the following parameters: An S-parameter threshold accuracy of 0.01; adaptive meshing at three automatically-generated points over the frequency range; and 15 adaptive iterations maximum per frequency. Fig. 37 shows the difference in mesh quality of an SRR after an adaptive meshing procedure is carried out.

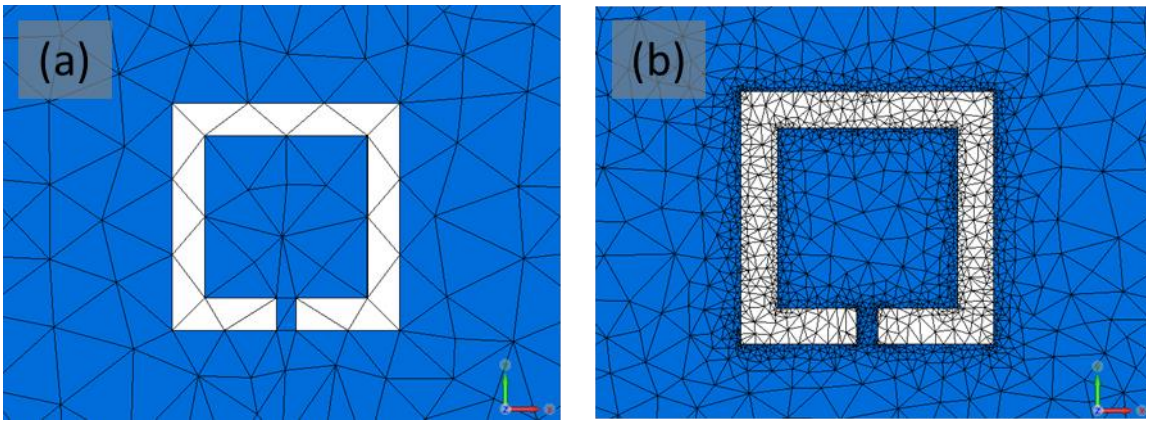

Fig. 37. Adaptive meshing procedure. The mesh after 1 pass of adaptive refinement is shown in (a). The mesh after 11 passes of adaptive refinement is shown in (b).

After simulating a device, a post-processing step must be carried out in order to directly compare the simulation results with the measurements. One of the outputs of the simulation is an S-parameter matrix. An S-parameter matrix represents all the possible combinations of field amplitude ratios between the waves entering and exiting every port. The S21 component of the S-parameter matrix is roughly equivalent to the "sample" measurement in THz-TDS. The only difference between the two is that the simulation lacks an outgoing transmission coefficient and the substrate Fabry-Perot coefficient, due to the infinite half-plane used in simulation. Similarly, the S21 component for a simulation with a substrate without an SRR will be nearly equivalent to the "reference" measurement in THz-TDS, but lacking the same outgoing transmission coefficient and Fabry-Perot term.

For the post-processing step, the S21 (sample) is divided by the S21 (reference), to create a simulated transmission coefficient. The simulated transmission coefficient is identical to the THz-TDS transmission equation, since the missing transmission and FP

coefficients in the simulation “reference” and “sample” measurements would have canceled out anyways when diving the two measurements with one another.

3.6. Metal SRR on quartz

As a preliminary design, SRRs were fabricated on quartz and measured in the TPS Spectra 3000. The purpose of this study was to verify that the SRRs resonated at the frequency predicted by simulations and theory. The fabrication steps are outlined in the paragraph below. The dimensions of the various SRRs produced are shown in Table 3. The mask design used for this and subsequent SRR samples is shown in the Appendix.

First, the SRR designs were patterned onto a quartz wafer using the 1818 patterning method mentioned earlier. After patterning, a 20 nm / 280 nm layer of Ti / Au was thermally evaporated onto the wafer. The wafer was then sent to AFRL to be diced. Upon dicing, the wafer pieces were individually lifted off with scotch tape and an ultrasonic bath. After examining the sample under a microscope, it was noted that there were some places with missing SRRs and some leftover metal ‘squares’ after liftoff, as

Table 3. The dimensions of split-ring resonators fabricated on quartz. All dimensions are in μm.

Square Length	Line Width	Gap Width	Metal Thickness	Period
30	5	3	0.300	150
30	5	5	0.300	150
30	5	10	0.300	150
20	5	3	0.300	100
20	5	5	0.300	100
20	5	10	0.300	100
10	3	3	0.300	50
10	3	4	0.300	50
10	3	5	0.300	50

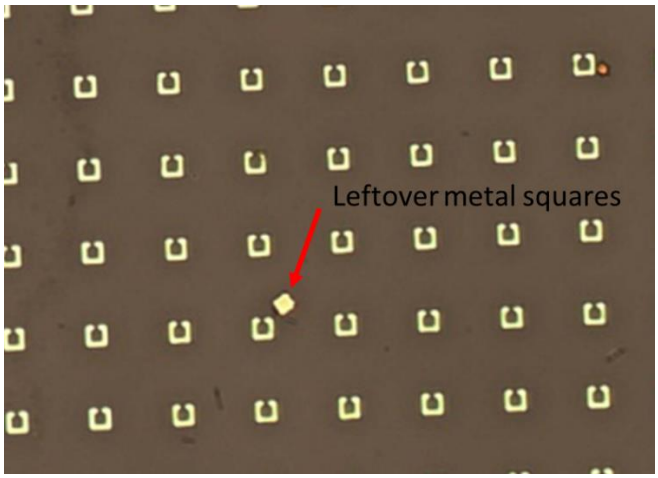

Fig. 38. SRRs patterned in gold. The red arrow marks a square of gold which remained after liftoff. These were scattered very sparsely throughout the array.

shown in Fig. 38, but there were not enough of these to cause a significant difference in measurements for the purpose of this study.

After liftoff, the devices were ready to be measured in the TPS Spectra 3000 THz-TDS system using the method described in an earlier section. A blank piece of quartz from the same wafer as the SRR devices was used for the reference measurement. During the measurement of the SRRs, the samples were rotated such that the SRR gaps were on the right side of the SRR in order to couple its LC resonance mode correctly with the vertically polarized electric field in the test chamber [32].

3.7. Metal SRR on i-Si

A set of SRRs was also made on a 1-mm-thick, intrinsic silicon wafer. The purpose of this study was to investigate the effect that a thicker, higher-index substrate would have on the measurement accuracy of a metal SRR pattern. Due to the significant thickness of the silicon wafer used in this study, dicing was not initially used. Instead, the

wafer was cleaved using a handheld, diamond-tipped scribing tool. Because of the inherent inaccuracy involved when using a handheld cleaving tool, the wafer was split into pieces before patterning. The bi-layer patterning process was used for the i-Si SRRs. A description of the bi-layer process is described in the lithographic patterning section. The dimensions of the SRRs are shown in Table 4.

After patterning, a 20-nm / 280-nm layer of Ti / Au was evaporated on the substrate. For the lift-off procedure, the majority of the deposited metal was first removed with scotch tape. Next, the sample was submerged in acetone and placed in an ultrasound bath for 10 minutes. This lifted off any remaining undesirable metal and removed the 1805 layer. Next, the wafer was placed in a heated (95 °C) 1165 solution bath for one minute, which removed the SF-11.

The SRRs on intrinsic silicon were measured in the TPS THz-TDS with the same method as the SRRs on quartz. A piece of intrinsic silicon from the same wafer was used for the reference measurement in this case.

Table 4. Dimensions of split-ring resonators (SRRs) fabricated on intrinsic silicon. The basic SRR dimensions were the same, while the periodicity of the SRRs were varied from closely to widely spaced. All dimensions are in μm.

Square Length	Line Width	Gap Width	Metal Thickness	Period
20	5	3	0.300	28
20	5	3	0.300	39
20	5	3	0.300	50
20	5	3	0.300	100
20	5	3	0.300	120

3.8. Printed SRRs

In addition to microfabrication techniques such as metal evaporation and sputtering, additive technologies can also be used to deposit patterns of metals. An Optomec AJ-300 aerosol jet printer was used to create an array of SRRs on quartz. Clariant Prelect TPS 50, a nanoparticle-based silver ink, was used for the print. The ink was atomized ultrasonically using the Optomec UA-Max atomizer, and was sintered after the deposition. During the sintering process, the print was heated to 95 ºC for 30 minutes to dry off any excess solvent, and then further heated to 220 ºC for 60 minutes in order to fully sinter.

Two arrays of SRRs were printed, one on 490-micron quartz and the other on 1-mm intrinsic silicon. A unit cell of each of the prints is shown in Fig. 39. The printed SRRs were designed to have a 50-micron length, 10-micron line width, and a 10-micron gap length. The SRRs on quartz were spaced with a periodicity of 150 microns, and the

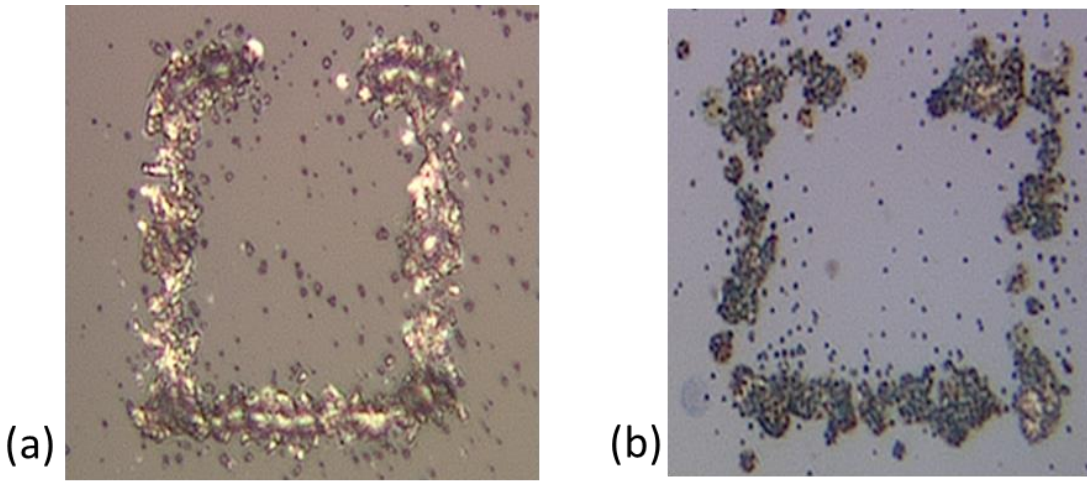

Fig. 39. Printed split-ring resonators on (a) quartz and (b) silicon

SRRs on silicon were spaced with a periodicity of 80 microns. As with the previously mentioned SRR designs, these printed SRRs were measured using the THz-TDS system.

3.9. GeTe-Incorporated SRRs

Two structures were created using GeTe as an active layer. The first structure consists of SRRs entirely made out of GeTe. The second structure is composed of gold SRRs with rectangles of GeTe in the gaps. Both devices were fabricated on the same 1-mm intrinsic silicon used for the previous SRRs, and used the bi-layer liftoff process. The GeTe was uniformly RF sputtered using Denton Discovery 18 sputtering system. A 99.999% pure, 50/50 GeTe target was used for the deposition, and the chamber was set to a pressure of 10 mTorr with a 20.1 sccm flow of argon. The thicknesses of the deposited layers were approximately 300 nm. In the second structure, gold was thermally evaporated to a thickness of 280 nm with a 20-nm titanium adhesion layer beneath it.

Images of the two GeTe-incorporated designs are shown in Fig. 40. SRRs in both designs were 20 microns long, with a 5-micron line width and a 3-micron gap width. The SRRs were spaced with a 39-micron periodicity. For the GeTe-gapped metal SRR design, the GeTe rectangles were 14 microns wide and 10 microns tall. The rather large size of the GeTe rectangles helped alleviate alignment tolerances.

The devices were measured in the TPS Spectra 3000 with the in-situ thermal heating module described in an earlier section. Measurements were taken at 50 ºC increments, except for the approximate area of the transition temperature of GeTe. In this region, between 180 and 220 ºC, a 10 ºC step was taken instead. After reaching the

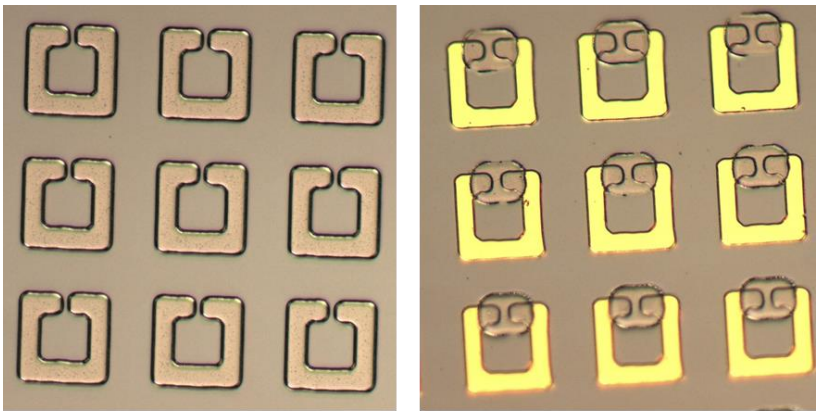

Fig. 40. Microscope image of the fabricated GeTe-incorporated split-ring resonators (SRRs). (a) SRRs composed entirely of GeTe (b) Gold SRRs with a GeTe rectangle in the capacitive gaps

maximum allowable temperature of the module (250 ºC), additional measurements were taken at 50 ºC decrements towards room temperature.

3.10. GeTe Laser Pulsing

GeTe has been shown in the literature to be resettable via laser pulses [109], [110]. In this experiment, a Heidelberg µPG 101 mask writer was utilized in order to attempt laser pulse resetting of GeTe. 18-mW and 120-mW power settings were both used with varied pulse intervals.

A reduced version of the indirect heating characterization design was used as the test design for the laser pulsing study. This design included the NiCr contact pad layer, the GeTe contact pad layer, and the GeTe layer. The NiCr contact pad layer was not needed for laser pulsing, but was included in the design since that layer had all of the necessary alignment marks. The GeTe layer was deposited to 150 nm.

After the test wafer was fabricated, the wafer was heated on a hot plate in excess of 5 minutes at 250 ºC in order to crystallize the GeTe films. GeTe resistances were measured in the Micromanipulator probe station for an initial GeTe measurement. After initial resistance measurements, the reticles were placed in the mask writer. The mask writer was set to laser expose a rectangular shape that was approximately the size of one reticle of the test design. The mask writer was manually aligned to the center of a specific reticle for each measurement. Various laser powers and exposure lengths were tested, as shown in Table 5. After all the desired laser exposures were finished, the resistance between GeTe contact pads of numerous devices was measured for each reticle.

Table 5. Laser exposure powers and pulse durations

Laser Power (mW)	Pulse Length (% of Maximum)
18	100
18	50
120	100
120	50

3.11. GeTe Indirect Heating Characterization

3.11.1. GeTe Indirect Heating Test Devices

In order to verify that GeTe could be successfully amorphized and crystallized using electrical pulses, a five-layer test structure was designed, fabricated, and tested, using El-Hinnawy's indirect heating design as a starting point. Fig. 41 shows a top-down view of one device. The full mask consists of a large array of this device, with each column having devices of a slightly different geometry. The following three geometry variables were parameterized: The length width of the GeTe area, the width of the GeTe,

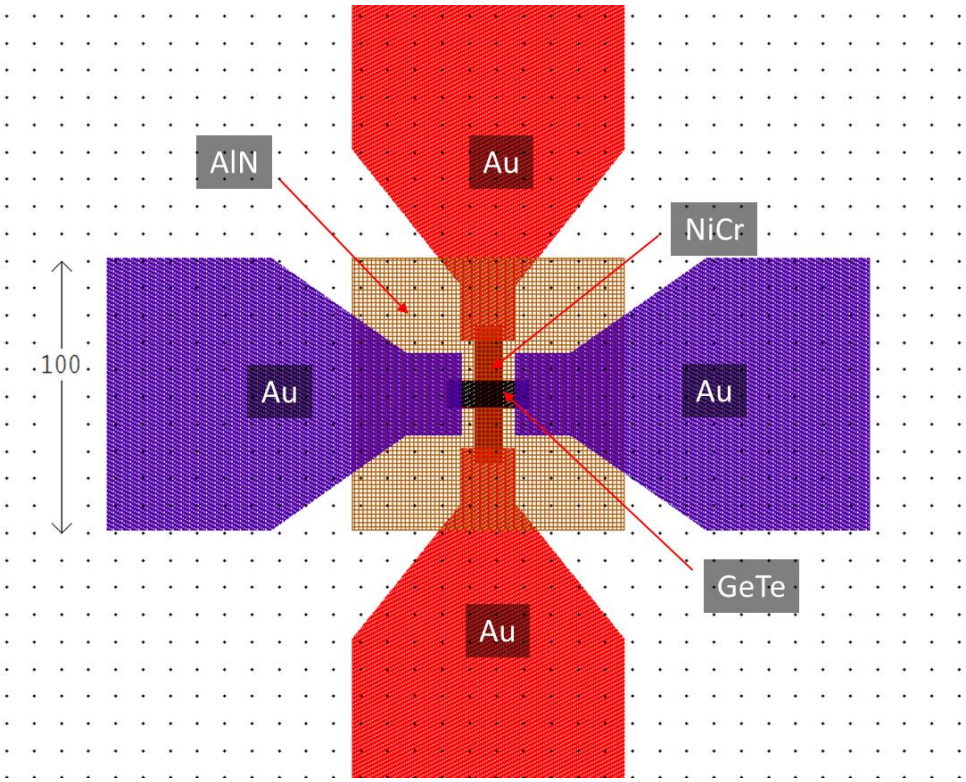

Fig. 41. Layout of the indirect heating test structure. The scale is in micrometers.

and the width of the NiCr heater. The target thicknesses and the deposition methods for each of the deposited layers in the initial are shown in Table 6.

Table 6. Materials used in germanium telluride indirect heating study

Material	Thickness (nm)	Deposition Method
Substrate Insulator (Si_3N_4)	~300	Pre-deposited on Si Wafer
Thin film resistor (NiCr)	30 - 90	DC Sputtering
Ti / Au Pads for NiCr	20 / 280	Thermal Evaporation
Dielectric Barrier (AlN or Si_3N_4)	45 - 150	RF Sputtering
Phase Change Material (GeTe)	150 - 300	RF Sputtering
Ti / Au Pads for GeTe	20 / 280	Thermal Evaporation

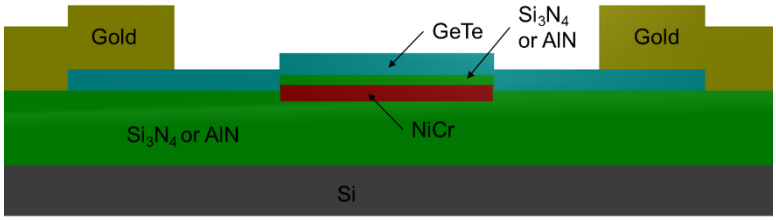

Fig. 42. Side view of indirect heating device, showing initial layer stackup.

The layers were each patterned using the same bilayer liftoff process that was used for the SRRs on intrinsic silicon. The bilayer process helped improve the success rate for the sputtering depositions. The layers in the initial design were ordered as shown in Table 6 (lowest layer shown first), and are visualized in Fig. 42.

3.11.2. Steady State Thermal Simulation

The indirect heating test structure was simulated in a steady-state thermal simulation using the Coventorware software by Coventor. The relevant material parameters (heat capacity, thermal conductivity, density) of crystalline GeTe were taken from [130], [131]. Two types of electro-thermal simulations were carried out: a steady-state and transient solution. A steady-state solution is simpler and faster, and was used to get a rough estimate at the voltage required to sufficiently heat the GeTe layer for amorphization. The more complex transient solution was used with the previously determined voltage to verify that the GeTe layer would reach the optimum temperature during the short duration of the joule heating pulses.

A model of the device in the Coventorware software is shown in Fig. 43. Since the main purpose of this model was to verify the amorphization pulse, the material properties of crystalline GeTe were used in the model.

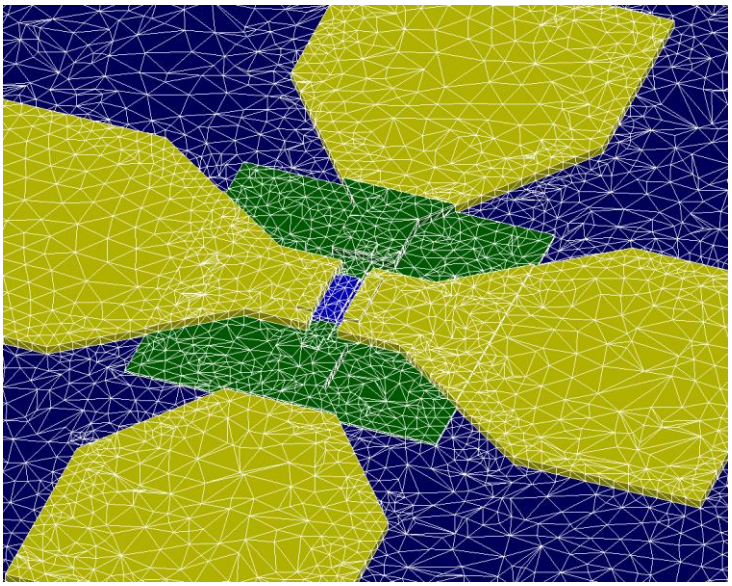

Fig. 43. Tetrahedrally meshed Coventorware model of germanium telluride indirect heating device

3.12. Summary

This chapter discussed the simulation, fabrication, and measurement techniques utilized for a wide range of experiments on SRRs and GeTe. In the next chapter, all of the data from these experiments will be presented, with analysis of this data in the subsequent chapter.

4. Data

4.1. Material Extraction

Transmission measurements of silicon, sapphire, and quartz substrates were carried out with the TPS Spectra 3000. The measured data was subsequently placed in a fixed-point iteration scheme in order to calculate the complex indices of refraction of the three materials. Figures 44-46 show the acquired and derived data.

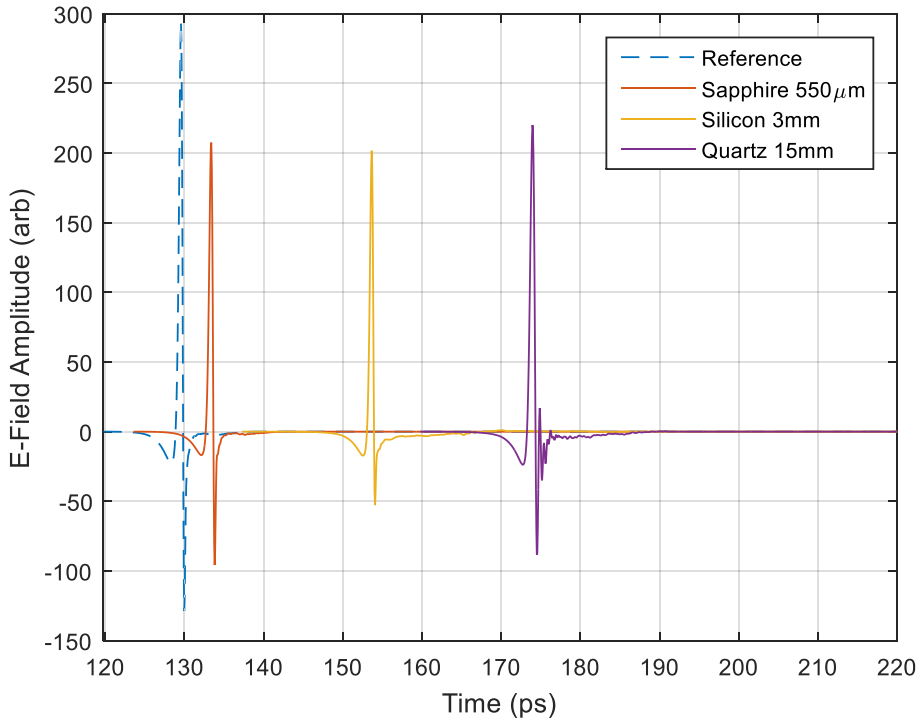

Fig. 44. Transmitted electric field data of bare substrate samples.

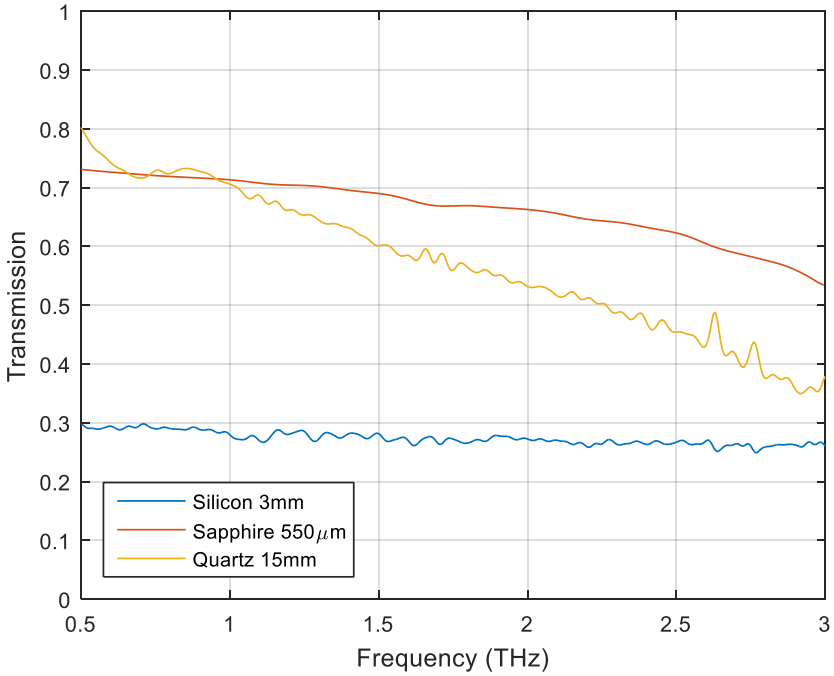

Fig. 45. Transmission responses of silicon, sapphire, and quartz wafers.

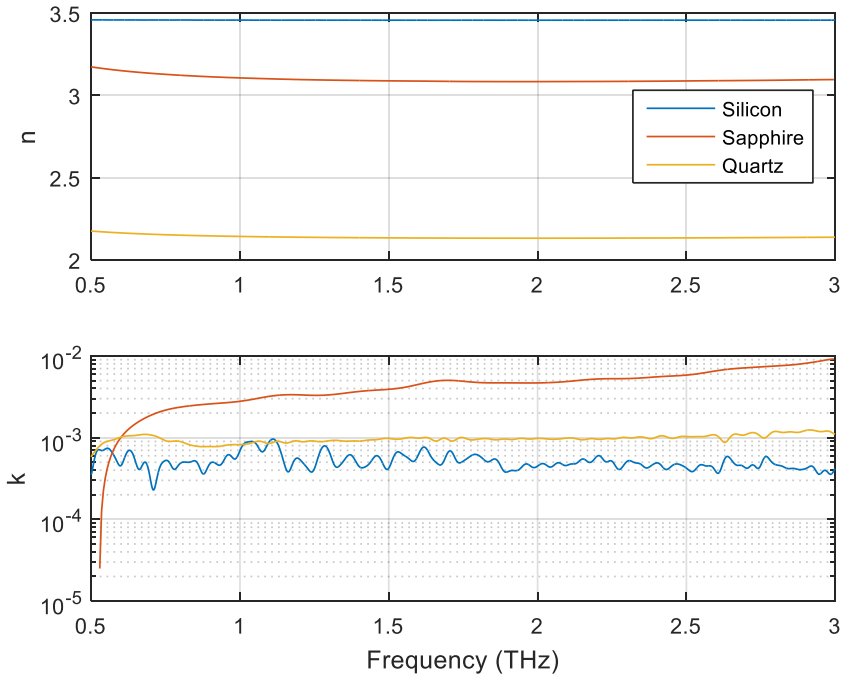

Fig. 46. Complex indices of refraction, calculated using fixed-point iteration.

4.2. SRR Simulations

Multiple simulations in CST were performed. Figures 47-50 show the simulated transmission for SRRs in free space and on silicon and quartz substrates, and Tables 7-9 numerically compare the resonant frequencies from simulation and analysis. The dimensions of actually fabricated SRRs were used in the simulation in order to be able to compare some of the results with measured data.

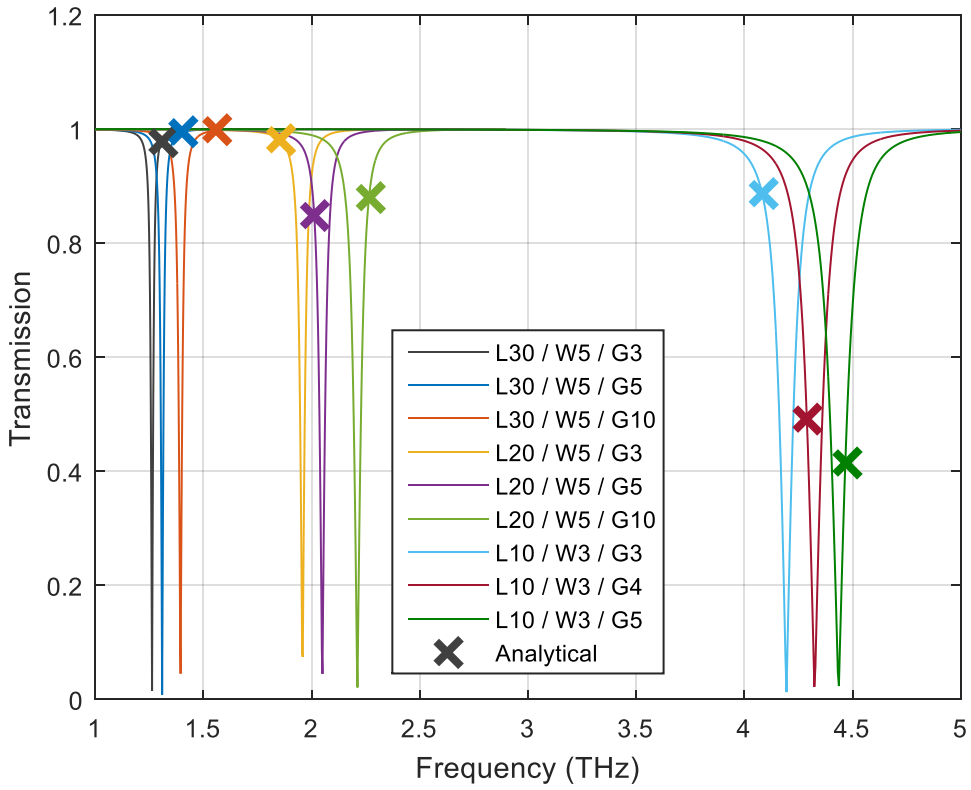

Fig. 47. Comparison between simulated and analytically calculated LC resonance points of split-ring resonators without a substrate backing. Higher order resonances are not shown.

Table 7. Comparison between analytical and simulated resonant frequencies of split-ring resonators suspended in free space. All frequencies are in terahertz. f_{sim} are the resonant frequencies determined through simulation; f_{LC} are the LC resonances calculated using the capacitance equation of (90) and the inductance equation (93); f_{nom} are resonant frequencies calculated with the ideal LC equation (27); and f_{plas} are plasmon resonant frequencies determined with (89).

Geometry	f_{sim}	f_{LC}	% Error	f_{nom}	% Error	f_{plas}	% Error
L30 / W5 / G3	**1.260**	**1.300**	-3.330	**1.233**	2.158	**1.282**	-1.750
L30 / W5 / G5	**1.310**	**1.400**	-7.290	**1.592**	-21.492	**1.304**	0.431
L30 / W5 / G10	**1.390**	**1.560**	-11.960	**2.251**	-61.927	**1.364**	1.897
L20 / W5 / G3	**1.960**	**1.850**	5.390	**1.849**	5.652	**1.948**	0.610
L20 / W5 / G5	**2.050**	**2.010**	1.950	**2.387**	-16.455	**2.000**	2.439
L20 / W5 / G10	**2.210**	**2.260**	-2.330	**3.376**	-52.769	**2.143**	3.038
L10 / W3 / G3	**4.190**	**4.080**	2.810	**4.775**	-13.953	**4.054**	3.245
L10 / W3 / G4	**4.320**	**4.280**	0.900	**5.513**	-27.622	**4.167**	3.549
L10 / W3 / G5	**4.440**	**4.460**	-0.500	**6.164**	-38.830	**4.286**	3.475

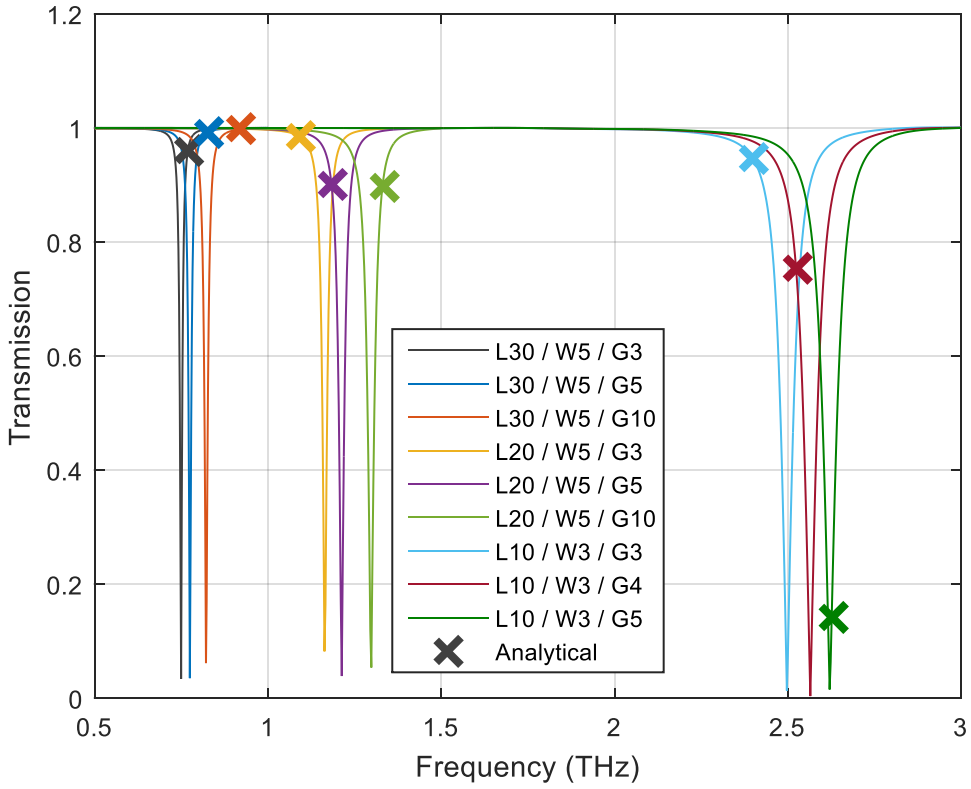

Fig. 48. Comparison between simulated and analytically calculated LC resonances of split-ring resonators with a quartz backing. Higher order resonances are not shown.

Table 8. Comparison between analytical and simulated resonant frequencies of split-ring resonators on a quartz substrate. All frequencies are in terahertz. f_{sim} are the resonant frequencies determined through simulation; f_{LC} are the LC resonances calculated using the capacitance equation of (90) and the inductance equation (93); f_{nom} are resonant frequencies calculated with the ideal LC equation (27); and f_{plas} are plasmon resonant frequencies determined with (89).

Geometry	f_{sim}	f_{LC}	% Error	f_{nom}	% Error	f_{plas}	% Error
L30 / W5 / G3	**0.750**	**0.770**	-2.490	**0.725**	3.360	**0.754**	-0.501
L30 / W5 / G5	**0.770**	**0.830**	-6.740	**0.936**	-21.522	**0.767**	0.407
L30 / W5 / G10	**0.820**	**0.920**	-11.910	**1.323**	-61.379	**0.802**	2.229
L20 / W5 / G3	**1.160**	**1.090**	6.210	**1.087**	6.275	**1.145**	1.266
L20 / W5 / G5	**1.210**	**1.180**	2.480	**1.404**	-15.998	**1.176**	2.822
L20 / W5 / G10	**1.300**	**1.330**	-2.580	**1.985**	-52.689	**1.260**	3.089
L10 / W3 / G3	**2.500**	**2.400**	3.860	**2.807**	-12.286	**2.383**	4.660
L10 / W3 / G4	**2.560**	**2.520**	1.640	**3.241**	-26.618	**2.450**	4.308
L10 / W3 / G5	**2.620**	**2.630**	-0.190	**3.624**	-38.321	**2.520**	3.828

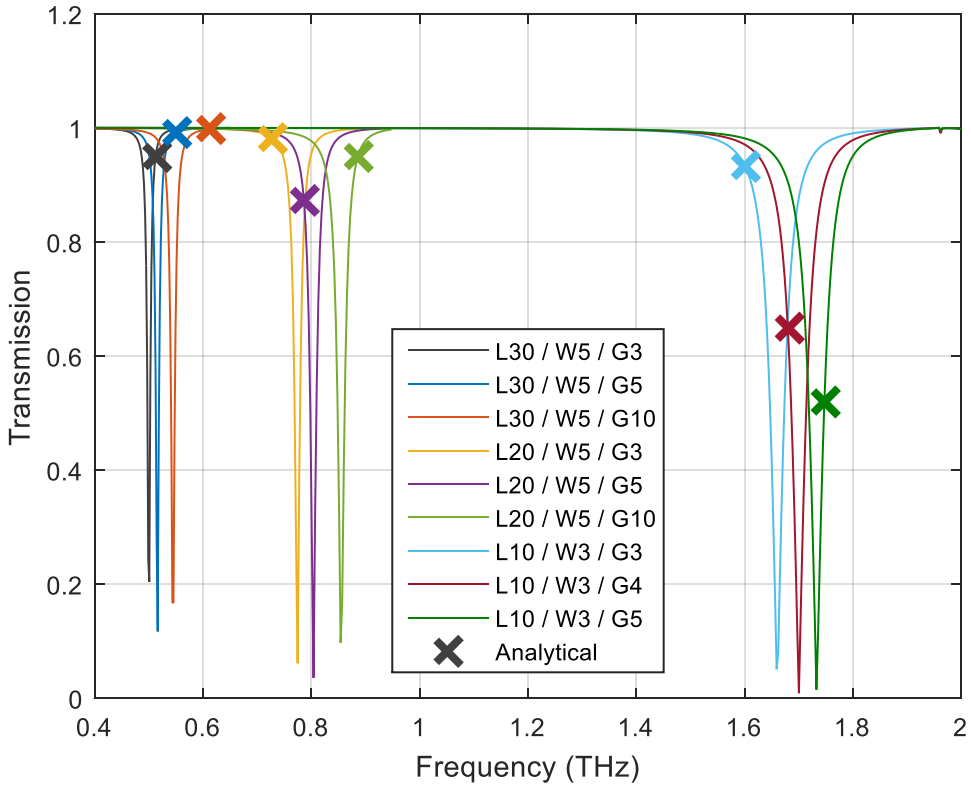

Fig. 49. Comparison between simulated and analytically calculated LC resonances of split-ring resonators with a silicon backing. Higher order resonances are not shown.

Table 9. Comparison between analytical and simulated resonant frequencies of split-ring resonators on a silicon substrate. All frequencies are in terahertz. f_{sim} are the resonant frequencies determined through simulation; f_{LC} are the LC resonances calculated using the capacitance equation of (90) and the inductance equation (93); f_{nom} are resonant frequencies calculated with the ideal LC equation (27); and f_{plas} are plasmon resonant frequencies determined with (89).

Geometry	f_{sim}	f_{LC}	% Error	f_{nom}	% Error	f_{plas}	% Error
L30 / W5 / G3	**0.500**	**0.510**	-2.140	**0.483**	3.445	**0.502**	-0.412
L30 / W5 / G5	**0.520**	**0.550**	-6.660	**0.623**	-19.858	**0.511**	1.771
L30 / W5 / G10	**0.550**	**0.610**	-12.220	**0.881**	-60.259	**0.534**	2.908
L20 / W5 / G3	**0.770**	**0.730**	6.230	**0.724**	5.953	**0.763**	0.926
L20 / W5 / G5	**0.800**	**0.790**	2.020	**0.935**	-16.861	**0.783**	2.098
L20 / W5 / G10	**0.850**	**0.890**	-3.860	**1.322**	-55.545	**0.839**	1.276
L10 / W3 / G3	**1.660**	**1.600**	3.630	**1.870**	-12.637	**1.588**	4.362
L10 / W3 / G4	**1.700**	**1.680**	1.180	**2.159**	-27.002	**1.632**	4.018
L10 / W3 / G5	**1.730**	**1.750**	-0.930	**2.414**	-39.531	**1.678**	2.988

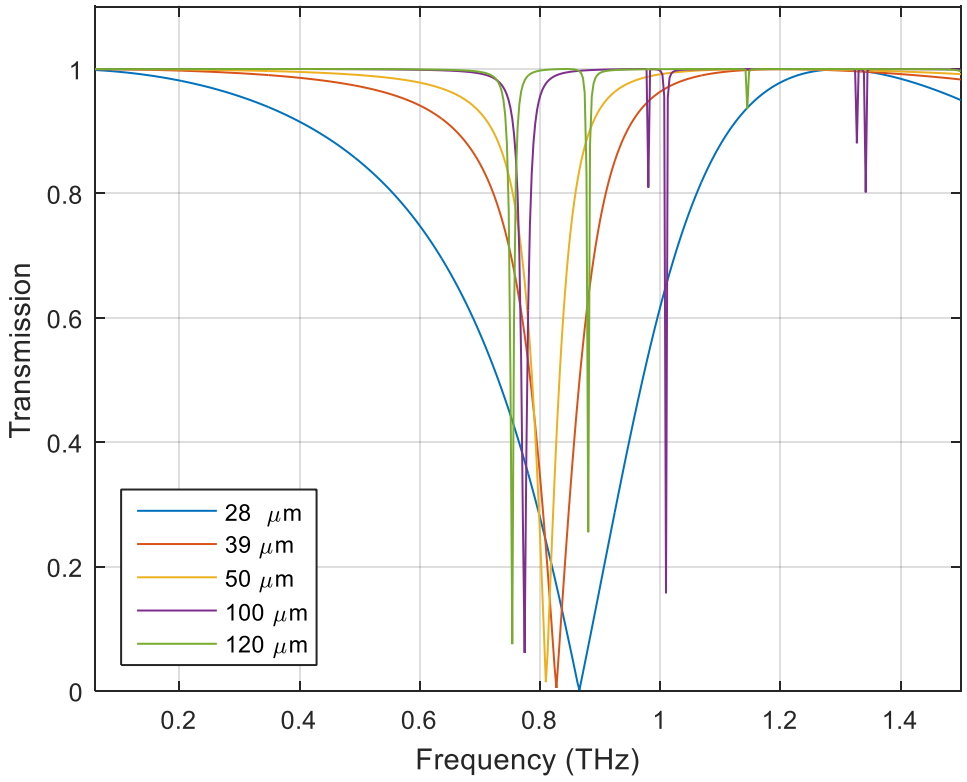

Fig. 50. Simulated results of split-ring resonators (SRRs) on intrinsic silicon, with varying periodicity. The SRRs have a side length of 20 microns, a line width of 5 microns, and a gap width of 3 microns.

4.3. Metal SRRs on Quartz

The transmission coefficients from 300-nm-thick, gold SRRs on 500-µm quartz of various dimensions were measured and compared to simulated data. Results are shown in Figures 51-53.

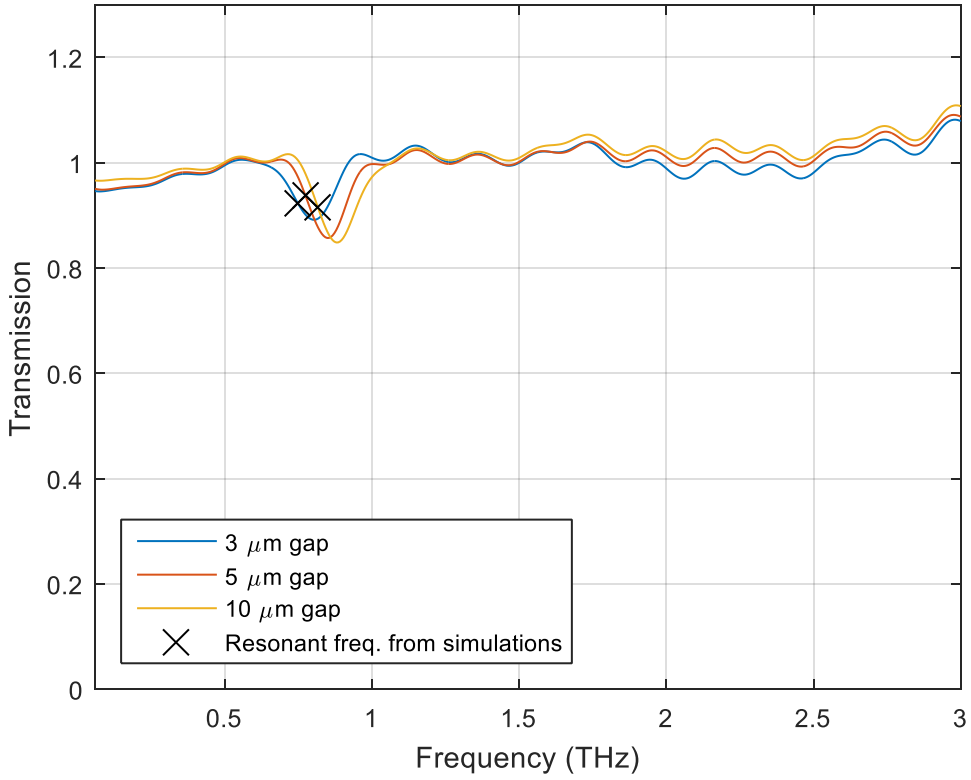

Fig. 51. Split-ring resonators with 30-µm side lengths and 5-µm wire widths.

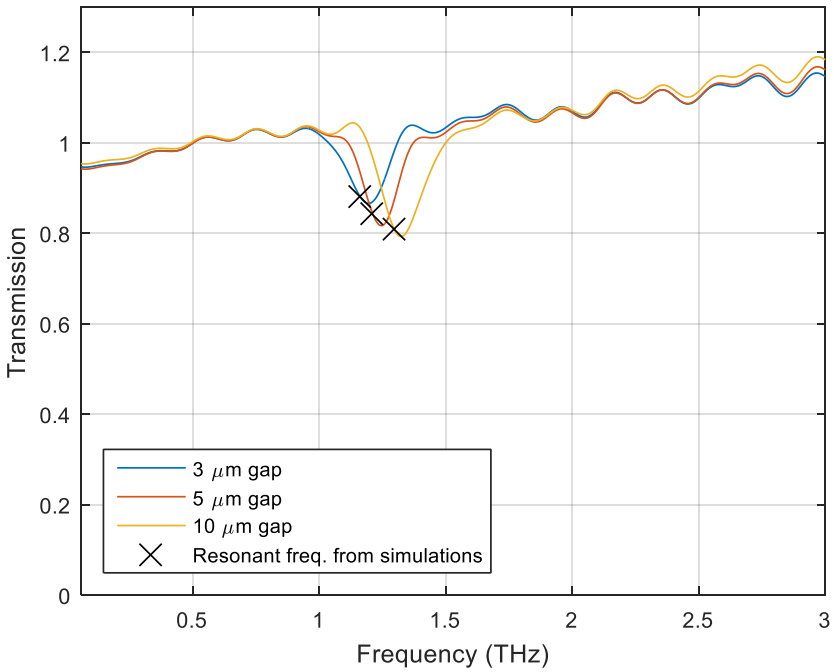

Fig. 52. Split-ring resonators with 20-µm side lengths and 5-µm wire widths.

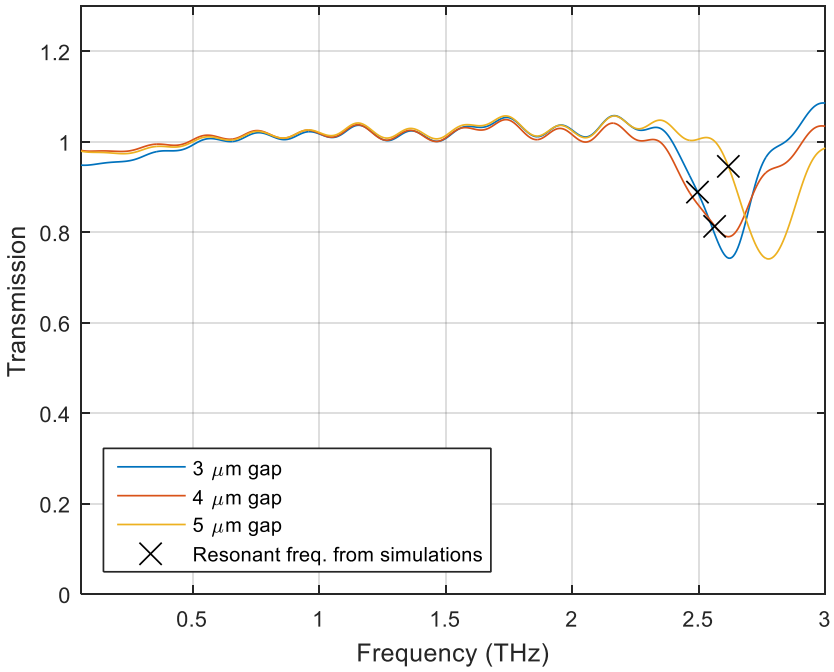

Fig. 53. Split-ring resonators with 10-µm side lengths and 3-µm wire widths.

4.4. Metal SRRs on Intrinsic Silicon

The transmission coefficients from 300-nm-thick, gold SRRs on 1-mm silicon were measured and compared to simulated data. Results are shown in Fig. 54.

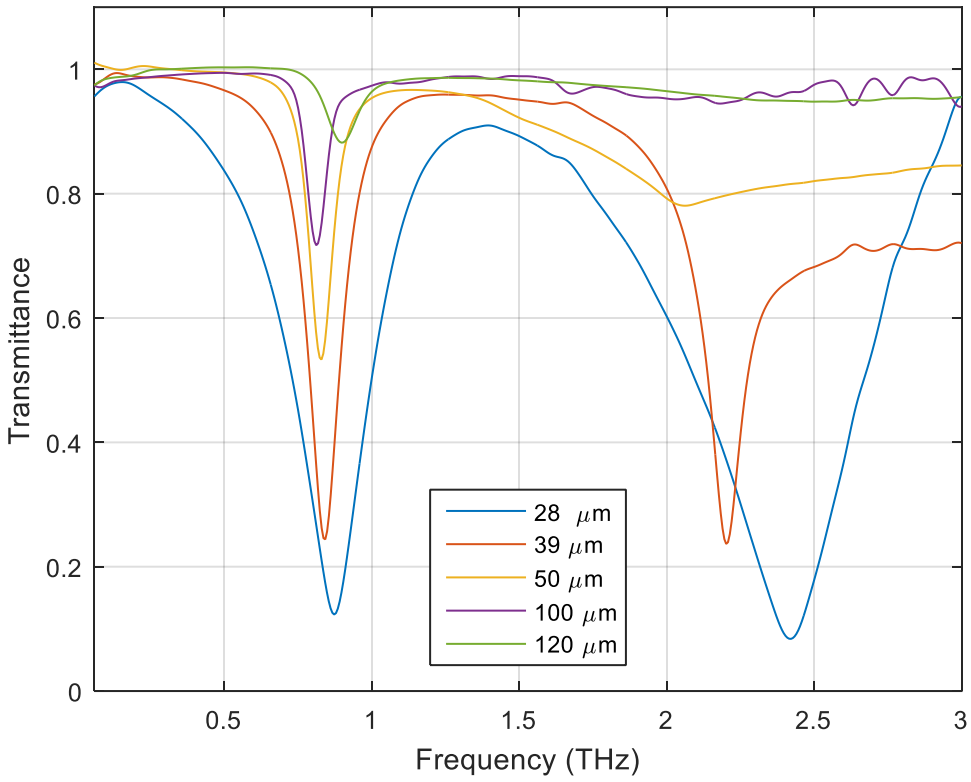

Fig. 54. Variations of transmission on periodicity of split-ring resonators on 1mm intrinsic silicon.

4.5. Printed SRRs

Scanning electron microscope (SEM) images of the two SRR prints are shown in Figures 55 and 56. Figures 57 and 58 show simulated and measured data for the inkjet-printed SRRs. One set of SRRs was printed on quartz, and the other was printed on silicon.

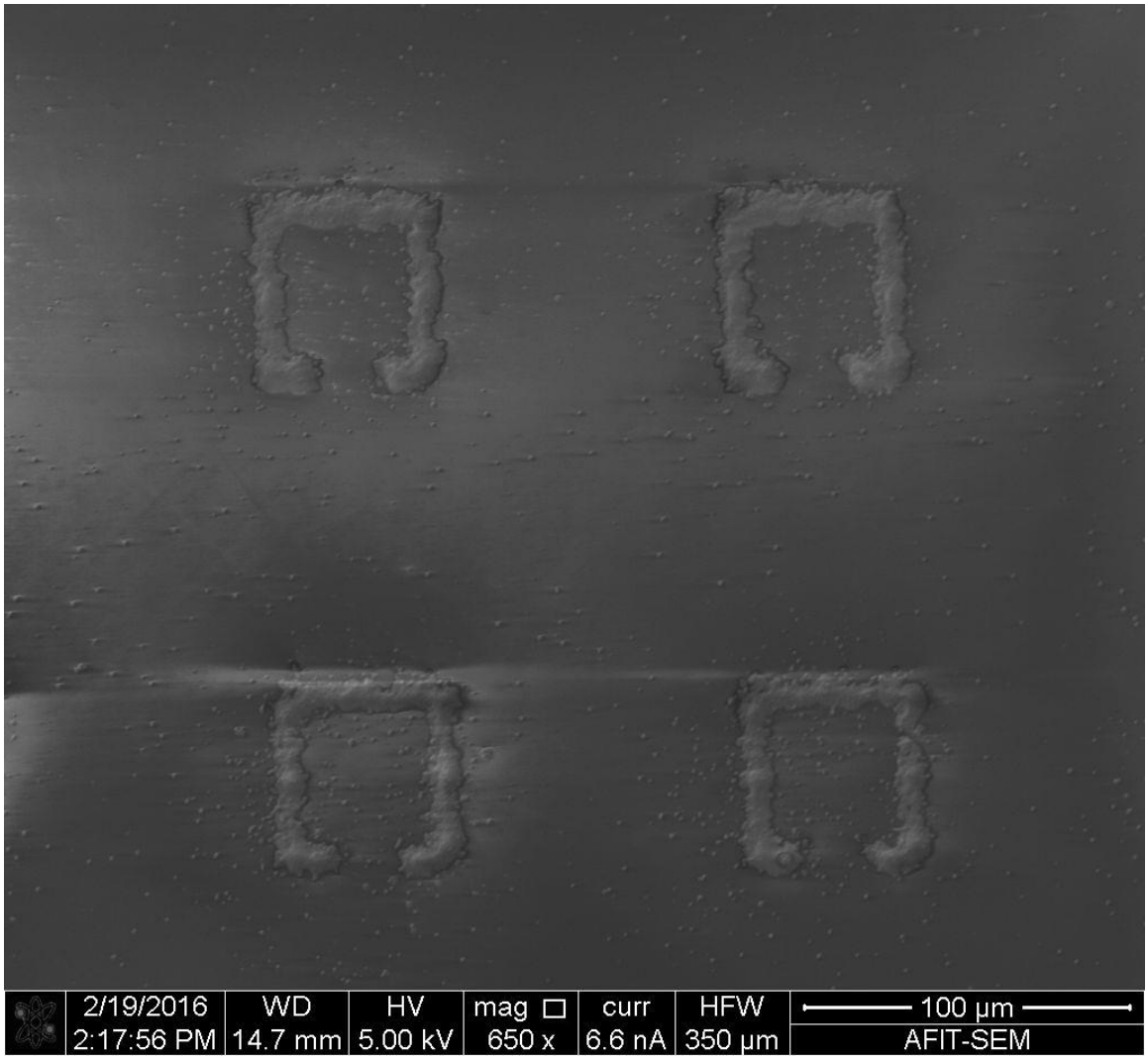

Fig. 55. Scanning electron microscope image of split ring resonators printed on quartz substrate.

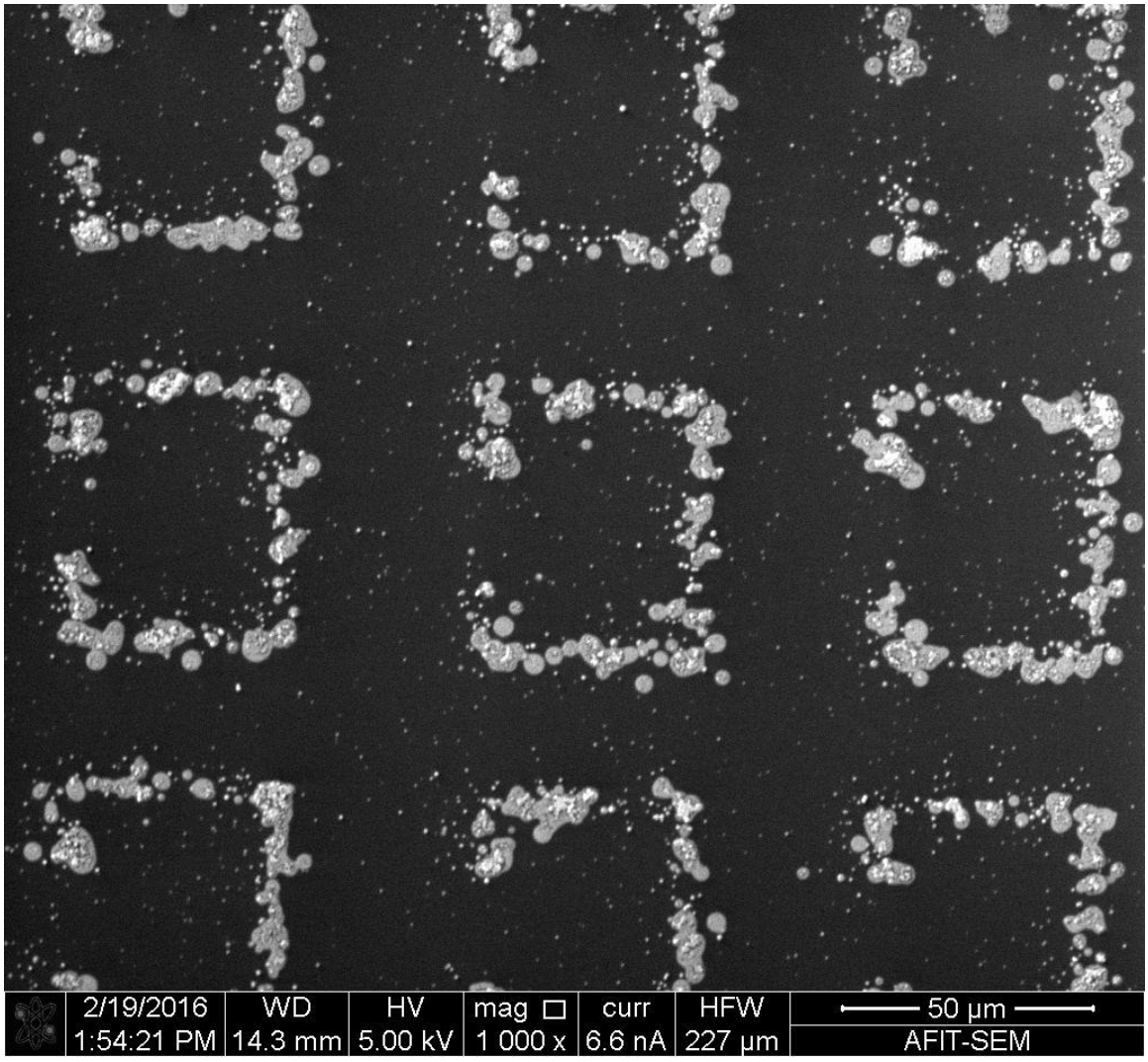

Fig. 56. Scanning electron microscope image of printed split ring resonators on silicon substrate

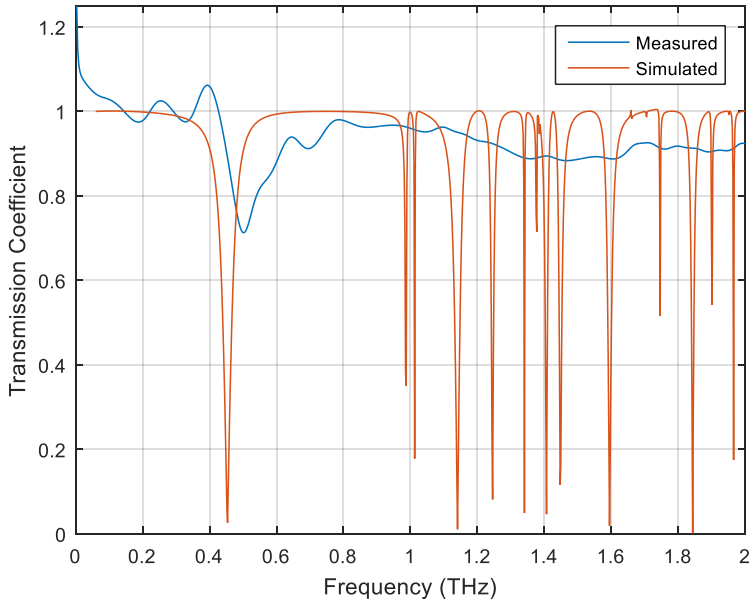

Fig. 57. Transmission response of printed split-ring resonators on quartz, compared with simulation.

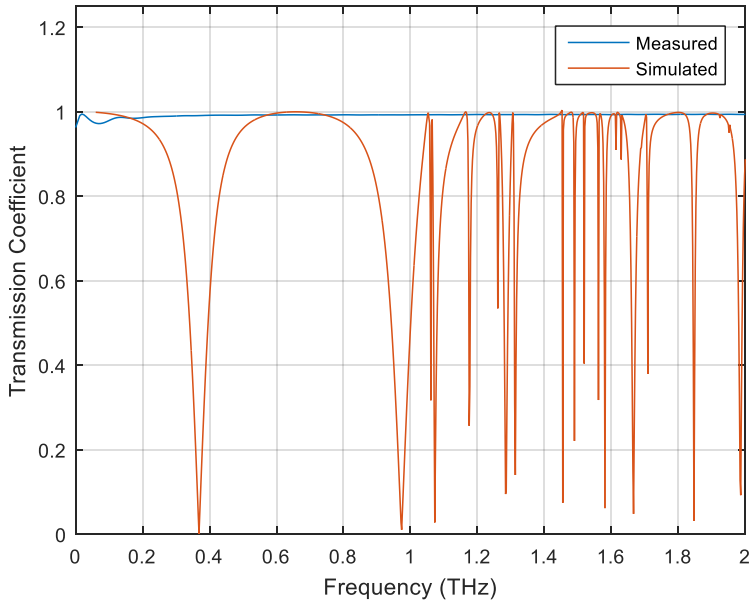

Fig. 58. Transmission response of printed split-ring resonators on silicon, compared with simulated results.

4.6. GeTe-Incorporated SRRs

4.6.1. GeTe SRRs

An SEM image of an array of GeTe SRRs is shown in Fig. 59. Measured data of GeTe SRRs on 1-mm silicon substrate is shown in Figures 60-62. The samples were measured with in-situ heating, showing the temperature dependence of the response of the SRRs before and after crystallization of the GeTe.

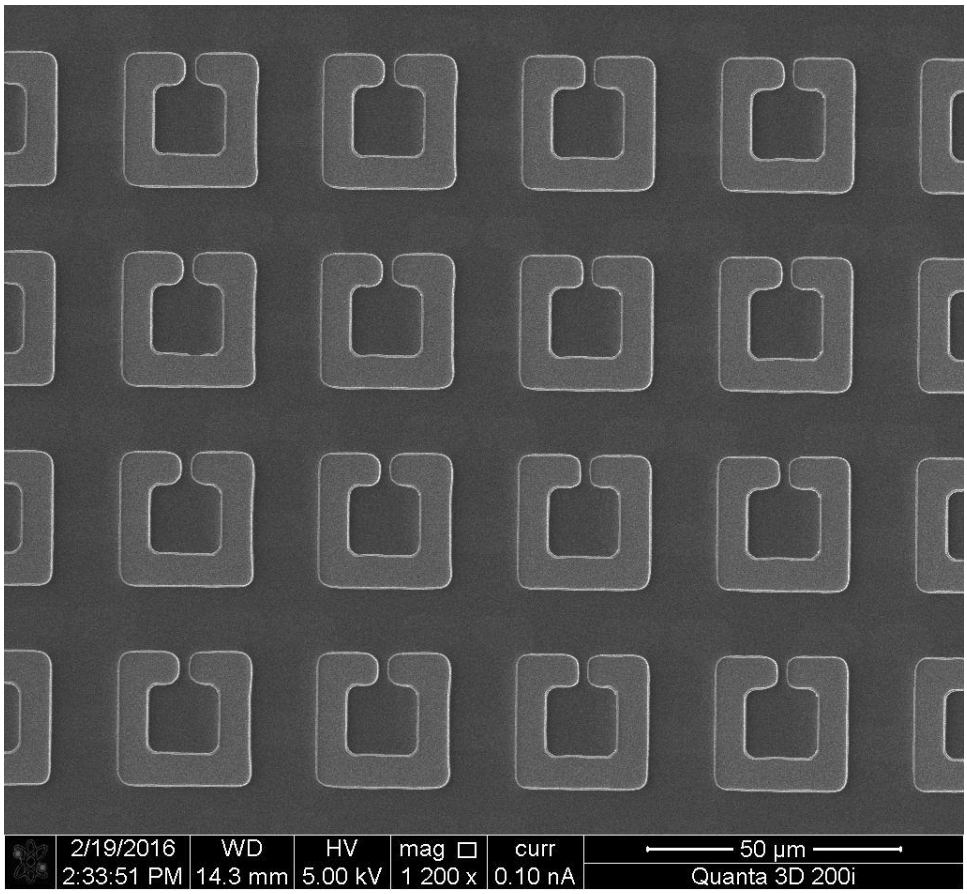

Fig. 59. Scanning electron microscope image of germanium telluride split-ring resonators.

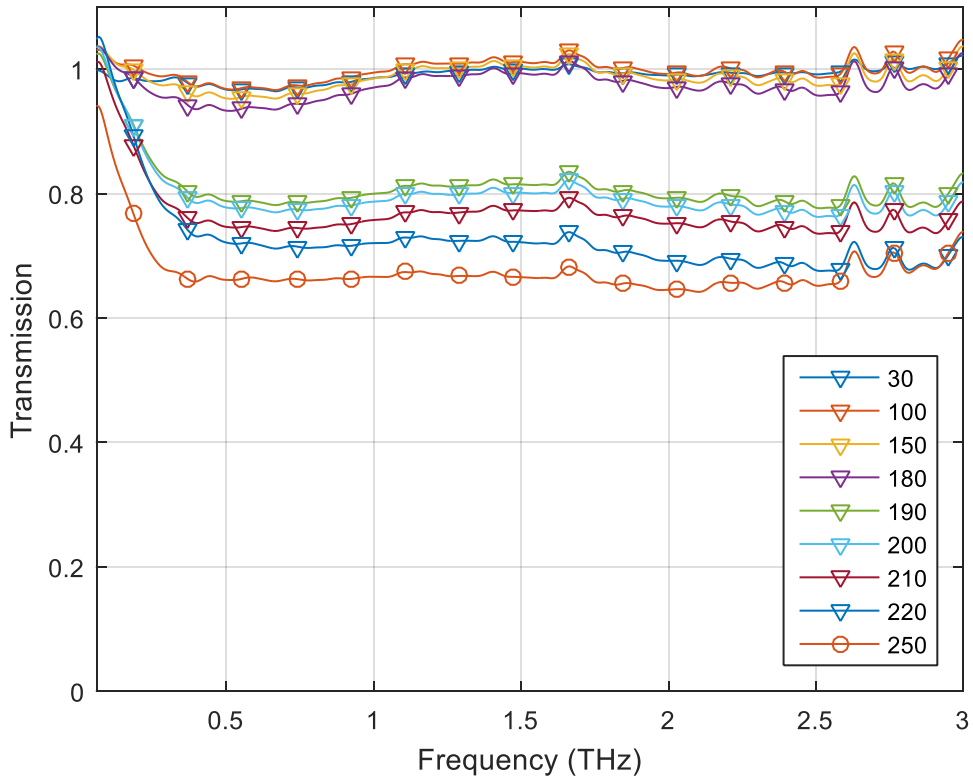

Fig. 60. Transmission measurements with in-situ thermal heating of 300-nm germanium telluride split-ring resonators, increasing temperature in Celsius.

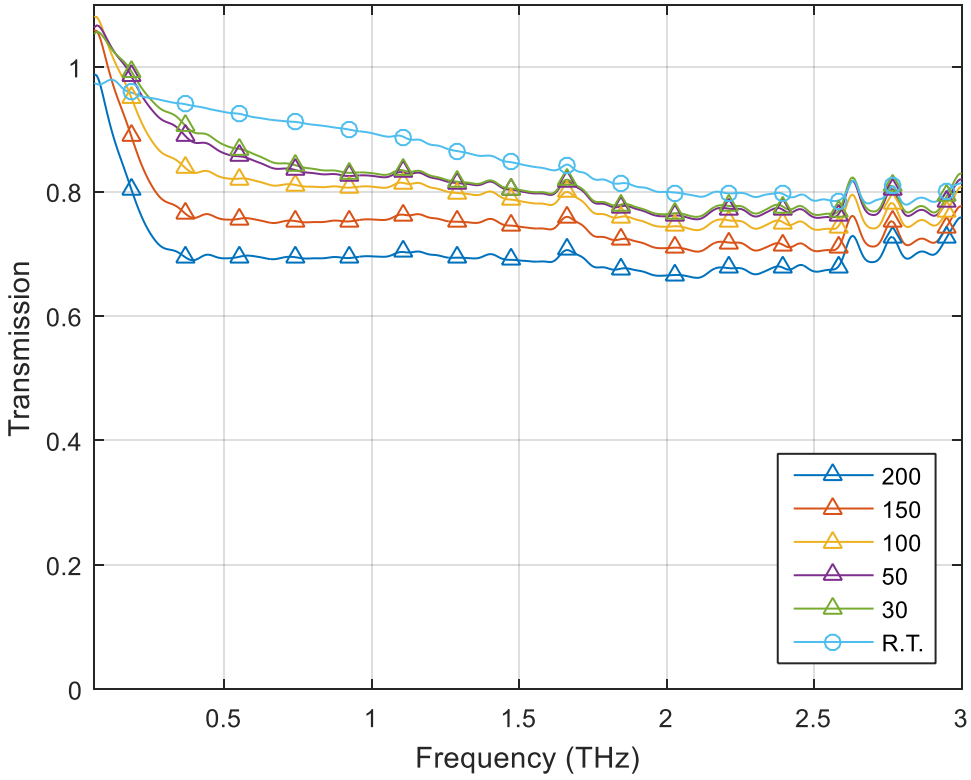

Fig. 61. Transmission measurements with in-situ heating of 300-nm germanium telluride split-ring resonators, decreasing temperature in Celsius. The last measurement labeled "R.T." was taken more than 24 hours after the in-situ tests were finished.

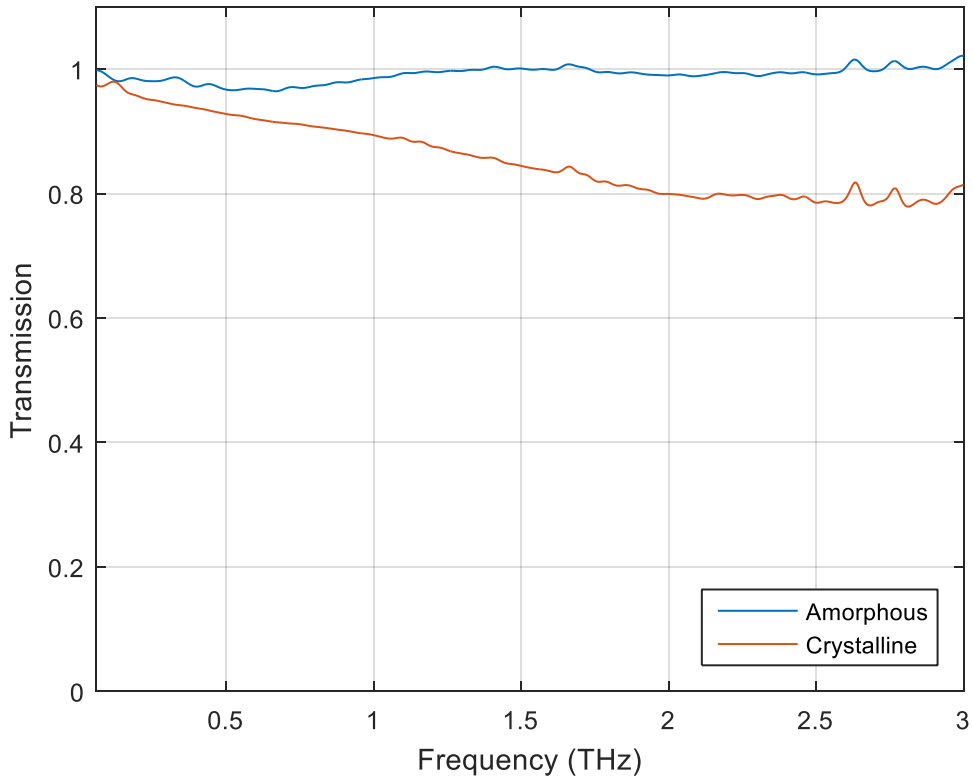

Fig. 62. Final transmission measurements of 300-nm germanium telluride split-ring resonators, amorphous and crystalline.

4.6.2. Gold SRRs with GeTe Gaps

An SEM image of gold SRRs with GeTe gaps is shown in Fig. 63. Measured data of gold SRRs with GeTe in their gaps is shown in Figures 64-66. The SRRs are on 1-mm silicon substrate. The samples were measured with in-situ heating, showing the temperature dependence of the response of the SRRs before and after crystallization of the GeTe.

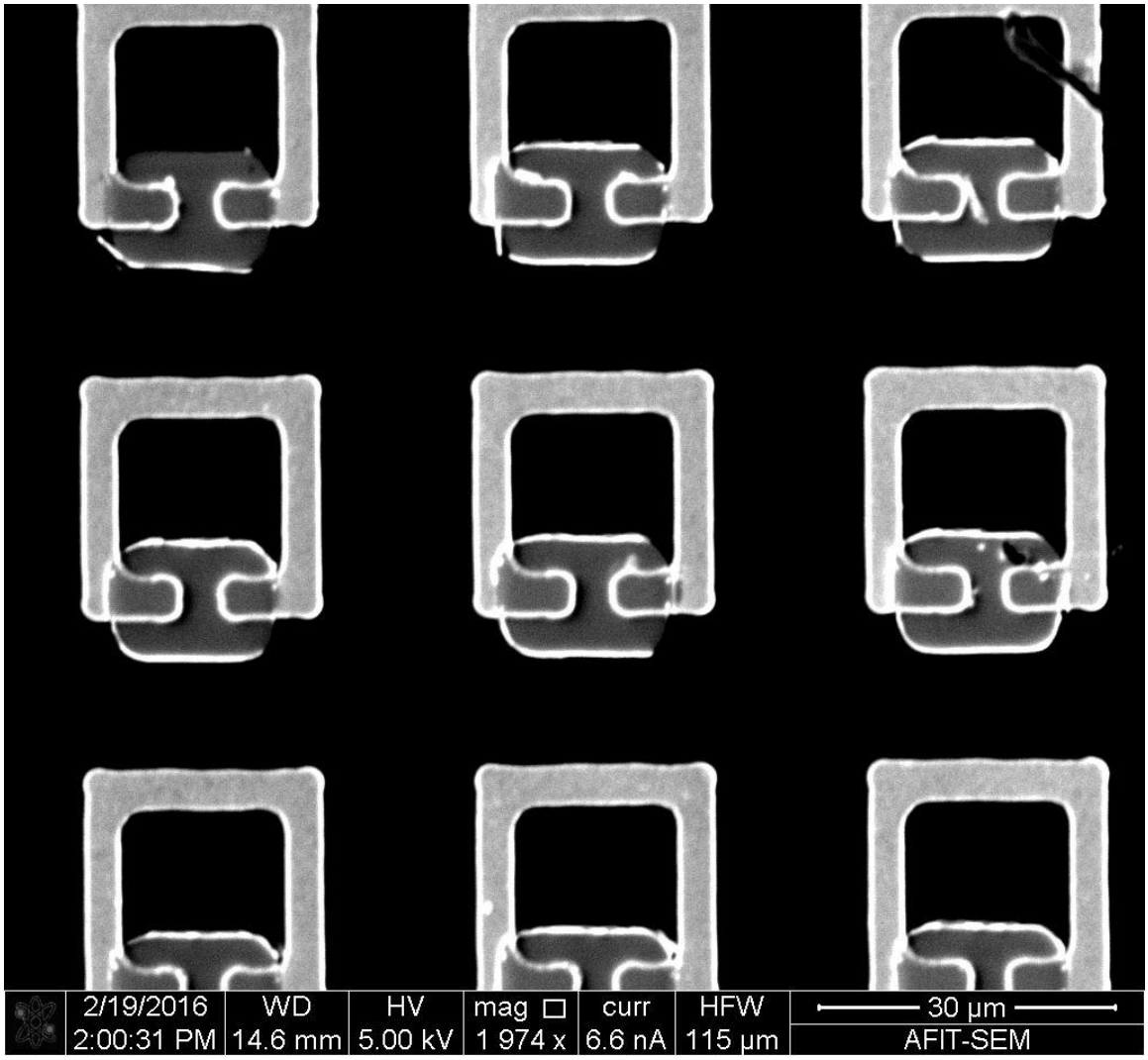

Fig. 63. Scanning electron microscope image of gold split ring resonators with germanium telluride in gap regions.

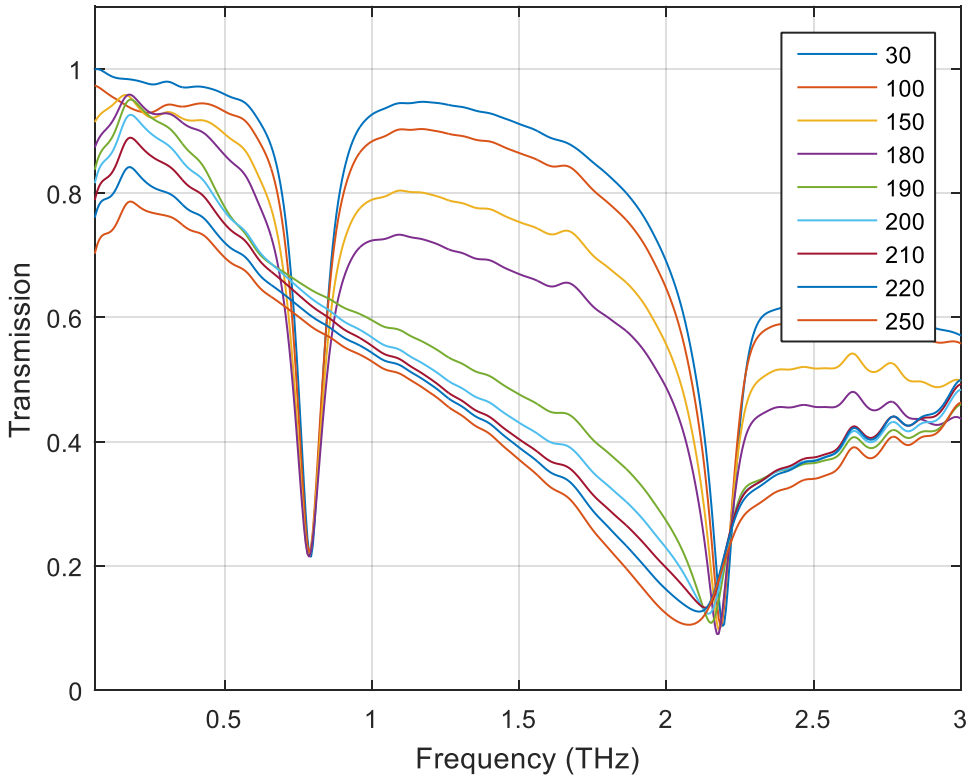

Fig. 64. Transmission measurements with in-situ heating of 300-nm gold split-ring resonators with 300-nm germanium telluride gaps, increasing temperature in Celsius.

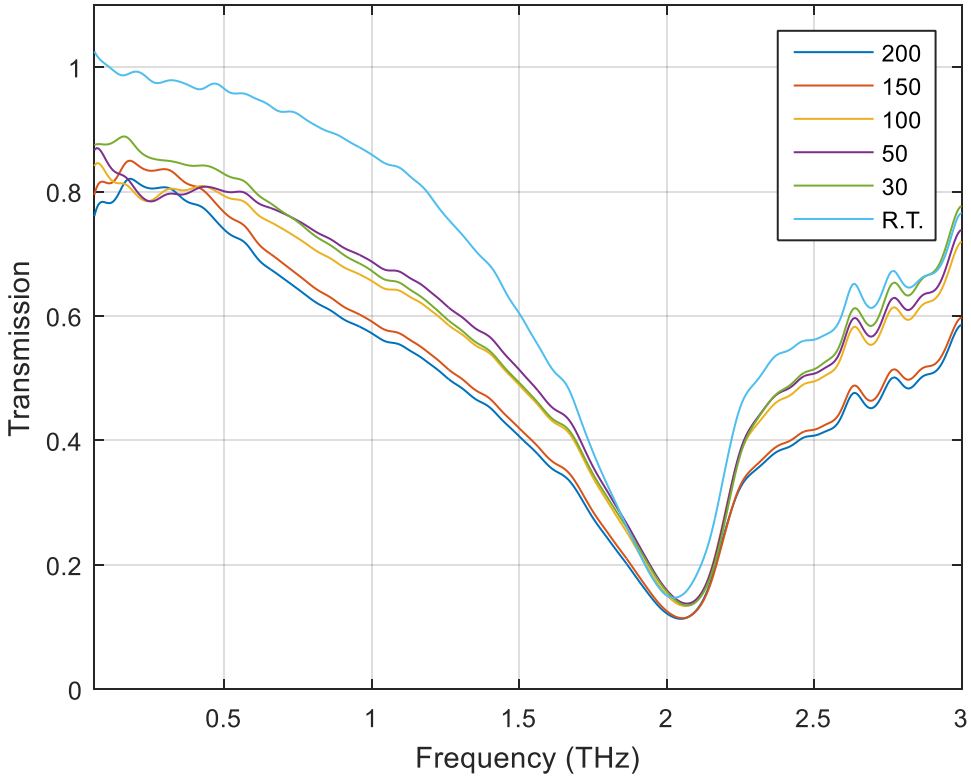

Fig. 65. Transmission measurements with in-situ heating of 300-nm gold split-ring resonators with 300-nm germanium telluride gaps, with decreasing temperature in Celsius. The last measurement labeled "R.T." was taken more than 24 hours after the in-situ tests were finished.

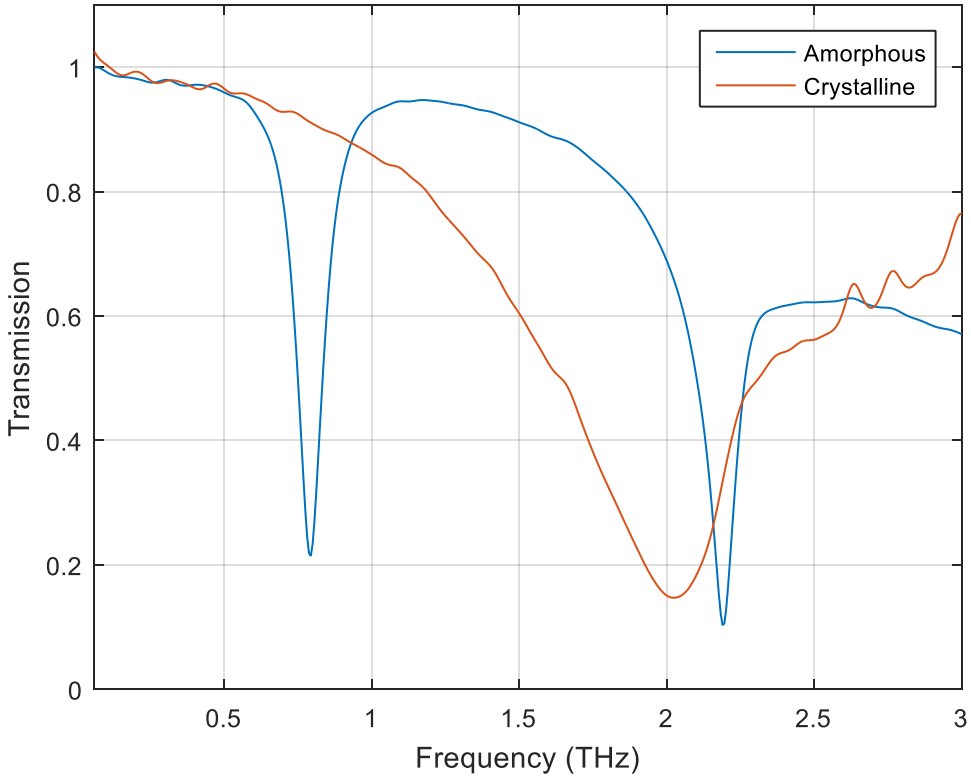

Fig. 66. Final transmission coefficients of 300-nm thick gold split-ring resonators with 300-nm thick germanium telluride gaps, amorphous and crystalline.

4.7. GeTe Indirect Heating Characterization

The following section contains data from the various components of the GeTe indirect heating study. The first section contains data from Coventorware simulations, and the second section contains measured data from the fabricated indirect heating devices.

4.7.1. GeTe Indirect Heating Simulations

A model of the GeTe indirect heating design was imported into Coventorware and simulated. A steady-state simulation with a parametric sweep over voltages was used to determine an appropriate voltage to reach the melting point of GeTe. Images from this

simulation are shown in Figures 67 and 68. A transient simulation, shown in Fig. 69, was subsequently performed to verify that the GeTe would reach its melting point in the short duration of the voltage pulse.

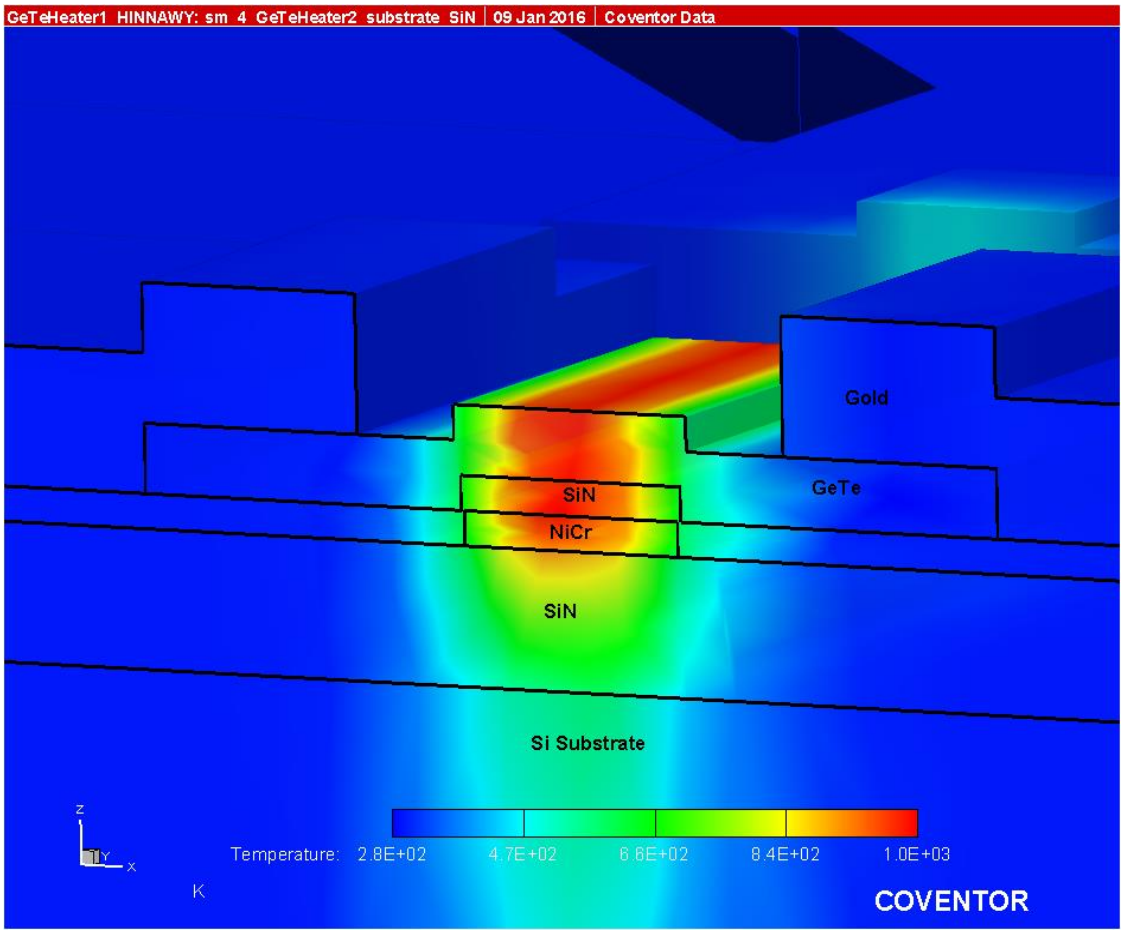

Fig. 67. Steady-state simulation of a germanium telluride (GeTe) indirect heating design at 25 V. The model is cut open to show the cross-sectional area of the Nichrome (NiCr) thin film resistor and the heat distribution along the length of the GeTe layer.

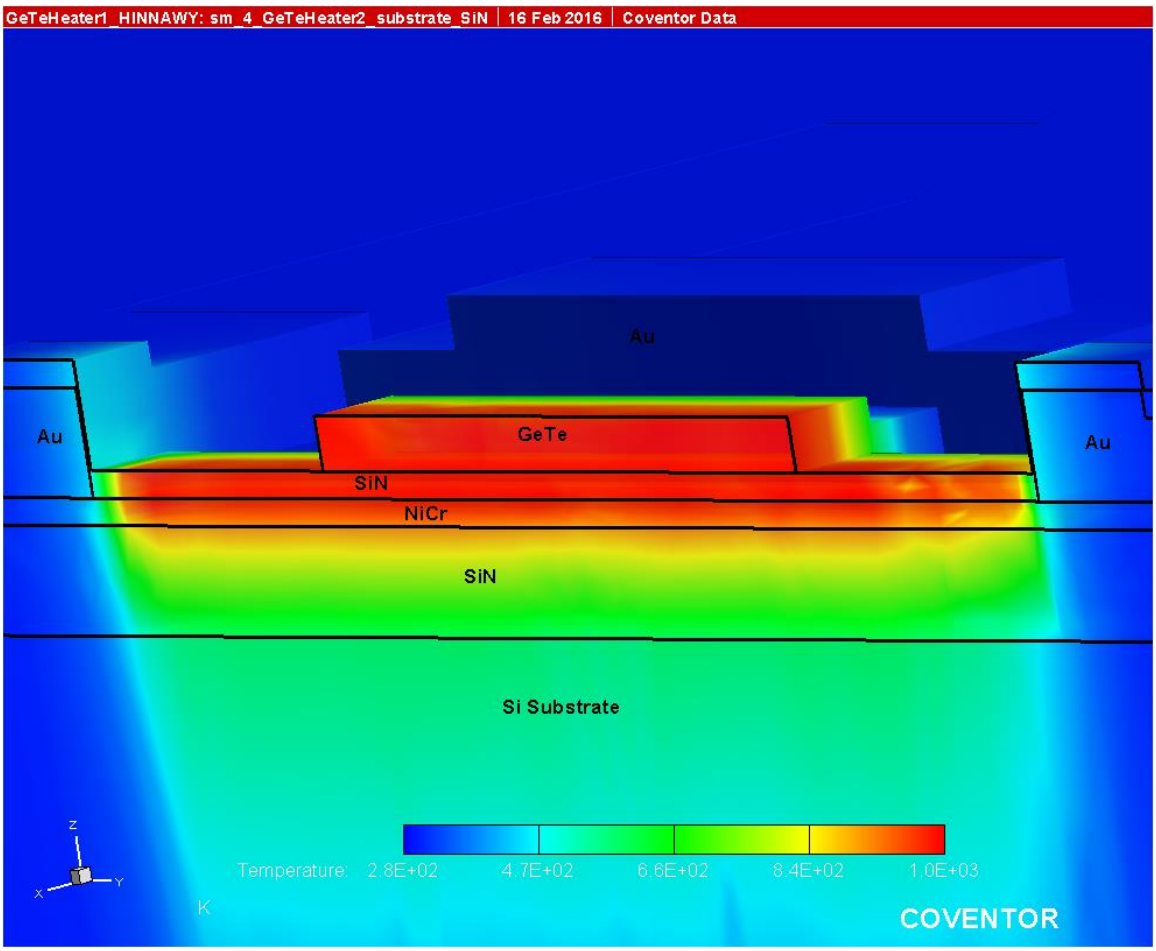

Fig. 68. Steady-state simulation of a germanium telluride (GeTe) indirect heating design at 25 V. The model is cut open to show the cross-sectional area in the center of the GeTe area and the heat distribution along the length of the thin film resistor.

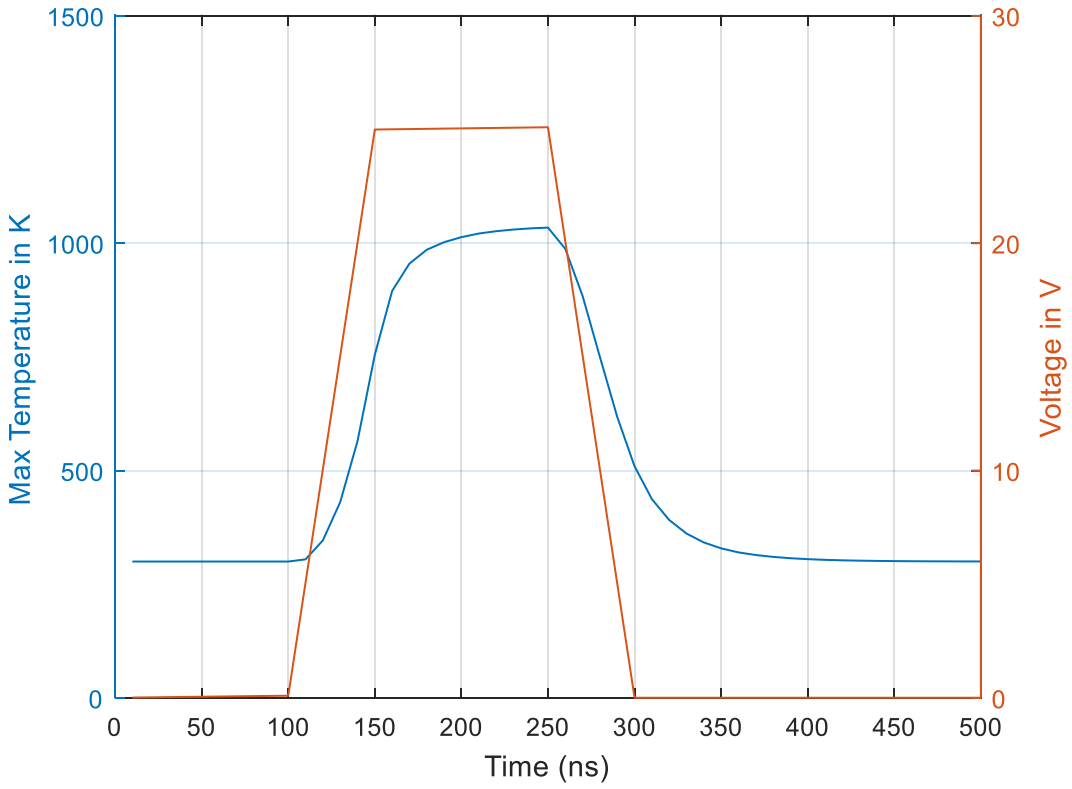

Fig. 69. Germanium telluride indirect heating simulation of a transient voltage pulse.

4.7.2. GeTe Indirect Heating Devices

Many variations on the indirect heating design described in the methodology section were fabricated. Fig. 70 shows an SEM image of a finished device. Table 10 describes the layer thicknesses and the results of the indirect heating tests for each variation. Some of the wafers exhibited a visible and resettable change in GeTe color when thermally pulsed at certain voltage values. These values are shown in Table 11, and an example of the visible transition is shown in Fig. 71. Fig. 72 shows images and varying resistance values of a device after several voltage pulses in succession.

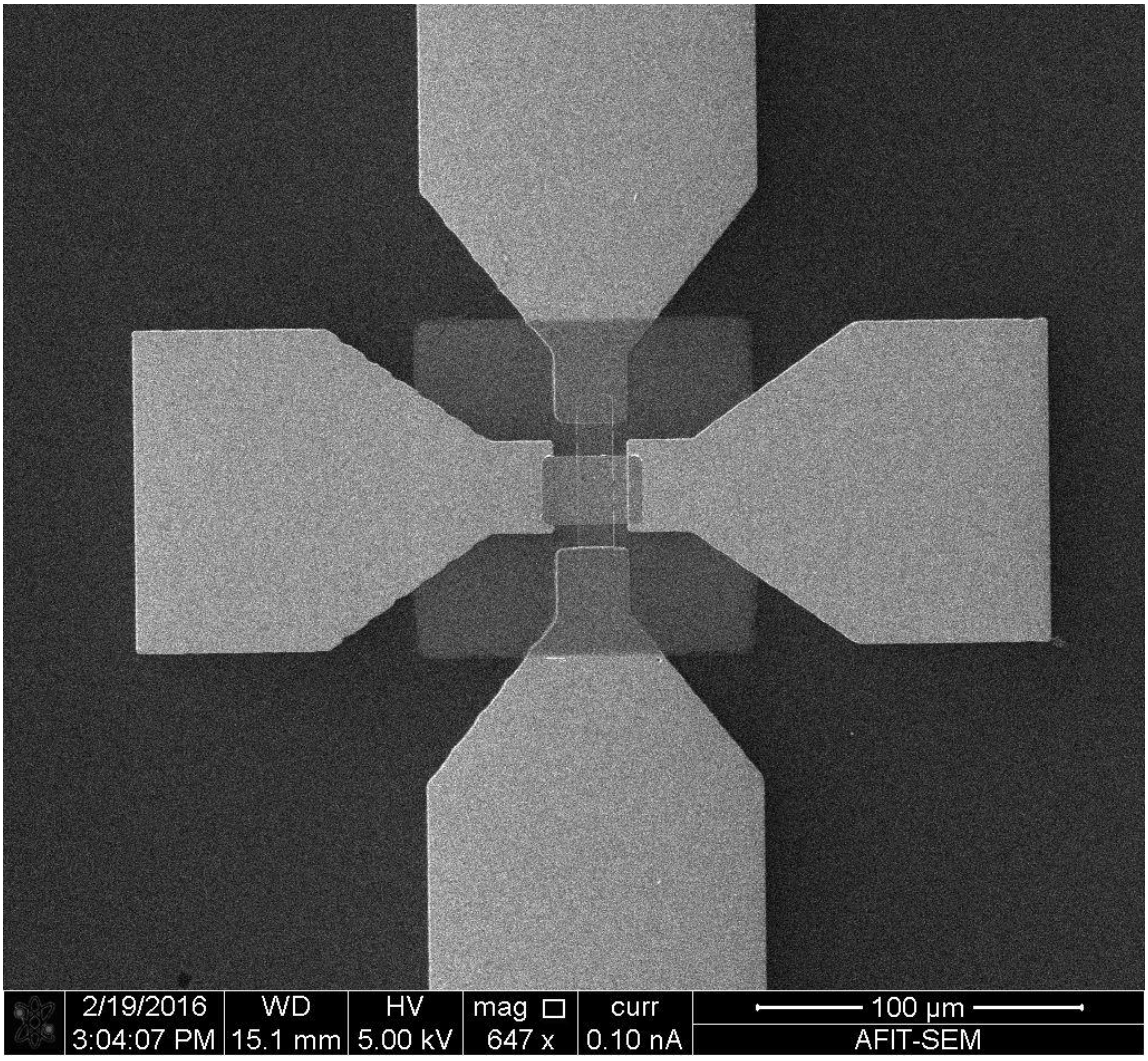

Fig. 70. A scanning electron microscope image of a finished indirect heating device

Table 10. Layer thickness and orders for various indirect heating test wafers, as well as qualitative success results. All thicknesses are in nanometers, and the layer order starts from the bottom upwards. Measured thicknesses are in bold underneath the nominal thicknesses. Wafers marked with an asterisk used Silicon Nitride (Si_3N_4) as the dielectric barrier instead of Aluminum Nitride.

		W1a		**W1b**		**W2a**		**W2b**		**W3**	
		Thick.	#	Thick.	#	Thick.	#	Thick.	#	Thick.	#
NiCr Resistor	Nom.	75	1	75	1	30	1	30	1	50	1
	Meas.	**80.5**		**80.5**		**32.2**		**32.2**		**50.4**	
Resistor Pads	Nom.	300	2	300	2	300	2	300	2	300	2
	Meas.	**284**		**284**		**312.2**		**312.2**		**311**	
AlN Barrier	Nom.	50	3	50	3	75	3	150	3	75	3
	Meas.	**45.5**		**45.5**		**N/A**		**157.3**		**79.7**	
GeTe	Nom.	150	4	150	5	150	5	250	5	150	5
	Meas.	**N/A**		**147.5**		**N/A**		**259**		**144.9**	
GeTe pads	Nom.	300	5	300	4	300	4	300	4	300	4
	Meas.	**373.9**		**373.9**		**N/A**		**333.9**		**300.8**	
Thermal Set		**N/A**		**No**		**N/A**		**Yes**		**Yes**	
Electronic Reset		**N/A**		**N/A**		**N/A**		**No**		**Yes**	
Electronic Set		**N/A**		**N/A**		**N/A**		**N/A**		**Yes**	

		W4		**W5**		**W6a***		**W6b***		**W6c***	
		Thick.	#	Thick.	#	Thick.	#	Thick.	#	Thick.	#
NiCr Resistor	Nom.	50	4	50	4	30	1	30	1	30	1
	Meas.	**48.5**		**47.6**		**33**		**33**		**33**	
Resistor Pads	Nom.	300	5	300	5	300	2	300	2	300	2
	Meas.	**314.4**		**N/A**		**345.3**		**345.3**		**345.3**	
AlN or Si_3N_4 Barrier	Nom.	75	3	75	3	30	3	30	3	30	3
	Meas.	**75.1**		**72.2**		24.93		24.93		24.93	
GeTe	Nom.	150	1	150	2	300	5	150	5	150	5
	Meas.	**129.9**		**136.6**		**332.1**		**192**		**192**	
GeTe pads	Nom.	300	2	300	1	300	4	300	4	300	4
	Meas.	**317.9**		**340.9**		**366.8**		**366.8**		**366.8**	
Thermal Set		**No**		**N/A**		**No**		**No**		**No**	
Electronic Reset		**No**		**N/A**		**N/A**		**N/A**		**N/A**	
Electronic Set		**N/A**		**N/A**		**N/A**		**N/A**		**N/A**	

Table 11. Pulse parameters of a specific geometry (10µm resistor width, 20µm x 20 µm germanium telluride dimensions), resulting in visible change in germanium telluride layer

Pulse Type	Pulse Voltage (V)	Pulse Power (W)	Pulse Length (µs)
Reset	**20-32.5**	**4.66 – 12.27**	**1**
Set	**12.5**	**1.59 – 1.87**	**> 1**
Reset	**25**	**7.6**	**2**
Set	**10**	**1.18 – 1.92**	**> 2**
Reset	**27**	**8.36**	**0.100**

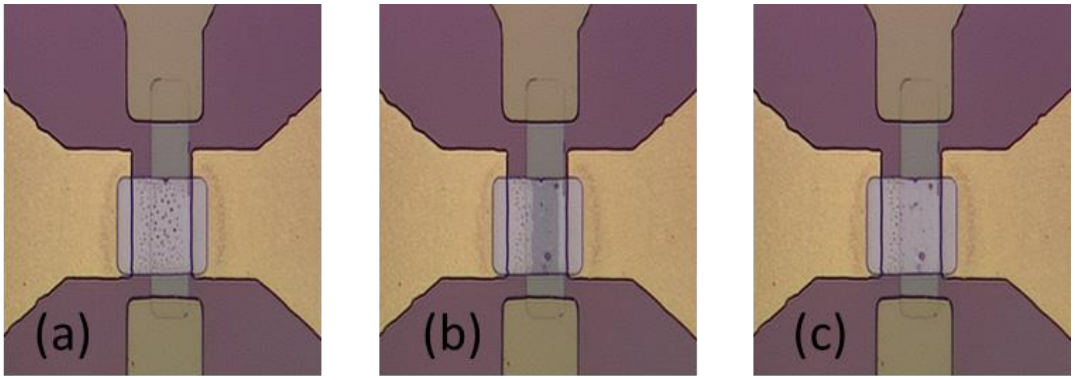

Fig. 71. Visible, reversible change in germanium telluride layer with voltage pulsing. (a) Before any tests. (b) After a 25-V, 2-ns pulse. (c) After an additional 12.5-V, 2-ns pulse.

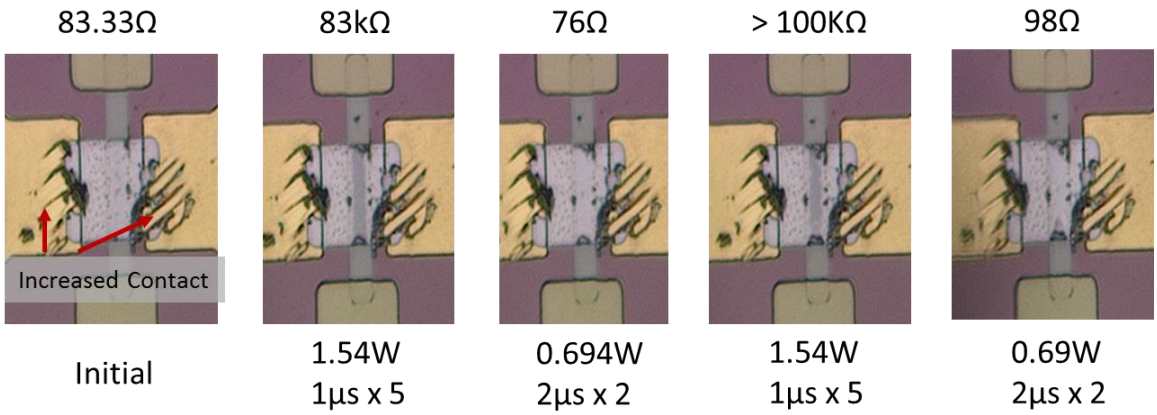

Fig. 72. Variation of germanium telluride resistance with successive voltage pulses. The resistances shown at the top of each image were formed after the pulses at the bottom of each image were transmitted. The physically enhanced contact surfaces are marked with red arrows in the initial image. In the ">100kΩ" measurement, the resistance slightly exceeded the maximum measurable resistance of the low-voltage resistance measurement setup.

4.8. GeTe Laser Pulsing

Table 12 shows average resistivities of the GeTe test pieces before and after various levels of laser exposure in the Heidelberg µPG 101 mask writer. The GeTe layers in all of the devices were 150 nm.

Table 12. Results of laser exposure on germanium telluride test pieces.

Laser Power (mW)	Pulse Percent	Average Resistivity (Ω · µm)	Standard Deviation (Ω · µm)
before crystallization	N/A	4.06 (10^6)	0.315 (10^6)
after crystallization	N/A	2.63	0.576
18	100	3.18	0.307
18	50	2.75	.398
12	100	3.00	.332
120	50	2.81	.392

4.9. Summary

This section includes the data for all the experiments performed in this work. These experiments include the material extraction study, SRR simulations, fabricated gold SRR measurements, fabricated GeTe-incorporated SRR measurements, and GeTe indirect heating results. In the next section, the collected data from all the experiments will be thoroughly analyzed.

5. Analysis

5.1. Material Extraction

This section analyzes the results from the material extraction experiment on quartz, silicon, and sapphire. The three samples were fortunately thick enough to allow the main THz pulse to be distinguished from its Fabry-Perot (FP) reflections via windowing. In thinner samples, the Fabry-Perot reflections can partially overlap with the original transmitted pulse, which in turn will cause Fabry-Perot oscillations to appear in the frequency-domain response of the sample. Fig. 73(b) is an example of what a transmission curve would look like if the signal is not properly windowed. The "period" of oscillations in the frequency domain is proportional to the index of refraction and thickness of the material.

The type of window used on the truncated window can also affect the transmission coefficient. A simple rectangular windowing function can introduce high-frequency ringing artifacts, so windows with a smoother transition to zero are typically utilized. All of the collected data (plotted in Fig. 45) has been windowed using an asymmetric Hann window centered on the peak value of the pulse, as shown in Fig. 73(a).

Fig. 44 showed the reference and three substrate pulses in the time domain. As mentioned in the theory section, the time delays of the pulses are a function of the substrate thickness as well as their refractive index n. The amplitudes of the pulses are mostly a function of the substrate thickness, refractive index n, and the attenuation coefficient k. Quartz has the largest time delay because its thickness is an order of

magnitude larger than the other two samples. Other than that, not much can be said about the substrates until the complex indices of refraction are calculated.

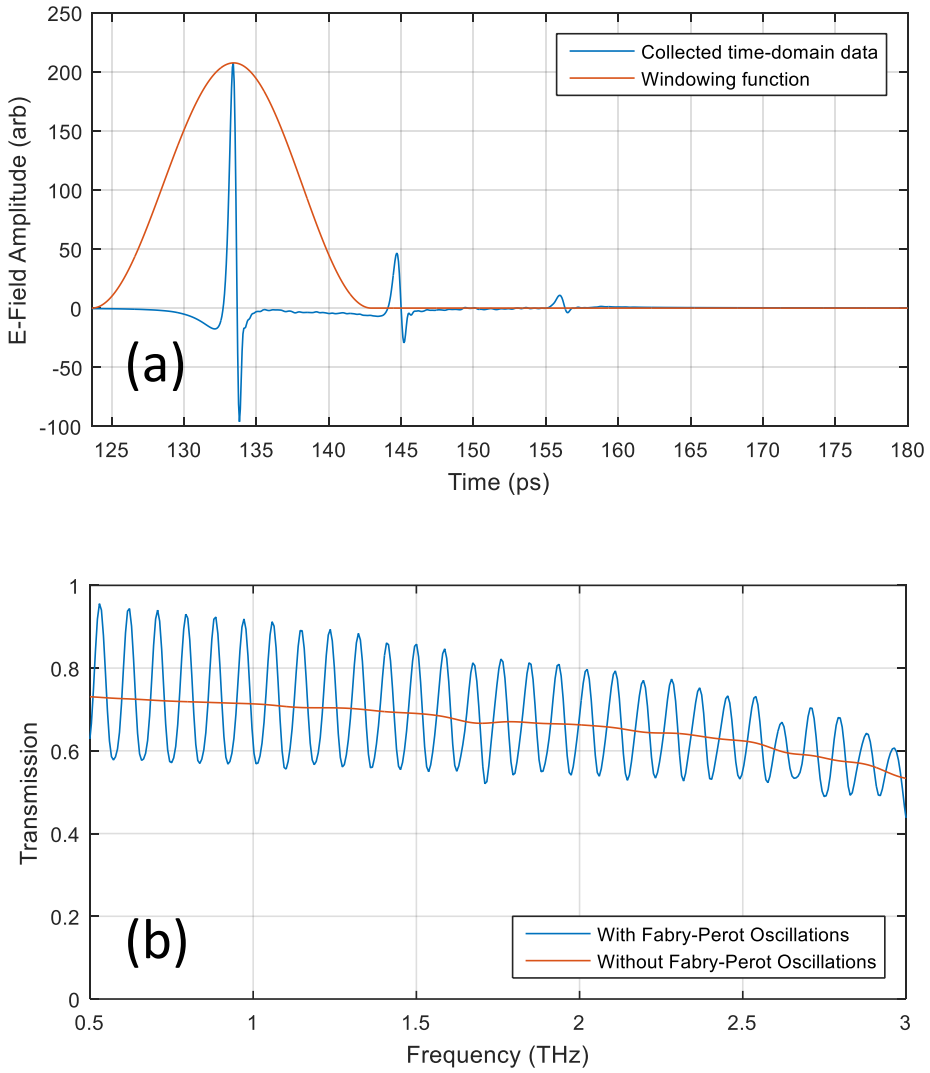

Fig. 73. Effects of windowing and truncation on a sapphire sample. a) The left is an example of time domain data of a transmitted pulse, as well as the windowing function used to truncate the pulse and eliminate further resonances. b) The right plot shows the effect of windowing on the spectrum of the signal.

A precise determination of the complex index of refraction of the measured data can be extracted by utilizing the fixed-point iteration procedure outlined in the theory section. Fixed-point iteration can extract the most useful parameters from the measured data, but also requires some amount of computation power. Complex index of refraction data was also calculated using the even more complicated Newton-Rhapson iteration algorithm in order to verify the accuracy of the fixed-point algorithm. As expected, Fig. 74 shows that the two methods converge to identical values of the complex index of refraction, with only a few slight differences due to differing convergence criterion.

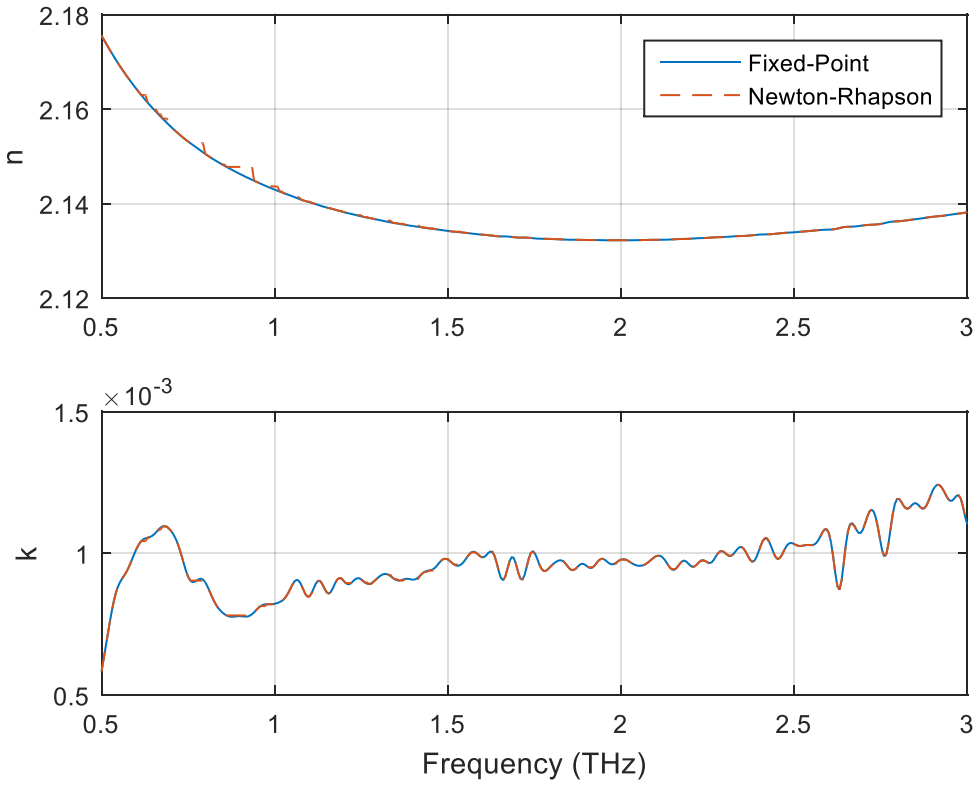

Fig. 74. Comparison of the calculated indices of quartz using fixed-point iteration and the Newton-Rhapson method.

The imaginary coefficient of the complex index of refraction, k, is related to the amount of attenuation an electromagnetic wave experiences when traveling through a given medium. The amplitude of electromagnetic waves traveling through a low-loss, non-magnetic medium exponentially decays as

$$\tilde{E} = \tilde{E}_0 \exp\left[-\frac{\omega k}{c} z\right] = \tilde{E}_o \exp\left[-\frac{\alpha}{2} z\right], \quad (89)$$

where ω is angular frequency, c is the speed of light, z is the depth into the material, and α is the power absorption coefficient.

As equation (89) shows, loss depends on both k and ω. When looking at total absorption as a function of depth, it makes the most sense to combine the ωk/c term into a single term, which in this case is α, the power absorption coefficient. The division by 2 is due to the fact that α is the power absorption coefficient, and the wave power is proportional to E^2. The absorption coefficient α can easily be determined from k, and is shown in Fig. 75.

When the parameter retrieval process was used on the silicon substrate, initial results showed that the attenuation coefficient k and the power absorption coefficient α were negative across the entire frequency band, as shown by the dashed curve in the bottom half of Fig. 76. This is a non-physical result, since that would imply that electromagnetic waves were gaining energy as they passed through the material, and there is no active component in the substrate which would cause that.

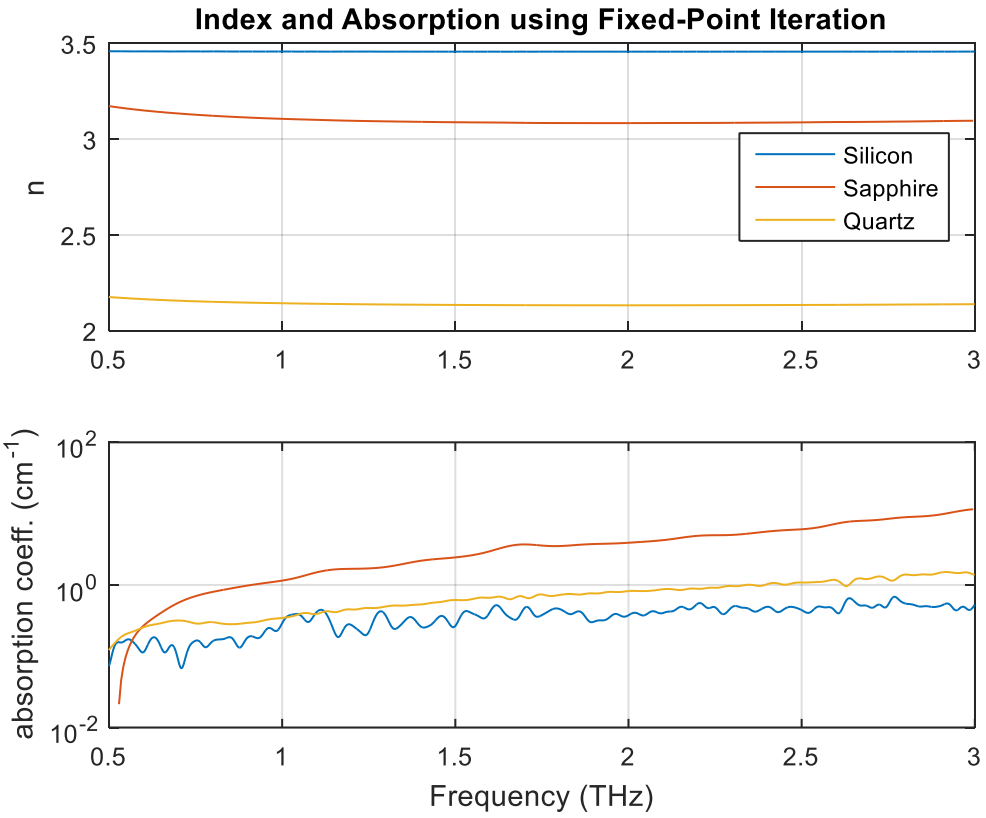

Fig. 75. Index and absorption coefficient of various substrates.

Although optical pumping has been shown to affect the THz properties of semiconductors such as silicon [36], the creation of photoexcited carriers via optical pumping would increase the absorption, not cause it to appear negative. Furthermore, the samples in this study were placed in a closed chamber with no light illumination. Past research has also shown that high incident THz field amplitudes on silicon can cause absorption saturation in the material [132]–[134]. However, the THz fields in this experiment were not strong enough to cause this sort of saturation.

There are two likely causes for the appearance of a negative absorption constant. The first possibility is that the THz machine simply does not have the precision needed to determine the loss in such a low loss material like silicon. The second reason may be due to changes to the pulse shape (and thus spectral distribution) caused by the sample itself, as mentioned in [135]. The solution to this and the first problem can be found by using the slightly modified extraction procedure from [135]. In this method, instead of using open air as a reference, the first transmitted pulse is used as a reference, and the second transmitted pulse (first Fabry-Perot resonance) is used as the sample pulse, as in Fig. 77.

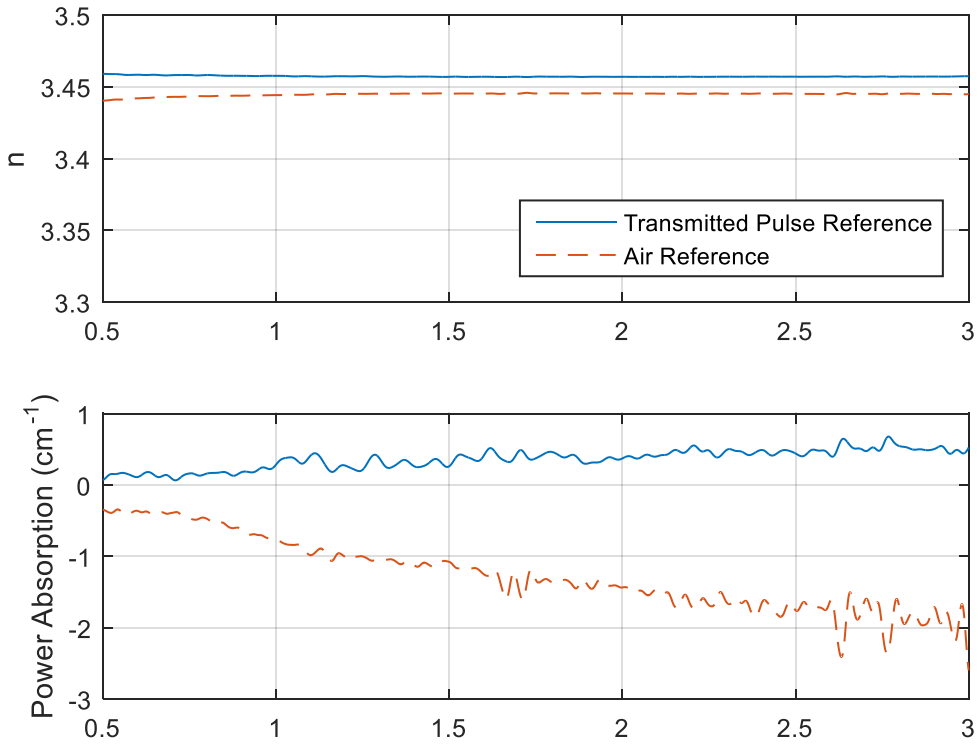

Fig. 76. Improvement in results of silicon substrate after switching the reference to the first transmitted pulse.

These two pulses are expected to have a more similar shape with each other than with the open air pulse. In addition, the wave propagates twice the thickness of the sample between the reference and sample measurements, in comparison to once the thickness in the original method. This allows more time for the wave to attenuate, which can then be more readily measured within the precision of the THz spectrometer. As shown in Fig. 76, this improved measurement gave a much more realistic value for the absorption coefficient. It was also interesting to note that either method resulted in essentially the same value for the real component of the index of refraction.

5.1.1. Overall evaluation of substrates

Fig. 46 showed the final measurement results for the complex indices of refraction of silicon, sapphire, and quartz. The main purpose of this material extraction study was to determine which material would serve as the idea substrate for planar metamaterial applications. As mentioned earlier in the theory section, the best substrate for metamaterials would have an index of refraction close to that of vacuum. Substrates

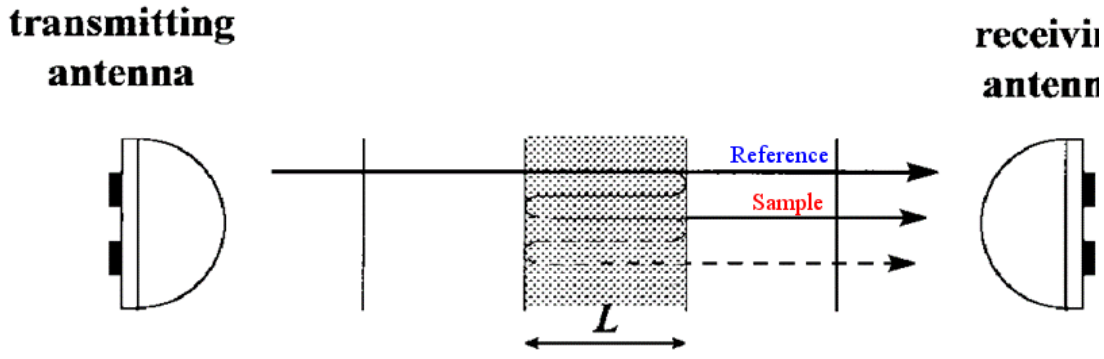

Fig. 77. Diagram showing signals used for improved measurement method for low-loss samples [37].

with a Re{ñ} close to unity would result in less red-shifting of SRR resonant frequencies, and materials with a Im{ñ} will have minimized losses through the substrate. With these two criteria, it is clear that silicon has the lowest loss, while quartz has the lowest index of refraction. Sapphire had both a high index of refraction and significantly more loss than the other two materials. Although quartz does not have the lowest attenuation, its attenuation coefficient is sufficiently low. Therefore, for minimizing both red-shifting and loss, quartz would be to best substrate to utilize for metamaterials.

This examination on the complex indices of silicon, sapphire, and quartz did not take into account the effects of birefringence. Birefringence is a phenomenon where the index of refraction of a material varies depending on the polarization of the incident light, and its origins lie in the crystal structure of the material. Sapphire is known to be strongly birefringent, and quartz is very slightly birefringent [135]. In this investigation, though, the sapphire and quartz wafers were cut perpendicular to the crystal orientations which would have caused birefringence, so birefringent effects were unable to be measured.

5.2. SRR Simulations and Characterization

The aim of this section is to compare the analytical equations for the SRR LC resonance with the simulation results obtained via CST Microwave Studio. An analytical equation can be very useful in order to predict an actual device's resonance without having to utilize a computer simulation. In addition, discerning the reasons between the agreement, or disagreement, between simulated and analytical predictions help gain a more physical understanding of the device operation.

In the following analysis, the best model for capacitance was determined to be the sum of Equations (49) and (54). This summed capacitance is

$$\mathrm{C_{tot}} = C_{Boul} + C_{surf}, \tag{90}$$

With Equations (43), (50), and (54) repeated here for convenience,

$$\begin{aligned} \mathrm{C_{Boul}} &= \frac{2\pi\ \varepsilon\ \mathrm{r_{eff}}}{\tan^{-1}\frac{g}{\mathrm{r_{eff}}}}, \\ \mathrm{r_{eff}} &= \frac{w\sqrt{\pi}}{2\ln\frac{4w}{t}}, \end{aligned} \tag{91}$$

$$\mathrm{C_{surf}} = \frac{2\ \varepsilon_0(h+w)}{\pi}\ln\frac{4}{\pi}\frac{l}{g}. \tag{92}$$

Simulated electrostatic calculations from [70] were compared with various capacitance formulas in order to determine which would be best for SRR geometries. The formulas found to align closest with numerical data were the Kuester-Boulgakov and Kuester Small Plate formulas (Equations (49) and (51), respectively), which were identical to each other within numerical precision. The former was used for the final formula because it had a simpler form. The surface capacitance was found to add a significant contribution to the overall capacitance.

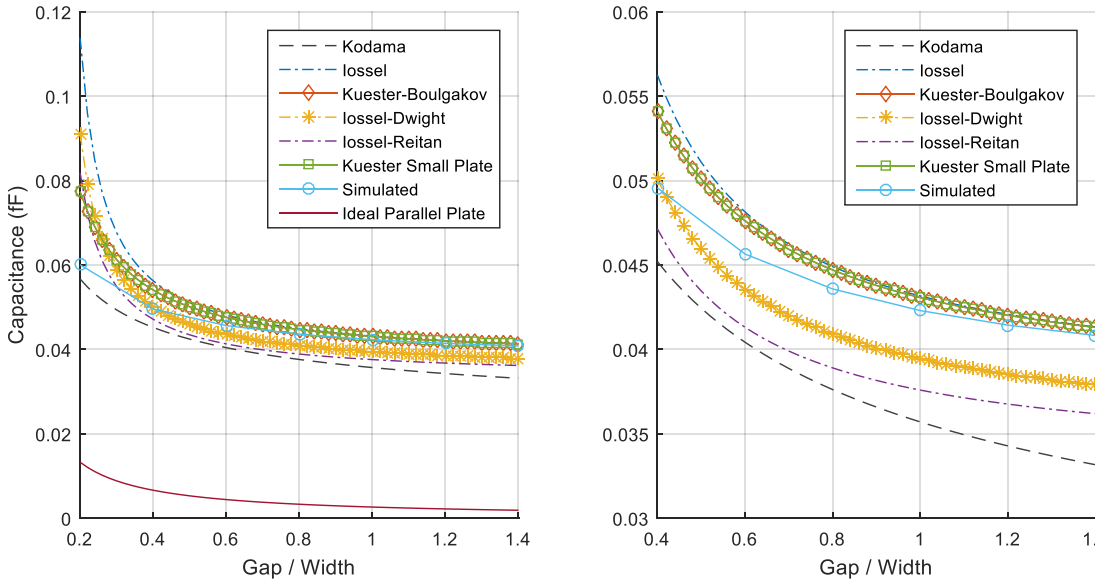

Fig. 78. Comparison of various capacitance formulas with simulated capacitances. (a) shows the inadequacy of the ideal parallel-plate formula in large-gap scenarios. (b) is a zoomed in version, showing the difference in errors between the formulas [52], [58], [59], [68], [70], [159]**.**

Once an accurate equation for capacitance was determined, multiple inductance equations were used in conjunction with the capacitance equation to predict the resonances of SRRs suspended in free space, simulated with CST. The inductance equation that produced the most accurate approximations was the thin-tape model of Equations (37) and (38). The subsequent total inductance, calculated by first substituting Equations (37) and (38) into Equations (31) and (32), then substituting Equations (31) and (32) into Equation (30), is given by

$$\mathrm{L_{tot}} = 2\frac{\mu}{\pi}\left(d\ln\left(\frac{d+\sqrt{d^2+R^2}}{R}\cdot\frac{d+\sqrt{d^2+D^2}}{D}\right) - \left(\sqrt{d^2+R^2}+\sqrt{d^2+D^2}\right)+(R+D)\right), \tag{93}$$

with

$$d = l - w, \tag{94}$$

$$R = t\,e^{3/2}, \tag{95}$$

$$D = \exp\left[\frac{1}{2t}\left(4d\tan^{-1}\frac{t}{d} + t(-3+\ln[d^2+t^2]) - \frac{d^2\ln\left[1+\frac{t^2}{d^2}\right]}{t}\right)\right]. \tag{96}$$

This inductance model predicts the inductance of an infinitesimally thin tape bent into the shape of a square loop. This model approximated the SRR inductance better than the other inductance models shown in the theory section because of the varying surface current distribution in the SRR at resonance, as shown in Fig. 79. There is almost zero current on the front and back surfaces of the SRR; the majority of the current is crowded along the inner edge of the SRR, with some additional current located on the outer edge of the SRR as well. If the outer edge current is neglected, the current can be seen as flowing only along the inner surface of the SRR, which explains why the infinitesimally thin tape model was effective in correctly predicting the resonant frequency.

The kinetic inductance, which becomes significant at high frequencies as mentioned in the theory section, was not included in these inductance calculations for two reasons. First, the simulations used perfect electrical conductors for the SRRs for simplicity, which would not have any kinetic inductance associated with them. It was

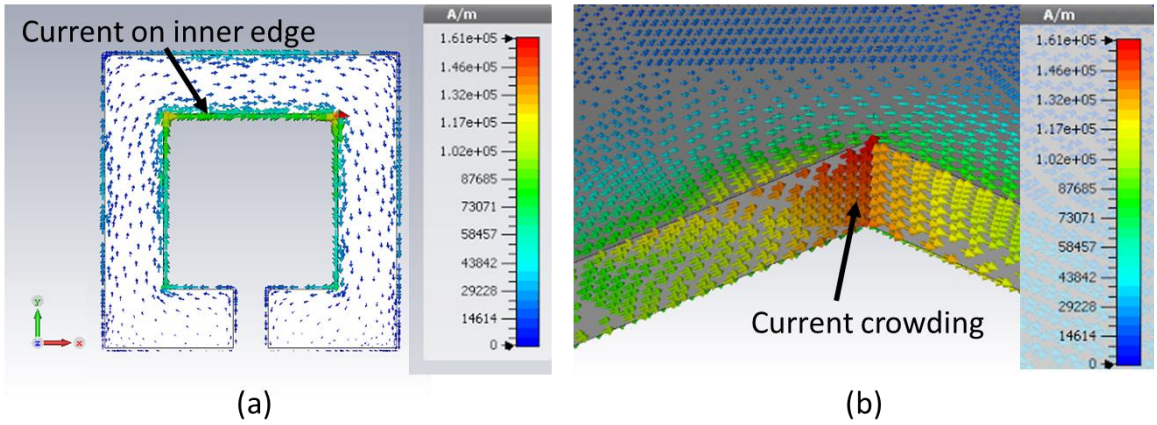

Fig. 79. Surface current distribution in a split-ring resonator (SRR) at resonance. The top level view in (a) shows how the current is concentrated on the inner edge of the SRR. An inner corner view is shown in (b), where the current crowding in the corner is very noticeable.

unfeasible to use lossy metal models in the simulation, due to the small thickness of the SRRs. In addition, calculated values of the kinetic inductance, using the plasma frequency of gold, were found to be smaller than the loop inductance by three orders of magnitude. Therefore, for the THz frequency range, the kinetic inductance of SRRs can be considered negligible.

Comparisons between some simulated and analytical LC resonance points of SRRs without a substrate are shown in Fig. 47 and Table 7. The parameter L corresponds to square side length, W to line width, and G to gap length. The thicknesses of all of the SRRs were 300 nm. The geometries of these SRRs are the same as the ones which were fabricated in later experiments.

Overall, the simulated and analytical resonance points aligned very nicely with each other. The largest deviation occurred with the largest set of SRRs. It is unclear why the largest SRRs deviated the most, as it could have been caused by a multiple number of factors, due to the many approximations used in the analytical equations. For example, the approximation of using the equivalent square perimeter in the circular surface capacitance formula may only be valid for small squares, or perhaps the current on the outer surface of the SRR becomes more significant at larger geometries, which would make the thin tape approximation less valid. Nevertheless, the analytical equations were able to predict the resonant frequencies of the SRRs within a reasonable degree of accuracy for this study.

In addition to the SRRs suspended in free space, SRRs on silicon and quartz substrate were also simulated in CST in order to verify the accuracy of the empirical, "effective homogeneous dielectric constant" method of accounting for the substrate material, which was mentioned earlier in the theory section. The measured material parameters from the material extraction section were used in these simulations.

As an initial guess, α was set exactly to 0.5 and the resulting analytical resonances were compared to the simulations. Figures 48 and 49, and Tables 8 and 9 show visual and numerical comparisons of the analytical and simulated predictions. Setting $\alpha = 0.5$ was found to be a very accurate approximation, with approximately the same amount of accuracy in the analytical formulas as compared to the SRRs without a substrate. The reason why 0.5 was such an accurate approximation is likely due to the fact that the SRRs are very thin compared to their other dimensions: 0.3-micron thickness versus a 3- to 5-

micron width. As such, the electric field lines are essentially split in half, with half in the substrate and half in air.

In addition the analytical LC formula described here, Tables 7-9 also show the calculated resonant frequencies using the ideal LC model in Equation (27) and the lowest order plasmon resonant frequency model in Equation (56) with $m = 1$. As expected, the ideal LC model only provided a good (~5%) approximation when the size of the gaps were small, due to the invalidity of the ideal capacitor model at large gap distances. The plasmon frequency model was found to predict the simulated frequencies surprisingly well, with more accuracy than the proposed analytical LC model for the SRRs with 30- and 20-micron side lengths.

All of the measured and simulated SRR results assumed an incident electromagnetic THz wave with its electric field oriented with the gap of the SRR. As described in an earlier section, a metamaterial with SRRs can result in a biaxial material if the SRRs are tetragonally periodic and are in an isotropic host medium. Since the SRRs were oriented with their gaps in line with the incident electric field, the resulting response is due to the ε_{11} and μ_{11} elements of the permittivity and permeability tensors, with the coordinate system oriented as shown in Fig. 18.

5.2.1. Summary

An analytical equation for the resonant frequency of SRRs was developed, proposed, and compared to simulations. In addition to validating the equation, the simulations helped gain some insight as to why certain terms were utilized, such as the thin tape inductance loop model. The simulations were also beneficial for comparison with measured results of SRRs.

5.3. Metal SRR on Quartz

The preliminary set of quartz SRRs was fabricated in order to verify that the resonance points match between simulation and actual measurements. As seen on the plots in Figures 51-53, the measured resonant frequencies line up quite nicely with the simulated results. The small amount of deviation seen between the data could be caused by the tolerance limits of the photolithography process. The deviation is the largest for the smallest SRRs, which would have experienced the most deformation since their dimensions were at the very limit of the fabrication tolerances.

Another major difference between the simulated and measured results was the depth of the resonant notch. The measured resonant notches were all not much better than 0.8 transmission at their lowest point, but the devices were expected to have a transmission very close to zero at their notch points. One factor that led to this discrepancy was signal processing of the pulses. In order to remove Fabry-Perot oscillations, the time-domain sample and reference signals had to be windowed almost immediately after the propagation of the main pulse. Although this successfully eliminated the Fabry-Perot oscillations, it also truncated part of the oscillations related to the resonance, which in turn made the notch appear shallower than it should have been. Fig. 80(a) shows the truncation of the SRR resonance. The short, sinusoidal oscillations appearing immediately after the initial pulse are caused by the resonance of the SRR. As seen in Fig. 80, after applying the windowing function, the transmission significantly worsens.

In order to properly ascertain the correct resonant depth of the device, the time delay between the first transmitted pulse and the first Fabry-Perot reflection needs to be

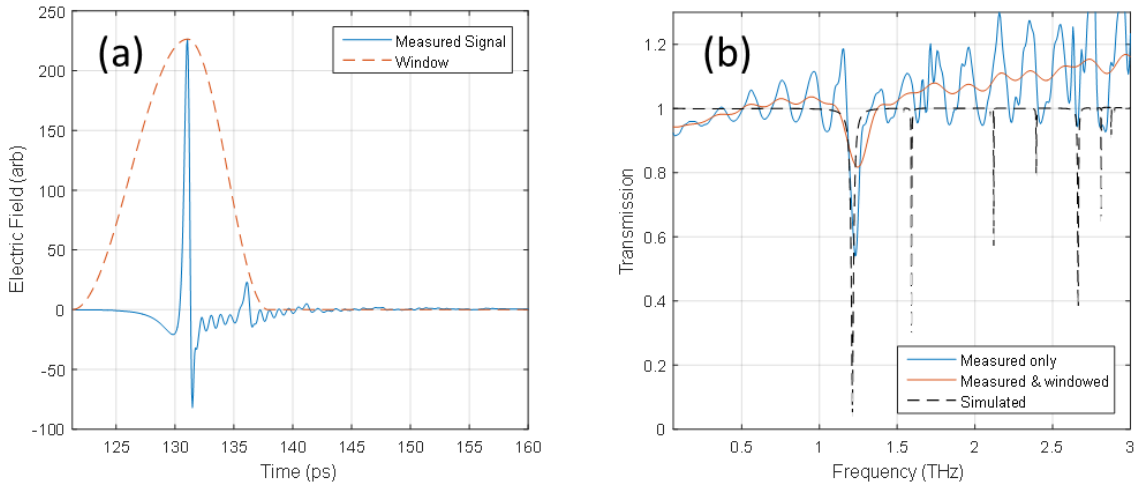

Fig. 80. Comparison between raw measured, measured / windowed, and simulated data. (a) Original pulse and the windowing function used in processing. (b) Effects of windowing on the transmission depth.

increased, so that the windowing function can eliminate the Fabry-Perot resonance without affecting the SRR resonance. This can be accomplished by using a substrate with a larger thickness and/or a higher index of refraction.

The measured, non-windowed transmission curve in Fig. 80(b) has a significantly deeper notch, but its depth is still not in line with the simulated data, which has transmission as low as 0.05 at its lowest point. The reason for this is likely due to ohmic losses in the metal, which would smother resonances with a small bandwidth. For example, in Fig. 80(b), the narrowest part of the main resonance was eliminated, and the narrow, higher order resonances in did not appear at all in the measured transmission curves.

5.3.1. Summary

SRRs on quartz substrate were fabricated and tested. The data from the quartz SRR measurements showed that the resonant frequencies of THz SRRs can be accurately predicted with simulations. However, there were some discrepancies with the depth of the resonant notches. In order to address this discrepancy, another set of SRRs on a different substrate was fabricated and tested.

5.4. Metal SRR on Silicon

As a follow-up to the quartz SRR study, several SRRs were fabricated on thick, intrinsic silicon. The thicker, higher-index silicon allowed for improved signal windowing, as mentioned in the earlier section. Since the previous results from quartz SRRs have already established the agreement between simulated and measured resonance frequencies for a wide range of SRR sizes, the SRRs in this study all had the same geometry: 20-micron side lengths, 5-micron line widths, and 3-micron gap widths. Instead of ring geometry, these SRRs had varied periodic spacing. Simulated results for this study are shown in Fig. 50 and measured results in Fig. 54. A side-by-side comparison of a few results are shown in Fig. 81 as well, for clarity.

The varying periodicity of the SRRs had a few effects on the LC resonance of the SRR array: a deeper notch, a slight shift of the resonant frequency, and a broader bandwidth [45]. Both of these effects can clearly be seen in Fig. 50 and Fig. 81(a).

The deeper notch can be understood in two ways. A decreased periodicity, meaning a higher packing density, would result in a stronger response simply because there are more SRR units available for the incident THz wave to interact with. In addition, as the proximity between individual SRR elements is decreased, the elements

will begin to couple with each other, causing an even stronger resonance that has a slightly shifted frequency and a wider bandwidth [30], [41], [45].

These strengthened notches still did not fall all the way to zero, however, due to ohmic losses in the metal. To verify this claim, simulations with incorporated gold losses were created using THz conductivity data of gold from [136]. The dataset from [136] did not contain conductivity data for films as thick as 300 nm, so the conductivity used in this simulation was linearly extrapolated from the results of the thinner films for a rough approximation. These simulations are shown in Fig. 82. When loss is included in simulations, the lowest points of the SRR LC resonance notches near 0.8 THz agree more closely between simulation and measurement. Previous studies have shown that ohmic losses in SRRs can be reduced by using rounded shapes instead of having sharp corners, and by using thicker layers of metal [137].

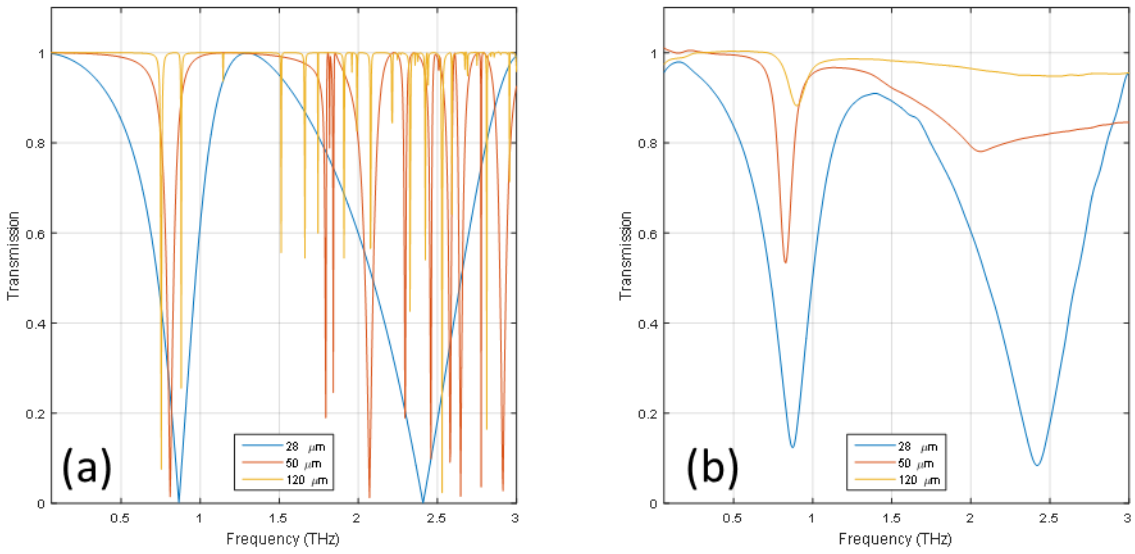

Fig. 81. Side-by-side comparison of (a) simulated and (b) measured results of SRRs on intrinsic silicon with varied periodicity.

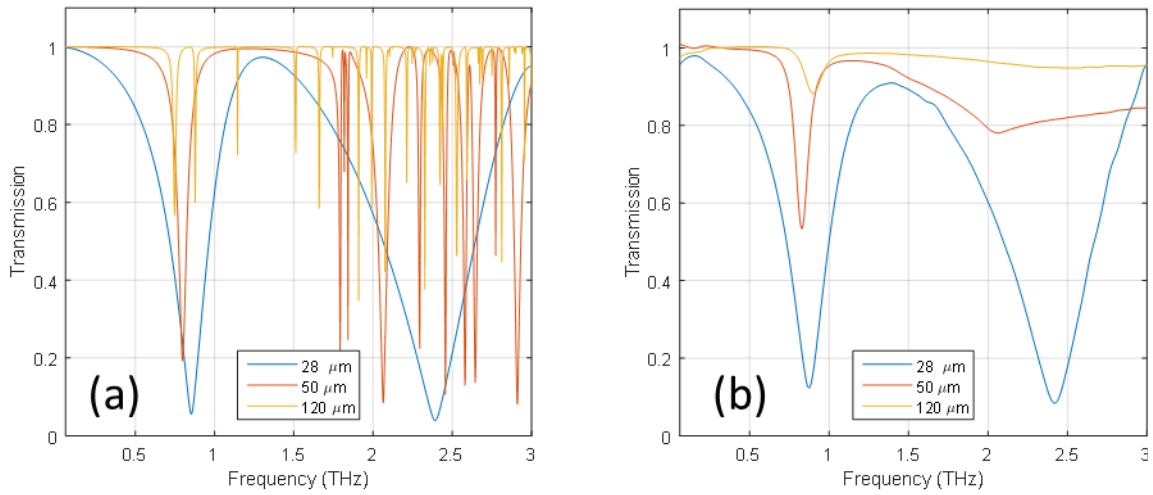

Fig. 82. Side-by-side comparison of (a) simulated with gold losses and (b) measured results of SRRs on intrinsic silicon with varied periodicity.

One other discrepancy between simulated and measured results is that the multiple higher-order resonances of the simulated Fig. 82(a) seemingly become smoothed and averaged out in the measurements of Fig. 82(b). This smoothing effect was initially thought to be the effect of losses in the gold substrate, but was found not to be the case, or else the higher-frequency responses in the left- and right-hand sides of Fig. 82 would have been similar. This smoothing effect, then, is caused by some other unknown factor, perhaps related to the THz measurement setup or quantum effects not modeled by the simulation software.

These lossy simulations also gave some good insight into the internal current distribution and higher-order resonances of the SRRs. Fig. 83 shows the internal and surface current distribution in the upper left inside corner of the SRR at resonance. Unlike the lossless model shown earlier in Fig. 79, this model includes the current distribution within the SRR. Even with a loss-incorporated model, though, it can be seen

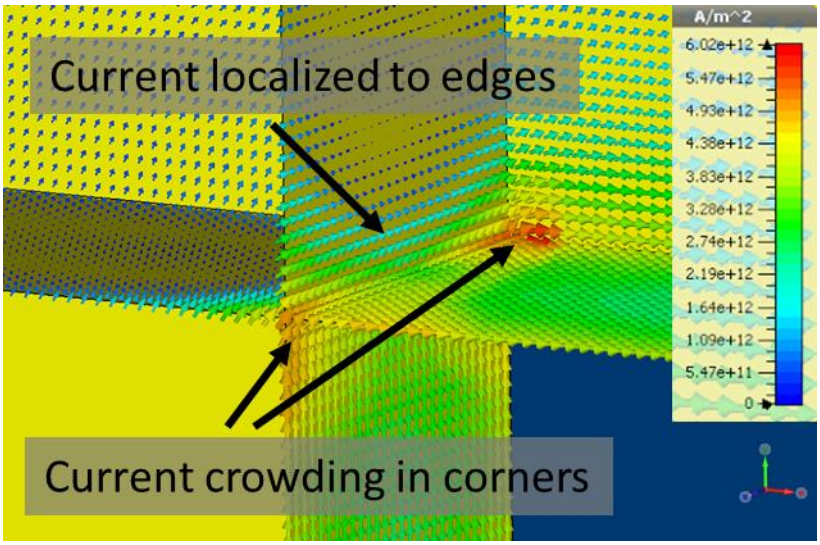

Fig. 83. Simulation of internal and surface current distribution in one of the inner corners of a gold SRR at resonance.

that the majority of the current is confined to the inner faces of the SRR, with some additional current crowding along the edges and corners of the metal. This explains why the earlier, lossless models were found to be accurate. In terms of determining the resonant frequency, gold can be viewed as a perfect electrical conductor in the THz range.

Comparison of the peak current distribution at LC resonance and the next highest resonance is shown in Fig. 84. At the LC resonance, all of the current faces the same direction along the shape of the SRR at any given instant. Since quasi-statics is assumed to be valid at the LC resonance, this is an expected outcome. In addition, the increase in current density at the top of the SRR explains why this resonance can also be viewed as the lowest-order plasmon resonance, with a half wavelength of the plasmon resonance fitting along the the perimeter of the SRR. At the higher-order resonance, the current direction changes twice along the perimeter of the SRR. These pivot points are the nodes

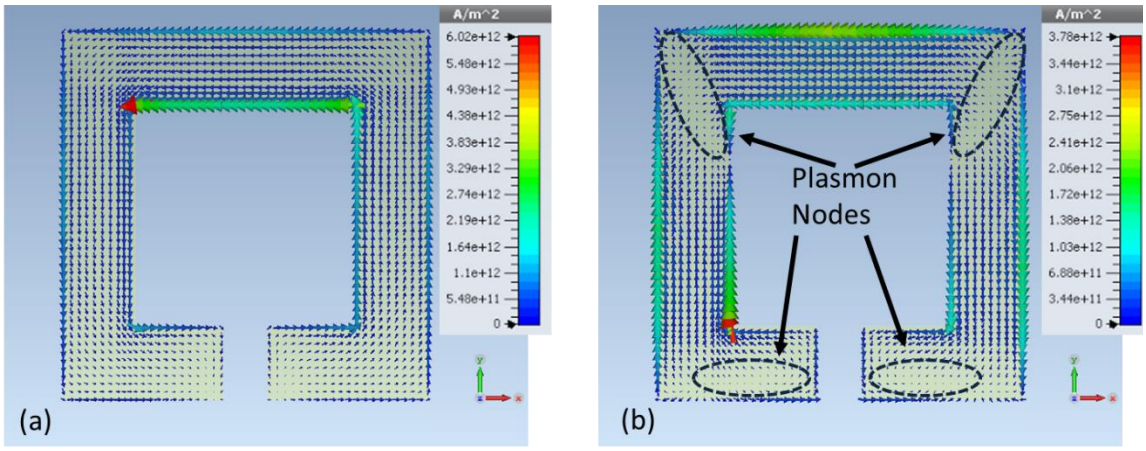

Fig. 84. Current distribution of gold split-ring resonators at (a) LC resonance and (b) next lowest plasmonic resonance, with nodes circled.

of a higher order plasmon mode, with the mode wavelength (54.04 μm) approximately equal to the two thirds of the perimeter of the SRR (51.33 μm).

5.4.1. Summary

This study of SRRs on a thick silicon backing has addressed many of the issues seen in the earlier study with quartz SRRs. By decreasing the periodicity of the SRRs, the overall resonant response of the structure can be greatly increased. In terms of experimental investigations, a thick substrate with a high index of refraction helps separate Fabry-Perot reflections from the main pulse, and aids in cleaner time windowing. The broad smoothing of many higher-order resonances was an interesting feature of the measured results not seen in simulations, even when the simulations incorporated ohmic losses. The cause of this discrepancy, although unclear, is thought to possibly be related to the THz-TDS measurement setup. The lossy simulation was also examined in detail to view the internal current distribution in the SRRs, showing localized current on the inner edges of the ring (very similar to the lossless models

calculated earlier), and the resonant current distribution was viewed to see the shape of the LC resonance and the next lowest plasmonic resonance.

5.5. Printed SRRs

The printed quartz and silicon SRR transmission responses compared with simulations are shown in Figures 57 and 58. The quartz SRR response has a distinct resonance, but the resonant dip is not very low, and there are many oscillations in the response. In order to deepen the notch, the next batch of SRRs was designed with a tighter packing density, and was fabricated on a thick silicon substrate to allow easy windowing of the time domain signal. In order to match the simulations as closely to the fabricated geometries, the SRRs were imaged in a scanning electron microscope (SEM) and the printed SRR lengths, line widths, gaps, and periodicities were measured from the resulting image and used in simulations. Even with this step, the measured quartz resonance SRR was slightly shifted from the simulated quartz resonance. As seen in both the optical and SEM images, the printed SRRs were not perfect, with curved corners, especially around the capacitive gaps. Rounded gap sides would reduce the effective plate size of the SRR capacitance, which would slightly lower the capacitance of the structure and thus slightly increase the resonant frequency of the device.

While the quartz simulation and measurement results agreed moderately well, the measured silicon response was completely flat and did not match simulated results at all. The reason for the difference is not related to the substrate, but rather the print parameters. The printing machine can only print a certain amount before the equipment must be stopped and cleaned. This is a common shortfall of the inkjet printing process [125]. Due to the much tighter packing density requirement put forth for the silicon

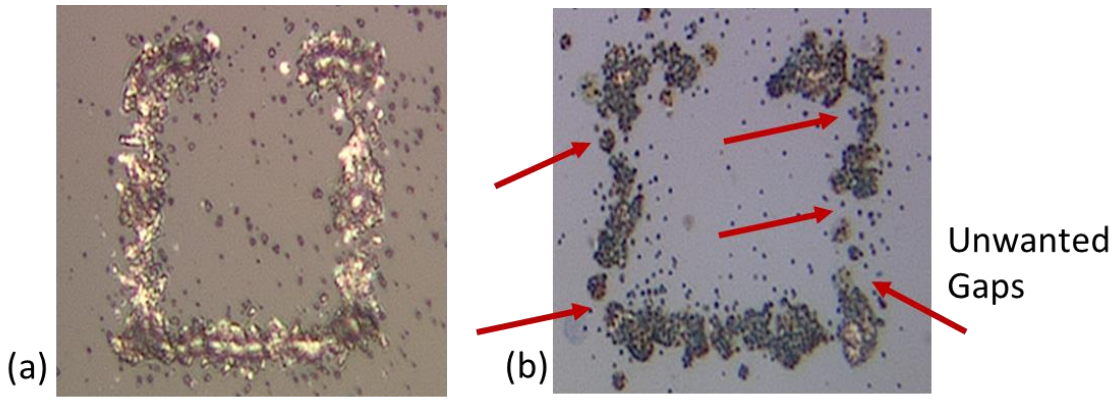

Fig. 85. Comparison of the (a) quartz split-ring resonator and the (b) silicon split-ring resonator, highlighting the various gaps in the silicon ring.

SRRs, the print had to be stopped before more than one layer of material could be deposited for each SRR element. This led to discontinuous gaps in the silicon SRR, as shown in Fig. 85(b). With too many large gaps in the ring, the SRR is no longer able to resonate at the desired frequency.

5.6. GeTe-Incorporated SRRs

5.6.1. GeTe SRRs

The transmission data from the GeTe SRRs before, during, and after thermal heating are shown in Figures 60 through 66. With sufficient heating, the GeTe SRRs crystallized and turned metallic, somewhere between 180 and 190 ºC. This phase change persisted after subsequent cooling of the sample. Further heating past the crystallization temperature resulted in a decrease in transmission, seemingly indicating that the sample was becoming more conductive at higher temperatures. However, past studies have shown that GeTe becomes *less* conductive at higher temperatures [138]. Therefore, the

slow rise in conductivity seen in Fig. 66 is instead possibly caused by the increase of free carriers with increased temperature in the semiconducting silicon substrate [139].

In Fig. 61, there is also a marked difference between the last in-situ measurement taken at 30 ºC and the subsequent room temperature (R.T.) measurement, which are expected to be nearly identical. The R.T. measurement was taken greater than 24 hours after the last in-situ measurement. This mismatch was likely caused by gradual changes in the strength of the transmitted terahertz pulse over time. Due to the length of time required to adequately heat and cool the chamber, the last few in-situ measurements are typically taken more than 6 hours after the initial reference measurement. In an ideal THz measurement scenario, the sample measurement is taken immediately after the reference measurement in order to minimize the effects of these gradual changes. However, since the measured devices are placed in a heated, evacuated chamber, the reference cannot be re-measured in between every in-situ temperature measurement. To get a more accurate measurement of the final change in the sample after heating, the sample needs to be re-measured with a fresh reference; this was accomplished with the R.T. measurement.

After heating past the crystallization temperature, resonances similar to that of the gold SRRs were expected to appear in the THz transmission response. Although the overall transmission through the SRRs did decrease, the decrease was very slight; they did not have sharp resonances like those of the gold SRRs. This was subsequently corroborated with simulations of the structures. Comparisons between simulated and measured data are shown in Fig. 86. For the simulations, THz conductivity and permittivity data of GeTe in the amorphous and insulating states were taken from measured data in [104] and [140]. The absence of resonances is likely due to ohmic

losses in the GeTe. Although GeTe becomes conductive when crystallized, it is not as ideal as other metals, like gold, for conducting at THz speeds. These ohmic losses in crystalline GeTe are enough to over-damp the oscillations which would normally occur in the SRR at resonance. In terms of a lumped-element RLC model, the SRR's resistance (created by the ohmic losses in the GeTe) dominates over its relatively smaller loop inductance and capacitance, which leads to typical resistive behavior in the transmission response, i.e. broadband attenuation.

5.6.2. SRRs with GeTe gaps

The transmission data from the GeTe-gapped SRRs before, during, and after thermal heating are shown in Figures 60 through 66. Somewhere between 180 and 190 ºC, the thermally induced crystallization of the GeTe resulted in a change in the transmission behavior, which persisted after subsequent cooling of the sample. As with

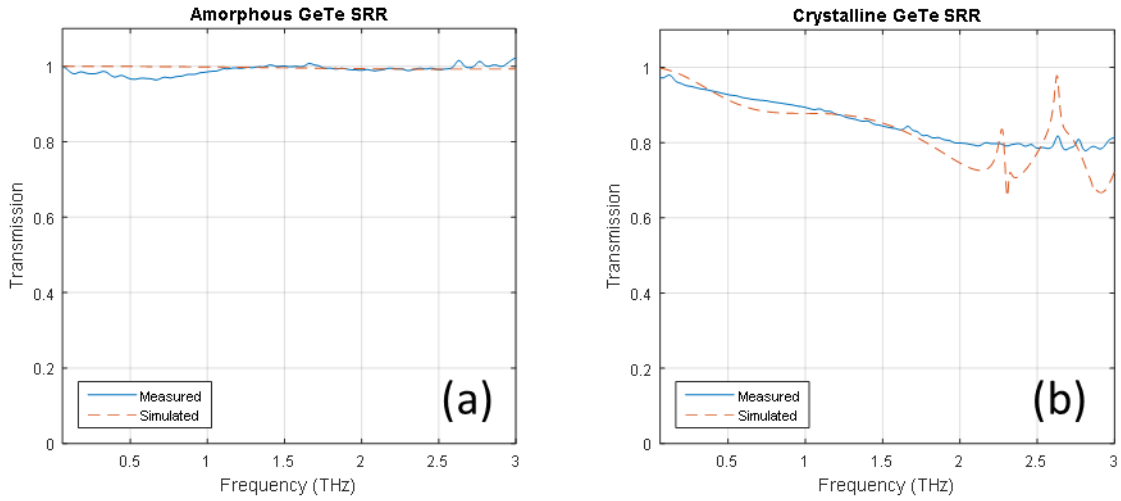

Fig. 86. Measurement and simulation of germanium telluride split-ring resonators in the amorphous phase (a) and the crystalline phase (b).

the earlier in-situ study, an additional R.T. measurement was taken with a new reference to get a more accurate measurement of the post-crystallized response.

Unlike with the full GeTe SRRs, the pre- and post-crystallization transmission responses of the GeTe-gapped SRRs were drastically different from each other. Prior to crystallization, the GeTe-gapped SRRs acted as a normal split-ring resonator. The GeTe-gapped LC resonance frequency, 0.783 THz, was slightly lower than the LC resonance of a standard gold SRR, at 0.818 THz. The slight red-shift in the resonance frequency was caused by the higher dielectric constant of the GeTe in the SRR gap. This led to a slightly higher gap capacitance, which led to a slightly lower resonant frequency. After crystallization, the GeTe shorted the SRR gap and significantly altered the response of the SRR, changing it to that of a simple ring resonator. Using the same GeTe model from the simulations of the full GeTe SRR, these GeTe-gapped SRRs were also simulated, with good agreement between simulation and measurement, as shown in Fig. 87.

Looking again at an RLC model, it is clear why the GeTe-gapped SRRs showed a much more pronounced difference in the pre- and post- crystallized response compared with the full GeTe SRRs. Compared with the full GeTe SRR, the smaller square piece of GeTe has a much smaller resistance since it has nearly the same cross section but a fraction of the length. With a smaller resistance, the GeTe layer's intended purpose of shorting the SRR gap is much more pronounced.

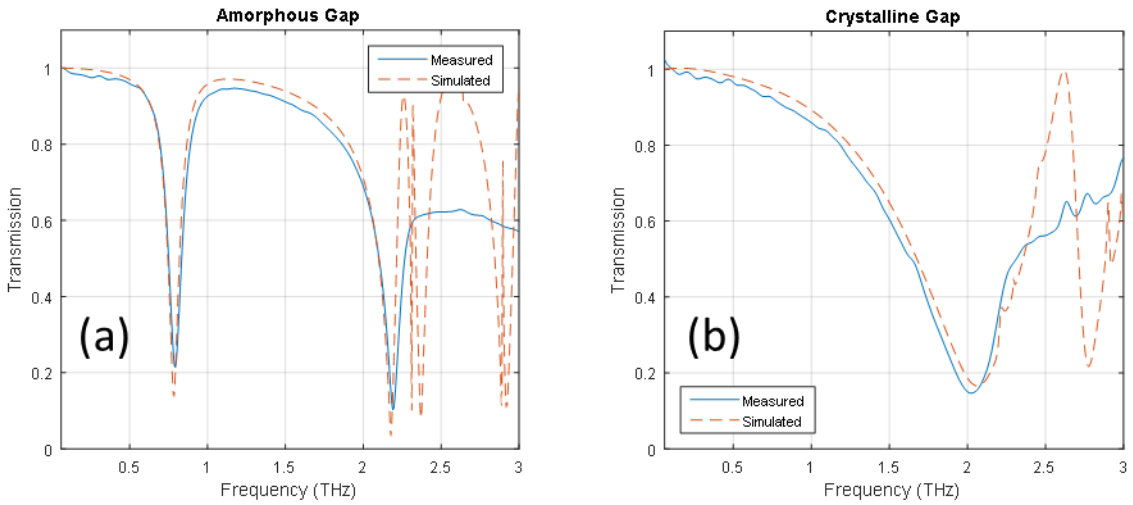

Fig. 87. Measurement and simulation of gold split-ring resonators with germanium telluride gaps in the amorphous phase (a) and the crystalline phase (b).

5.6.3. Summary

The GeTe-incorporated SRR designs produced some very interesting transmission results. The full GeTe SRRs did not have a strong LC response, but its varied transmittance over the THz frequency range could possibly have some applications. The GeTe-gapped SRRs displayed a significant difference in transmission, which can potentially be exploited in a wide range of applications, from THz modulation to temperature sensing.

5.7. GeTe Laser Pulsing

The data from before and after various laser pulsing of GeTe test devices was shown in Table 12. To maintain the same metric throughout devices of various geometries, resistivities calculated from the basic resistivity formula $\rho = R\,A/L$ was used, in which ρ is the resistivity, R is the measured resistance, A is the cross-sectional

area of the GeTe section, and L is the length of the GeTe film between the metal contact pads.

None of the tested laser pulses resulted in a significant change in resistivity in the GeTe layer. This means the lasers in the two Heidelberg μPG 101 systems were simply not powerful enough to provide the amount of heat necessary to raise the GeTe films to the amorphization temperature. However, there are still some interesting details in the resistivity data that are worth analyzing.

The subsequent analysis on the indirect Joule heating devices found that a majority of the test devices had a bad contact resistance between the GeTe films and their contact pads. This was not the case with the laser pulsing test devices. The GeTe resistivities before crystallization were very consistent, with a standard deviation less than ten percent of the average. This is an expected outcome, even when taking the bad contact resistances into account. Most of the contact resistances seen on the earlier study typically were in the tens of kΩ range. The amorphous GeTe, being an insulator, had resistances in the tens of MΩ. Therefore, the contact resistances are negligible, since they can in general be considered in series with the GeTe film resistance

After crystallization, these devices had very low contact resistances, which was surprising, given the fact that their design was very similar to wafers in the indirect heating experiment that had bad contact resistances. This may have been caused by an overall decreased amount of residual material on this wafer since it had fewer process steps than the indirect heating devices.

The GeTe laser pulsing study did not result in successful transitioning of GeTe films, due to the fact that the laser strengths were not strong enough. This would normally be the sort of possibility that can be modeled using one of the laser heating equations mentioned in the theory section, but unfortunately a lack of information on the Heidelberg system meant that many important modeling parameters, including per-unit-area intensity and pulse length, could not be accurately determined. A more effective approach for future experimentation would be to utilize a laser with known parameters that can be modeled and have predicted outcomes compared with experiment.

5.8. GeTe Indirect Heating

The fabrication of the GeTe indirect heating devices was not a straightforward process, and involved many design iterations. In total, six wafers were processed via surface micromachining, each with slight modifications of the initial indirect heating design. The various wafer iterations, as well as their layer thicknesses and ordering, are shown in Table 10. The first design to be fabricated, W1a, was not completed due to complications with the GeTe layer during the final processing step. Fabrication of W2a was also cut short due to problems during the AlN liftoff. The majority of useful and successful data came from the W3 design. Before analyzing the successful results from that design, though, some of the shortcomings of this design will be analyzed in detail.

5.8.1. High Contact Resistances and Current Crowding

The most important problem found with many of the indirect heating devices was a problem with the resistance measurements across the GeTe rectangles. Although visible changes in the color of the film were observed before and after pulses were transmitted, the resistance measurement between the GeTe contact pads did not increase as expected.

Furthermore, the resistances of all the devices were in the 10 to 20 kΩ range after crystallization, which was many orders of magnitude higher than their expected values of 5 to 100 Ω. Also, the measured resistances did not scale with the dimensions of the GeTe rectangles. For instance, with all other dimensions held constant, the 10-micron-long GeTe rectangles were expected to be twice as resistive as the 5-micron-long GeTe rectangles. Instead, their resistances were within 15 percent of each other. The fact that the resistances do not scale with the geometry indicated that in all of the devices for this design, there was a 10 to 20 kΩ resistance in series with the GeTe layer, causing all the measured resistances to be in the tens of kΩs instead of tens of Ωs. This is caused by a large amount of contact resistance between the gold contact pads and the GeTe layer.

The contact resistance could the result of a Schottky interface. Crystalline GeTe has an experimentally determined work function of 4.9 ±0.2 eV [141] and reported values of the work function of gold vary based on the source, with some stating 4.75 eV [139] and others stating 5.1 eV [142]. This means that there could possibly be a Schottky contact between the layers if the GeTe work function is greater than the gold work function [139]. However, since crystalline GeTe is a degenerate p-type semiconductor at room temperature [138], the potential barrier in the Schottky junction will be very thin (nanometers thick) and carriers would be expected to easily tunnel across the barrier [139]. Using GeTe parameters from [138] and a first-order approximation for the space charge depth [139], the barrier width in the hypothetically worst case Schottky scenario was found to be less than 4 nm, meaning that this interface should still offer a significant amount of conduction through tunneling. After reviewing measurements of other ohmic tunneling contacts with degenerate semiconductors in the literature [143], a conservative

estimate for the contact resistances in the indirect heating devices was determined: on the order of 10 Ω or less. Therefore, a Schottky barrier cannot be the only factor accounting for the 10-20 kΩ resistances seen in the indirect heating devices.

When GeTe crystallizes, the number of dangling bonds at material interfaces increases due to a sudden change in the coordination number of the material [144]. An annealing process at 300 ºC (at approximately 100 ºC above the crystallization temperature) can help transform the dangling bonds into metallic bonds, and was found to reduce the contact resistance of the interface by around one order of magnitude [145]. A rapid thermal anneal of the samples might reduce the contact resistances even further.

Another possible source of contact resistance is residual photoresist from earlier processing steps. One main oversight in the fabrication process for this design was that the devices were not cleaned in the plasma asher prior to any of the metallization steps. This would have helped remove any residual photoresist or other organic contaminants that were present on the gold film, and also provide a cleaner surface on the dielectric barrier for which the GeTe film to adhere.

In addition to pre-metallization cleaning, a simple switch in the ordering of the GeTe and GeTe contact pad layers would also have improved the resistances by straightening out the current path between the contact pad and the GeTe film. A similar problem occurred in NiCr layer in the W4 design. The W4 wafer design was the inverted version of the W3 design, with GeTe underneath the dielectric barrier and NiCr above the barrier. In these devices, the NiCr resistive heater melted before any resistive changes could be detected in the GeTe layer. Fig. 88 shows one such damaged device. The reason

for the resistive heater melting is fairly clear. As shown in Fig. 89, currents along that particular path can have a tendency to bunch up at the edge, especially if there is residue on the edges of the film that cause further funneling of the current. In this scenario, the strong currents produced during the amorphization pulse generated a large amount of heat when passing through the narrower, more resistive section by the edge of the gold pad, which caused the NiCr to locally melt in that area. This problem can be avoided by depositing the NiCr layer before its gold contacts, to keep the NiCr layer (and thus the electrical conduction path) flat.

The crystallized GeTe layer on the bottom of the W4 design had slightly better contact resistances than the W3 design, with resistances in the 200 Ω – 1 kΩ range. The

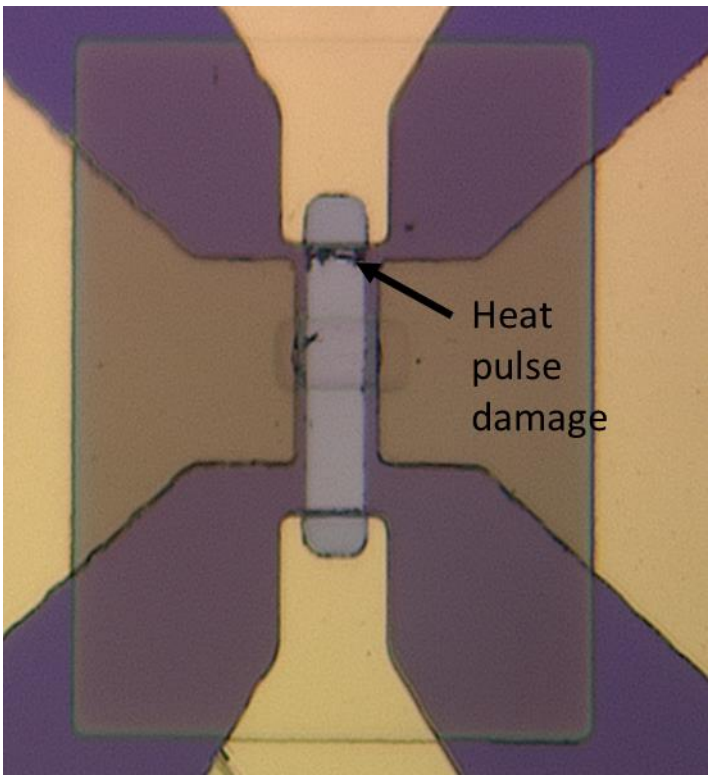

Fig. 88. Damaged nichrome layer after a 15-V, 1-μs pulse in the W4 design

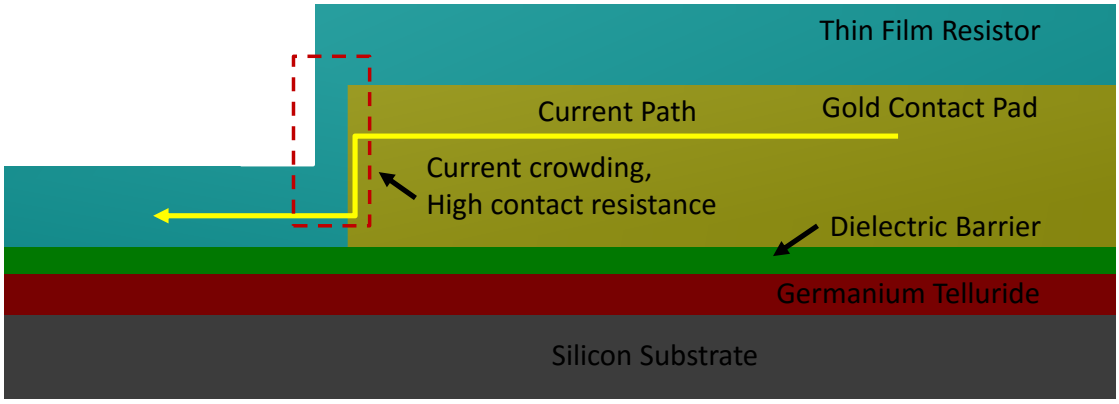

Fig. 89. Current crowding and high contact resitance near the edge of the gold contact pad in designs with the thin film resistor above the dielectric barrier

improved contact is probably due to the relative positioning of the GeTe layer, which was deposited before (i.e. below) the gold contact pads. However, the resistance values were still much higher than expected, and still did not scale properly with geometry, indicating that there remained a contact resistance of 300 to 400 Ω between the GeTe films and the contact pads.

The W2b design was the only fabricated wafer in the indirect heating study to have most GeTe resistances in the expected range of 5 – 100 Ω, indicating the presence of a good, low contact resistance between the GeTe pads and the GeTe films. However, there were still approximately 30 to 40 devices per reticle (out of 300 devices in one reticle) which had unusually high GeTe resistances in the tens and hundreds of kΩs. Nevertheless, this was an improvement over previous wafers. The reason for the consistently better contact resistances is the increased GeTe thickness in the W2b design, which created a wider current path near the edge of the gold contact pad.

Despite testing a wide variety of pulse voltages and widths, the devices in the W2b design could not be amorphized. The combination of a thicker AlN layer and a thicker GeTe layer meant that devices in the W2b design needed much stronger voltage pulses in order to transmit through the AlN and melt-quench the GeTe layer. Stronger voltages, however, are more likely to cause permanent damage to the films. The W2b design also had a slightly thinner NiCr resistor layer compared to other designs, which meant that the resistors could not handle as high voltages as the resistors in other designs.

5.8.2. Aluminum Nitride Leakage Current

Another problem found in the W2b, W3, and W4 designs was an unexpectedly low electrical isolation between the GeTe contact pads and the NiCr contact pads. Since these pads are separated by a layer of AlN, the electrical isolation is expected to be higher. The cause of the low isolation was initially thought to be caused by the edges of the NiCr resistor puncturing through the AlN film and making electrical contact with the GeTe layer above it. However, this hypothesis was ruled out when the same isolation issues were found during the testing of the W2b design, which had a thick, 150 nm dielectric barrier layer – five times thicker than the NiCr heater underneath it.

The AlN film itself was the actual cause of the poor isolation between the gold pads. AlN is a well-known piezoelectric material [146]–[148], but piezoelectricity would not affect a DC resistance measurement. Instead, the measured leakage current was due to the Poole-Frenkel effect, which is current emission caused by a lowering of the Coulomb potential barrier in an insulator when there is a strong enough electric field [149]. This effect has been observed in AlN in earlier studies in the literature [150], [151]. The presence of the Poole-Frenkel effect is significant in this particular GeTe

application because the AlN is in parallel with the GeTe layer. When the GeTe is crystallized, its low resistance will cause it to have dominant current flow over the AlN layer. When the GeTe is amorphized, reaching resistances in the tens of MΩ, the AlN could have an effective resistance anywhere between 30 to 150 kΩ (depending on the input voltage), which would siphon a large amount of current away from the GeTe film and cut down the resistivity contrast by two to three orders of magnitude. The measured voltage versus resistance characteristic curve between two probes spaced approximately 100 µm apart on an AlN film is shown in Fig. 90.

5.8.3. Wafers with Silicon Nitride Films

After determining the leakage current effect in AlN, the W5 wafer in progress was shelved, and the W6a, b, and c designs, which used Si_3N_4 dielectric barriers, were fabricated. Unfortunately, none of the W6 designs were able to be thermally set at the very beginning of their test procedures. Unlike with the earlier designs, these devices measured open-circuit voltages, indicating that there was a significant issue with the contact between the gold pads and the GeTe films. Despite having a GeTe layer thicker than that of the W2b design, the W6b design did not have any devices with low resistances between GeTe contact pads. The W6c design simply had some sort of bad GeTe deposition, which is evident from the obvious discoloration of the normally silver-white film, as shown in Fig. 91(b).

The reasons for the failure of the other two designs, W6a and b, are likely related to problems caused by excess thermal heating of the film. After heating the reticles at 300 ºC for 5 minutes, the GeTe resistances were checked on the micromanipulator to verify crystallization of the films. Since the resistances were not as low as expected, the reticles

were placed back on a hot plate with an increased temperature to 350 ºC for 15 more minutes. After this bake, the larger columns of GeTe on the wafer were filled with blisters (see Fig. 91(c)), and the GeTe films between contact pads showed open voltage resistances. A significant difference between the thermal expansion coefficients of GeTe and Si_3N_4 most likely caused the GeTe films to undergo large amounts of stress, leading to permanent damage of the film [139], [152]–[154]. Residual debris underneath the GeTe (due to the lack of pre-metallization cleaning) may have also contributed to the film damage as well.

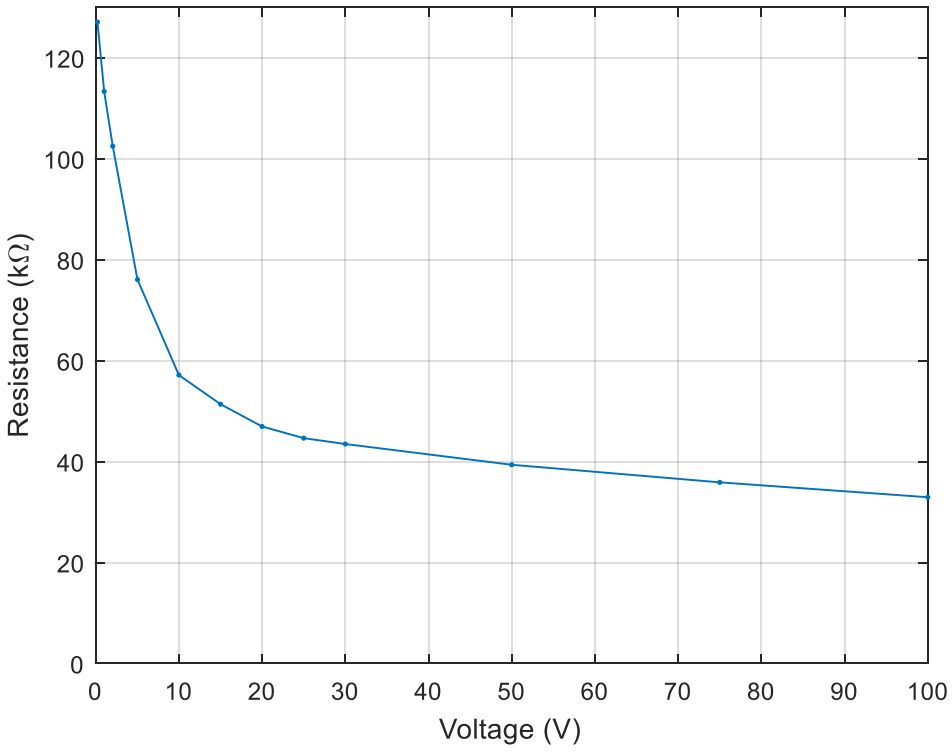

Fig. 90. Resistance as a function of voltage across an aluminum nitride thin film.

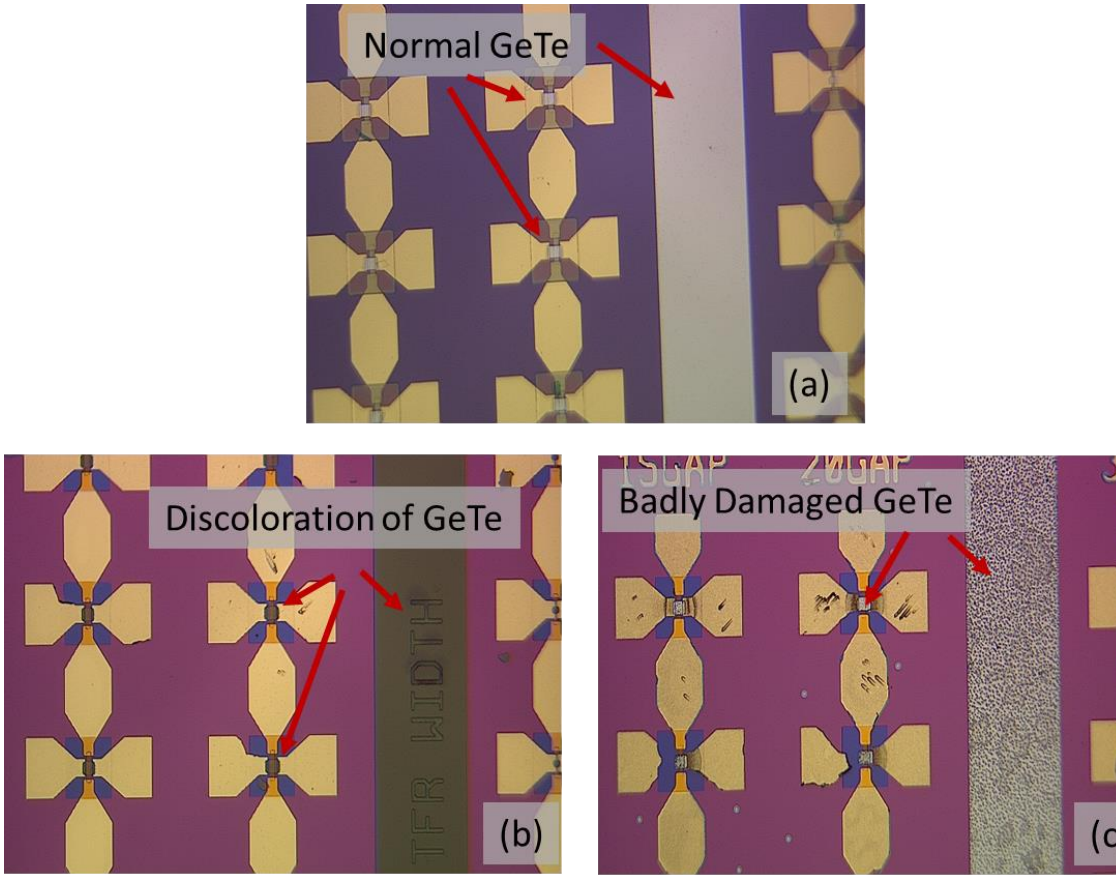

Fig. 91. (a) shows a wafer with a normal layer of GeTe. The image in (b) shows a discolored GeTe film indicating a bad deposition, and (c) is a GeTe film damaged by excessive heating.

5.8.4. Reversible Optical Contrast

The W3 design had the most success in displaying optical and electrical switching. Initial voltage pulse testing of W3 showed that there were a few combinations of voltage amplitude and pulse width that resulted in a reversible change in the color of the GeTe film; these parameters are shown in Table 11 for a specific device geometry. There were additional combinations that did result in GeTe film darkening, but these values also resulted in significant damaging of the GeTe film as well. Coventorware simulations of heating devices, shown in Figs 67-69, predicted that voltages around 25 V

(for the larger, less resistive heater) would heat the GeTe film just past its melting point, thus causing amorphization. The successful pulse parameters in Table 11 are relatively close to this value.

Voltage pulsing showed clear changes in the color of the GeTe film, but was not very repeatable. After 2-3 cycles between on/off, the amorphization pulses start causing permanent damage to the GeTe layer, similar to what is shown in Fig. 92(a). In addition, the shorter, 5-micron GeTe rectangles were unable to be amorphized without damaging the film, as shown in Fig. 92(b). The damage seen in the GeTe films is caused by a difference in the linear thermal coefficients of GeTe and the underlying material, which will induce stresses in thin films and can cause delamination [152], [153]. The linear thermal coefficients of expansion, in 10^{-6} / K, of GeTe, AlN, and Si_3N_4 are: 0.187 [154], 2.56 [155], and 2.8 [139], respectively; the volumetric thermal coefficient of expansion of GeTe from [154] was divided by three in order to get an approximation for the corresponding linear expansion value [155], [156].

The coefficients of expansion between GeTe and the other two materials differ by more than an order of magnitude, which causes a significant amount of stress in the GeTe film when a device is heated. This induced stress in concentrated on the edges of the film, making those locations the initial sites for film delamination [152], [157]. Once the GeTe film is locally separated from the underlying dielectric, repeated transmission of high temperature amorphization pulses will only serve to promote further delamination of the film in that localized area, as well as spontaneously create other delaminated spots. The shorter, 5-micron height GeTe film was more prone to being affected by small deformations in the film caused by the thermal pulses because it had more edges relative

to its total area. This explains why the devices with 5 micron GeTe heights, like the one shown in Fig. 92(b), were consistently failing.

This problem could be solved by placing another thick layer of dielectric on top of the GeTe layer, effectively sandwiching the GeTe between two square pieces of dielectric. This may help prevent the GeTe layer from delaminating as easily by restricting its ability to curl or bubble upwards after a strong thermal pulse. Strong thermal pulses would still cause large amounts of stress in the GeTe film, however, which could cause other sorts of defects to appear across the area of the film, such as blisters and cracks. Another possible solution to reduce delamination would be by introducing residual compressive stresses on the GeTe film at room temperature, which can be accomplished by depositing GeTe on a heated substrate (though not too hot, or else

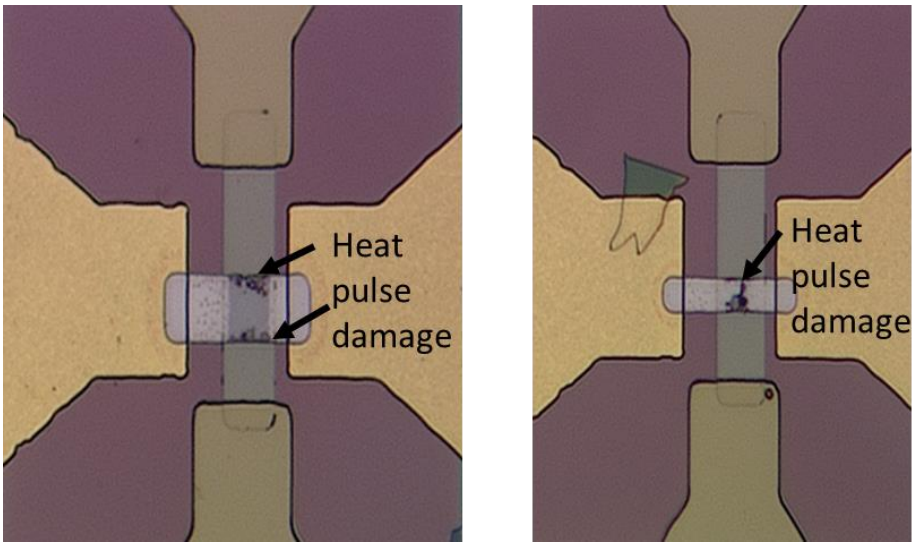

Fig. 92. Germanium Telluride (GeTe) switch with damage. (a) shows a 10-µm-length device after 50-V, 2-µs pulse, showing damage in the upper and lower edges of the GeTe rectangle. (b) shows a 5-µm-length device, with damage all along the middle of the GeTe path after a 25-V, 2-µs pulse.

compressive stress-induced defects may occur at room temperature). By starting off in a compressed state at room temperature, the GeTe films would experience less tensile stress when heated during thermal pulses.

5.8.5. Reversible Electrical Resistance Change

The resistance change caused by the onset of the optical contrast could not be easily measured due to the contact resistances of the devices as well as the effective resistance caused by the Poole-Frenkel effect in the AlN film. In order to be able to detect any sort of resistance change, the contact resistance needed to be eliminated or mitigated from the devices. This was accomplished by forcing probe tips downwards near the gold-GeTe interface, which helped create enhanced electrical contact points between the two substances. The marks caused by this method are clearly seen in Fig. 72. This method lowered the resistances from the 20-kΩ range to below 100 Ω, which was sufficient enough for the subsequent experimental verification of the electrical resistance change.

The shift in resistance caused by pulses was verified to be repeatable, at least until the point when the slow accumulation of delamination caused the device to stop working, as mentioned earlier. As the images in Fig. 72 depict, the resistance across the GeTe layer changed by around three orders of magnitude between set and reset pulses. GeTe is expected to have six orders of magnitude between its phase-change states, so a natural question to ask is what happened to the other three orders of magnitude. Around an order of magnitude can be explained by the rough electrical contact technique used for this measurement, which does not create a perfect contact. The device shown in Fig. 72 is normally expected to have a 10-20-Ω resistance in its crystalline state, instead of 80-90 Ω. The rest, as described in Section 5.8.2, is due to the Poole-Frenkel effect in the AlN

film, which effectively in parallel with the GeTe resistance, and provides a bypass path for incoming current when the GeTe film is amorphous. To mitigate the effect of the Poole-Frenkel leakage current, resistances were calculated using an ohmmeter and a very low voltage source. However, even at the resistance measurement voltage of 0.1 V, Fig. 90 shows that the Poole-Frenkel leakage effect would create an effective resistance in the 100-kΩ range. This essentially means that the measured resistance of amorphous GeTe will not exceed a certain threshold around 100 kΩ. This is evident from the voltage pulse resistance measurements.

5.8.6. Summary

The GeTe indirect heating testing was a partial success.. There were a few errors in the design of many of the indirect heating wafers, such as the deposition of gold pads before the interconnecting GeTe or NiCr layers, causing unwanted current crowding near the edges of the gold pads, and the lack of pre-metallization plasma cleaning to avoid undesirable contact resistances from residual photoresist and other particles. An additional dielectric barrier above the final device may help mitigate device breakdown and promote repeatability of switching. Despite its high thermal conductivity, AlN was found to be a poor choice for the dielectric barrier due to the noticeable Poole-Frenkel-type leakage current that it causes during resistance measurements.

Notwithstanding the various difficulties during fabrication and testing, there was some evidence of an effective reset, where the color of the film visibly darkened, and the accompanying change in resistivity was also shown to exist. With a few design and fabrication modifications, successful and repeatable indirect GeTe switching can be achieved.

6. Conclusions

The main purposes of this thesis were to gain a fuller understanding of THz metamaterials and to develop some novel meta-atom structures using germanium telluride (GeTe). Many tasks have been accomplished to fulfill this aim. The frequency-dependent characterization of the complex index of refraction of quartz, silicon, and sapphire has been determined in the THz frequency range using THz time-domain spectroscopy (THz-TDS), and has shown that both quartz and silicon are prime candidates as substrates for metamaterial applications.

In an analysis of split-ring resonators (SRRs), the capacitances and inductances which make up the unit cell have been investigated in depth, and an original equation for determining the LC resonances of SRRs has been proposed. Several SRR structures have been simulated as well as fabricated and tested on quartz and silicon substrates, showing good agreement between theory, simulation, and testing. The importance of periodicity for increased coupling strength and the use of thicker substrates for improved time windowing of the output THz pulses were two of the main conclusions drawn from these studies.

SRRs were also printed using an inkjet printer and measured with THz-TDS. THz resonances were obtained with the initial design, but further improvements on the resonance strength of the printed SRRs were extremely difficult to accomplish because those improvements conflicted with some fundamental limitations and drawbacks of inkjet printing, requiring that the printer run for extremely long periods of time without fail.

Two novel GeTe-incorporated structures were fabricated and tested. The first structure, the full GeTe SRR, did not have a strong resonance, with a transmission response similar to a thin-film response. The second device, the GeTe-gapped SRR, had a sharp difference in response between crystalline phases of its incorporated GeTe layer, especially near the normal LC resonance of the SRR. The operation of both of these devices was also computer simulated with incorporated data on both phases of GeTe, with very good agreement between results.

Thermal transitioning of GeTe via indirect Joule heating and laser pulsing was investigated. Laser heating was largely unsuccessful due to a lack of a strong enough laser source, but the indirect Joule heating experiments showed limited amounts of success in transitioning GeTe from the crystalline to amorphous states.

6.1. Applications

Metamaterial devices are an important enabling technology in the field of THz applications, especially because of the lack of strong, usable THz resonances in ordinary materials. Metamaterials can serve as novel phase shifters, near-field imagers, lenses, and even transmitters for THz radiation. Active metamaterials add a new degree of flexibility as well. The GeTe-gapped SRR fabricated in this work can act as a thermal fuse in thermal sensing applications, with an adjustable temperature cutoff possible by varying film thicknesses or the stoichiometry of the GeTe layer. With a sufficient electrical or control mechanism, the GeTe-gapped SRR can also serve as a modulator for THz communications. The field of THz devices itself is a growing field, with many potential applications in hazardous material screening, medical imaging, and military / consumer

communications; as this field grows, the field of THz metamaterials will be sure to follow.

6.2. Future work

There is a myriad of future research that can follow this current research effort. THz material characterization (complex index of refraction, conductivity) of thin films can be challenging and difficult, and would benefit from more robust methods of thin film characterization. This would also help in the characterization of metamaterial thin films, in order to verify that they indeed have the material qualities for which they were designed.

This research focused mainly on the singly split SRR for its overall simplicity, but it is not the best SRR for all applications. In reality, there are many different types of useful planar metamaterial unit cells, including electric split-ring resonators, U- and Z-shaped resonators, etc. The many types of THz metamaterial unit cells could be compared to understand the advantages and disadvantages of each one.

Also beneficial would be to explore methods to create methods of coupling with the magnetic component of THz waves. Most THz metamaterials are thin films, mostly due to compatibility with existing integrated circuit technologies. This does not allow for easy coupling with the magnetic field of normally incident waves.

With most THz metamaterials being planar, another research possibility would be to devise novel cleanroom methods to easily fabricate three-dimensional metamaterials, perhaps even one with a region of negative-index operation. Processes such as 3D-printing and electroplating may be useful for that end.

The inkjet printing of SRRs was difficult because printing metamaterial structures with strong resonances required a large amount of densely packed SRRs. However, finding a compromise between printability and a strong resonant response should be possible. More effort can be invested in exploring the ways that additive manufacturing techniques can be utilized for THz metamaterials.

This work explored two different GeTe-incorporated SRR structures. There are many other ways that a tunable material such as GeTe can be incorporated to make novel structures. GeTe could be combined with other sources of tunability, such as MEMS or photoconductivity, to create ultra-flexible metamaterials with multiple bands of operation.

Finally, effective and compact methods of reliably transitioning GeTe—with optical and electrical methods— is an important topic to continuously develop in order to ensure the relevance and importance of GeTe for THz and metamaterial applications.

References

[1] R. Marqués, F. Martín, and M. Sorolla, *Metamaterials with Negative Parameters: Theory, Design and Microwave Applications*, 1st ed. Hoboken: Wiley, 2013.

[2] M.-H. Lu, L. Feng, and Y.-F. Chen, "Phononic crystals and acoustic metamaterials," *Mater. Today*, vol. 12, no. 12, pp. 34–42, Dec. 2009.

[3] V. G. Veselago, "The Electrodynamics of Substances with Simultaneously Negative Values of ε and μ," *Sov. Phys. Uspekhi*, vol. 10, no. 4, p. 509, 1968.

[4] J. B. Pendry, A. J. Holden, D. J. Robbins, and W. J. Stewart, "Low frequency plasmons in thin-wire structures," *J. Phys. Condens. Matter*, vol. 10, no. 22, p. 4785, 1998.

[5] J. B. Pendry, A. J. Holden, D. J. Robbins, and W. J. Stewart, "Magnetism from conductors and enhanced nonlinear phenomena," *Microw. Theory Tech. IEEE Trans.*, vol. 47, no. 11, pp. 2075–2084, Nov. 1999.

[6] S. A. Cummer, B.-I. Popa, D. Schurig, D. R. Smith, and J. Pendry, "Full-wave simulations of electromagnetic cloaking structures," *Phys. Rev. E*, vol. 74, no. 3, p. 36621, Sep. 2006.

[7] P. Collins and J. McGuirk, "A novel methodology for deriving improved material parameter sets for simplified cylindrical cloaks," *J. Opt. A Pure Appl. Opt.*, vol. 11, no. 1, p. 15104, 2009.

[8] L. Pei-Ning, L. You-Wen, M. Yun-Ji, and Z. Min-Jun, "A Multifrequency Cloak with a Single Shell of Negative Index Metamaterials," *Chinese Phys. Lett.*, vol. 28, no. 6, p. 64206, 2011.

[9] F. Bilotti, S. Tricarico, and L. Vegni, "Plasmonic Metamaterial Cloaking at Optical Frequencies," *Nanotechnology, IEEE Trans.*, vol. 9, no. 1, pp. 55–61, Jan. 2010.

[10] B. Erik, H. Heinz-Wilhelm, and M. F. Kimmitt, *Terahertz techniques*. Springer, 2012.

[11] R. A. Cheville, "Terahertz Spectroscopy: Principles and Applications (Optical Science and Engineering)," in *Terahertz Spectroscopy: Principles and Applications (Optical Science and Engineering)*, 1st ed., S. L. Dexheimer, Ed. CRC Press, 2007, p. 39.

[12] J.-S. Rieh, S. Jeon, and M. Kim, "An overview of integrated THz electronics for communication applications," in *Circuits and Systems (MWSCAS), 2011 IEEE 54th International Midwest Symposium on*, 2011, pp. 1–4.

[13] P. H. Siegel, "Terahertz technology," *Microw. Theory Tech. IEEE Trans.*, vol. 50, no. 3, pp. 910–928, Mar. 2002.

[14] A. Redo-Sanchez and X.-C. Zhang, "Terahertz Science and Technology Trends," *Sel. Top. Quantum Electron. IEEE J.*, vol. 14, no. 2, pp. 260–269, Mar. 2008.

[15] R. A. Lewis, *Terahertz Physics*, 1st ed. Cambridge University Press, 2013.

[16] J. F. Federici, L. Moeller, and K. Su, "6 - Terahertz wireless communications," in

Handbook of Terahertz Technology for Imaging, Sensing and Communications, D. Saeedkia, Ed. Woodhead Publishing, 2013, pp. 156–214.

[17] N. E. Glauvitz, R. A. Coutu, I. R. Medvedev, and D. T. Petkie, "Terahertz Photoacoustic Spectroscopy Using an MEMS Cantilever Sensor," *Microelectromechanical Syst. J.*, vol. 24, no. 1, pp. 216–223, Feb. 2015.

[18] N. Glauvitz, S. Blazevic, R. Coutu, M. Kistler, I. R. Medvedev, and D. Petkie, "A MEMS Photoacoustic Detector of Terahertz Radiation for Chemical Sensing," *Procedia Eng.*, vol. 47, pp. 730–733, 2012.

[19] R. Newberry, N. Glauvitz, R. A. Coutu, I. R. Medvedev, and D. Petkie, "Fabrication of microelectromechanical systems (MEMS) cantilevers for photoacoustic (PA) detection of terahertz (THz) radiation," *Proc. SPIE*, vol. 8973. pp. 897302–897308, 2014.

[20] P. Y. Han, M. Tani, M. Usami, S. Kono, R. Kersting, and X.-C. Zhang, "A direct comparison between terahertz time-domain spectroscopy and far-infrared Fourier transform spectroscopy," *J. Appl. Phys.*, vol. 89, no. 4, pp. 2357–2359, 2001.

[21] B. Ferguson and X.-C. Zhang, "Materials for terahertz science and technology," *Nat Mater*, vol. 1, no. 1, pp. 26–33, Sep. 2002.

[22] J. F. Federici, B. Schulkin, F. Huang, D. Gary, R. Barat, F. Oliveira, and D. Zimdars, "THz imaging and sensing for security applications—explosives, weapons and drugs," *Semicond. Sci. Technol.*, vol. 20, no. 7, p. S266, 2005.

[23] D. Zimdars and J. S. White, "Terahertz reflection imaging for package and personnel inspection," *Proc. SPIE*, vol. 5411. pp. 78–83, 2004.

[24] Y. C. Shen, P. C. Upadhya, E. H. Linfield, H. E. Beere, and A. G. Davies, "Ultrabroadband terahertz radiation from low-temperature-grown GaAs photoconductive emitters," *Appl. Phys. Lett.*, vol. 83, no. 15, p. 3117, 2003.

[25] L. Duvillaret, F. Garet, and J.-L. Coutaz, "A reliable method for extraction of material parameters in terahertz time-domain spectroscopy," *Sel. Top. Quantum Electron. IEEE J.*, vol. 2, no. 3, pp. 739–746, Sep. 1996.

[26] W. Withayachumnankul, B. Ferguson, T. Rainsford, S. P. Mickan, and D. Abbott, "Material parameter extraction for terahertz time-domain spectroscopy using fixed-point iteration," in *Microtechnologies for the New Millennium 2005*, 2005, pp. 221–231.

[27] D. Grischkowsky, S. Keiding, M. van Exter, and C. Fattinger, "Far-infrared time-domain spectroscopy with terahertz beams of dielectrics and semiconductors," *J. Opt. Soc. Am. B*, vol. 7, no. 10, pp. 2006–2015, Oct. 1990.

[28] R. D. Averitt, W. J. Padilla, H. T. Chen, J. F. O'Hara, A. J. Taylor, C. Highstrete, M. Lee, J. M. O. Zide, S. R. Bank, and A. C. Gossard, "Terahertz metamaterial devices," in *Proc. SPIE*, 2007, vol. 6772, p. 677209.

[29] W. Withayachumnankul and D. Abbott, "Metamaterials in the Terahertz Regime," *Photonics Journal, IEEE*, vol. 1, no. 2, pp. 99–118, Aug. 2009.

[30] P. Gay-Balmaz and O. J. F. Martin, "Electromagnetic resonances in individual and

coupled split-ring resonators," *J. Appl. Phys.*, vol. 92, no. 5, pp. 2929–2936, 2002.

[31] T. J. Yen, W. J. Padilla, N. Fang, D. C. Vier, D. R. Smith, J. B. Pendry, D. N. Basov, and X. Zhang, "Terahertz Magnetic Response from Artificial Materials," *Science (80-.).*, vol. 303, no. 5663, pp. 1494–1496, 2004.

[32] N. Katsarakis, T. Koschny, M. Kafesaki, E. N. Economou, and C. M. Soukoulis, "Electric coupling to the magnetic resonance of split ring resonators," *Appl. Phys. Lett.*, vol. 84, no. 15, pp. 2943–2945, 2004.

[33] K. Aydin, K. Guven, N. Katsarakis, C. Soukoulis, and E. Ozbay, "Effect of disorder on magnetic resonance band gap of split-ring resonator structures," *Opt. Express*, vol. 12, no. 24, pp. 5896–5901, Nov. 2004.

[34] M. Shamonin, E. Shamonina, V. Kalinin, and L. Solymar, "Resonant frequencies of a split-ring resonator: Analytical solutions and numerical simulations," *Microw. Opt. Technol. Lett.*, vol. 44, no. 2, pp. 133–136, 2005.

[35] J. Zhou, T. Koschny, M. Kafesaki, E. N. Economou, J. B. Pendry, and C. M. Soukoulis, "Saturation of the magnetic response of split-ring resonators at optical frequencies.," *Phys. Rev. Lett.*, vol. 95, no. 22, p. 223902, Nov. 2005.

[36] W. J. Padilla, a. J. Taylor, C. Highstrete, M. Lee, and R. D. Averitt, "Dynamical Electric and Magnetic Metamaterial Response at Terahertz Frequencies," *Phys. Rev. Lett.*, vol. 96, no. 10, p. 107401, Mar. 2006.

[37] C. Rockstuhl, F. Lederer, C. Etrich, T. Zentgraf, J. Kuhl, and H. Giessen, "On the reinterpretation of resonances in split-ring-resonators at normal incidence," *Opt. Express*, vol. 14, no. 19, pp. 8827–8836, 2006.

[38] S. G. McMeekin, A. Z. Khokhar, B. Lahiri, R. M. De La Rue, and N. P. Johnson, "Analysis of resonant responses of split ring resonators using conformal mapping techniques," *Proc. SPIE*, vol. 6581. p. 65810V–65810V–8, 2007.

[39] H.-T. Chen, J. F. O'Hara, A. K. Azad, A. J. Taylor, R. D. Averitt, D. B. Shrekenhamer, and W. J. Padilla, "Experimental demonstration of frequency-agile terahertz metamaterials," *Nat Phot.*, vol. 2, no. 5, pp. 295–298, May 2008.

[40] T. D. Corrigan, P. W. Kolb, A. B. Sushkov, H. D. Drew, D. C. Schmadel, and R. J. Phaneuf, "Optical plasmonic resonances in split-ring resonator structures: an improved LC model," *Opt. Express*, vol. 16, no. 24, pp. 19850–19864, Nov. 2008.

[41] R. S. Penciu, K. Aydin, M. Kafesaki, T. Koschny, E. Ozbay, E. N. Economou, and C. M. Soukoulis, "Multi-gap individual and coupled split-ring resonator structures," *Opt. Express*, vol. 16, no. 22, pp. 18131–18144, Oct. 2008.

[42] H. Tao, A. Strikwerda, C. Bingham, W. J. Padilla, X. Zhang, and R. D. Averitt, "Dynamical control of terahertz metamaterial resonance response using bimaterial cantilevers," in *Progress in Electromagnetics Research Symposium*, Electromagnetics Academy, 2008, pp. 856–859.

[43] V. Delgado, O. Sydoruk, E. Tatartschuk, R. Marqués, M. J. Freire, and L. Jelinek, "Analytical circuit model for split ring resonators in the far infrared and optical frequency range," *Metamaterials*, vol. 3, no. 2, pp. 57–62, 2009.

[44] O. Sydoruk, E. Tatartschuk, E. Shamonina, and L. Solymar, “Analytical formulation for the resonant frequency of split rings,” *J. Appl. Phys.*, vol. 105, no. 1, p. -, 2009.

[45] R. Singh, C. Rockstuhl, and W. Zhang, “Strong influence of packing density in terahertz metamaterials,” *Appl. Phys. Lett.*, vol. 97, no. 24, p. -, 2010.

[46] J. C. Maxwell, *A Treatise on Electricity and Magnetism*, vol. 1. Dover, 1954.

[47] E. B. Rosa and F. W. Grover, “Formulas and Tables for the Calculation of Mutual and Self-Inductance,” *Bull. Bur. Stand.*, vol. 8, pp. 1–287, 1912.

[48] F. W. Grover, “Formulas and Tables for the Calculation of the Inductance of Coils of Polygonal Form,” *Sci. Pap. Bur. Stand.*, vol. 18, pp. 737–762, 1922.

[49] E. B. Rosa, “The self and mutual inductances of linear conductors,” *Bull. Bur. Stand.*, vol. 4, pp. 301–344, 1908.

[50] E. B. Rosa and L. Cohen, “On the self-inductance of circles,” *Bull. Bur. Stand.*, vol. 4, pp. 149–159, 1907.

[51] A. E. Ruehli, “Inductance Calculations in a Complex Integrated Circuit Environment,” *IBM J. Res. Dev.*, vol. 16, no. 5, pp. 470–481, Sep. 1972.

[52] E. F. Kuester, “Explicit Approximations for the Static Capacitance of a Microstrip Patch of Arbitrary Shape,” Boulder, 1986.

[53] G. J. Sloggett, N. G. Barton, and S. J. Spencer, “Addendum to ‘Fringing fields in disc capacitors,’” *J. Phys. A. Math. Gen.*, vol. 20, no. 12, p. 4061, 1987.

[54] G. R. Kirchhoff, “Zur Theorie des Condensators,” *Monatsberichte der K̈oniglich Preußischen Akad. der Wissenschaften zu Berlin*, vol. 42, pp. 144–162, 1877.

[55] J. C. Cooke, “The Coaxial Circular Disc Problem,” *ZAMM - J. Appl. Math. Mech. / Zeitschrift für Angew. Math. und Mech.*, vol. 38, no. 9–10, pp. 349–356, 1958.

[56] R. Serini, “Capacit`a del condensatore elettrico a piatti circolari infinitamente sottile,” *Rend. Accad. d. L. Roma*, vol. 6, no. 1, pp. 527–533, 1925.

[57] S. J. N. Shaw, “Circular-Disk Viscometer and Related Electrostatic Problems,” *Phys. Fluids*, vol. 13, no. 8, 1970.

[58] Y. Y. Iossel, E. S. Kochanov, and G. Strunskii, *The Calculation of Electrical Capacitance*. Defense Technical Information Center, 1971.

[59] H. B. Dwight, “The Calculation of Resistances to Ground and of Capacitance,” *J. Math. Phys.*, vol. 10, no. 1, pp. 50–74, 1931.

[60] A. E. H. Love, “Some Electrostatic Distributions in two Dimensions,” *Proc. London Math. Soc.*, vol. s2–22, no. 1, pp. 337–369, 1924.

[61] W. H. Chang, “Analytical IC Metal-Line Capacitance Formulas (Short Papers),” *Microw. Theory Tech. IEEE Trans.*, vol. 24, no. 9, pp. 608–611, Sep. 1976.

[62] H. J. Wintle, “Capacitance corrections for the guard, edge and corner situations,” in *Electrical Insulation, 1990., Conference Record of the 1990 IEEE International Symposium on*, 1990, pp. 435–438.

[63] G. T. Carlson and B. L. Illman, “The circular disk parallel plate capacitor,” *Am. J.*

Phys., vol. 62, no. 12, pp. 1099–1105, 1994.

[64] Y. Zhang and A. H. Zemanian, "Contributions of corner singularities of the capacitances of interconnections wires," in *Circuits and Systems, 1995. ISCAS '95., 1995 IEEE International Symposium on*, 1995, vol. 2, pp. 1420–1423 vol.2.

[65] C. Hwang, "Edge Charge Singularity of Conductors," *J. Korean Phys. Soc.*, vol. 45, pp. 551–553, 2004.

[66] R. E. Matick and A. E. Ruehli, "Accurate 3-D Capacitance of Parallel Plates From 2-D Analytical Superposition," *IEEE Trans. Components, Packag. Manuf. Technol.*, vol. 3, no. 2, pp. 299–305, Feb. 2013.

[67] E. T. B. Gross and R. B. Wise, "Grounding Grids for High-Voltage Stations. II - Resistance of Large Rectangular Plates [includes discussion]," *Power Appar. Syst. Part III. Trans. Am. Inst. Electr. Eng.*, vol. 74, no. 3, Jan. 1955.

[68] D. K. Reitan and T. J. Higgins, "Accurate determination of the capacitance of a thin rectangular plate," *Am. Inst. Electr. Eng. Part I Commun. Electron. Trans.*, vol. 75, no. 6, pp. 761–766, Jan. 1957.

[69] F. De Meulenaere and J. van Bladel, "Polarizability of some small apertures," *Antennas Propagation, IEEE Trans.*, vol. 25, no. 2, pp. 198–205, Mar. 1977.

[70] C. H. Kodama and R. A. Coutu, "Determining the non-ideal parallel-plate capacitance of a split-ring resonator gap," in *Advanced Electromagnetic Materials in Microwaves and Optics (METAMATERIALS), 2015 9th International Congress on*, 2015, pp. 343–345.

[71] R. Marqués, F. Medina, and R. Rafii-El-Idrissi, "Role of bianisotropy in negative permeability and left-handed metamaterials," *Phys. Rev. B*, vol. 65, no. 14, p. 144440, Apr. 2002.

[72] A. G. Knisley, "Biaxial Anisotropic Material Development and Characterization using Rectangular to Square Waveguide," Air Force Inst Tech, 2015.

[73] R. E. Newnham, *Properties of Materials : Anisotropy, Symmetry, Structure: Anisotropy, Symmetry, Structure*. OUP Oxford, 2004.

[74] V. Dmitriev, "Symmetry Principles and Group-Theoretical Methods in Electromagnetics of Complex Media," in *Theory and Phenomena of Metamaterials*, F. Capolino, Ed. 2009.

[75] V. Dmitriev, "Tables of the second rank constitutive tensors for linear homogeneous media described by the point magnetic groups of symmetry," *Prog. Electromagn. Res.*, vol. 28, pp. 43–95, 2000.

[76] A. K. Azad and W. Zhang, "Resonant terahertz transmission in subwavelength metallic hole arrays of sub-skin-depth thickness," *Opt. Lett.*, vol. 30, no. 21, pp. 2945–2947, Nov. 2005.

[77] M. Rahm, J.-S. Li, and W. Padilla, "THz Wave Modulators: A Brief Review on Different Modulation Techniques," *J. Infrared, Millimeter, Terahertz Waves*, vol. 34, no. 1, pp. 1–27, 2013.

[78] K. Fan and W. J. Padilla, "Dynamic electromagnetic metamaterials," *Mater.*

Today, vol. 18, no. 1, pp. 39–50, Jan. 2015.

[79] H.-T. Chen, W. J. Padilla, J. M. O. Zide, A. C. Gossard, A. J. Taylor, and R. D. Averitt, "Active terahertz metamaterial devices," *Nature*, vol. 444, no. 7119, pp. 597–600, Nov. 2006.

[80] I. B. Vendik, O. G. Vendik, M. A. Odit, D. V Kholodnyak, S. P. Zubko, M. F. Sitnikova, P. A. Turalchuk, K. N. Zemlyakov, I. V Munina, D. S. Kozlov, V. M. Turgaliev, A. B. Ustinov, Y. Park, J. Kihm, and C.-W. Lee, "Tunable Metamaterials for Controlling THz Radiation," *Terahertz Sci. Technol. IEEE Trans.*, vol. 2, no. 5, pp. 538–549, Sep. 2012.

[81] K. Fan, H. Y. Hwang, M. Liu, A. C. Strikwerda, A. Sternbach, J. Zhang, X. Zhao, X. Zhang, K. A. Nelson, and R. D. Averitt, "Nonlinear Terahertz Metamaterials via Field-Enhanced Carrier Dynamics in GaAs," *Phys. Rev. Lett.*, vol. 110, no. 21, p. 217404, May 2013.

[82] D. Shrekenhamer, S. Rout, A. C. Strikwerda, C. Bingham, R. D. Averitt, S. Sonkusale, and W. J. Padilla, "High speed terahertz modulation from metamaterials with embedded high electron mobility transistors," *Opt. Express*, vol. 19, no. 10, pp. 9968–9975, May 2011.

[83] R. A. Coutu, P. J. Collins, E. A. Moore, D. Langley, M. E. Jussaume, and L. A. Starman, "Electrostatically Tunable Meta-Atoms Integrated With In Situ Fabricated MEMS Cantilever Beam Arrays," *Microelectromechanical Syst. J.*, vol. 20, no. 6, pp. 1366–1371, Dec. 2011.

[84] F. Ma, L. Yu-Sheng, Z. Xinhai, and C. Lee, "Tunable multiband terahertz metamaterials using a reconfigurable electric split-ring resonator array," *Light Sci Appl*, vol. 3, p. e171, May 2014.

[85] H. Tao, W. J. Padilla, X. Zhang, and R. D. Averitt, "Recent Progress in Electromagnetic Metamaterial Devices for Terahertz Applications," *Sel. Top. Quantum Electron. IEEE J.*, vol. 17, no. 1, pp. 92–101, Jan. 2011.

[86] C. H. Lam, "History of Phase Change Materials," in *Phase Change Materials: Science and Applications*, 1st ed., S. Raoux and M. Wuttig, Eds. New York, NY: Springer, 2009, pp. 1–14.

[87] A. H. Gwin, "Materials Characterization and Microelectronic Implementation of Metal-Insulator Transition Materials and Phase Change Materials," Air Force Inst Tech, 2015.

[88] A. H. Gwin, C. H. Kodama, T. V Laurvick, R. A. Coutu, and P. F. Taday, "Improved terahertz modulation using germanium telluride (GeTe) chalcogenide thin films," *Appl. Phys. Lett.*, vol. 107, no. 3, p. -, 2015.

[89] D. Bouyge, A. Crunteanu, J.-C. Orlianges, D. Passerieux, C. Champeaux, A. Catherinot, A. Velez, J. Bonache, F. Martin, and P. Blondy, "Reconfigurable bandpass filter based on split ring resonators and vanadium dioxide (VO2) microwave switches," in *Microwave Conference, 2009. APMC 2009. Asia Pacific*, 2009, pp. 2332–2335.

[90] M. J. Dicken, K. Aydin, I. M. Pryce, L. A. Sweatlock, E. M. Boyd, S. Walavalkar,

J. Ma, and H. A. Atwater, “Frequency tunable near-infrared metamaterials based on VO2 phase transition,” *Opt. Express*, vol. 17, no. 20, pp. 18330–18339, Sep. 2009.

[91] T. Driscoll, H.-T. Kim, B.-G. Chae, B.-J. Kim, Y.-W. Lee, N. M. Jokerst, S. Palit, D. R. Smith, M. Di Ventra, and D. N. Basov, “Memory Metamaterials,” *Science (80-.).*, vol. 325, no. 5947, pp. 1518–1521, 2009.

[92] B. Gholipour, J. Zhang, J. Maddock, K. F. Macdonald, D. W. Hewak, and N. I. Zheludev, “All-optical, non-volatile, chalcogenide phase-change meta-switch,” in *Lasers and Electro-Optics Europe (CLEO EUROPE/IQEC), 2013 Conference on and International Quantum Electronics Conference*, 2013, p. 1.

[93] Z. L. Sámson, S.-C. Yen, K. F. MacDonald, K. Knight, S. Li, D. W. Hewak, D.-P. Tsai, and N. I. Zheludev, “Chalcogenide glasses in active plasmonics,” *Phys. status solidi – Rapid Res. Lett.*, vol. 4, no. 10, pp. 274–276, 2010.

[94] Z. L. Sámson, K. F. MacDonald, F. De Angelis, B. Gholipour, K. Knight, C. C. Huang, E. Di Fabrizio, D. W. Hewak, and N. I. Zheludev, “Metamaterial electro-optic switch of nanoscale thickness,” *Appl. Phys. Lett.*, vol. 96, no. 14, 2010.

[95] J. Feinleib, J. DeNeufville, S. C. Moss, and S. R. Ovshinsky, “Rapid Reversible Light-Induced Crystallization of Amorphous Semiconductors,” *Appl. Phys. Lett.*, vol. 18, no. 6, 1971.

[96] S. R. Ovshinsky, “Reversible Electrical Switching Phenomena in Disordered Structures,” *Phys. Rev. Lett.*, vol. 21, no. 20, pp. 1450–1453, Nov. 1968.

[97] L. van Pieterson, “Experimental Methods for Material Selection in Phase-change Recording,” in *Phase Change Materials: Science and Applications*, 1st ed., S. Raoux and M. Wuttig, Eds. New York, NY: Springer, 2009, pp. 81–98.

[98] W. Wełnic and M. Wuttig, “Reversible switching in phase-change materials,” *Mater. Today*, vol. 11, no. 6, pp. 20–27, 2008.

[99] P. Fons, “Short and Long-Range Order in Phase Change Materials,” in *Phase Change Materials: Science and Applications*, 1st ed., S. Raoux and M. Wuttig, Eds. New York, NY: Springer, 2009, pp. 149–174.

[100] N. Yamada, “Development of Materials for Third Generation Optical Storage Media,” in *Phase Change Materials: Science and Applications*, 1st ed., S. Raoux and M. Wuttig, Eds. New York, NY: Springer, 2009, pp. 199–226.

[101] N. Pashkov, G. Navarro, J.-C. Bastien, M. Suri, L. Perniola, V. Sousa, S. Maitrejean, A. Persico, A. Roule, A. Toffoli, G. Reimbold, B. De Salvo, O. Faynot, P. Zuliani, and R. Annunziata, “Physical and electrical characterization of Germanium or Tellurium rich GexTe1−x for phase change memories,” in *2011 Proceedings of the European Solid-State Device Research Conference (ESSDERC)*, 2011, pp. 91–94.

[102] A. H. Edwards, A. C. Pineda, P. A. Schultz, M. G. Martin, A. P. Thompson, and H. P. Hjalmarson, “Theory of persistent, p-type, metallic conduction in c-GeTe,” *J. Phys. Condens. Matter*, vol. 17, no. 32, p. L329, 2005.

[103] A. V Kolobov, J. Tominaga, P. Fons, and T. Uruga, “Local structure of

crystallized GeTe films," *Appl. Phys. Lett.*, vol. 82, no. 3, 2003.

[104] F. Kadlec, C. Kadlec, and P. Kužel, "Contrast in terahertz conductivity of phase-change materials," *Solid State Commun.*, vol. 152, no. 10, pp. 852–855, 2012.

[105] N. El-Hinnawy, P. Borodulin, B. Wagner, M. R. King, J. S. Mason, E. B. Jones, S. McLaughlin, V. Veliadis, M. Snook, M. E. Sherwin, R. S. Howell, R. M. Young, and M. J. Lee, "A Four-Terminal, Inline, Chalcogenide Phase-Change RF Switch Using an Independent Resistive Heater for Thermal Actuation," *Electron Device Lett. IEEE*, vol. 34, no. 10, pp. 1313–1315, Oct. 2013.

[106] N. El-Hinnawy, P. Borodulin, B. P. Wagner, M. R. King, E. B. Jones, R. S. Howell, M. J. Lee, and R. M. Young, "Low-loss latching microwave switch using thermally pulsed non-volatile chalcogenide phase change materials," *Appl. Phys. Lett.*, vol. 105, no. 1, p. -, 2014.

[107] N. El-Hinnawy, P. Borodulin, E. B. Jones, B. P. Wagner, M. R. King, J. S. Mason, J. Bain, J. Paramesh, T. E. Schlesinger, R. S. Howell, M. J. Lee, and R. M. Young, "12.5 THz Fco GeTe Inline Phase-Change Switch Technology for Reconfigurable RF and Switching Applications," in *2014 IEEE Compound Semiconductor Integrated Circuit Symposium (CSICS)*, 2014, pp. 1–3.

[108] G. Hummel, Y. Hui, and M. Rinaldi, "Switchable Aluminum Nitride MEMS Resonator Using Phase Change Materials," in *Proceedings of the 2014 Solid-State Sensors, Actuators and Microsystems Workshop (Hilton Head 2014)*, 2014.

[109] W. Gawelda, J. Siegel, C. N. Afonso, V. Plausinaitiene, A. Abrutis, and C. Wiemer, "Dynamics of laser-induced phase switching in GeTe films," *J. Appl. Phys.*, vol. 109, no. 12, 2011.

[110] X. Sun, E. Thelander, P. Lorenz, J. W. Gerlach, U. Decker, and B. Rauschenbach, "Nanosecond laser-induced phase transitions in pulsed laser deposition-deposited GeTe films," *J. Appl. Phys.*, vol. 116, no. 13, 2014.

[111] K. B. Lee, *Principles of Microelectromechanical Systems*. Hoboken: Wiley-IEEE Press, 2011.

[112] P. Nukala, R. Agarwal, X. Qian, M. H. Jang, S. Dhara, K. Kumar, A. T. C. Johnson, J. Li, and R. Agarwal, "Direct Observation of Metal–Insulator Transition in Single-Crystalline Germanium Telluride Nanowire Memory Devices Prior to Amorphization," *Nano Lett.*, vol. 14, no. 4, pp. 2201–2209, Apr. 2014.

[113] D. Ielmini, "Phase Change Memory Device Modeling," in *Phase Change Materials: Science and Applications*, 1st ed., S. Raoux and M. Wuttig, Eds. New York, NY: Springer, 2009, pp. 299–329.

[114] R. Bez, R. J. Gleixner, F. Pellizzer, A. Pirovano, and G. Atwood, "Phase Change Memory Cell Concepts and Designs," in *Phase Change Materials: Science and Applications*, 1st ed., S. Raoux and M. Wuttig, Eds. New York, NY: Springer, 2009, pp. 355–380.

[115] D. Sands, "Pulsed Laser Heating and Melting," in *Heat Transfer - Engineering Applications*, V. Vikhrenko, Ed. InTech, 2011, p. 400.

[116] J. H. Bechtel, "Heating of solid targets with laser pulses," *J. Appl. Phys.*, vol. 46,

no. 4, p. 1585, 1975.

[117] M. von Allmen and A. Blatter, *Laser-Beam Interactions with Materials*. Springer-Verlag Berlin Heidelberg, 1995.

[118] M. K. El-Adawi, M. A. Abdel-Naby, and S. A. Shalaby, "Laser heating of a two-layer system with constant surface absorption: an exact solution," *Int. J. Heat Mass Transf.*, vol. 38, no. 5, pp. 947–952, Mar. 1995.

[119] S. A. Campbell, *Fabrication Engineering at the Micro- and Nanoscale*, 4th ed. New York: Oxford University Press, 2013.

[120] F. Laermer and A. Schilp, "Method of anisotropically etching silicon." Google Patents, 1996.

[121] S. E. Lyshevski, *MEMS and NEMS: systems, devices, and structures*. CRC Press, 2002.

[122] V. Saile, "Introduction: LIGA and Its Applications," in *LIGA and Its Applications*, Wiley-VCH Verlag GmbH & Co. KGaA, 2009, pp. 1–10.

[123] P. Rai-Choudhury, *Handbook of Microlithography, Micromachining, and Microfabrication: Micromachining and microfabrication*. SPIE Optical Engineering Press, 1997.

[124] K. V Wong and A. Hernandez, "A review of additive manufacturing," *ISRN Mech. Eng.*, vol. 2012, 2012.

[125] S. H. Huang, P. Liu, A. Mokasdar, and L. Hou, "Additive manufacturing and its societal impact: a literature review," *Int. J. Adv. Manuf. Technol.*, vol. 67, no. 5, pp. 1191–1203, 2012.

[126] W. E. Frazier, "Metal Additive Manufacturing: A Review," *J. Mater. Eng. Perform.*, vol. 23, no. 6, pp. 1917–1928, 2014.

[127] Teraview Ltd, "TPS Spectra 3000: Terahertz (THz) spectrometer with modular sample compartment for transmission and ATR analysis," 2008. [Online]. Available: http://www.teraview.com/downloads/TPS_Spectra_3000.pdf.

[128] Computer Simulation Technology AG, "CST Microwave Studio: Workflow and Solver Overview," 2015.

[129] Computer Simulation Technology AG, "CST Studio Suite: Help Documentation," 2015. .

[130] P. Nath and K. L. Chopra, "Thermal conductivity of amorphous and crystalline Ge and GeTe films," *Phys. Rev. B*, vol. 10, no. 8, pp. 3412–3418, Oct. 1974.

[131] O. Madelung, U. Rössler, and M. Schulz, Eds., "Germanium telluride (GeTe) heat capacity, density, melting point," in *Non-Tetrahedrally Bonded Elements and Binary Compounds I SE - 834*, vol. 41C, Springer Berlin Heidelberg, 1998, pp. 1–3.

[132] G. Kaur, P. Han, and X.-C. Zhang, "Terahertz induced nonlinear effects in doped Silicon observed by open-aperture Z-scan," in *Infrared Millimeter and Terahertz Waves (IRMMW-THz), 2010 35th International Conference on*, 2010, pp. 1–2.

[133] J. Hebling, M. C. Hoffmann, H. Y. Hwang, K.-L. Yeh, and K. A. Nelson, "Observation of nonequilibrium carrier distribution in Ge, Si, and GaAs by terahertz pump terahertz probe measurements," *Phys. Rev. B*, vol. 81, no. 3, p. 35201, Jan. 2010.

[134] S. Li, G. Kumar, and T. E. Murphy, "Terahertz nonlinear conduction and absorption saturation in silicon waveguides," *Optica*, vol. 2, no. 6, pp. 553–557, Jun. 2015.

[135] J. Dai, J. Zhang, W. Zhang, and D. Grischkowsky, "Terahertz time-domain spectroscopy characterization of the far-infrared absorption and index of refraction of high-resistivity, float-zone silicon," *J. Opt. Soc. Am. B*, vol. 21, no. 7, pp. 1379–1386, Jul. 2004.

[136] N. Laman and D. Grischkowsky, "Terahertz conductivity of thin metal films," *Appl. Phys. Lett.*, vol. 93, no. 5, p. 051105, 2008.

[137] D. Ö. Güney, T. Koschny, and C. M. Soukoulis, "Reducing ohmic losses in metamaterials by geometric tailoring," *Phys. Rev. B*, vol. 80, no. 12, p. 125129, Sep. 2009.

[138] S. K. Bahl and K. L. Chopra, "Amorphous versus Crystalline GeTe Films. III. Electrical Properties and Band Structure," *J. Appl. Phys.*, vol. 41, no. 5, p. 2196, 1970.

[139] R. S. Muller, T. I. Kamins, and M. Chan, *Device Electronics for Integrated Circuits*, 3rd ed. New York, NY, 2003.

[140] F. Kadlec, C. Kadlec, P. Kuzel, and J. Petzelt, "Study of the ferroelectric phase transition in germanium telluride using time-domain terahertz spectroscopy," *Phys. Rev. B*, vol. 84, no. 20, p. 205209, Nov. 2011.

[141] E. K. Chua, L. P. Shi, M. H. Li, R. Zhao, T. C. Chong, T. E. Schlesinger, and J. A. Bain, "Band alignment between GeTe and SiO[sub 2]/metals for characterization of junctions in nonvolatile resistance change elements," *Appl. Phys. Lett.*, vol. 98, no. 23, p. 232104, 2011.

[142] S. Ramanathan, *Thin Film Metal-Oxides: Fundamentals and Applications in Electronics and Energy*. Springer US, 2009.

[143] A. Y. C. Yu, "Electron tunneling and contact resistance of metal-silicon contact barriers," *Solid. State. Electron.*, vol. 13, no. 2, pp. 239–247, Feb. 1970.

[144] E. K. Chua, L. P. Shi, R. Zhao, K. G. Lim, T. C. Chong, T. E. Schlesinger, and J. A. Bain, "Low resistance, high dynamic range reconfigurable phase change switch for radio frequency applications," *Appl. Phys. Lett.*, vol. 97, no. 18, p. 183506, 2010.

[145] E. K. Chua, R. Zhao, L. P. Shi, T. C. Chong, T. E. Schlesinger, and J. A. Bain, "Effect of metals and annealing on specific contact resistivity of GeTe/metal contacts," *Appl. Phys. Lett.*, vol. 101, no. 1, p. 012107, 2012.

[146] M.-A. Dubois and P. Muralt, "Stress and piezoelectric properties of aluminum nitride thin films deposited onto metal electrodes by pulsed direct current reactive sputtering," *J. Appl. Phys.*, vol. 89, no. 11, p. 6389, 2001.

[147] H. Okano, N. Tanaka, Y. Takahashi, T. Tanaka, K. Shibata, and S. Nakano, "Preparation of aluminum nitride thin films by reactive sputtering and their applications to GHz-band surface acoustic wave devices," *Appl. Phys. Lett.*, vol. 64, no. 2, p. 166, 1994.

[148] M.-A. Dubois and P. Muralt, "Properties of aluminum nitride thin films for piezoelectric transducers and microwave filter applications," *Appl. Phys. Lett.*, vol. 74, no. 20, p. 3032, 1999.

[149] J. G. Simmons, "Conduction in thin dielectric films," *J. Phys. D. Appl. Phys.*, vol. 4, no. 5, p. 613, 1971.

[150] D. Eom, S. Y. No, C. S. Hwang, and H. J. Kim, "Properties of aluminum nitride thin films deposited by an alternate injection of trimethylaluminum and ammonia under ultraviolet radiation," *J. Electrochem. Soc.*, vol. 153, no. 4, pp. C229–C234, 2006.

[151] A. H. Khan, J. M. Meese, T. Stacy, E. M. Charlson, E. J. Charlson, G. Zhao, G. Popovici, and M. A. Prelas, "Electrical characterization of aluminum nitride films on silicon grown by chemical vapor deposition," in *MRS Proceedings*, 1994, vol. 339, p. 637.

[152] H. Yu and J. W. Hutchinson, "Delamination of thin film strips," *Thin Solid Films*, vol. 423, no. 1, pp. 54–63, Jan. 2003.

[153] K. Tu, J. W. Mayer, and L. C. Feldman, *Electronic Thin Film Science: For Electrical Engineers and Materials Scientists*. Macmillan, 1992.

[154] H. Wiedemeier and P. A. Siemers, "The Thermal Expansion of GeS and GeTe," *Z. anorg. allg. Chem.*, vol. 481, pp. 299–304, 1977.

[155] G. A. Slack and S. F. Bartram, "Thermal expansion of some diamondlike crystals," *J. Appl. Phys.*, vol. 46, no. 1, p. 89, 1975.

[156] ASM International, *ASM ready reference: thermal properties of metals*. ASM International, 2002.

[157] R. M. Cannon, R. M. Fisher, and A. G. Evans, "Decohesion of Thin Films From Ceramic Substrates," in *Proc. of Mat. Res. Soc. Symp.*, 1986, pp. 799–804.

[158] H. Tao, A. C. Strikwerda, K. Fan, W. J. Padilla, X. Zhang, and R. D. Averitt, "MEMS based structurally tunable metamaterials at terahertz frequencies," *J. Infrared, Millimeter, Terahertz Waves*, vol. 32, no. 5, pp. 580–595, 2011.

[159] Y. Y. Iossel', "Method for deriving an upper bound for the capacitance of plates," *Sov. Phys Tech Phys*, vol. 28, no. 9, pp. 1027–1028, 1983.

[160] E. E. RUSSELL and E. L. Y. E. BELL, "Optical Constants of Sapphire in the Far Infrared," *J. Opt. Soc. Am.*, vol. 57, no. 4, pp. 543–544, Apr. 1967.

[161] W. Withayachumnankul, J. F. O'Hara, W. Cao, I. Al-Naib, and W. Zhang, "Limitation in thin-film sensing with transmission-mode terahertz time-domain spectroscopy," *Opt. Express*, vol. 22, no. 1, pp. 972–986, Jan. 2014.

[162] S. P. Mickan, K.-S. Lee, T.-M. Lu, E. Barnat, J. Munch, D. Abbott, and X.-C. Zhang, "Thin film characterization using terahertz differential time-domain

spectroscopy and double modulation," *Proc. SPIE*, vol. 4591. pp. 197–209, 2001.

[163] M. Naftaly and R. E. Miles, "Terahertz Time-Domain Spectroscopy for Material Characterization," *Proc. IEEE*, vol. 95, no. 8, pp. 1658–1665, Aug. 2007.

[164] S. K. Bahl, "Amorphous Versus Crystalline GeTe Films. II. Optical Properties," *J. Appl. Phys.*, vol. 40, no. 12, p. 4940, 1969.

[165] S. K. Bahl and K. L. Chopra, "Electrical and Optical Properties of Amorphous vs Crystalline GeTe Films," *J. Vac. Sci. Technol.*, vol. 6, no. 4, 1969.

[166] J. H. Coombs, A. P. J. M. Jongenelis, W. van Es-Spiekman, and B. A. J. Jacobs, "Laser-induced crystallization phenomena in GeTe-based alloys. II. Composition dependence of nucleation and growth," *J. Appl. Phys.*, vol. 78, no. 8, p. 4918, 1995.

[167] J. H. Coombs, A. P. J. M. Jongenelis, W. van Es-Spiekman, and B. A. J. Jacobs, "Laser-induced crystallization phenomena in GeTe-based alloys. I. Characterization of nucleation and growth," *J. Appl. Phys.*, vol. 78, no. 8, p. 4906, 1995.

[168] A. H. Edwards, A. C. Pineda, P. A. Schultz, M. G. Martin, A. P. Thompson, H. P. Hjalmarson, and C. J. Umrigar, "Electronic structure of intrinsic defects in crystalline germanium telluride," *Phys. Rev. B*, vol. 73, no. 4, p. 45210, Jan. 2006.

[169] A. G. Mikolaichuk, A. N. Kogut, and M. I. Ignativ, "Electrical properties of thin films of germanium telluride and selenide," *Sov. Phys. J.*, vol. 13, no. 7, pp. 919–921, 1970.

[170] T. Shiraishi, M. Iida, K. Shinohara, and D. Adler, "Electrical conduction mechanisms in amorphous GeTe thin films," *J. Non. Cryst. Solids*, vol. 45, no. 2, pp. 169–181, 1981.

[171] J. Kalb, F. Spaepen, and M. Wuttig, "Atomic force microscopy measurements of crystal nucleation and growth rates in thin films of amorphous Te alloys," *Appl. Phys. Lett.*, vol. 84, no. 25, p. 5240, 2004.

[172] Z. Piatek, B. Baron, T. Szczegielniak, D. Kusiak, and A. Pasierbek, "Self inductance of long conductor of rectangular cross section," *Prz. Elektrotechniczny (Electrical Rev.*, vol. 88, no. 8, pp. 323–326, 2012.

[173] Z. Piatek and B. Baron, "Exact closed form formula for self inductance of conductor of rectangular cross section," *Prog. Electromagn. Res. M*, vol. 26, pp. 225–236, 2012.

Appendix

A. Visual Bibliography

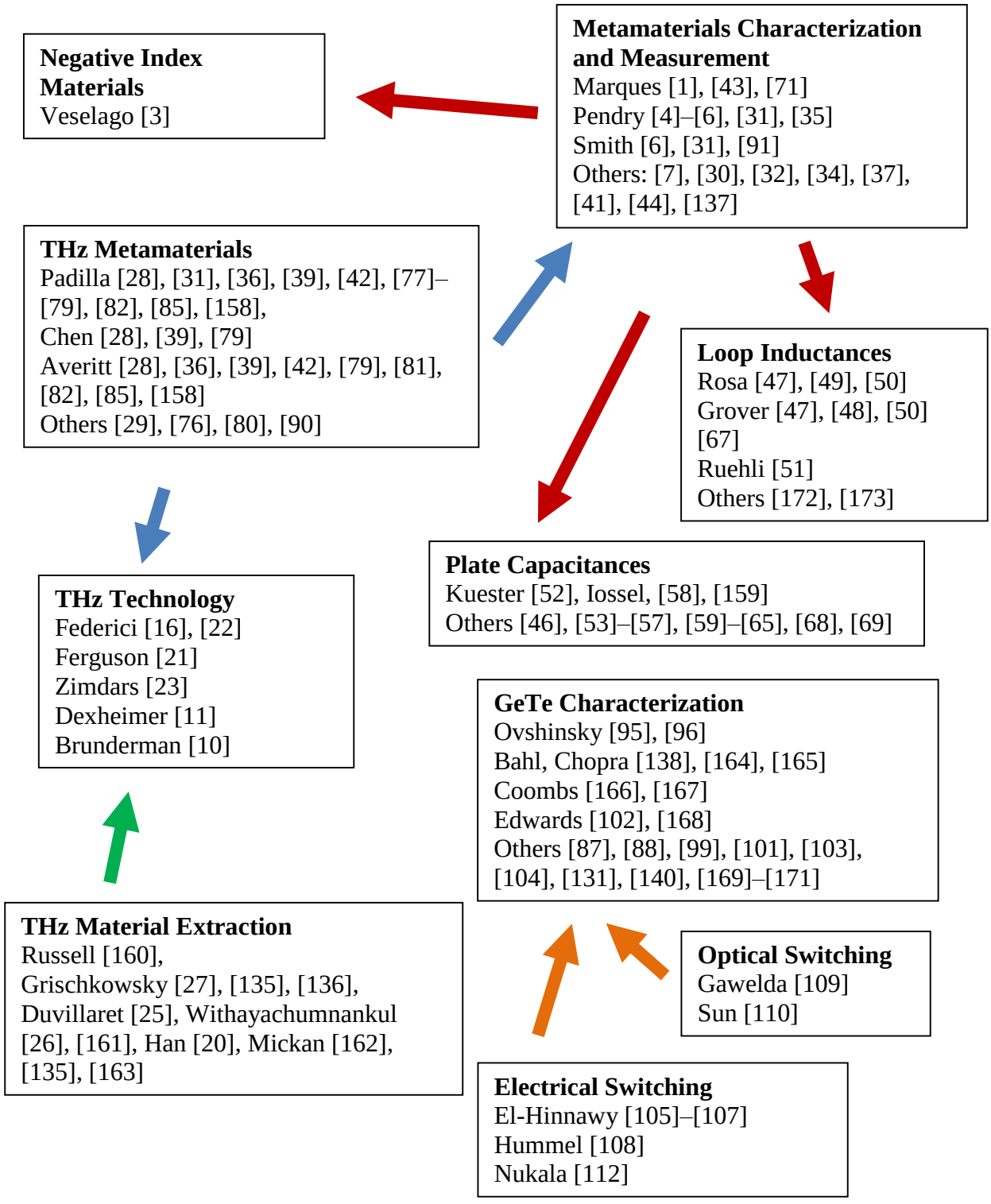

B. Process Followers

a. 1818 Liftoff Process Follower

Table 13. Process follower for 1818 patterning and liftoff.

Process Step
General Comments This follower describes the basic steps required to perform 1818 patterning and liftoff.
Cleaning of Wafer (Solvent Hood) □ Rinse in acetone for 30 sec at 500 rpm □ Rinse in methanol for 30 sec at 500 rpm □ Rinse in DI water for 30 sec at 500 rpm □ Dry with nitrogen on spinner at 500 rpm and on Texwipes □ Bake wafer on hot plate for 75 sec at 110°C
Cleaning of Mask (Solvent Hood) □ Rinse with acetone for 30 sec □ Rinse with methanol for 30 sec □ Rinse with de-ionized (DI) water for 30 sec □ Dry with nitrogen on Texwipes **NOTE: Mask must be silver side up when installed**
1818 Photoresist (Solvent Hood) □ Flood wafer with 1818 photoresist using dropper □ Spin wafer for 30 sec at 4,000 rpm; Ramp at 200 rpm/sec □ Bake wafer on hot plate for 75 sec at 110°C
Alignment & Exposure (EVG Mask Aligner) □ Use preset "1818" settings on EVG Mask Aligner. □ Align mask and wafer in x, y, and theta directions as necessary □ Expose for 7 sec
Develop of 1818 Photoresist (Base Hood) □ Spin wafer @ 500 rpm □ Flood with a (5:1) solution of (DI Water):(351 Developer) for 45 sec □ Rinse wafer with DI water for approx. 30 sec □ Dry with nitrogen on Texwipes
Inspection of Lithographic Process (Optical Microscope) □ Check the alignment. See how the smallest features turned out. □ Check for clean features with sharp definition □ If features look bad, the 1818 can be stripped with acetone and the procedure can be restarted from the 1818 application step
Pre-metallization Cleaning (Plasma Asher) □ Place wafer in O_2 plasma asher for 2 min at 75 W (default setting)
Deposition □ Deposit material on the patterned surface using thermal evaporation or sputtering.
Lift-off of 1818 Photoresist **(Ultrasound Bath, Solvent Hood, Optical Microscope)** □ Stick Scotch tape to wafer and attempt to pull material from surface

□ Put the wafer in a petri dish and place the dish in ultrasonic bath □ Using a beaker, fill the bath with water □ Submerge the wafer in the Petri dish with acetone □ Ultrasonic for approximately 5 min; continue longer if needed □ Rinse/spin with acetone, methanol, and DI water at 500 rpm, with 30 sec of each solvent. Dry with nitrogen. □ Check quality of lift-off using optical microscope, and repeat if necessary

b. Bilayer Liftoff Process Follower

Table 14. Process follower for bi-layer liftoff with SF-11 and 1805.

Process Step
General Comments This follower describes the basic steps required to perform bi-layer patterning and liftoff.
Cleaning of Wafer (Solvent Hood) □ Rinse in acetone for 30 sec at 500 rpm □ Rinse in methanol for 30 sec at 500 rpm □ Rinse in DI water for 30 sec at 500 rpm □ Dry with nitrogen on spinner at 500 rpm and on Texwipes □ Bake wafer on hot plate for 2 min at 200°C
Cleaning of Mask (Solvent Hood) □ Rinse with acetone for 30 sec □ Rinse with methanol for 30 sec □ Rinse with de-ionized (DI) water for 30 sec □ Dry with nitrogen on Texwipes **NOTE: Mask must be silver side up when installed**
SF-11 Photoresist (Solvent Hood) □ Flood wafer with SF-11 photoresist using dropper □ Spin wafer for 30 sec at 4,000 rpm; Ramp at 200 rpm/sec **NOTE: If processing a full wafer, use a cotton q-tip during spinning to collect strands of SF-11 as they fly off the wafer.** □ Bake wafer on hot plate for 2 min at 200°C
1805 Photoresist (Solvent Hood) □ Flood wafer with 1805 photoresist using dropper □ Spin wafer for 30 sec at 4,000 rpm; Ramp at 200 rpm/sec □ Bake wafer on hot plate for 75 sec at 110°C
Alignment & Exposure (EVG Mask Aligner) □ Use preset “1805” settings on EVG Mask Aligner. □ Align mask and wafer in x, y, and theta directions as necessary □ Expose for 2.5 sec
Developing of 1805 Photoresist (Base Hood) □ Spin wafer @ 500 rpm □ Flood with a (5:1) solution of (DI Water):(351 Developer) for 45 sec □ Rinse wafer with DI water for approx. 30 sec □ Dry with nitrogen on Texwipes
Inspection of Lithographic Process (Optical Microscope) □ Check the alignment. See how the smallest features turned out.

□ Check for clean features with sharp definition
□ If features look bad, the 1805 can be stripped with acetone without affecting the SF-11 layer, and the procedure can be restarted from the 1805 application step

Deep UV Exposure (Deep UV source)
□ Flood expose the sample for 200 seconds with the DUV source.
□ Verify the following settings on the source:
800 Watts **30 Volts**
19 MW/cm^2 **25 Amps**

Developing of SF-11 Photoresist (Base Hood)
□ Pour approx. half an inch of 101 developer in a container
□ Place wafer in container for 60 seconds with slow agitation
□ Rinse wafer with DI water for approx. 30 sec
□ Dry with nitrogen on Texwipes

Inspection of Lithographic Process (Optical Microscope)
□ Check for the desired slight undercutting of the SF-11
□ Examine smallest features to ensure undercutting does not adversely affect them
□ If features look bad, the 1805 must first be stripped with acetone, and then the SF-11 layer must be stripped with Remover PG (See last step)

Pre-metallization Cleaning (Plasma Asher)
□ Place wafer in O_2 plasma asher for 2 min at 75 W (default setting)

Deposition
□ Deposit material on the patterned surface using thermal evaporation or sputtering.

Lift-off of 1805 Photoresist
(Ultrasound Bath, Solvent Hood, Optical Microscope)
□ Stick Scotch tape to wafer and attempt to pull material from surface
□ Put the wafer in a petri dish and place the dish in ultrasonic bath
□ Using a beaker, fill the bath with water
□ Submerge the wafer in the Petri dish with acetone
□ Ultrasonic for approximately 5 min; continue longer if needed
□ Rinse/spin with acetone, methanol, and DI water at 500 rpm, with 30 sec of each solvent. Dry with nitrogen.
□ Check quality of lift-off using optical microscope, and repeat if necessary

Strip of SF-11 Photoresist (Solvent Hood)
□ Prepare two containers filled with 1-2 inches of Remover PG and place on a hot plate set to 80 C. Also prepare a container filled with IPA.
□ Place sample in one of the containers of Remover PG for 60 sec
□ Place sample in the other container of Remover PG for 60 sec
□ Remove sample from hot plate and place in IPA container for 60 sec
□ Rinse/spin with acetone, methanol, and DI water at 500 rpm, with 30 sec of each solvent. Dry with nitrogen.
□ Check quality of lift-off using optical microscope, and repeat if necessary

C. Masks

There were two main mask sets that were designed and utilized in this project. The first set was used to fabricate a planar array of split-ring resonators. The second set was designed to test the indirect heating of GeTe.

a. Split-Ring Resonator Mask Design

Fig. 93 shows two mask designs that were used to fabricate SRRs. The first mask shown in Fig. 93a was used to fabricate SRRs on quartz. Each section of the mask

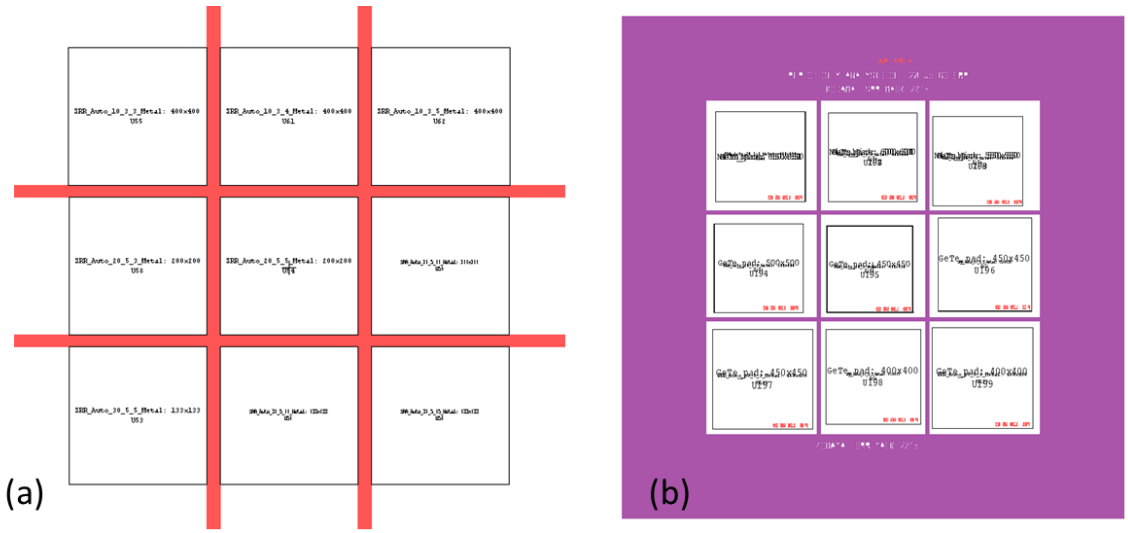

Fig. 93. Overview of two mask designs used to fabricate split-ring resonators (SRRs). Each mask consists of nine distinct SRR arrays. The individual SRRs in each blank white square were not rendered in the image due to their small size. The mask in (a) was used to fabricate SRRs of various dimensions on quartz substrates. The design in (b) was used to deposit SRRs with identical geometry but varying periodicity on silicon. It was also used to create germanium telluride-incorporated SRRs.

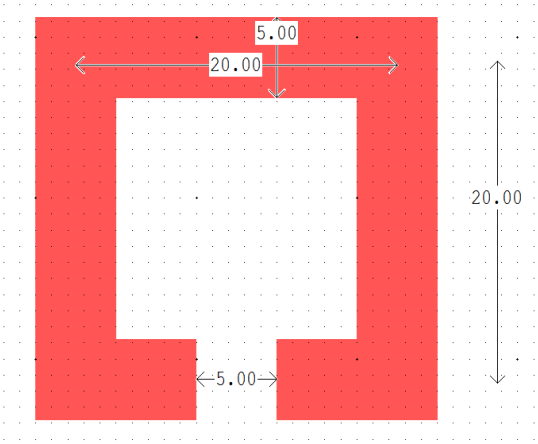

Fig. 94. Split-ring resonator element with dimensions.

contained a large array of SRRs with varied dimensions, specifically the ones shown in Fig. 94. In Fig. 93b, each of the mask sections contained identical SRRs (with a side length of 20 microns, gap width of 3 microns, and a line width of 5 microns), but had varied periodicity of the SRRs. This design also had an additional layer to allow the placement of GeTe films in the capacitive gaps of the SRRs, as shown in Fig. 95.

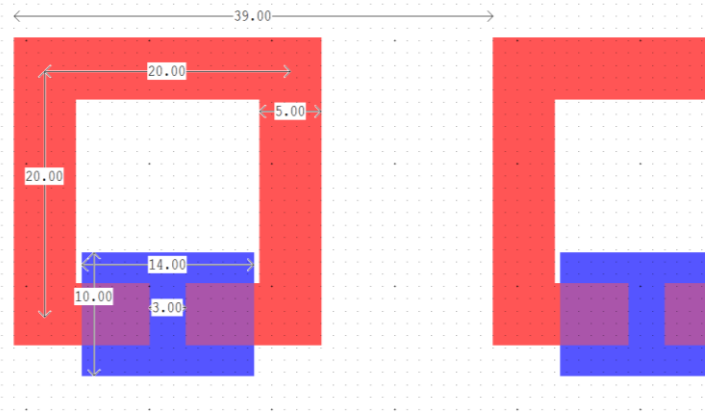

Fig. 95. Split-ring resonator elements with germanium telluride rectangles (blue) in their capacitive gaps, shown with dimensions.

i. Split-Ring Resonator Generator Code in L-Edit

A generator function was written in the L-EDIT software to aid in the speedy creation of SRR shapes during mask development. This code is shown below.

```
/*************************************************************************
*****
 * Cell Name: SRR
 * Creator : Christopher Kodama
 *
 * Revision History:
 * 24 Apr 2015     Generated by L-Edit

*************************************************************************
****/
#include <cstdlib>
#include <cmath>
#include <cstring>
#include <cstdio>
#include <string>

#define EXCLUDE_LEDIT_LEGACY_UPI
#include <ldata.h>


/* Begin -- Uncomment this block if you are using L-Comp. */
//#include <lcomp.h>
/* End */

/* TODO: Put local functions here. */
void SRR_main(void)
{
      int iTmpUpiReturnCode = LUpi_GetReturnCode();
      /* Begin DO NOT EDIT SECTION generated by L-Edit */
      LCell   cellCurrent = (LCell)LMacro_GetNewTCell();
      double  len   = LCell_GetParameterAsDouble(cellCurrent, "len");
      double  wid   = LCell_GetParameterAsDouble(cellCurrent, "wid");
      double  gap   = LCell_GetParameterAsDouble(cellCurrent, "gap");
      LLayer  layer  = LCell_GetParameterAsLayer(cellCurrent, "layer");
      double  plate_ht  = LCell_GetParameterAsDouble(cellCurrent,
"plate_ht");
      double  plate_wid = LCell_GetParameterAsDouble(cellCurrent,
"plate_wid");
      /* End DO NOT EDIT SECTION generated by L-Edit */

      if(LUpi_GetReturnCode())
      {
            LDialog_MsgBox("Error: Tcell failed to read parameters.");
            return;
      }
      LUpi_SetReturnCode(iTmpUpiReturnCode);


      /* Begin -- Uncomment this block if you are using L-Comp. */
      //LC_InitializeState();
      //LC_CurrentCell = cellCurrent;
```

```
	/* End */

	/* TODO: Put local variables here. */
	double s=100;//internal unit multiplier
	double x0 = 0;
	double y0 = 0;

	len = len*s;
	wid = wid*s;
	gap = gap*s;
	plate_ht = plate_ht*s;
	plate_wid = plate_wid*s;
	/* TODO: Begin custom generator code.*/
	LObject rectangleTop = LBox_New(cellCurrent, layer, -
(len+wid)/2,(len-wid)/2, (len+wid)/2, (len+wid)/2);
	LObject rectangleLeft = LBox_New(cellCurrent, layer, -(len+wid)/2,-
(len+wid)/2,-(len-wid)/2, (len+wid)/2);
	LObject rectangleRight = LBox_New(cellCurrent, layer, (len+wid)/2,-
(len+wid)/2,(len-wid)/2, (len+wid)/2);
	LObject rectangleBottom = LBox_New(cellCurrent, layer, -(len+wid)/2,-
(len-wid)/2, (len+wid)/2, -(len+wid)/2);
	LObject rectangleBottomLeg = LBox_New(cellCurrent, layer, -(wid/2), -
(len+wid)/2, (wid/2), -gap/2);
	LObject rectangleTopLeg = LBox_New(cellCurrent, layer, -(wid/2),
(len+wid)/2, (wid/2), gap/2);
	LObject rectangleBottomCap = LBox_New(cellCurrent, layer, -
(plate_wid/2), -gap/2, (plate_wid/2), -gap/2-plate_ht);
	LObject rectangleTopCap = LBox_New(cellCurrent, layer, -
(plate_wid/2), gap/2, (plate_wid/2), gap/2+plate_ht);
	//LObject rectangleBottom = LBox_New(cellCurrent, layer, -
(len+wid)/2,-(len-wid)/2, (len+wid)/2, -(len+wid)/2);
	//LObject rectangleBottomLeft = LBox_New(cellCurrent, layer, -
(len+wid)/2,-(len-wid)/2, -gap/2, -(len+wid)/2);
	//LObject rectangleBottomRight = LBox_New(cellCurrent, layer, gap/2,-
(len-wid)/2, (len+wid)/2, -(len+wid)/2);
	/* End custom generator code.*/
}
extern "C" int UPI_Entry_Point(void)
{
	SRR_main();
	return 1;
}
```

b. Indirect Heating Mask Design

Figs 96, 97, and 98 describe the mask design for the GeTe indirect heating experiment. A wide variety of individual devices were fabricated, with three main dimensions being varied: length of the GeTe rectangles, height of the GeTe rectangles, and the width of the NiCr heater. These varied dimensions are highlighted in yellow in Fig. 96. To avoid confusion during fabrication and testing, the design included several labeled areas describing the dimensions of the devices and the corresponding layers of the alignment marks. This is shown in Fig. 97. Each reticle contained 10 copies each of 30 unique devices, for a total of 300 devices per reticle. As shown in Fig. 98b, in the full design,16 reticles were arrayed on a three inch wafer.

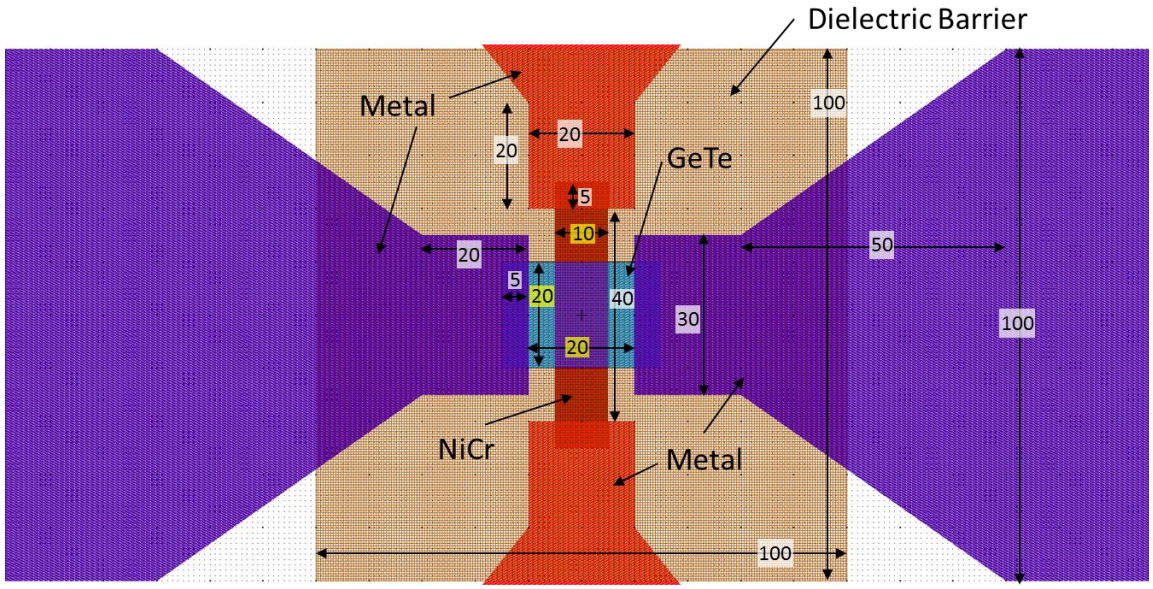

Fig. 96. Zoomed in view of an indirect heating test device, showing device dimensions and materials. The dimensions highlighted in yellow were parametrically varied throughout a reticle.

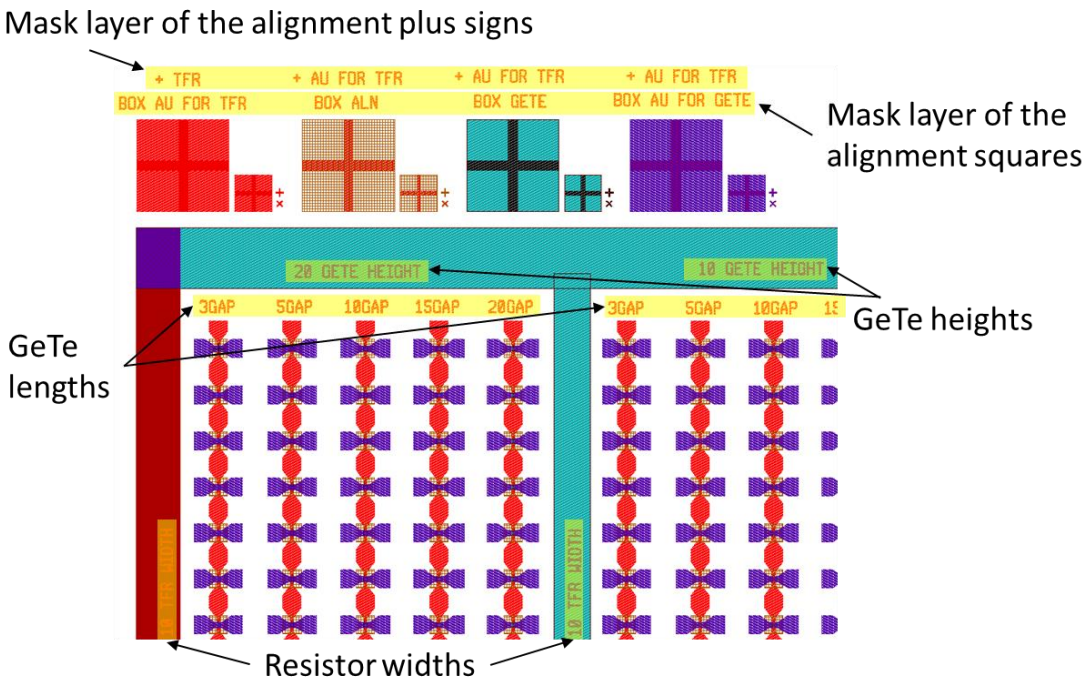

Fig. 97. Labeling scheme used to identify the geometries of each indirect heating test device and the alignment squares of each layer.

As in the SRR mask design, generating functions were utilized to alleviate the tedious and repetitive nature of mask design, as well as to mitigate design error. Two functions were utilized for this design. The first function was utilized to make the geometries necessary for the gold contact pads for the GeTe and NiCr films. The second function was designed to generate a single indirect heating device based on user-input values for the length and width of the GeTe film and the width of the NiCr film.

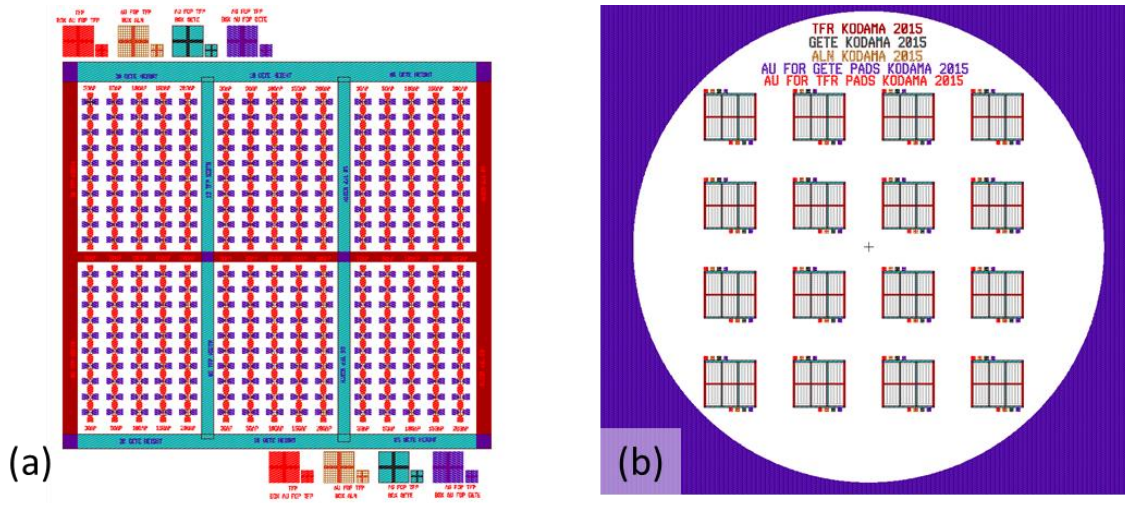

Fig. 98. The image in (a) displays an overview of a single reticle of devices. Each reticle contains 30 unique reticle geometries, each with ten copies, for a total of 300 devices per reticle. (b) shows an image of the entire mask for a three-inch wafer, with 16 reticles total.

i. Indirect Heating Generator Code: Contact Pads

```
/**************************************************************************
*****
 * Cell Name: contactPad
 * Creator : Christopher Kodama
 *
 * Revision History:
 * 17 Sep 2015     Generated by L-Edit

**************************************************************************
****/
#include <cstdlib>
#include <cmath>
#include <cstring>
#include <cstdio>
#include <string>

#define EXCLUDE_LEDIT_LEGACY_UPI
#include <ldata.h>


/* Begin -- Uncomment this block if you are using L-Comp. */
//#include <lcomp.h>
```

```
/* End */

/* TODO: Put local functions here. */
void contactPad_main(void)
{
	int iTmpUpiReturnCode = LUpi_GetReturnCode();
	/* Begin DO NOT EDIT SECTION generated by L-Edit */
	LCell   cellCurrent = (LCell)LMacro_GetNewTCell();
	double  width_outer = LCell_GetParameterAsDouble(cellCurrent,
"width_outer");
	double  width_inner = LCell_GetParameterAsDouble(cellCurrent,
"width_inner");
	double  length_outer = LCell_GetParameterAsDouble(cellCurrent,
"length_outer");
	double  length_inner = LCell_GetParameterAsDouble(cellCurrent,
"length_inner");
	double  length_taper = LCell_GetParameterAsDouble(cellCurrent,
"length_taper");
	LLayer  metal_layer = LCell_GetParameterAsLayer(cellCurrent,
"metal_layer");
	/* End DO NOT EDIT SECTION generated by L-Edit */

	if(LUpi_GetReturnCode())
	{
		LDialog_MsgBox("Error: Tcell failed to read parameters.");
		return;
	}
	LUpi_SetReturnCode(iTmpUpiReturnCode);

	/*--------------------------------------*/
	LFile pFile = LCell_GetFile( cellCurrent );

	/* Clear out existing elements */
	LLayer pLayer;
	for ( pLayer = LLayer_GetList( pFile ); pLayer; pLayer =
LLayer_GetNext( pLayer ) )
	{
		LObject pObj;
		LObject pObj_next;
		for ( pObj = LObject_GetList( cellCurrent, pLayer ); pObj; pObj
= pObj_next )
		{
			pObj_next = LObject_GetNext( pObj );
			LObject_Delete( cellCurrent, pObj );
		}
	}
	/* Clear out existing ports */
	LPort pPort, pPort_next;
	for ( pPort = LPort_GetList( cellCurrent ); pPort; pPort = pPort_next
)
	{
		pPort_next = LPort_GetNext( pPort );
		LPort_Delete( cellCurrent, pPort );
	}
	/* Clear out existing instances */
	LInstance pInst;
	LInstance pInst_next;
	for ( pInst = LInstance_GetList( cellCurrent ); pInst; pInst =
pInst_next )
	{
```

```
            pInst_next = LInstance_GetNext( pInst );
            LInstance_Delete( cellCurrent, pInst );
      }
      /*--------------*/

      /* Begin -- Uncomment this block if you are using L-Comp. */
      //LC_InitializeState();
      //LC_CurrentCell = cellCurrent;
      /* End */

      /* TODO: Put local variables here. */
      double s=1000;
      LMagnification one_magnif = {1,1};
      /* TODO: Begin custom generator code.*/
      LObject inner_area = LBox_New(cellCurrent,metal_layer, (-
length_inner)*s, (width_inner/2)*s,(0)*s, (-width_inner/2)*s);
      LObject outer_area = LBox_New(cellCurrent,metal_layer, (-
length_outer)*s, (width_outer/2)*s,(0)*s, (-width_outer/2)*s);
      LTransform_Ex99 outer_tx = LTransform_Set_Ex99((-length_inner -
length_taper)*s,(0)*s,LNormalOrientation,one_magnif);
      LObject_Transform_Ex99(outer_area,outer_tx);

      LPoint taper_points[4];
      taper_points[0] = LPoint_Set(-length_taper*s, width_outer/2*s);
      taper_points[1] = LPoint_Set(0, width_inner/2*s);
      taper_points[2] = LPoint_Set(0,-width_inner/2*s);
      taper_points[3] = LPoint_Set(-length_taper*s, -width_outer/2*s);

      LObject taper_area = LPolygon_New(cellCurrent,metal_layer,
taper_points, 4);
      LTransform_Ex99 taper_tx = LTransform_Set_Ex99((-
length_inner)*s,(0)*s,LNormalOrientation,one_magnif);
      LObject_Transform_Ex99(taper_area, taper_tx);
      /* End custom generator code.*/
}
extern "C" int UPI_Entry_Point(void)
{
      contactPad_main();
      return 1;
}
```

ii. Indirect Heating Generator Code: Full Device

```
      /*********************************************************************
***********
       * Cell Name: test_structure
       * Creator : Christopher Kodama
       *
       * Revision History:
       * 17 Sep 2015     Generated by L-Edit

*********************************************************************
****/
      #include <cstdlib>
      #include <cmath>
      #include <cstring>
      #include <cstdio>
      #include <string>
```

```
	#define EXCLUDE_LEDIT_LEGACY_UPI
	#include <ldata.h>


	/* Begin -- Uncomment this block if you are using L-Comp. */
	//#include <lcomp.h>
	/* End */

	/* TODO: Put local functions here. */
	void test_structure_main(void)
	{
		int iTmpUpiReturnCode = LUpi_GetReturnCode();
		/* Begin DO NOT EDIT SECTION generated by L-Edit */
		LCell   cellCurrent = (LCell)LMacro_GetNewTCell();
		double  gete_test_gap = LCell_GetParameterAsDouble(cellCurrent,
"gete_test_gap");
		double  gete_height = LCell_GetParameterAsDouble(cellCurrent,
"gete_height");
		double  tfr_width = LCell_GetParameterAsDouble(cellCurrent,
"tfr_width");
		/* End DO NOT EDIT SECTION generated by L-Edit */

		if(LUpi_GetReturnCode())
		{
			LDialog_MsgBox("Error: Tcell failed to read
parameters.");
			return;
		}
		LUpi_SetReturnCode(iTmpUpiReturnCode);

		/*--------------------------------------*/
		LFile pFile = LCell_GetFile( cellCurrent );

		/* Clear out existing elements */
		LLayer pLayer;
		for ( pLayer = LLayer_GetList( pFile ); pLayer; pLayer =
LLayer_GetNext( pLayer ) )
		{
			LObject pObj;
			LObject pObj_next;
			for ( pObj = LObject_GetList( cellCurrent, pLayer );
pObj; pObj = pObj_next )
			{
				pObj_next = LObject_GetNext( pObj );
				LObject_Delete( cellCurrent, pObj );
			}
		}
		/* Clear out existing ports */
		LPort pPort, pPort_next;
		for ( pPort = LPort_GetList( cellCurrent ); pPort; pPort =
pPort_next )
		{
			pPort_next = LPort_GetNext( pPort );
			LPort_Delete( cellCurrent, pPort );
		}
		/* Clear out existing instances */
		LInstance pInst;
		LInstance pInst_next;
```

```
            for ( pInst = LInstance_GetList( cellCurrent ); pInst; pInst =
pInst_next )
            {
                  pInst_next = LInstance_GetNext( pInst );
                  LInstance_Delete( cellCurrent, pInst );
            }
            /*--------------*/

            /* Begin -- Uncomment this block if you are using L-Comp. */
            //LC_InitializeState();
            //LC_CurrentCell = cellCurrent;
            /* End */

            /* TODO: Put local variables here. */
            double s=1000;
            LMagnification one_magnif = {1,1};
            LCell gete_pad = LCell_Find(pFile,"gete_pad");
            LCell tfr_pad = LCell_Find(pFile,"tfr_pad");
            double tfr_height_padding = 10;
            double gete_width_padding = 5;
            double aln_square_size = 100;
            LLayer gete_layer = LLayer_Find(pFile, "GeTe");
            LLayer tfr_layer = LLayer_Find(pFile, "TFR");
            LLayer aln_layer = LLayer_Find(pFile, "ALN");
            double gete_pad_width = 30;

            LTransform_Ex99 gete_pad_left_tx = LTransform_Set_Ex99((-
gete_test_gap/2)*s,(0)*s,LNormalOrientation,one_magnif);
            LTransform_Ex99 gete_pad_right_tx =
LTransform_Set_Ex99((gete_test_gap/2)*s,(0)*s,LRotate180,one_magnif);
            LTransform_Ex99 tfr_pad_top_tx =
LTransform_Set_Ex99((0)*s,(gete_pad_width/2 +
tfr_height_padding/2)*s,LNormalOrientation,one_magnif);
            LTransform_Ex99 tfr_pad_bottom_tx =
LTransform_Set_Ex99((0)*s,(-gete_pad_width/2 -
tfr_height_padding/2)*s,LRotate180,one_magnif);
            /* TODO: Begin custom generator code.*/
            LInstance gete_pad_left = LInstance_New_Ex99(cellCurrent,
gete_pad, gete_pad_left_tx, LPoint_Set(1,1), LPoint_Set(1,1));
            LInstance gete_pad_right = LInstance_New_Ex99(cellCurrent,
gete_pad, gete_pad_right_tx, LPoint_Set(1,1), LPoint_Set(1,1));
            LInstance tfr_pad_top = LInstance_New_Ex99(cellCurrent,
tfr_pad, tfr_pad_top_tx, LPoint_Set(1,1), LPoint_Set(1,1));
            LInstance tfr_pad_bottom = LInstance_New_Ex99(cellCurrent,
tfr_pad, tfr_pad_bottom_tx, LPoint_Set(1,1), LPoint_Set(1,1));

            LObject tfr = LBox_New(cellCurrent,tfr_layer, (-tfr_width/2)*s,
(gete_pad_width/2 + tfr_height_padding)*s,(tfr_width/2)*s, (-
gete_pad_width/2 - tfr_height_padding)*s);
            LObject gete = LBox_New(cellCurrent,gete_layer, (-
(gete_test_gap)/2 - gete_width_padding)*s,
(gete_height/2)*s,((gete_test_gap)/2 + gete_width_padding)*s, (-
gete_height/2)*s);
            LObject aln = LBox_New(cellCurrent,aln_layer, -
(aln_square_size/2)*s,(aln_square_size/2)*s,(aln_square_size/2)*s,-
(aln_square_size/2)*s);
            /* End custom generator code.*/
      }
      extern "C" int UPI_Entry_Point(void)
      {
```

```
            test_structure_main();
            return 1;
      }
```

D. Programming Code

Some components of the analysis in this thesis required computations over large arrays of data. Matlab was used in order to process and visualize the data. Mathematica was also used to help understand some analytical concepts. These functions are shown in the sections below.

a. Using Mathematica to determine form of material tensors from symmetry

```
e=Array[Subscript[ϵ,##]&,{3,3}];
u=Array[Subscript[μ,##]&,{3,3}];
xi=Array[Subscript[ξ,##]&,{3,3}];
zeta=Array[Subscript[ζ,##]&,{3,3}];
Oha = {{0,-1,0},{0,0,-1},{-1,0,0}};
Ohb = {{0,-1,0},{1,0,0},{0,0,1}};
Rx={{1,0,0},{0, -1, 0},{0, 0, -1}};
Ry={{-1,0,0},{0, 1, 0},{0, 0, -1}};
Rz={{-1,0,0},{0, -1, 0},{0, 0, 1}};
Rz4={{Cos[α],-Sin[α],0},{Sin[α], Cos[α], 0},{0, 0, 1}}/.α->π/2;
Inv={{-1,0,0},{0, -1, 0},{0, 0, -1}};
Mx={{-1,0,0},{0, 1, 0},{0, 0, 1}};
My={{1,0,0},{0, -1, 0},{0, 0, 1}};
Mz={{1,0,0},{0, 1, 0},{0, 0, -1}};
Rxy1 = RotationMatrix[\[Pi], {1, 1, 0}];
Rxy2 = RotationMatrix[\[Pi], {-1, 1, 0}];

(*Symmetry conditions for a medium with Subscript[O, h] symmetry *)
Solve[#.e == e.# & /@ {Oha, Ohb}];
e /. %[[1]] // MatrixForm
Solve[#.xi == Det[#] xi.# & /@ {Oha, Ohb}];
xi /. %[[1]] // MatrixForm

(*Symmetry conditions for an SRR without z-plane symmetry *)
Solve[#.e == e.# & /@ {Mx, Rz}];
e /. %[[1]] // MatrixForm
Solve[#.xi == Det[#] xi.# & /@ {Mx, Rz}];
xi /. %[[1]] // MatrixForm

(*Symmetry conditions for an SRR without z-plane symmetry *)
(*And also assuming anti-unitary operators*)
Solve[#.e == e.# & /@ {Mx, Rz, Mz}];
e /. %[[1]] // MatrixForm
Solve[#.xi == Det[#] xi.# & /@ {Mx, Rz, Mz}];
xi /. %[[1]] // MatrixForm

(*Symmetry conditions for an SRR with z-plane symmetry *)
(*And also assuming anti-unitary operators*)
Solve[#.e == Transpose[e].# & /@ {Mx, Rz}];
e /. %[[1]] // MatrixForm
```

```
Solve[Flatten[{#.xi == -Det[#] Transpose[
     zeta].#, #.zeta == -Det[#] Transpose[xi].#} & /@ {Mx, Rz}]];
xi /. %[[1]] // MatrixForm

(*Symmetry conditions for a square loop*)
Solve[#.e == e.# & /@ {Mx, Mz, My, Rz, Ry, Rx, Rz4, Inv, Rxy1, Rxy2}];
e /. %[[1]] // MatrixForm
Solve[#.xi == Det[#] xi.# & /@ {Mx, Mz, My, Rz, Ry, Rx, Rz4, Inv}];
xi /. %[[1]] // MatrixForm

(*Symmetry conditions for a square loop*)
(*And also assuming anti-unitary operators*)
Solve[#.e == Transpose[e].# & /@ {Mx, Mz, My, Rz, Ry, Rx, Rz4, Inv,
  Rxy1, Rxy2}];
e /. %[[1]] // MatrixForm
Solve[Flatten[{#.xi == -Det[#] Transpose[
     zeta].#, #.zeta == -Det[#] Transpose[xi].#} & /@ {Mx, Mz,
   My, Rz, Ry, Rx, Rz4, Inv}]];
xi /. %[[1]] // MatrixForm
```

b. Importing data from the TPS Spectra 300 into Matlab

```
function [ S ] = TPSimport2( fname, varargin )
%TPSIMPORT Used in conjunction with the TPS Spectra machine to produce data
%compatible with MATLAB. The input should be a .csv file, exported from
%the machine, which includes all possible output data for a given
%measurement.
% Example:
% S = TPSimport( 'I/KODAMA/datafile.csv' )
% The output S is a struct. The data in the scruct can be accessed in the
% following manner:
% Scanner Position
%  S.pos
% Sample Time-Domain Electric Field
%  S.Et_s
% Frequency
%  S.f
% Sample Frequency-Domain Electric Field Magnitude
%  S.Ef_s
% Sample Frequency-Domain Electric Field Phase (Rad)
%  S.Ep_s
% Reference Time-Domain Electric Field
%  S.Et_r
% Reference Frequency-Domain Electric Field Magnitude
%  S.Ef_r
% Reference Frequency-Domain Electric Field Phase (Rad)
%  S.Ep_r
% Transmittance (Ef_s/Ef_r) Magnitude
%  S.Tf
% Transmittance (Ef_s/Ef_r) Phase (Rad)
%  S.Tp
% Absorbance log10(Tf)
%  S.Af
% Time delay between start of reference and sample tiome domain data
%  S.td

 %%Setting up input parsing and default options
 options = inputParser;

 addParameter(options, 'useFFT',false);
```

```
addParameter(options, 'window', @(x) ones(x,1) );
addParameter(options, 'wind_opt','');
addParameter(options, 'trunc', 0);
addParameter(options, 'removeEcho', 0);
addParameter(options, 'autoEchoFind', 0);
addParameter(options, 'echoDelay', 0);
addParameter(options, 'echoAtten', 0);
addParameter(options, 'oscillationFilter', struct('n',0,'th',0));
addParameter(options, 'exemptReferenceFromTrunc', 0);
addParameter(options, 'exemptReferenceFromEcho', 0);
addParameter(options, 'smoothTf',0);
addParameter(options, 'pre_trunc',0);
addParameter(options, 'noIFFT',0);
addParameter(options, 'sample_is_reference',0);
parse(options, varargin{:});

useFFT = options.Results.useFFT;
window = options.Results.window;
wind_opt = options.Results.wind_opt;
trunc = options.Results.trunc;
removeEcho = options.Results.removeEcho;
autoEchoFind = options.Results.autoEchoFind;
echoDelay = options.Results.echoDelay;
echoAtten = options.Results.echoAtten;
oscillationFilter = options.Results.oscillationFilter;
exemptReferenceFromTrunc = options.Results.exemptReferenceFromTrunc;
exemptReferenceFromEcho = options.Results.exemptReferenceFromEcho;
smoothTf = options.Results.smoothTf;
pre_trunc = options.Results.pre_trunc;
noIFFT = options.Results.noIFFT;
sample_is_reference = options.Results.sample_is_reference;

%importing data from the Teraview machine
D=importdata(fname,',',2);

Tf = D.data;

f_name = D.colheaders(3);
if (strcmp(f_name,'Terahertz (THz)'))
 f = Tf(~isnan(Tf(:,3)),3)*1e12;
elseif strcmp(f_name,'Wavenumber (cm-1)')
 f = Tf(~isnan(Tf(:,3)),3)*3e8*100; % converting wavenumber (cm-1) to
hertz
end

%converting x axis units to time units
%conversion factors empirically determined.
t_name = D.colheaders(1);
t_data = Tf(:,[1,7]);
t_conv_fac = 1;
if strcmp(t_name,'Scanner position (mm)')
 t_conv_fac = 20/3;
elseif strcmp(t_name,'Optical Delay (mm)')
 t_conv_fac = 10/3;
end

%converting picoseconds to seconds
t_conv_fac = t_conv_fac*1e-12;
t_data = t_data * t_conv_fac;
```

```
%computing time delay between start times of the reference and sample
%time domain data
td = t_data(1,1) - t_data(1,2);

%modifying phase data of sample electric field to account for time
%delay

Ep_s = Tf(~isnan(Tf(:,6)),6);

%manually calculating transmittance and absorbance

%need to take the square root of the data, since the data is power
%spectrum, while amplitude spectrum is what is wanted for most material
%parameter extraction data.
Ef_s = sqrt(Tf(~isnan(Tf(:,4)),4));
Ep_r = Tf(~isnan(Tf(:,12)),12);

Ef_r = sqrt(Tf(~isnan(Tf(:,10)),10));

%Since transmittance is manually calculated, the Tf in the file is not
%needed, but is included in the ouput in case it is wanted.
Tf_old = Tf(~isnan(Tf(:,14)),14);

%Removes possible NaN data points which have been known to appear in
%the imported data.
t_s = t_data(~isnan(t_data(:,2)),1);
t_r = t_data(~isnan(t_data(:,2)),2);
t_s_old = t_s;
t_r_old = t_r;

%Delta time between time points
DT = t_r_old(2) - t_r_old(1);

%Removes possible NaN data points
Et_s = Tf(~isnan(Tf(:,2)),2);
Et_r = Tf(~isnan(Tf(:,8)),8);

%Since Et_s and Et_r are ifft-calculated from the fourier transformed
%data in the data file, the Et_s and Et_r originally in the file are
%not needed, but are available in the output object as well.
Et_s_old = Et_s;
Et_r_old = Et_r;


NFFT = length(Ef_r) * 2;

% This section calculates the time domain signal values using the ifft
% of the spectrum data, if desired.
if(useFFT && ~noIFFT)
 Ef_r_full = [Ef_r; flipud(Ef_r)];
 Ep_r_full = [Ep_r; -flipud(Ep_r)];
 Ef_s_full = [Ef_s; flipud(Ef_s)];
 Ep_s_full = [Ep_s; -flipud(Ep_s)];
 NFFT = length(Ef_r_full);


 Et_r = ifft((Ef_r_full) .* exp(1i * Ep_r_full), 'symmetric');
 Et_s = ifft((Ef_s_full) .* exp(1i * Ep_s_full), 'symmetric');

 t_r = t_r_old(1) + linspace(0, 1./f(end)./2.*NFFT, NFFT);
```

```
 t_s = t_s_old(1) + linspace(0, 1./f(end)./2.*NFFT, NFFT);
 DT = t_r(2) - t_r(1);
end

trunc_pt = t_r < t_r_old(end);
num_padding = 0;
num_padding_front = 0;
num_padding_ref_addl = 0;

%This section handles two parts. First, it truncates the time domain
%signal and applies a window if the settings dictate so. Second, it
%takes the fourier transform of the time domain data.
if(trunc && useFFT)
 %finds the index where the truncation should begin
 [~, trunc_ind] = min(abs(t_s - trunc));

  %If the options dictate that the reference should be exempt from
  %truncation, then only the sample is truncated (by replacing the
  %ending part of it with zeros)
  if(exemptReferenceFromTrunc)
   Et_s(trunc_ind:end) = ...
    zeros(length(Et_s(trunc_ind:end)),1);
  else
   num_padding = num_padding + length(Et_r(trunc_ind:end));
   Et_r(trunc_ind:end) = [];
   Et_s(trunc_ind:end) = [];
  end

end

%sometimes, the initial part of the signal is desired to be truncated.
if(pre_trunc)
 [~, pre_trunc_ind] = min(abs(t_s - pre_trunc));
 num_padding_front = length(Et_s(1:pre_trunc_ind));

 if(sample_is_reference)
  Et_r = Et_s(1:pre_trunc_ind-1);
  num_padding_ref_addl = length(Et_s(pre_trunc_ind:end));
  t_r = t_s;
  td = 0;
 end
 Et_s(1:pre_trunc_ind) = [];

end

%if desired, this code can automatically detect and filter out echoes
%using a simple echo removal filter.
 if(useFFT && removeEcho)

 if(autoEchoFind == 1)
  [pks,pklocs,~,prominences] = findpeaks(Et_r);
  [~,sorted] = sort(prominences,'descend');
  pks = pks(sorted);
  pklocs = pklocs(sorted);
  echoAtten = pks(2)/pks(1);
  N = pklocs(2) - pklocs(1);
  echoAtten2 = pks(3) / pks(1);
  N2 = pklocs(3) - pklocs(2);
  a = [1 zeros(1,N),echoAtten,zeros(1,N2),echoAtten2];
 else
```

```
 N = floor(echoDelay ./ DT);
 a = [1 zeros(1,N),echoAtten];
end



Et_s_noEcho = filter(1,a,Et_s);

 if(exemptReferenceFromEcho)
 Et_r_noEcho = Et_r;
 else
 Et_r_noEcho = filter(1,a, Et_r);
 end


Et_r = Et_r_noEcho;
Et_s = Et_s_noEcho;
end

if(useFFT)

 [~, Et_r_pk_ind] = max(Et_r);
 [~, Et_s_pk_ind] = max(Et_s);
 Et_r_left_num = Et_r_pk_ind;
 Et_s_left_num = Et_s_pk_ind;
 Et_r_right_num = length(Et_r) - Et_r_left_num;
 Et_s_right_num = length(Et_s) - Et_s_left_num;
 %These if statements apply different variations of windowing to the
 %time signals.
 if(strcmp(wind_opt,'direct'))
  %directly apply the windowing function to the signal
  wind_s = window(length(Et_s));
  wind_r = window(length(Et_r));
 elseif(strcmp(wind_opt,'pk_sym_small'))
  %Apply the windowing function, but with the window centered on
  %the peak of the signal and using the smaller of two possible
  %windows.
  Et = Et_r;
  Et_left_num = Et_r_left_num;
  Et_right_num = Et_r_right_num;
  if(Et_left_num < Et_right_num)
   partial_wind = window(Et_left_num*2);
   wind = [partial_wind; zeros(length(Et)-Et_left_num*2,1)];
  else
   partial_wind = window(Et_right_num*2);
   wind = [zeros(length(Et) - Et_right_num*2,1); partial_wind];
  end
  wind_r = wind;

  Et = Et_s;
  Et_left_num = Et_s_left_num;
  Et_right_num = Et_s_right_num;
  if(Et_left_num < Et_right_num)
   partial_wind = window(Et_left_num*2);
   wind = [partial_wind; zeros(length(Et)-Et_left_num*2,1)];
  else
   partial_wind = window(Et_right_num*2);
   wind = [zeros(length(Et) - Et_right_num*2,1); partial_wind];
  end
  wind_s = wind;
```

```
elseif(strcmp(wind_opt,'pk_sym'));
 %Apply the windowing function, but with the window centered on
 %the peak of the signal and using the larger of two possible
 %windows (window gets truncated).
 Et = Et_r;
 Et_left_num = Et_r_left_num;
 Et_right_num = Et_r_right_num;
 if(Et_left_num > Et_right_num)
  full_wind = window(Et_left_num*2);
  wind = full_wind(1:length(Et));
 else
  full_wind = window(Et_right_num*2);
  wind = full_wind(end-length(Et)+1:end);
 end
 wind_r = wind;

 Et = Et_s;
 Et_left_num = Et_s_left_num;
 Et_right_num = Et_s_right_num;
 if(Et_left_num > Et_right_num)
  full_wind = window(Et_left_num*2);
  wind = full_wind(1:length(Et));
 else
  full_wind = window(Et_right_num*2);
  wind = full_wind(end-length(Et)+1:end);
 end
 wind_s = wind;

elseif(strcmp(wind_opt,'pk_asym'))
 %Apply the windowing function, but with the window centered on
 %the peak of the signal and both sides extending
 %non-symetrically to the ends of the signal.
 Et_left_num = Et_r_left_num;
 Et_right_num = Et_r_right_num;

 left_wind = window(Et_left_num*2);
 left_wind = left_wind(1:Et_left_num);
 right_wind = window(Et_right_num*2);
 right_wind = right_wind(end-Et_right_num+1:end);
 wind_r = [left_wind; right_wind];



 Et_left_num = Et_s_left_num;
 Et_right_num = Et_s_right_num;

 left_wind = window(Et_left_num*2);
 left_wind = left_wind(1:Et_left_num);
 right_wind = window(Et_right_num*2);
 right_wind = right_wind(end-Et_right_num+1:end);
 wind_s = [left_wind; right_wind];

else
 wind_s = window(length(Et_s));
 wind_r = window(length(Et_r));
end

%Adds some additional padding to account for any previous
%truncation operations
```

```
 Et_s = [zeros(num_padding_front,1);Et_s;zeros(num_padding,1)];
 Et_r = [Et_r;zeros(num_padding+num_padding_ref_addl,1)];

 wind_s = [zeros(num_padding_front,1);wind_s;zeros(num_padding,1)];
 wind_r = [wind_r;zeros(num_padding+num_padding_ref_addl,1)];

 Et_s_old = Et_s;
 Et_r_old = Et_r;

 %applies the windows
 Et_s = Et_s .* wind_s;
 Et_r = Et_r .* wind_r;

 %calculates the FFT
 EF_s = fft(Et_s,NFFT);
 EF_r = fft(Et_r,NFFT);


 EF_s = EF_s(1:NFFT/2+1);
 EF_r = EF_r(1:NFFT/2+1);


 f = linspace(0,1,NFFT/2+1)'/(2*DT);

 Ep_r = unwrap((angle(EF_r)) );

 Ep_s = unwrap( angle(EF_s) - 2*pi*f*td );

 Ef_r = abs(EF_r);
 Ef_s = abs(EF_s);

else
 wind_s = zeros(size(Et_s));
 wind_r = zeros(size(Et_r));
end

Tf = Ef_s .* Ef_r ./ (Ef_r).^2;
Tp = unwrap(Ep_s - Ep_r);

%specialized function to remove oscillations from the Transmission
%function due to fabry perot oscillations
if(oscillationFilter.n ~= 0)
 Tf = reflect_remove(f,Tf,oscillationFilter.n, oscillationFilter.th);
 Tp = reflect_remove(f,Tp,oscillationFilter.n, oscillationFilter.th);
end

%specialized function to smooth the transmission function
if(smoothTf)
 [~,locs,~,~] = findpeaks(Tf(f<3e12));
 diffs = diff(sort(locs));
 diffs = diffs(diffs > mean(diffs));
 smooth_window = round(mean(diffs));
 Tf = smooth(Tf,smooth_window);
end

%calculating absorbance from the transmission data.
Af = log10(Tf.^2);

%assembles a struct with all the data organized in it.
S = struct('t_r',t_r,...
```

```
    't_s', t_s,...
    'Et_s',Et_s,...
    'f',f,...
    'Ef_s',Ef_s,...
    'Ep_s',Ep_s,...
    'Et_r',Et_r,...
    'Ef_r',Ef_r,...
    'Ep_r',Ep_r,...
    'Tf',Tf,...
    'Tp',Tp,...
    'Af',Af,...
    'td',td,...
    'wind_s',wind_s,...
    'wind_r',wind_r,...
    'Et_r_old',Et_r_old,...
    't_s_old',t_s_old,...
    't_r_old',t_r_old,...
    'Et_s_old',Et_s_old,...
    'wind_r_old',0,...
    'wind_s_old',0,...
    'Tf_old',Tf_old,...
    'Dt',t_r(2) - t_r(1));


end
```

c. Specialized unwrapping of phase data to avoid error propagation at lower frequencies

```
function [ Hp_adj ] = linphase_unwrap( Hp, f, f_unwrap )
%LINPHASEUNWRAP Unwraps the phase of a function Hp. Assuming there is a
%significant amount of error at low frequencies, this function first
%unwraps the entire function and then analyzes the phase at frequencies
of
%f_unwrap and higher. Assuming linear phase propagation, the phase
values
%at those frequencies are linearly modeled and used to extrapolate the
%value of the phase shift at DC. This value is then subtracted from the
%entire dataset to get an improved value for the phase unwrap.


f_interp = f(f > f_unwrap);
f_no_interp = f(f <= f_unwrap);
Hp_interp = Hp(f > f_unwrap);
Hp_no_interp = Hp(f <= f_unwrap);

%unwraps backwards
Hp_no_interp = unwrap(Hp_no_interp(end:-1:1));
%makes it the right direction again
Hp_no_interp = Hp_no_interp(end:-1:1);
Hp_interp = unwrap(Hp_interp);

dif_check = Hp_interp(1) - Hp_no_interp(end);
if((dif_check) > 0)
 Hp_no_interp = Hp_no_interp + 2 * pi;
```

```
end


func = fit(f_interp/1e12,Hp_interp,'poly1');
phase_shift = func.p2;


Hp_adj = [Hp_no_interp; Hp_interp] - phase_shift;

end
```

d. Calculating indices of refraction using the Newton-Rhapson extraction method

This function relies on the use of several other helper functions in order to calculate some functions, namely (18), (19), and (20), as well as all of their first and second derivatives. Due to the excessive length of these helper functions, they have not been included in this appendix.

```
function Dat = ncalc_duvillaret(importfile, frange, L, varargin)
%Calculate an approximation for the index of refraction using data from
%terahertz time domain spectroscopy (THz-TDS) and an newton-rhapson-based
%algorithm developed by Duvillaret et al. in 1996.
%Parameters:
%importfile is either a csv datafile from TPS Spectra 3000 or an object
%outputted from the TPSimport script
%L is the length of the sample
%frange is the range of frequencies used for the approximation
%Optional Options:
% N3_c_fname : file name of the substrate, if the material of interest is
% deposited on a substrate. Default to ' ' for no substrate
% usingFP : a boolean, use this if the iteration should attempt to remove
% Fabry-Perot oscillations.
% gen_nkplot : set to true if you would like a figure plot in the generated
% output object (default: 1)
% maxiter: the maximum amount of iterations (default: 50), will stop after
this amount
% even if tolerances are not met.
% D_Tmeas: The amount of tolerance on the transmission coefficient
% measurement during THz TDS. Default 0.01
% D_L: the amount of tolerance on the thickness measurement of the sample,
% default to 1e-6 or 1 micrometer.
% D_Tmeas_arg: the amount of tolerance on the phase of the transmission
% coefficient measurement during THz TDS. Default 0.1.

fmin = frange(1);
fmax = frange(2);

%setting some default parameters
```

```
%index of refraction of air
%speed of light
Nair = 1;
c = 3e8;
N1 = Nair;

options = inputParser;
addParameter(options, 'N3_c_fname',' ');
addParameter(options, 'usingFP',0);
addParameter(options, 'gen_nkplot',1);
addParameter(options, 'maxiter', 500);
addParameter(options, 'D_Tmeas_abs', 0.01);
addParameter(options, 'D_L', 1e-6);
addParameter(options, 'D_Tmeas_phase', 0.1);

parse(options, varargin{:});

N3_c_fname = options.Results.N3_c_fname;
usingFP = options.Results.usingFP;
gen_nkplot = options.Results.gen_nkplot;
maxiter = options.Results.maxiter;
D_Tmeas_abs = options.Results.D_Tmeas_abs;
D_L = options.Results.D_L;
D_Tmeas_phase = options.Results.D_Tmeas_phase;

if(strcmp(N3_c_fname,' '))
 N3 = Nair;
else N3 = 0;
end

if(isstruct(importfile))
 S = importfile;
else
 S = TPSimport(importfile); % see for details: help TPSimport
end
f = S.f;
w = 2*pi*f;

Tmeas = S.Tf.*exp(1i*S.Tp);

freqrange = f > fmin & f < fmax;
Tmeas = Tmeas(freqrange);
w = w(freqrange);
f = f(freqrange);

Tmeas_abs = abs(Tmeas);
Tmeas_phase = linphase_unwrap(angle(Tmeas), f, 1e12);

%creates substrate n if necessary
%Preparing n3_c
if(N3 == 0)
 if(iscell(N3_c_fname))
  n_substrate = N3_c_fname{2};
  n_substrate_f = N3_c_fname{1};
 else
 %For the case when a substrate is present
  n_substrate_data = open(N3_c_fname);
  n_substrate = n_substrate_data.ns_c;
  n_substrate_f = n_substrate_data.f;
 end
```

```
 N3 = interp1(n_substrate_f,n_substrate,f,'spline');
else
 N3 = N3*ones(size(w));
end

% end of substrate creation code

n2_calc = -c./(w*L).*Tmeas_phase + Nair;
k2_A = (n2_calc - real(N1)).* (n2_calc - real(N3))./...
 ((n2_calc + real(N1)).*(n2_calc + real(N3))).*...
 cos(2*n2_calc.*w*L/c);
k2_D = (n2_calc + real(N1)).* (n2_calc + real(N3))./...
 (2.*n2_calc.*(real(N1) + real(N3))).*...
 exp(-(-imag(N3)).*w*L/c).*...
 Tmeas_abs;


cardan_root = @(p,q) (-q/2 + sqrt(q.^2/4 + p.^3/27)).^(1/3)...
 +(-q/2 - sqrt(q.^2/4 + p.^3/27)).^(1/3);

k2_calc = abs((log(cardan_root(1./k2_A, -k2_D./k2_A)).*(-c./(w.*L))));

Ks = 1:length(w);
Kinit = Ks(1);
n2_calc_K = n2_calc(Kinit);
k2_calc_K = k2_calc(Kinit);


for K=Ks
 w_K = w(K);
 N3_K = N3(K);
 Tmeas_abs_K = Tmeas_abs(K);
 Tmeas_phase_K = Tmeas_phase(K);
 iter = 1;

 while(iter < maxiter)
  if(usingFP)
   [FP_abs, FP_phase] = FP_func(N1, n2_calc(K), k2_calc(K), N3_K, w_K, L,
c);
   Tmeas_abs_K = Tmeas_abs(K)./FP_abs;
   Tmeas_phase_K = Tmeas_phase(K) - FP_phase;
  end

  [drho, dphi] = drho_dphi_func(Tmeas_abs_K, Tmeas_phase_K, ...
   N1, n2_calc_K, k2_calc_K, N3_K, Nair, w_K, L, c, usingFP);


  [D_drho, D_dphi] = ...
   D_drho_dphi_func(Tmeas_abs_K, N1, N3_K, w_K, L, c, usingFP, n2_calc_K,
k2_calc_K, D_Tmeas_abs, D_Tmeas_phase, D_L);
  if( (dphi < abs(D_dphi) / 10) && (abs(drho) < D_drho / 10))
   %fprintf('condition met in %d iterations\n', iter);
   break;
  end
  [grad_delta, A] = delta_func_derivs(Tmeas_abs_K, Tmeas_phase_K, N1,
n2_calc_K, k2_calc_K, N3_K,...
   Nair, w_K, L, c, usingFP);

  r_K = [n2_calc_K; k2_calc_K];
  r_Kplus1 = r_K - A\grad_delta;
```

```
  n2_calc_K = r_Kplus1(1);
  k2_calc_K = (r_Kplus1(2));
  iter = iter + 1;

 end
 if iter==maxiter
  fprintf('warning! max iterations reached \n')
 end
 n2_calc(K) = n2_calc_K;
 k2_calc(K) = k2_calc_K;
end
nkplot = 0;
if(gen_nkplot)
 nkplot = figure('visible','off');
 subplot(2,1,1)
 plot(f,n2_calc);grid on;
 ylabel n
 title 'Complex Index of Refraction'
 subplot(2,1,2)
 plot(f,(k2_calc));grid on;
 ylabel k
 xlabel 'Frequency'
end

[Tcalc_abs, Tcalc_phase] = T_func(N1, n2_calc, k2_calc, N3, Nair, w, L, c,
usingFP);
Tcalc = Tcalc_abs .* exp(1i*Tcalc_phase);
alpha = 4*pi.*f.*k2_calc/c;
Dat = struct(...
 'n', n2_calc,...
 'k', k2_calc,...
 'n_c', n2_calc - 1i.*k2_calc,...
 'Tmeas',Tmeas,...
 'Tmeas_phase',Tmeas_phase,...
 'Tmeas_abs',Tmeas_abs,...
 'Tcalc',Tcalc,...
 'Tcalc_abs',Tcalc_abs,...
 'Tcalc_phase',Tcalc_phase,...
 'f',f,...
 'wn',f/c/100,...
 'delta',c./2./w./(k2_calc),...
 'alpha',alpha/100,... % in cm-1
 'attn',exp(-alpha*L),... % in percent
 'S',S,'nkplot',nkplot);
end
```

e. Calculating indices of refraction using Fixed-Point Iteration

```
function Dat = ncalc_fixpt(importfile, frange, L, varargin)
%Calculate the fixed point iteration approximation for index of refraction
%using data from THz time domain spectroscopy.
%Parameters:
%importfile is either a csv datafile from TPS Spectra 3000 or an object
%outputted from the TPSimport script
%L is the length of the sample
```

```
%frange is the range of frequencies used for the approximation
%Optional Options:
% N3_c_fname : file name of the substrate, if the material of interest is
% deposited on a substrate. Default to ' ' for no substrate
% useFP : use this if the iteration should attempt to remove
% Fabry-Perot oscillations. Set useFP to the number of FP oscillations
% you would like to remove, and set to -1 if you would like to try to
% remove all of them (default 0).
% gen_nkplot : set to true if you would like a figure plot in the generated
% output object (default: 1)
% extraction_type: sets the type of extraction.
% 'ref_T1' (default) means that the open-air reference will be used as the
% calculation reference, and the first transmitted pulse would be used as
% the sample calculation.
% T1_FP1 means that the first transmitted pulse will be used as reference,
% and the first Fabry-Perot reflection will be used as the sample
% calculation.
% and etc, for ref_FP2 and T1_FP2
% maxiter: the maximum amount of iterations (default: 50), will stop after
this amount
% even if tolerances are not met.
% toln2: tolerance on the n value for the material under test. default 1e-5
% tolk2: tolerance on the k value for the material under test. default 1e-9

fmin = frange(1);
fmax = frange(2);

%setting some default parameters
%index of refraction of air
%speed of light
Nair = 1;
c = 3e8;
N1 = Nair;

%Parsing optional variables and their defualt values
options = inputParser;
addParameter(options, 'N3_c_fname',' ');
addParameter(options, 'useFP',0);
addParameter(options, 'gen_nkplot',1);
addParameter(options, 'extraction_type',1);
addParameter(options, 'maxiter', 50);
addParameter(options, 'toln2', 1e-5);
addParameter(options, 'tolk2', 1e-9);
parse(options, varargin{:});

N3_c_fname = options.Results.N3_c_fname;
useFP = options.Results.useFP;
gen_nkplot = options.Results.gen_nkplot;
extraction_type = options.Results.extraction_type;
maxiter = options.Results.maxiter;
toln2 = options.Results.toln2;
tolk2 = options.Results.tolk2;

if(strcmp(N3_c_fname,' '))
 N3 = Nair;
else N3 = 0;
end

if(isstruct(importfile))
 S = importfile;
```

```
else
 S = TPSimport2(importfile);
end

f = S.f;
w = f*2*pi;


Tmeas = (S.Tf).*exp(1i*(S.Tp));
%Truncating the frequency values to the desired range
freqrange = f > fmin & f < fmax;
%Truncating the transmission values to the desired range
Tmeas = (Tmeas(freqrange));
w = w(freqrange);
f = f(freqrange);

f_unwrap = 1e12;


Tmeas_abs = (abs(Tmeas));
%Linearly unwrapping phase as described by withayachumnankul et
%al. in 2005
Tmeas_phase = linphase_unwrap(angle(Tmeas), f, f_unwrap);

%Preparing n3_c, if it is defined.
if(N3 == 0)
 %For the case when a substrate is present
 n_substrate_data = open(N3_c_fname);
 n_substrate = n_substrate_data.ns_c;
 n_substrate_f = n_substrate_data.f;
 N3 = interp1(n_substrate_f,n_substrate,f,'spline');
else
 N3 = N3*ones(size(w));
end


%Preallocating array containing complex index of refraction of sample
n2_calc_vals = zeros(size(Tmeas,1),maxiter);
k2_calc_vals = zeros(size(Tmeas,1),maxiter);

%Initial guess for complex index of refraction (surprisingly accurate)
n2_calc_vals(:,1) = -c./(w*L).*Tmeas_phase + Nair;
k2_calc_vals(:,1) = -c./(w*L).*log(Tmeas_abs);

n2_calc = n2_calc_vals(:,1);
k2_calc = k2_calc_vals(:,1);

%Other parameters, as required by the paper, dealing with Fabry-Perot
%reflections. Initial Fabry-Perot Estimate is 1.

FP = ones(size(Tmeas_abs));

%different coefficients and products needed if different references and
%sample signals are used
if(strcmp(extraction_type,'ref_FP1'))
 coeff = @(n2_calc, k2_calc)...
  (4*(n2_calc - 1i * k2_calc) .*(N3)) ./ ((n2_calc - 1i * k2_calc + N1) .*
(n2_calc - 1i * k2_calc + N3))...
  .* ...
```

```
  ((N1 - (n2_calc - 1i * k2_calc))./ (n2_calc - 1i * k2_calc + N1) .* (N3 -
(n2_calc - 1i * k2_calc))./ (n2_calc - 1i * k2_calc + N3));
 prod = 3;
 use_Nair = 1;
elseif(strcmp(extraction_type,'T1_FP1'))
 coeff = @(n2_calc, k2_calc)...
  ((-N1 + (n2_calc - 1i * k2_calc))./ (n2_calc - 1i * k2_calc + N1) .* (-N3
+ (n2_calc - 1i * k2_calc))./ (n2_calc - 1i * k2_calc + N3));
 prod = 2;
 use_Nair = 0;
elseif(strcmp(extraction_type,'ref_FP2'))
 coeff = @(n2_calc, k2_calc)...
  (4*(n2_calc - 1i * k2_calc) .*(N3)) ./ ((n2_calc - 1i * k2_calc + N1) .*
(n2_calc - 1i * k2_calc + N3))...
  .* ...
  ((-N1 + (n2_calc - 1i * k2_calc))./ (n2_calc - 1i * k2_calc + N1) .* (-N3
+ (n2_calc - 1i * k2_calc))./ (n2_calc - 1i * k2_calc + N3)).^2;
 prod = 5;
 use_Nair = 1;
elseif(strcmp(extraction_type,'T1_FP2'))
 coeff = @(n2_calc, k2_calc)...
  ((-N1 + (n2_calc - 1i * k2_calc))./ (n2_calc - 1i * k2_calc + N1) .* (-
N3 + (n2_calc - 1i * k2_calc))./ (n2_calc - 1i * k2_calc + N3)).^2;
 prod = 4;
 use_Nair = 0;
else
 coeff = @(n2_calc, k2_calc)...
  (4*(n2_calc - 1i * k2_calc) .*(N3)) ./ ((n2_calc - 1i * k2_calc + N1) .*
(n2_calc - 1i * k2_calc + N3));
 prod = 1;
 use_Nair = 1;
end

%Actual fixed-point iteration starts here
 for K=2:(maxiter)

  FP_abs = abs(FP);
  FP_phase = angle(FP);

  TmeasFP_abs = Tmeas_abs./FP_abs;
  TmeasFP_phase = linphase_unwrap(Tmeas_phase - FP_phase, f, f_unwrap);


  n2_calc = 1./prod.* (use_Nair.*Nair - c./(w*L) .* (...
  TmeasFP_phase...
  - (angle(coeff(n2_calc, k2_calc))...
  )...
   ) );


  k2_calc = 1./prod .* -c./(w*L) .* (...
  log( TmeasFP_abs ) - ...
   log(abs(...
     coeff(n2_calc, k2_calc)...
     ))...
  );

  N2_calc = n2_calc - 1i .* k2_calc;

  if(useFP == -1)
```

```
  FP = (...
   (1 - ((N2_calc - N1).*(N2_calc - N3) ./ ((N2_calc + N1).*(N2_calc + N3))
) .* exp(-2*(1i)*N2_calc.*w*L/c))...
   ).^(-1);
  FP(isnan(FP)) = 1;
  elseif(useFP)
   R2 = (N2_calc - N1)./ (N2_calc + N1) .* (N2_calc - N3)./ (N2_calc + N3);
   P2 = exp(-1i .* N2_calc .* w .* L ./ c);
   FP = 0;
   for k = 0:useFP
    FP = FP + (R2.*P2).^k;
   end
  else
   FP = 1;
  end

  %Checking to see if the values have converged for n and k
  conv_range = (f > 0.5e12 & f < 3e12);
  [diffn2, maxdifn2loc] = max(abs(n2_calc_vals(conv_range,K-1) -
n2_calc(conv_range)));
  [diffk2, maxdifk2loc] = max(abs(k2_calc_vals(conv_range,K-1) -
k2_calc(conv_range)));

  n2_calc_vals(:,K) = n2_calc;
  k2_calc_vals(:,K) = k2_calc;

  if (diffn2 < toln2 && diffk2 < tolk2)
   %disp(['converged in ' num2str(K) ' iterations!']);
   break;
  end

 end


n2_calc_final = n2_calc_vals(:,K);
k2_calc_final= k2_calc_vals(:,K);

%Display error messages if the solution did not seem to converge
if(K == maxiter)
 conv_range_f = f(conv_range);
 disp('warning max num iterations reached');
 disp([num2str(diffn2) ' at ' num2str(conv_range_f(maxdifn2loc)/1e12)]);
 disp([num2str(diffk2) ' at ' num2str(conv_range_f(maxdifk2loc)/1e12)]);
 disp(['absorbance diff of '
num2str(4*pi.*conv_range_f(maxdifk2loc).*diffk2/c/100) ' cm-1']);
end


N2_calc_final = n2_calc_final - 1i * k2_calc_final;

nkplot = 0;

if(gen_nkplot)
 nkplot = figure('visible','off');
 subplot(2,1,1)
 plot(f,n2_calc_final);grid on;
 ylabel n
 title 'Complex Index of Refraction'
 subplot(2,1,2)
 plot(f,(k2_calc_final));grid on;
```

```
 ylabel k
 xlabel 'Frequency'
end

Tcalc = coeff(n2_calc_final, k2_calc_final) .* exp(-1i .*
(prod.*(n2_calc_final - 1i*k2_calc_final) - Nair).* w .* L./c)*FP;
Tcalc_abs = abs(Tcalc);
Tcalc_phase = unwrap(angle(Tcalc));

alpha = 4*pi.*f.*k2_calc_final/c;
Dat = struct(...
 'n', n2_calc_final,...
 'k', k2_calc_final,...
 'n_c', N2_calc_final,...
 'Tmeas',Tmeas,...
 'Tmeas_phase',Tmeas_phase,...
 'Tmeas_abs',Tmeas_abs,...
 'Tcalc',Tcalc,...
 'Tcalc_abs',Tcalc_abs,...
 'Tcalc_phase',Tcalc_phase,...
 'f',f,...
 'wn',f/c/100,...
 'delta',c./2./w./(k2_calc_final),...
 'alpha',alpha/100,...%in inverse centimeters
 'attn',exp(-alpha*L),...
 'S',S,'nkplot',nkplot);
```

REPORT DOCUMENTATION PAGE

Form Approved
OMB No. 0704-0188

PLEASE DO NOT RETURN YOUR FORM TO THE ABOVE ADDRESS.

1. REPORT DATE *(DD-MM-YYYY)*	2. REPORT TYPE	3. DATES COVERED *(From - To)*
24-03-2016	Master's Thesis	Sept 2014 – March 2016

4. TITLE AND SUBTITLE

Tunable Terahertz Metamaterials with Germanium Telluride Components

5a. CONTRACT NUMBER

5b. GRANT NUMBER

5c. PROGRAM ELEMENT NUMBER

6. AUTHOR(S)

Kodama, Christopher H, 2d Lt, USAF

5d. PROJECT NUMBER

16G143

5e. TASK NUMBER

5f. WORK UNIT NUMBER

7. PERFORMING ORGANIZATION NAME(S) AND ADDRESS(ES)

Air Force Institute of Technology
Graduate School of Engineering and Management (AFIT/EN)
2950 Hobson Way
Wright-Patterson AFB OH 45433-7765

8. PERFORMING ORGANIZATION REPORT NUMBER

AFIT-ENG-MS-16-M-025

9. SPONSORING/MONITORING AGENCY NAME(S) AND ADDRESS(ES)

Air Force Office of Scientific Research (AFOSR)
Attn: Kenneth Goretta, Program Officer
875 N. Randolph St, Suite 325, Room 3024
Arlington, VA 22203-1768
(703) 696-7349, kenneth.goretta@us.af.mil

10. SPONSOR/MONITOR'S ACRONYM(S)

AFOSR/RTA

11. SPONSOR/MONITOR'S REPORT NUMBER(S)

12. DISTRIBUTION/AVAILABILITY STATEMENT

Distribution statement A.
Approved for public release; distribution is unlimited.

13. SUPPLEMENTARY NOTES

This work is declared a work of the U.S. Government and is not subject to copyright protection in the United States.

14. ABSTRACT

Terahertz (THz) technology is an emerging field with many exciting applications. THz waves can be used to locate explosives and illicit drugs in security applications, or DNA and other molecule resonances in medical applications. THz frequencies represent the next level of modern, high-speed computing, but they also can be used for covert battlefield communications links. Metamaterials are an integral part of THz technology because they can be used to create exotic material properties—permittivities and permeabilities—in a part of the frequency spectrum that is otherwise rather empty and passive. This work aims to acquire a fuller understanding of THz metamaterials in terms of background and theory, and then use this understanding to create a few novel, actively tunable structures using the phase-change material germanium telluride.

15. SUBJECT TERMS

metamaterials, germanium telluride, split-ring resonator, phase change material

16. SECURITY CLASSIFICATION OF:			17. LIMITATION OF ABSTRACT	18. NUMBER OF PAGES	19a. NAME OF RESPONSIBLE PERSON
a. REPORT	b. ABSTRACT	c. THIS PAGE			Dr. Ronald A. Coutu, Jr, AFIT/ENG
U	U	U	UU	243	19b. TELEPHONE NUMBER *(Include area code)* (937) 255-1906 x7230, ronald.coutu@afit.edu